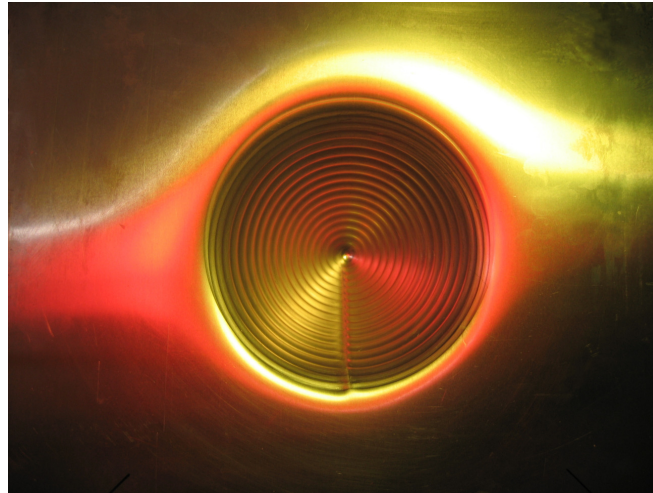


The Mechanics of Incremental Sheet Forming



Kathryn Jackson

Pembroke College

February 2008

This dissertation is submitted for the degree of Doctor of Philosophy

University of Cambridge
Department of Engineering





“Incremental sheep farming?”

HRH The Duke of Edinburgh

December 2004

Preface

This dissertation is the result of my own work and includes nothing which is the outcome of work done in collaboration except where specifically indicated in the text. No part of this dissertation has been or is currently being submitted for any other qualification at this or any other university.

This dissertation is 56,104 words in length and contains 62 figures, which is within the limits set by the Degree Committee for Engineering.

Kathryn Jackson

February 2008

Abstract

Incremental sheet forming (ISF) is a flexible process where an indenter moves over the surface of a sheet of metal to form a 3D shell incrementally by a progression of localised deformation. Despite extensive research into the process, the deformation mechanics is not fully understood. This thesis presents new insights into the mechanics of ISF applied to two groups of materials: sheet metals and sandwich panels.

A new system for measuring tool forces in ISF is commissioned. The system uses six loadcells to measure reaction forces on the workpiece frame. Each force signal has an uncertainty of ± 15 N. This is likely to be small in comparison to tool forces measured in ISF.

The mechanics of ISF of sheet metals is researched. Through-thickness deformation and strains of copper plates are measured for single-point incremental forming (SPIF) and two-point incremental forming (TPIF). It is shown that the deformation mechanisms of SPIF and TPIF are shear parallel to the tool direction, with both shear and stretching perpendicular to the tool direction. Tool forces are measured and compared throughout the two processes. Tool forces follow similar trends to strains, suggesting that shear parallel to the tool direction is a result of friction between the tool and workpiece.

The mechanics of ISF of sandwich panels is investigated. The mechanical viability of applying ISF to various sandwich panel designs is evaluated by observing failure modes and damage under two simple tool paths. ISF is applicable to metal/polymer/metal sandwich panels. This is because the cores and faceplates are ductile and largely incompressible, and therefore survive local indentation during ISF without collapse. Through-thickness deformation, tool forces and applicability of the sine law for prediction of wall thickness are measured and compared for a metal/polymer/metal sandwich panel and a monolithic sheet metal. The mechanical results for ISF of sheet metals transfer closely to sandwich panels. Hence, established knowledge and process implementation procedures derived for ISF of monolithic sheet metals may be used in the future for ISF of sandwich panels.

Key Words

Incremental sheet forming

Sheet metal

Sandwich panel

Deformation mechanics

Tool forces

Sine law

Acknowledgements

Firstly, I would like to thank my supervisor, Dr. Julian Allwood, for his advice and guidance throughout the project. I would also like to thank my advisor, Prof. Ian Hutchins, for productive review meetings.

I gratefully acknowledge the EPSRC for providing a studentship which financially supported this research.

Generous donation of sandwich panel samples from several sources enabled experimental work to be carried out. I would like to express warm thanks to Johan ter Maat of Corus Hylite for providing Hylite®, Philipp Zach of Alulight International for providing Alulight®, Olivier Brun of Arcelor Commercial FCSE for providing Sollight® and Anders Axelsson of Lamera for providing Hybrix®. Further thanks go to Philipp Zach for carrying out foaming of precursor Alulight® in Sweden.

I would like to thank Martin Landert of the Department of Materials Science and Metallurgy, University of Cambridge, with whom I collaborated with for the first trials of ISF of sandwich panels.

Warm thanks go to Will Eve of Inca Digital Printers Ltd for printing grid patterns on sandwich panels and sheet metals for strain measurement, free of charge.

I would like to thank Len Howlett of the Materials Lab at Cambridge University Engineering Department for his continual support and guidance throughout the PhD, and Alan Heaver of the Mechanics Lab for his support and advice for microscopy and mechanical testing.

I am very grateful to all the workshop staff at the Institute for Manufacturing and CUED main site for their technical support. In particular, I would like to thank Alistair Ross for technical advice and organising workshop resources, Richard Christmas for preparation of sheet metal blanks, Steve Robinson for water jet cutting and John Beavis for precise preparation of various pieces. Further thanks go to Stewart Fordham of the IfM and Simon Smith for re-wiring the tool force measuring system.

Finally, I would like to thank Neil Houghton for his skilled design of the ISF machine, and continuing technical support throughout the project.

Publications

Some of the material in this thesis has been presented at conferences and published in journal papers. These papers are listed below.

Journal Papers

Jackson, K. P., Allwood, J. M. and Landert, M., 2008. *Incremental Forming of Sandwich Panels*. Journal of Materials Processing Technology. Article in press.

Jackson, K. P. and Allwood, J. M., 2008. *The Mechanics of Incremental Sheet Forming*. Journal of Materials Processing Technology. Article in press.

Conference Papers

Allwood, J. M., Houghton, N. E. and Jackson, K. P., 2005. *The Design of an Incremental Sheet Forming Machine*. In: SheMet'05 International Conference on Sheet Metal. Erlangen, Germany. pp. 471-478.

Jackson, K. P. and Allwood, J. M., 2006. *Incremental Sheet Forming Research at Cambridge University*. In: 4th JSTP International Seminar on Precision Forging. Nara, Japan. pp. 207-210.

Raithatha, A. M., Jackson, K. P., Duncan, S. R. and Allwood, J. M., 2006. *New Method for Modeling Plastic Deformation in Incremental Sheet Forming*. In: Joint Conferences of 2006 IEEE Conference on Control Applications (CCA), 2006 IEEE Computer Aided Control Systems Design Symposium (CACSD) and 2006 IEEE International Symposium on Intelligent Control (ISIC). Munich, Germany.

Jackson, K. P., Allwood, J. M. and Landert, M., 2007. *Incremental Forming of Sandwich Panels*. In: SheMet'07 International Conference on Sheet Metal. Palermo, Sicily. pp. 591-598.

Raithatha, A. M., Duncan, S., Jackson, K. and Allwood, J., 2007. *Second Order Cone Programming in Modeling Incremental Deformation*. In: American Control Conference. New York City.

Table of Contents

1.	Introduction	1
2.	Review	6
2.1	Equipment and Methods of Implementation of ISF	7
2.1.1	Workpiece Support and Indenter Configurations	8
2.1.2	Machines for Tool Driving	12
2.1.3	Indenter Design	15
2.1.4	Procedures for Process Implementation	17
2.2	Experimental Methods of Analysis of ISF	20
2.2.1	Geometry and Geometric Accuracy	20
2.2.2	Strains	21
2.2.3	Tool Force	22
2.2.4	Thickness after Forming and Surface Roughness	23
2.3	Numerical Methods of Analysis of ISF	23
2.3.1	Integration Scheme	24
2.3.2	Element Type and Mesh Size	26
2.4	Results of Analysis of ISF	28
2.4.1	Applicable Materials and Sheet Thickness	28
2.4.2	Surface Finish	29
2.4.3	Deformation Mechanics	31
2.4.4	Tool Forces	38
2.4.5	Forming Limits	41
2.4.6	Geometric Accuracy	45
2.4.7	Uniformity of Wall Thickness	47
2.4.8	Economic and Ecological Implications	48
2.5	Sandwich Panel Forming	49
2.5.1	Metal/Polymer/Metal Sandwich Panels	51
2.5.2	Metal/Metal Fibre/Metal Sandwich Panels	52
2.5.3	Metal/Metal Foam/ Metal Sandwich Panels	53
2.6	Scope of Present Research	54
3.	Commissioning of a Tool Force Measuring System	56
3.1	Tool Force System Design	57
3.1.1	Design of Amplifier Circuit	58

3.1.2	Design of Software for Reading Tool Force and Position.....	59
3.2	Calibration of Tool Force System.....	60
3.2.1	Calibration of APCI-ADADIOCS Card.....	61
3.2.2	Combination of Sectional Calibrations	63
3.3	Accuracy of Tool Force System	64
3.3.1	Calibration Accuracy.....	64
3.3.2	Drift.....	68
3.3.3	Noise	70
3.3.4	Combination of Errors.....	72
3.4	Summarising Comments	73
4.	The Mechanics of Incremental Forming of Sheet Metals	74
4.1	Through-thickness deformation in SPIF and TPIF	75
4.1.1	Selection and Characterisation of Materials.....	75
4.1.2	Preparation of Sheets.....	77
4.1.3	Forming.....	78
4.1.4	Separation of Plates and Measurement of Deformation.....	80
4.1.5	Analysis of Deformation.....	81
4.1.6	Experimental Error.....	84
4.1.7	Results and Observations	91
4.1.8	Summary of Findings.....	97
4.2	Comparison of Tool Forces in SPIF and TPIF	98
4.2.1	Method	98
4.2.2	Results and Observations	101
4.2.3	Summary of Findings.....	106
4.3	Discussion	106
4.3.1	Comparison of Strains to Previously Published Results	106
4.3.2	Comparison of Mechanisms of SPIF and TPIF to the Idealised Mechanism	108
4.3.3	The Accuracy of the Sine Law Prediction of Thickness	109
4.3.4	Comparison of Tool Forces to Deformation Mechanics	112
4.3.5	Discussion of Trends in Strains.....	116
4.3.6	Transferability of the Results to Other ISF Processes.....	119
4.4	Concluding Remarks	123
5.	The Mechanics of Incremental Forming of Sandwich Panels	124
5.1	The Mechanical Feasibility of ISF of Various Sandwich Panel Designs	125
5.1.1	Selection of Materials.....	125

5.1.2	Design of Tool Paths	126
5.1.3	Failure Modes and Damage.....	127
5.1.4	Results and Observations	129
5.1.5	Summary of Findings	134
5.2	Comparison of the Influence of ISF on a Sandwich Panel and Sheet Metal.....	135
5.2.1	Selection of Materials.....	135
5.2.2	Influence of Tool Radius and Vertical Pitch on Tool Force.....	137
5.2.3	Displacement of Upper and Lower Surfaces and Accuracy of the Sine Law.....	144
5.2.4	Summary of Findings	148
5.3	Discussion	148
5.3.1	Mapping of the Mechanical Feasibility of ISF of Sandwich Panels	148
5.3.2	Trends in Deformation of MS/PP/MS and Aluminium.....	150
5.3.3	Trends in Tool Forces of MS/PP/MS and Aluminium	151
5.3.4	The Accuracy of the Sine Law Prediction of Thickness	154
5.4	Concluding Remarks	155
6.	Summary and Outlook	157
6.1	Summary.....	158
6.2	Outlook	159
6.2.1	Further Research for the Mechanics of ISF.....	159
6.2.2	Alternative Techniques for ISF of Metal Foam Sandwich Panels.....	161
6.2.3	Real-Time Process Control	162
6.2.4	Future Machine Designs.....	163
	Appendix – Calculation of Experimental Errors.....	165
A.1	Derivation of Absolute Error in Strain ϵ_{11}.....	168
A.2	Derivation of Absolute Error in Strain γ_{13}.....	169
A.3	Derivation of Absolute Error in Strain γ_{23}.....	173
A.4	Derivation of Absolute Error in Wall Thickness t_I	174
	References	157

1. Introduction

Incremental sheet forming (ISF) is an umbrella term describing a diverse range of processes in which a sheet of metal is formed into a 3D shell by a simple tool causing a progression of localised deformation. The most ancient forms of metal forming processes were manual incremental forming processes, including spinning, where a craftsman forms a rotating workpiece over a mandrel, and repoussé or chasing, in which impressions are formed on a sheet of metal by hammering against a sack filled with sand. One of the earliest examples of an incrementally formed sheet metal product, where the flat disk is likely to have been formed by forging, is the Nebra sky disc, dated to c. 1600 BC (Fig. 1).



Fig. 1. The Nebra sky disc (c. 1600BC)

Despite its ancient roots, it is only in the last two decades that the usage and capabilities of ISF have grown significantly. This can be attributed to two main factors. Firstly, advances in manufacturing technology, particularly the development of computer numerically controlled (CNC) machinery, has enabled what is traditionally a skilled craft to be carried out with some level of automation. Secondly, a growing interest in customisation has brought about a motivation for developing forming processes which do not require specialised tooling. Tooling can be prohibitively expensive when considering small batch sizes or one-offs.

The need for flexibility of the process to enable the widest possible range of products to be formed has caused a growing interest in one particular variant of ISF: asymmetric incremental sheet forming. In this process a computer numerically controlled (CNC) indenter moves over the surface of a sheet of metal along an asymmetric path, usually of contours or a spiral of descending depth, defining the form of the product. Hence a diverse range of asymmetric products can be formed without specialised tooling by moving the tool along an appropriately designed path. The phrase ‘incremental sheet forming’ has therefore recently become most strongly associated with asymmetric CNC incremental sheet forming processes, and shall take this meaning throughout the rest of this thesis. The most basic form of asymmetric ISF is single-point incremental forming (SPIF) (Fig. 2a), where a sheet of metal is clamped rigidly around its edges and formed on one surface by a single indenter. This can be compared to a conventional deep-drawing process in which a blank holder allows a sheet of metal to be drawn between a male and female die set which define the complete shape of the product, as illustrated in Fig. 2b.

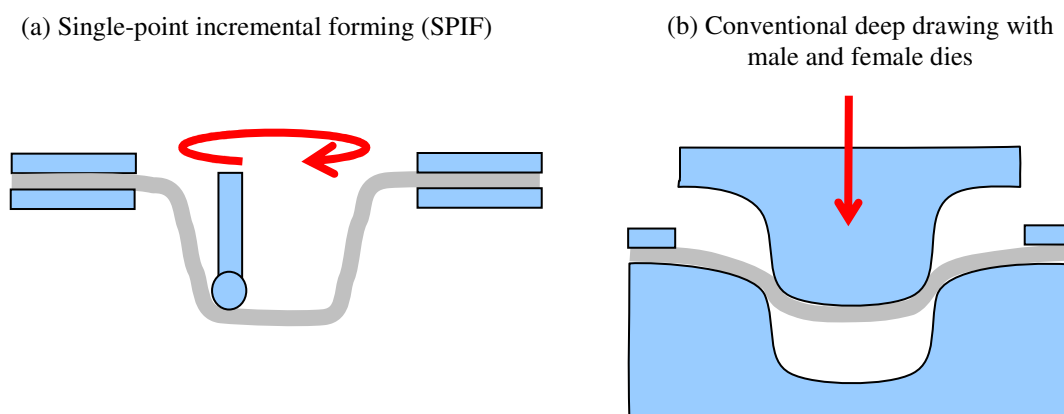


Fig. 2. Comparison of single-point incremental forming (SPIF) (a) and deep drawing (b).

The potential applications of ISF are diverse and include specialised medical products such as ankle supports (Ambrogio et al [1]), dental prosthetics (Tanaka et al [2, 3]), surfaces of dies and moulds (Allwood et al [4]), cranial implants (Duflou et al [5]), solar ovens for third world applications (Jeswiet et al [6]) and automobile panels (Matsui et al [7]). Dies with surfaces formed by ISF are shown in Fig. 3a, and a 1/8 size model of the leading end of a shinkansen, formed by Amino in Japan, is shown in Fig. 3b.

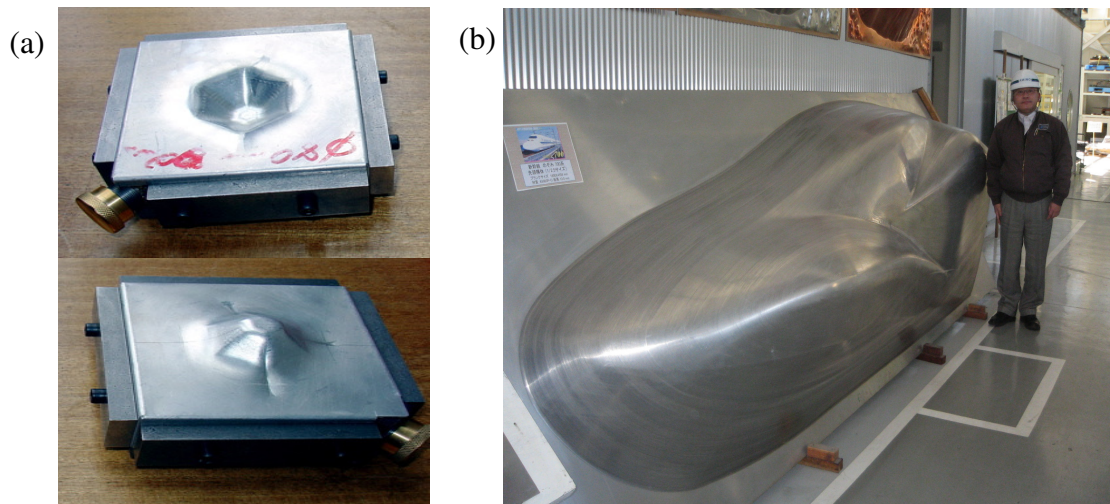


Fig. 3. Products formed by ISF: (a) inexpensive dies with surfaces formed by ISF; (b) a 1/8 scale model of the leading end of a shinkansen (Japanese bullet train), made by Amino in Japan.

Academic and industrial interest in ISF has grown significantly over the last decade, with particular interest in Japan, Europe and Canada. Research has focussed on three main areas: development of tooling and methods of tool path design to enable a wider range of products to be formed to a higher quality; measurement of the influence of process design variables on process capabilities; and investigation of the process mechanics through numerical simulation and measurement of tool forces. An understanding of the deformation mechanism is fundamental to allowing accurate numerical models of the process to be developed for tool path design and process control, and to develop an understanding of the increased forming limits observed in ISF in comparison to pressing. Despite extensive research, the mechanics of the process are not well understood; results are limited and have not been fully supported by experimental verification. Furthermore, research on the mechanics of ISF has focussed on only one group of materials: sheet metals. The applicability of the process to alternative groups of materials, such as composite sandwich panels, and the associated deformation mechanics, is not well understood. The aim of this thesis is therefore to provide new insights into the deformation mechanics of ISF applied to two groups of materials: sheet metals and sandwich panels.

Previous work in the areas of incremental sheet forming and sandwich panel forming are reviewed in Chapter 2, highlighting the main gaps in current knowledge and leading to a definition of the scope of the current work. A tool force system is designed and commissioned in Chapter 3 in preparation for experimental work reported later in the thesis. Chapter 4 investigates the mechanics of incremental forming of sheet metals, including measurements of through-thickness deformation of specially prepared copper plates, and comparison of tool forces in SPIF and TPIF. The deformation mechanics of ISF of sandwich panels is researched in Chapter 5, leading to the summary and outlook of the work in Chapter 6.

2. Review

To provide a basis for the research presented in this thesis, this chapter is a review of previous work carried out in two relevant areas: incremental sheet forming and sandwich panel forming. A wide body of previous research on incremental sheet forming will be distilled into four sections: equipment and methods of implementation of ISF; experimental methods of analysis of ISF; numerical methods of analysis of ISF and results of analysis of ISF. Forming of sandwich panels is a less broad area of research and hence previous work can be reviewed concisely under three formable sandwich panel designs: metal/polymer/metal sandwich panels; metal/metal fibre/metal sandwich panels; and metal/metal foam/metal sandwich panels. The chapter ends with a definition of the scope of the present work with the aim of addressing some of the gaps in the knowledge which were highlighted in the review.

Research in ISF has been mapped in four previous reviews over the last seven years. Shima [8] completed the first review of the state of the art of ISF in 2001, which describes the main variations in equipment and experimental set-up including unusual innovations such as incremental micro-forming. A second review of the field was given by Hagan and Jeswiet in 2003 [9]. This review covers some principal results for spinning and shear forming, in addition to modern asymmetric ISF methods. In 2005 a broader review of ISF was provided by Jeswiet et al [10], which received contributions from the leaders of the key European and Canadian research groups. This included equipment configurations, tool path design procedures and the main results in terms of accuracy, forming limits and surface finish. However, the review mainly focussed on progress in Europe and Canada; many novel innovations of ISF developed in Japan were not reviewed, possibly because Japanese work is often published in the Japanese language. In 2006, Allwood and Utsonomiya [11] provided the first review of flexible metal forming innovations in Japan, ranging from extrusion of bar, forming of tubes, flexible rolling and rotary sheet forming processes. In a related field, a review of spinning, shear forming and flow forming processes by Wong et al [12] was written in 2003. This gives a detailed history of the evolution and key results of rotary sheet forming processes, some of which, including the development of the ‘sine law’, is directly relevant to research in ISF. The review presented in this chapter will build on the previous reviews by providing a new analysis of up-to-date literature from around the globe.

2.1 Equipment and Methods of Implementation of ISF

The equipment used for ISF consists of three main components: the workpiece support and configuration of indenters; the machinery for driving the indenter; and the design of the indenter itself. A diverse range of designs of all three of these components have been explored with the ultimate aim of creating a process that is fully flexible and capable of forming the widest possible range of geometries. The way in which this equipment is used can be described by the process implementation procedure, from product design to finished product. The equipment used for ISF and process implementation procedures are reviewed below.

2.1.1 Workpiece Support and Indenter Configurations

The two most common forms of ISF are known as single point incremental forming (SPIF) and two-point incremental forming (TPIF), as defined by Jeswiet et al [10]. SPIF involves forming a clamped workpiece with a single mobile indenter. The clamp can either be a generic shape that is larger than the perimeter of the formed part (Fig. 4a) or can support the perimeter of the formed part (Fig. 4b). The first configuration has the advantage of being the only fully flexible method of ISF requiring no product-specific tooling, but the disadvantage of allowing for large geometric errors due to the workpiece being largely unsupported. This method is often used for products with unusual or uniquely shaped perimeters, for example an ankle support by Ambrogio et al [1] and a cranial implant by Duflou et al [5]. The second configuration (Fig. 4b) has the advantage of constraining deformation outside the perimeter of the tool path but the disadvantage of requiring a clamp that is specific to the perimeter of the product. This is more commonly used where the perimeter of the product is a simple shape. For example, Duflou et al [13] used a circular frame to support cones that were formed by SPIF, whilst Jeswiet et al [6] used a rectangular frame to support the perimeter of a solar cooker formed by SPIF. In both SPIF configurations, it is only possible to form concave geometries with no re-entrant features.

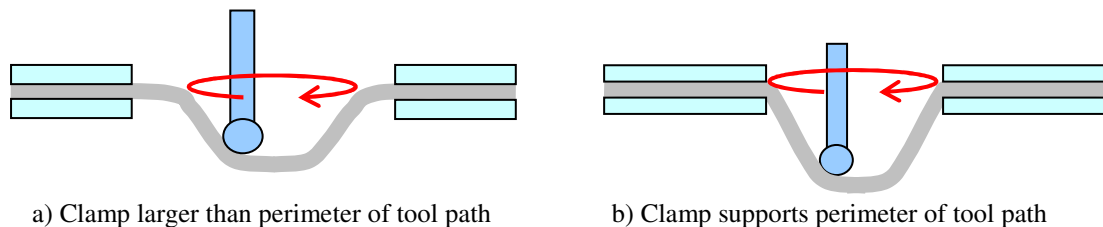


Fig. 4. Single-point incremental forming (SPIF): (a) clamp is a generic shape that is larger than the perimeter of the formed part; (b) the shape of the clamp defines the perimeter of the formed part.

In TPIF the workpiece is formed by two tools which have been used in five different configurations: one mobile indenter and a narrow central support post (Fig. 5a); one mobile indenter and a partial die which has a shaped upper surface defining the profile of the product (Fig. 5b); one mobile indenter and a full positive die defining the full shape of the product (Fig. 5c); one mobile indenter and a full negative die defining the full shape of the product (Fig. 5d); and two fully mobile indenters (Fig. 5e). TPIF has two key advantages over SPIF: (1) deformation of the sheet is more constrained and

hence a higher accuracy can be achieved; and (2) re-entrant features can be formed depending on the range of movement of the indenter(s). However, it has the disadvantage of requiring specialised tooling for all configurations apart from where two mobile indenters are used. Although TPIF is therefore not a fully flexible process, it has the advantage over pressing that only one die is required and this can be made out of inexpensive and soft material suitable for rapid machining such as wood or polymer. This is significantly cheaper than hardened steels traditionally used for pressing.

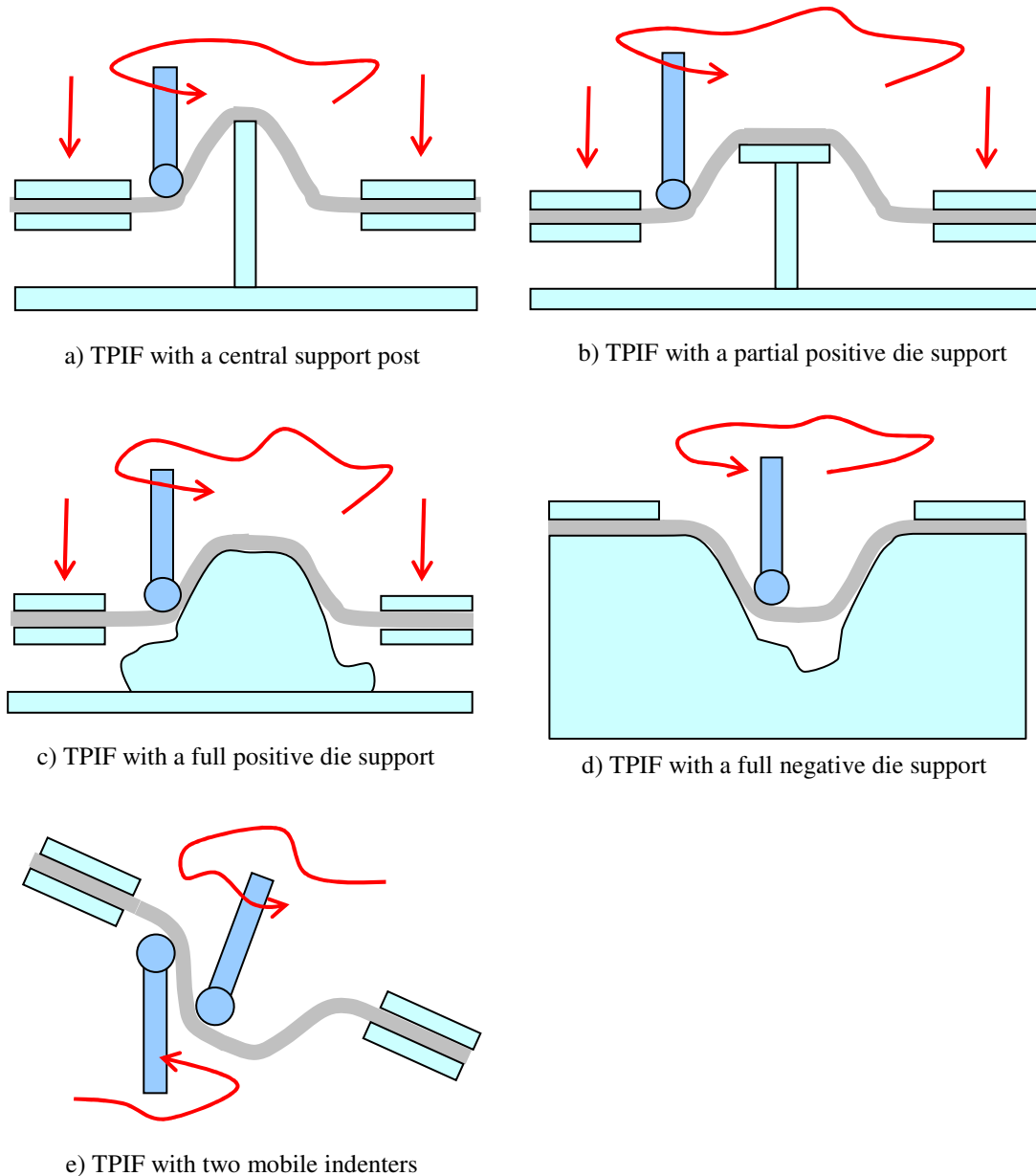


Fig. 5. Configurations of two-point incremental forming (TPIF): (a) one mobile indenter and a central support post; (b) one mobile indenter and a partial positive die support; (c) one mobile indenter and a full positive die support; (d) one mobile indenter and a full negative die support; and (e) two mobile indenters.

TPIF with a central support post (Fig. 5a) was the original configuration of TPIF, first used by Matsubara in 1994 [14]. In this configuration either the support post can move upwards or the workpiece frame can move downwards to increase the depth of the product on successive laps of the indenter. TPIF with a partial positive die support (Fig. 5b) has been used more recently, for example by Hirt et al [15] for forming square-based truncated pyramids. TPIF against a full positive die support (Fig. 5c), which offers greater constraint of the deformation, was used for example by Ceretti et al [16] to form a truck differential housing. This is also the preferred method of the Japanese company Amino, manufacturer of ISF machines, due to the constraint offered by the positive die. This raises the interesting observation that, from an industrial perspective, the most effective method of achieving accuracy is to sacrifice flexibility in preference of constraint of the deformation by a positive die support; other methods for improving geometric accuracy, as reviewed later in Section 2.4.6, are not yet implemented. TPIF against a negative die (Fig. 5d) was used by Giardini et al [17] for a concave shell in an investigation of the influence of working parameters on product quality. However, the advantages of using a negative die as opposed to no die at all were not explained, although the negative die is likely to offer little or no reaction against the sheet being formed other than at the point of contact of the indenter for simple concave geometries. Finally, TPIF with two mobile indenters (Fig. 5e) is the most flexible configuration of ISF, and was originally developed by Yoshikawa et al [18] in 1999. More recently this has been implemented using two robot arms by Meier et al [19], and using synchronisation of a robot arm with an X-Y-Z table by Maidagan et al [20]. Although this technique offers the greatest flexibility and a wide diversity of products which it is possible to form, it is the most complicated to implement in terms of tool path planning and machine synchronisation.

A range of alternative and less common designs of ISF have been developed for specialised applications. A process specifically for forming flanges, known as dieless flange forming, was developed by Powell and Andrew at the University of Cambridge in 1992 [21, 22]. This involves making repeated passes between rollers to create a flange around the edge of a sheet of metal. Potential applications were identified as airframes, architectural components and specialised vehicle parts. Flexible processes have been developed for forming sheets with gentle curvature without specialised

tooling. In 1999 Tanaka et al [23] developed a process where a sheet of metal is curved by repeatedly pressing between upper and lower elastic tools whilst translating sideways between punches. A similar process for curving sheet metal in two directions was developed by Yoon and Yang in 2001 [24], where the elastic tool was replaced with a punch set consisting of four rigid lower support punches and one upper central punch. In 2003 Yoon and Yang [25] developed incremental roll forming for curving unsupported sheets in two directions, where the rigid punch set was replaced by a set of rollers which allowed the sheet to remain in constant contact with the tool, therefore reducing the process time. A further specialised development of ISF is incremental forming of foils on a microscopic scale, demonstrated by Saotome and Okamoto in 2001 [26]. Potential applications include micro-electro-mechanical system parts and micro devices. For experimental evaluation of 2D simplified FE models, Muresan et al [27] developed a tool and blank holder which allows approximately plane strain forming. A horizontal cylindrical tool forms the workpiece by moving backwards and forwards against a positive die.

Clamping of the workpiece in both SPIF and TPIF has almost always involved using a continuous frame to rigidly clamp around the edge of the workpiece. However, Ceretti et al [16] experimented with a frame which supported the sheet on balls to allow material to flow into the deformation area. This was found to reduce thinning in TPIF against a positive die, but wrinkling occurred and hence it was not a suitable option. Tanaka et al [23] developed a novel workpiece support by using four opposing springs to hold the workpiece in a frame that pivots about two axes for ISF between two elastic tools. This design has three potential advantages over clamping with a rigid frame: (1) wasted flange material that is usually cut off around the perimeter of product held in a rigid frame can be avoided; (2) the edge of the product does not necessarily need to be flat in a 2-dimensional plane; and (3) any shape of product can be supported. However, this method has the disadvantage of virtually removing the force on the sheet that reacts against the indenter, and hence it can only be used when two opposing tools that are in equilibrium work against each other, such as the elastic tools used by Tanaka et al [23]. This novel configuration of clamping is illustrated in Fig. 6.

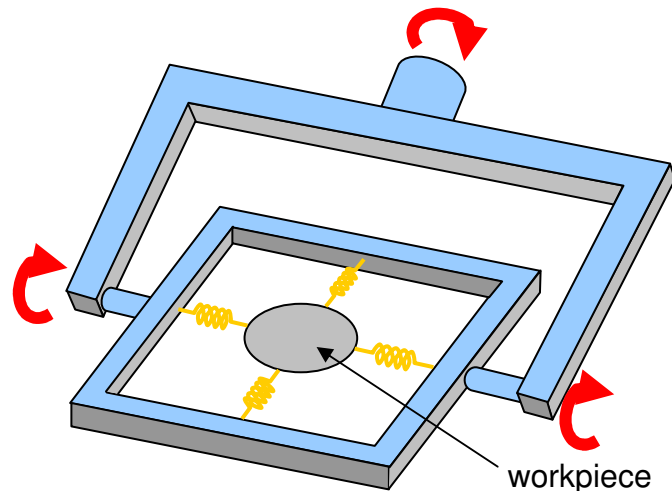


Fig. 6. Pivoted frame with coil springs developed by Tanaka et al [23] to support the workpiece in ISF between two elastic tools.

2.1.2 Machines for Tool Driving

The machinery which supports and drives the indenter in ISF has a significant influence on the process capabilities because it determines the allowable tool speed, positioning accuracy, complexity of tool path programming, limiting tool forces and degrees of freedom of movement. Specialised ISF machines are still not widely commercially available and are expensive; the only company manufacturing ISF machines is Amino in Japan and these range from approximately £100,000 to £200,000. Hence, most research groups working in the area have developed their own machines by adapting existing CNC milling machines.

For research purposes, the simplest machines in terms of power and control used for ISF are hand-powered and manually operated, as used by Iseki in 2002 for forming rectangular shells with vertical sides [28]. However, manual machines can be labour intensive and difficult to control along complicated tool paths, and therefore in order to achieve a higher level of automation suitable for an industrial environment most research groups have adapted widely available and easily programmable CNC milling machines by replacing the cutting tool with an indenter. One of the earliest examples of ISF on a numerically controlled machine was by Kitazawa at Shinshu University in Japan in 1993 [29]. Other groups using adapted CNC machines for ISF research include the Harbin Institute of Technology in China, KU Leuven in Belgium, the

University of Brescia and the University of Calabria in Italy, Queen's University in Canada, the University of Bath in England, the University of Dortmund in Germany and the University Lucian Blaga in Romania. The forming area used on adapted CNC milling machines for research is typically between 180 x 180 mm and 300 x 300 mm.

Despite the popularity of adapting CNC milling machines for ISF due to computerised tool path programming, a problem that has been reported recently is excessive wear on the bearings due to higher tool forces in ISF than conventional milling processes. A further limitation is that when the workpiece is mounted on a solid machine bed the underside is not accessible, and hence it is not possible to use a second indenter to form the workpiece from the opposite side or to observe the deformation from underneath. With the aim of overcoming some of these limitations, specialised ISF machines have been developed both by industry and by research groups. The earliest example of ISF on a custom-built numerically controlled machine was given by Iseki in 1992 [30]. Amino in Japan has developed machines of a range of sizes with a single mobile indenter suitable for SPIF or TPIF against a partial die, support post or full negative or positive die. More recently Amino has developed the Space Former, which combines stretching over a positive die with incremental forming, as described by Maki [31]. The smaller machines by Amino have the advantage of offering a stiff support for the indenter by allowing the indenter only to move vertically whilst the workpiece moves in the horizontal plane, as shown in Fig. 7a. The largest machine offered by Amino has a range of 6.5 x 2.5 m, and in this case the workpiece remains stationary whilst the indenter moves in the horizontal and vertical planes (Fig. 7b).

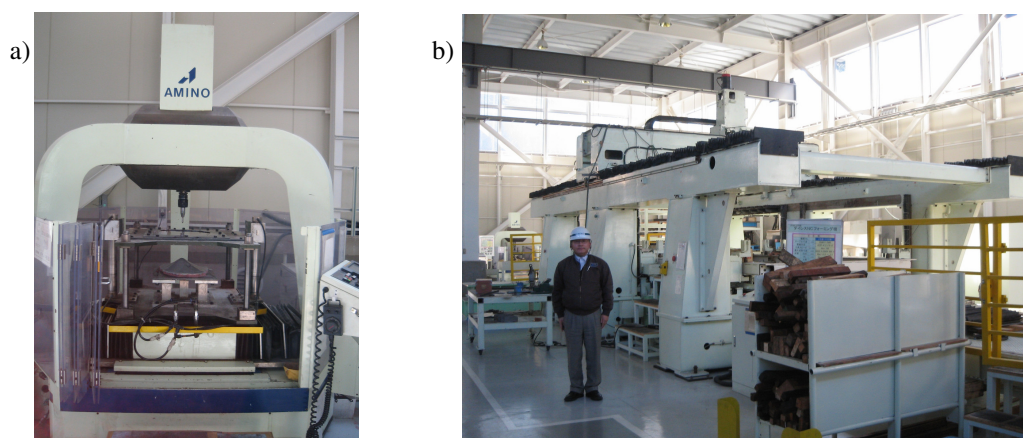


Fig. 7. Specialised ISF machines built by Amino: (a) one of the smallest machines beginning a TPIF program over a positive die; (b) the largest machine with a range of 2.5 x 6.5m.

A specialised rig for ISF was commissioned at the University of Cambridge in October 2004, developed by Allwood et al [32] (Fig. 8). This machine has the unique capability of offering simultaneous and real-time recording of tool force and tool position. The tool force is measured by six loadcells supporting the workpiece frame. The underside of the workpiece is accessible to enable support from underneath, a second indenter or observation with a stereovision camera. The indenter is designed to withstand forces up to 13 kN in the vertical direction and 6.5 kN in the horizontal directions.



Fig. 8. The specialised ISF rig at the University of Cambridge

Robot arms have been researched as a means of supporting and driving the indenter to increase the number of degrees of freedom and allow a greater range of movement in comparison to the machines described above. Meier et al [33] at Ruhr Bochum in Germany are using two large robot arms to form opposite sides of a workpiece mounted vertically, whilst Maidagan et al [20] have also developed a system where two robot arms move in unison to incrementally form a sheet of metal. Lamminen et al [34] in Finland have demonstrated successful TPIF using a single robot arm to form a horizontally mounted workpiece against a partial positive die, and Schäfer and Schraft [35] are using a robot arm for ISF with a hammering tool. However, problems have been reported in terms of positioning accuracy due to the moments on the robot arms, and hence sophisticated control systems are necessary to achieve a high geometric accuracy.

2.1.3 Indenter Design

The indenter for ISF consists of a working head which applies a localised force to the sheet to cause the deformation, a shaft separating the head from the machine and an interface to attach the tool to the machine. The most common design of forming head used for ISF is a sphere or spherical section because it is able to turn corners or roll across the surface whilst maintaining a smooth contact with the sheet for good surface finish, as well as being able to form the sheet from a wide range of angles. Jeswiet et al [6] and Leach et al [36] have used a simple method of welding a ball bearing to the end of a straight shaft, which allows vertical walls to be formed without interfering with the workpiece. In order to achieve greater stiffness than a straight shaft, Allwood et al [32] have designed a cone with external half-angle of 67.5° with a head of spherical section. Ceretti et al [16] have developed a tool post with a retracting mechanism to limit tool force on an adapted CNC milling machine used for ISF. A further variation on the tool support is to use several indenters attached to one rigid support base that move in unison in order to incrementally form several identical products simultaneously. Matsubara [37] demonstrated that a productivity approaching the rate of pressing for relatively small products can be achieved using this technique. The most common material used for indenters in ISF is hardened steel in order to withstand abrasive wear.

Spherical-headed tools have often been designed to roll over the surface to minimise sliding contact to improve surface finish on the sheet. Kim and Park [38] demonstrated that rolling contact also improves formability compared to non-rotating tools. Where tool rotation is driven and hence can be programmed, Jeswiet et al [10] have devised a formula to calculate tool rotation speed as a function of tool radius, tool linear speed and wall angle to minimise the sliding contact for driven rotating tools. Allwood et al [32] avoided designing a mechanism for driven rotation by mounting their indenter on low friction bearings, allowing it to rotate freely about a vertical axis due to friction between the tool and workpiece with the aim of achieving a rolling contact. Iseki [39], Hirt et al [40] and Kim and Park [38] have also avoided a driven rotation mechanism by using a tool head made of a ball-mounted spherical roller which can rotate about any axis.

The tool radius used for ISF is often chosen with no scientific basis other than being a convenient and practical size, which is usually between 5 mm and 15 mm. However,

tool radius does influence process capabilities; Kim and Park [38] found that there is an optimum diameter for formability of approximately 10 mm, Duflou et al [13] found that tool force increases linearly as tool diameter increases, and tool radius defines the minimum achievable feature radius. Matsubara [37] recommended that the tool radius should be around five times the thickness of the sheet to provide a compromise between galling that occurs with a small radius and loss of intricacy resulting from a large radius.

As an alternative to a continuous contact between the tool and workpiece, it is possible to achieve an incremental deformation using a succession of impacts applied by a hammering tool. Schäfer and Schraft [35] have investigated incremental forming with a robot to support a vibrating hammering tool, and reported that advantages over ISF with a continuous contact include low reaction forces, a highly localised deformation area and the elimination of friction between the tool and workpiece in the feed direction.

Rollers and waterjets have been investigated as alternative tool designs with the aim of overcoming some of the limitations of the conventional spherical-headed tools. Iseki [28] demonstrated how rollers and a spherical tool can be used to incrementally form shallow rectangular shells with vertical sides and sharp corners. Iseki [41] also showed how a high speed water jet can achieve a smoother surface finish than a conventional roller for a range of geometries formed in annealed aluminium, and is also cleaner because oil is not required. However, the deformation is not as localised as with a solid tool therefore a moving support is required underneath the workpiece to constrain the deformation. Iseki [42] found that a waterjet does not apply sufficient force for forming a stainless steel sheet and therefore used a combination of a waterjet and shot for this purpose. Emmens [43] demonstrated how waterjets can be used to incrementally form interesting design features in beverage cans by blasting from the inside.

Lubrication between the indenter and workpiece in ISF is essential to avoid surface damage, reduce wear on the tool and reduce tool forces. Kim and Park [38] found that surface finish is improved by lubricating the tool, but the best formability was actually achieved with no lubrication. Popular lubricants in ISF are engine oil, mineral oil and molybdenum disulphide grease. Ceretti et al [16] experimented with a Teflon coating on a tool to provide lubrication but found that this deteriorated quickly. Petek [44]

highlighted the negative environmental implications of using lubrication in ISF and suggested that a hard lubricant on the tool surface such as a carbon based coating or molybdenum disulphide is ecologically more favourable.

2.1.4 Procedures for Process Implementation

The procedures for process implementation describe how the equipment is used to create a product in ISF, from design to finished product. This is a further topic of research where the aim is to minimise the product development time whilst maximising the process capabilities within the constraints of the available equipment. Tool path design has received particular attention because, by nature of the process, a potentially infinite range of tool paths could be used to form any given product. One of the greatest challenges faced by researchers in the field of ISF is that the simplest tool path design - a spiral that fits the profile of the product geometry - will not result in a product of that geometry. This is because of non-localised plastic and elastic deformation that occurs outside the contact area of the tool and is difficult to predict. A further complication is the potential to exceed forming limits and rupture the sheet. In order to achieve the design requirements of a given product, production engineers also need to consider the complicated interaction between the process design variables (such as tool radius, tool rotation, tool speed, vertical pitch, etc.) on the process capabilities (such as surface finish, wall thickness and forming limits). The process implementation procedures that have been proposed for overcoming some of these challenges are reviewed below.

The starting point of an ISF process is usually a CAD drawing of the required product. This can be drawn directly into the CAD software by a designer or, as demonstrated by Ambrogio et al [1] for customised medical product manufacture, can be generated by a reverse engineering approach where a laser scans an object of the required finished shape. The next stage is usually to write a first instance of a tool path that will produce an approximation to the required geometry. This is most commonly a spiral that fits the profile of the required product with a fixed vertical, horizontal or tangential pitch, generated by CAD/CAM software such as Pro/Engineer, Unigraphics, Mechanical Desktop and MasterCam. For SPIF, the spiral tool path progresses inwards and downwards around a concave profile of the product geometry, whilst for TPIF the tool progresses outwards and downwards around a convex profile of the product geometry.

The next stage in the process implementation is selection of the process variables which are likely to affect the product qualities. The variables include tool radius, rotation speed, lubrication and linear speed, and the qualities affected include surface finish, tool force and forming limits. Although experiments have demonstrated the influence of these variables on process capabilities (reviewed in Section 2.4), in reality the variables are rarely optimised and instead are chosen based on practicality and user experience.

An optional next stage before forming the product is to correct this first guess of the tool path for improvement of geometric accuracy, avoidance of rupture or improvement of uniformity of wall thickness. The methods that have been developed for improving geometric accuracy by correction of the tool path are reviewed in Section 2.4.6. The tool path can be modified for avoidance of rupture by first predicting whether rupture is likely to occur under a first guess of the tool path, and then using an appropriate method to correct the tool path to avoid the likely rupture. Filice et al [45] showed how a finite element model can be used to predict whether forming limits will be exceeded under a first guess of the tool path, and Jeswiet et al [46] proposed that a safety envelope fitted around strains measured on products formed without failure can be used to predict whether failure will occur. However, experimental measurement of forming limits for every material is not practical, therefore Fratini et al [47] derived an equation for predicting forming limits from the material parameters. However, this model does not take into account the influence of process design factors such as tool radius and vertical pitch on forming limits, which have been shown elsewhere to have an effect (reviewed in Section 2.4.5). If it is predicted that the sheet is likely to fail under the first guess of tool path, the maximum achievable wall angle can be increased either by modifying the shape of the tool path or by using multipass schedules. Hirt et al [48] used a multi-stage strategy in TPIF to create vertical sides. Iseki [28] also achieved vertical sides with a multi-stage strategy and rollers instead of a conventional spherical tool. Jeswiet et al [49] used multiple intermediate passes with scaled-down vertical co-ordinates to increase the maximum wall angle achievable for a prototype headlight formed by SPIF, and Ceretti et al [16] used a multipass schedule to form a complicated feature by TPIF against a positive die support. The tool path can be modified further at this stage to improve the uniformity of the wall thickness distribution. This involves designing the tool path to allow material to displace horizontally as well as vertically when it is

formed, hence overcoming the thinning that usually occurs in conventional single-pass processes where material mainly only moves downwards, allowing steeper wall angles to be achieved. Tool paths for improved uniformity of wall thickness are reviewed in Section 2.4.7. The process implementation procedure and possible options for tool path correction are summarised in Fig. 9.

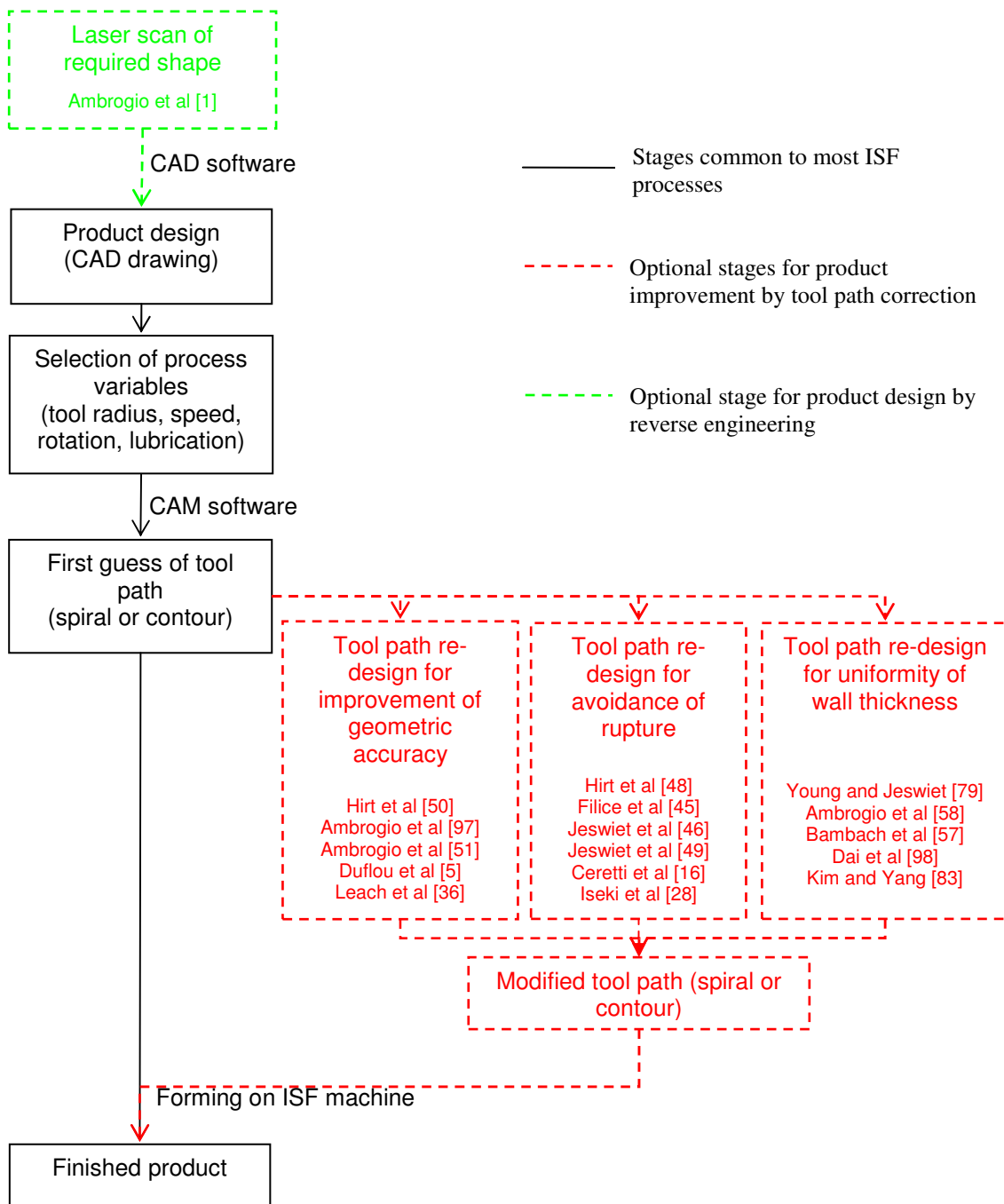


Fig. 9. Process implementation procedure for ISF on CNC machines showing options for tool path correction

2.2 Experimental Methods of Analysis of ISF

Experimental methods of analysis of ISF provide a reliable empirical insight into the process and have two advantages over the alternative approach of numerical simulation. Firstly, approximation of the material properties and process conditions, which is always required at some level for numerical models, is not required for experimental analysis. Secondly, information about the process is often more readily accessible by experimental approaches than numerical, depending on the complexity of model that would be required. Process characteristics that have been measured experimentally in ISF include geometry and geometric accuracy, strains, tool force, thickness after forming and surface finish. These experimental investigations have usually focussed on mapping the influence of process variables such as tool size, vertical pitch and sheet thickness on process characteristics. The experimental methods that have been used to measure each of these characteristics are reviewed and evaluated below, whilst the results of the investigations are reported later in Section 2.4.

2.2.1 *Geometry and Geometric Accuracy*

Measurements of geometry and geometric accuracy of sheets formed by ISF have been carried out both during and after forming, where the sheet may be measured whilst still mounted in the machine. Three principal methods have been used to measure geometry and geometric accuracy in ISF: co-ordinate measuring machines (CMMs); laser scanners; and 3D stereovision systems. Co-ordinate measuring machines provide a simple means of taking point-by-point measurements of the geometry of sheets formed by ISF after removal from the machine and have the advantage of being available in most engineering workshops. Meier et al [33] used a CMM to measure various frustums of pyramids and Hirt et al [50] used one to measure cross-sections for comparison to a FE model. However, this technique is time consuming, labour intensive, does not allow for measurement of the sheet whilst in the machine (i.e. before springback due to removal of the clamp) and can potentially lead to errors if the stylus is manually positioned. Laser scanners or stereovision systems are more suitable for rapid measurement of full 3D surfaces and can be used whilst the sheet is still in the machine. Laser scanners measure the geometry of a sheet by scanning across it in a line. Duflou et al [5] used a laser scanner to measure a formed sheet to an accuracy of $\pm 15\mu\text{m}$ and

Ambrogio et al [51] used a Minolta Vivid 300 laser scanner to accurately measure formed sheets, in both cases after removal from the machine. Sheets measured by a laser scanner have to be prepared with a non-reflective surface such as varnish to avoid high reflectance. A stereovision system offers the advantage over a laser scanner of imaging of the entire surface simultaneously; a scan is not required. Strains are calculated by comparing a pattern on the surface in the current position to the pattern at some earlier time measured by two calibrated CCD cameras. Hirt et al [50] have used an ARAMIS stereovision system and Watzeels et al [52] have used a LIMESS system. Although laser scanners and stereovision systems offer rapid and accurate 3D measurements, a problem that can be encountered is that the sheet surface can be partly obscured whilst it is mounted in the machine, and hence the full surface may not be measurable. In addition, painted-on patterns required for the optical systems can become detached during forming and 3D images can take several seconds to analyse. Overall, 3D stereovision systems offer the fastest measurement of the deformation of the sheet surface, but their usage is limited primarily due to expense and availability.

2.2.2 Strains

Three methods have been applied for measurement of strains on the surface of the sheet in ISF: strain gauges; measurement of grids applied to the surface; and stereovision systems. Strain gauges can be used to measure the development of strains at discrete points on the sheet surface throughout the forming process, as used by Kitazawa [29]. However, these have the limitations of being difficult to attach, measuring the strain over a finite area at discrete points only and failing under high strains. An alternative and more popular technique for measurement of strains across the full surface of the sheet after forming is by comparing the size of a grid of circles applied to the surface before forming to the size after forming. The grid can be applied easily using various techniques: Kitazawa [29] and Iseki [41] used a photographic technique; Shim and Park [53] and Lamminen [34] used electro-chemical etching; Kim and Park [38] manually scribed a grid of squares onto the surface; Filice et al [45] impressed the grid onto the sheet surface and Jeswiet et al [46] used silk-screen printing. For all of the above techniques, the grid pattern must be applied to the surface that is not contacted by the tool to avoid damage. Jeswiet et al [46] have suggested that using etching to apply the

grid can reduce the forming limits by causing stress concentrations, therefore printing techniques may be preferable. The major and minor (maximum and minimum) surface strains have been calculated by measuring the major and minor diameters of the distorted ellipses of the grid after forming using either a transparent measuring string (Lamminen [34]) or a tool maker's microscope (Kitazawa [29]). A limitation of the grid-based technique using circles is that the strain path is not known. Alternatively, an optical system as described above for measuring displacement can provide a rapid calculation of strains across the surface of the sheet throughout the process. Grid-based techniques are currently the most commonly used for measurement of surface strains in ISF because of their simplicity, low cost and applicability across the whole surface. However, as for measurement of geometry, optical systems offer the fastest analysis of strains but are an expensive option.

2.2.3 Tool Force

Three approaches have been used for measuring tool force in ISF: measurement of reaction forces on the workpiece support with a force dynamometer; measurement of forces on the tool post using strain gauges; and measurement of reaction forces on the workpiece support with loadcells. Duflou et al [13, 54] used a Kistler 9265B six-component table force dynamometer which showed good repeatability to measure reactions on the workpiece support. Bologna et al [55] used a force dynamometric table to measure forces on two axes. A limitation of the force dynamometer is that it has not yet been used to measure tool force simultaneously with tool position, and hence it has not been possible to resolve the tool force components relative to the instantaneous direction of the tool and instead only the tool forces in a fixed co-ordinate set are known. Alternatively, tool force has been measured by strain gauges on the tool post by Jeswiet et al [56]. This method has not subsequently been widely used because it has the disadvantage of poor accuracy due to horizontal force components being calculated from bending moments with a small bending arm. Overcoming these limitations, the ISF machine at Cambridge University is the only specialised rig to have a built-in system which allows simultaneous measurement of tool force with tool position. Allwood et al [32] mounted the workpiece frame on six loadcells to enable real-time force measurement on three axes.

2.2.4 Thickness after Forming and Surface Roughness

Rapid and automatic measurement of sheet thickness in ISF is difficult because points need to be measured accurately on opposing surfaces, where usually only one side is accessible to scanners or CMMs. The thickness at discrete points across a cut cross-section can therefore be manually measured using a micrometer after cutting the sheet, as used by Bambach et al [57]. Alternatively, a CMM can be used to measure the positions of points on opposite sides of the sheet and hence the sheet thickness can be calculated, as used by Ambrogio et al [58]. Surface roughness has been measured accurately under a range of process conditions by Hagan et al [59] using white light interferometry.

2.3 Numerical Methods of Analysis of ISF

Numerical investigations of ISF have focussed on the finite element (FE) technique for three main purposes: prediction of stresses and strains through the sheet and throughout the process that are not accessible using experimental techniques; prediction of the deformation in order to improve geometric accuracy through correction of the tool path; and prediction of tool forces for safety of machines and further insight into the deformation mechanics. Although insights into ISF have been gained through FE simulations, two major challenges to this approach are that the simulations are notoriously time consuming to implement and that through-thickness insights are limited. The simulations are time consuming because the tool paths in ISF are inherently long and require a large number of time steps to model the continually changing contact conditions and because the mesh size under the indenter needs to be fine to simulate accurately the localised deformation. Through-thickness insights are limited because shell elements are often chosen for simulations of the full sheet because the sheet is thin. A focus of model development is therefore to reduce processing times without compromising accuracy. Three of the principle areas of research are choice of integration scheme, element type and mesh size. The advances that have been made in each of these areas are evaluated below.

2.3.1 Integration Scheme

There are two options for integration scheme in FE of ISF: (1) the implicit method, which involves the solution of non-linear equations through an iterative procedure; and (2) the explicit method, which is based on dynamic equilibrium and requires solution of a set of linear independent equations at each step of the deformation path. A detailed explanation of the explicit and implicit formulations can be found in textbooks such as Belytschko et al [60]. As described by Bambach et al [61], explicit models are preferred for ISF because they are conditionally stable, whereas implicit models can fail to converge in contact problems. However, explicit models are stable on the condition that the time step is restricted to lower than a small threshold value, and hence explicit models are only practical if the tool speed or mass are artificially increased. This can cause artificial inertia effects which degrade the numerical results, hence a continuous check of ratio of kinetic energy to deformation energy is often employed, as used for example by Ambrogio et al [51].

Mass and speed scaling used in explicit models can allow a faster solution time than implicit models of the same process. He et al [62] found that an explicit model of SPIF of a cone of 50° wall angle had a solution time that was approximately one quarter that of an equivalent implicit model, although the actual duration and any mass or speed scaling which may have been used were not specified. Ambrogio et al [58] found that the processing time of a square-based pyramid formed to a depth of 30 mm by SPIF was reduced from approximately 300 hrs with an implicit formulation to a few hours with an explicit formulation in which tool speed was artificially increased from 0.017m/s to 40m/s. Bambach et al [57] reduced the processing time for a simple cone formed to a depth of 20 mm from 7.32 hrs required for an implicit model to 0.58 hrs using an explicit model. In both models, the tool was assumed to travel at constant speed, i.e. without acceleration or deceleration. The solution times of the order of a few hours reported above for explicit models are likely to be acceptable for production of one-off customised sheet metal parts. However, these solution times were measured for simple tool paths formed on small sheets to shallow depths; typical sheet metal products are likely to require much longer tool paths than these, and hence processing times will be significantly increased and are likely to be higher than the time taken to incrementally form the product.

Due to the mass scaling and speeding up of the tool that is often employed in explicit models, the accuracy of explicit models has often been evaluated and compared to that of similar implicit models both for prediction of wall thickness and prediction of geometry. In two previous studies, explicit models were found to be unsuitable for predictions of wall thickness due to instabilities whilst implicit models provide a stable solution. Ambrogio et al [58] found that an explicit model based on 30,000 4-node shell elements was unsuitable for prediction of wall thickness in SPIF due to stability problems. An implicit model of the same process modelled by 1000 8-node brick elements gave a stable solution but the maximum relative error of wall thickness of approximately 0.2 mm was high ($\approx 40\%$). He et al [62] found that an explicit FE prediction of wall thickness of a cone formed to a 50° wall angle by SPIF showed oscillations around the experimental values, whilst an implicit prediction was stable in the whole section had a low maximum error of approximately 0.1 mm ($\approx 12\%$). The authors have not suggested why these instability problems may arise or how they could be corrected. However, Bambach et al [57] developed an explicit model that predicted wall thickness after forming in SPIF to a similar accuracy as an implicit model. The implicit model, using a time step of 0.004 s, had a maximum error in wall thickness prediction of 11.7%, whilst the explicit model, which had a time step of 0.0001 s, had a slightly greater error of 15.6%. The above results show that, although explicit modelling can have instability problems for predictions of wall thickness, where instability has been avoided relative errors in wall thickness predictions are of similar magnitude to implicit predictions. These errors, which are of the range 10 to 15%, are likely to be accurate enough for most practical predictions of thinning in ISF.

Comparison of the accuracy of explicit models to implicit models for prediction of geometry has shown that in general explicit models achieve a similar accuracy to the implicit models. Bambach et al [57] found that the maximum error of an implicit prediction of geometry of a cone formed by SPIF was 1.09 mm, whilst the explicit prediction had a greater error of 1.82 mm. He et al [62] achieved a similar accuracy for geometry prediction for both an implicit model and an explicit model for the cross-section of a 50° cone formed by SPIF; both models predicted that the lower surface of the sheet would be approximately 1.5 mm higher than the experimentally measured position. Bambach et al [63] also reported that the greatest deviation between implicit

and explicit predictions of geometry occurred where the tool path was not smooth, e.g. where the tool incremented downwards. The authors suggested that this was a result of the high kinetic energy transmitted downwards, and further reported that the accuracy could be improved by using a smooth tool path along with suitable mass and time scaling. Although the accuracy of explicit models for prediction of geometry is similar to that of implicit models, the errors of approximately 1 to 2 mm described above are high in comparison to typical geometric tolerances and therefore may be too high for predictions of geometry in ISF.

2.3.2 Element Type and Mesh Size

The choice of element type and mesh size used in a FE model of ISF is a compromise between solution time and accuracy; the finer the mesh and the higher the number of degrees of freedom of the elements, the higher the accuracy but the longer the solution time. Remeshing has been attempted to locally refine the mesh at the actively yielding region under the indenter without significantly increasing processing time. Mesh sizes and element types that have been used in ISF are reviewed below.

Shell elements have often been used for complete models of ISF because they are relatively fast to solve. Shell elements are generally used for models where the thickness is much less than the length and the width and where through-thickness stresses are negligible (Abaqus Inc. [64]). There are two types of kinematic assumptions used in shell elements: (1) the normal to the midsurface remains straight and normal; or (2) the normal to the midsurface remains straight (Belytschko [60]). Hence, shell elements have the limitation that all strains are approximated as following a linear variation through the thickness, and that direct stresses normal to the mid-surface are zero. These assumptions are likely to limit the through-thickness insights into stress states under the indenter in ISF because it is unlikely that direct stresses normal to the mid-surface are zero, and it is likely that there is a variation of localised strains under the indenter that is non-linear. Despite these approximations, shell elements have been used to predict geometries and wall thickness to a satisfactory accuracy. However, large mesh sizes of the order of thousands of elements are required for simulations of complete products, and hence solution times can be slow even when

shell elements are used. For example, Hirt et al [65] used 6000 shell elements for an explicit simulation of wall thickness distribution of a 47° pyramid formed by TPIF, and the solution time was 100 hrs. The solution time is likely to increase significantly when more complicated and larger products typical of industrial applications are simulated.

Several layers of continuum elements with higher numbers of degrees of freedom have been preferred to shell elements for prediction of through-thickness stresses. Because this increases the solution time, continuum elements have generally only been used for simulations of sections of the sheet under the first few passes, instead of complete simulations with many passes. Bambach et al [61] predicted that using three continuum elements over the thickness of a sheet with 10,000 in-plane elements would require an unacceptable solution time of approximately 4 weeks to simulate a 47° pyramid. Instead the authors used a mesh of 9,600 brick elements with four layers over the thickness to simulate the through-thickness strains in a small section of sheet formed by SPIF. Henrard et al [66] used three layers of eight-node brick elements with one integration point to predict strains, tool force, thickness and geometry in a segment of a cone formed by SPIF, and reported that simulation took 15 to 20 hrs per 90° arc of the conical tool path. Watzeels et al [52] used a mesh of 15 x 30 8-node brick elements in three layers to simulate the strains in the first pass of an indenter in a straight line over half of a sheet of full size 182 x 182 x 1.2 mm. The mesh was chosen as a compromise between solution time and accuracy, although the solution time for this very simple tool path was not reported. Ambrogio et al [58] used 1000 8-node brick elements in two through-thickness layers for an implicit model of wall thickness distribution in a 90 mm x 90 mm square-based pyramid formed by SPIF. The solution time for this simple model was approximately 300 hrs. Although these simulations have provided useful through-thickness insights, there are two main difficulties in using continuum elements for simulation of ISF. Firstly, the solution times for simplified models using continuum elements reported above suggest that complete models using several layers of continuum elements are likely to be prohibitively long. Secondly, the aspect ratio of continuum elements has generally been high to limit the total number of elements. For example, the model of a square-based pyramid by Ambrogio et al [58] required elements that were approximately 2.8 x 2.8 x 0.5 mm, whilst the model of a single pass by Watzeels et al [52] required elements that were approximately 6 x 6 x 0.4 mm. These high aspect ratios are likely to reduce the accuracy of the solution.

Adaptive remeshing may overcome the problem of compromising through-thickness insights for solution speed. This allows a coarser mesh for most of the model, with a refined mesh in areas with a high field gradient, as described by Hirt et al [65]. Ambrogio et al [51] successfully used remeshing to achieve a low solution time of only 24 hrs for a model of ISF of a square-based pyramid formed by SPIF using 5000 4-node shell elements. However, Bambach et al [61] found that adaptive remeshing in PAM-STAMP software was not sufficient because it did not record the history data for the refined areas. Muresan et al [27] developed a new technique for element activation/deactivation with the aim of reducing the processing time. However, the processing time was actually increased in comparison to a conventional model because the active zone was large. Further development of remeshing is required for it to be practical for simulation of ISF on an industrial basis.

2.4 Results of Analysis of ISF

Results of previous analyses of ISF using the experimental and numerical methods above can be summarised into the following areas: range of materials and sheet thickness to which the process is applicable; surface finish and factors influencing it; the deformation mechanics; tool forces; forming limits; geometric accuracy; and uniformity of wall thickness. Further research has provided insight into the broader economic and ecological implications of the process. The extent of current knowledge of the process in each of these areas is reviewed below.

2.4.1 *Applicable Materials and Sheet Thickness*

It is likely that ISF could be applicable to a wide range of elastic-plastic materials, either metals or non-metals, which are ductile and have a non-zero elastic yield stress. This is because local deformation requires that the material can deform plastically under an indenter whilst having a yield stress that is sufficient for the material to react against the load of the indenter without yielding across most of the sheet. However, research in ISF so far has been mainly applied to metals only, the most common of which are annealed aluminium, stainless steels and mild steels due to high ductility. More unusual metals to which the process has been applied successfully include brass [47], copper [37, 47],

titanium [29, 37, 39, 67], gold [37], silver [37] and platinum [37]. The first research into the applicability of ISF to composite materials was carried out by Landert [68] in 2006, who showed that ISF can be used to form sandwich panels with metal faceplates and metal fibre or polymer cores. The findings of his research are reviewed in Section 2.5. Franzen et al [69] recently carried out the first work on ISF of PVC. It is likely that ISF will be applicable to other polymers.

ISF has been applied successfully to a wide range of sheet thickness that exceeds the range of most sheet metal applications. A structured search for applications of ISF by Allwood et al [70] found that most sheet metal products out of a range of 28 examples had a thickness between 0.4 and 3 mm. The minimum sheet thickness that can be formed by ISF is well below this range; ISF has been applied to foils from 10 μ m to 100 μ m using a specialised microforming apparatus designed by Tanaka et al [71]. The maximum sheet thickness for which successful forming has been achieved is 5 mm thick aluminium using an Amino machine, by Marko Jyllilä of Sheet Metal Innovations Ltd [72]. However, the mechanics limiting the maximum sheet thickness possible to form by ISF are not yet understood and so far this has been limited only by the strengths of machines that have been used, hence it is possible that even thicker sheets could be formed. Sheets used for research in ISF are usually in the range of 0.5 mm to 1.5 mm.

2.4.2 Surface Finish

A characteristic of products formed by ISF is that they usually have a striated surface finish due to the movement of the tool along overlapping contours. Hagan and Jeswiet [59] described this as a combination of large-scale waviness resulting from the tool path and small-scale roughness resulting from large surface strains. This can either be an advantage or a disadvantage of ISF in comparison to pressing depending on the application, and where it is a disadvantage measures can be taken to improve it. For example, surface finish is a critical requirement for car body panels and pressing inherently offers a smooth surface whereas ISF may not. Amino were able to overcome this problem by incrementally forming a car body panel with two sheets on top of each other and discarding the upper sheet. Alternatively, the surface finish can be improved by coating with paint or other substances. Painting was sufficient to disguise the

striations on the front panel of a tumble dryer manufactured by Amino in which the flange on the central orifice was formed by ISF, whilst coating with a reflective surface allowed a prototype headlamp formed by ISF to achieve high illumination requirements (Jeswiet et al [73]). The characteristic surface of ISF was an advantage for a bespoke light shade designed by Rachel Tomlinson of Cambridge University; the striated surface created a striking visual effect which would not be possible with pressing (Fig. 10).



Fig. 10. A bespoke light shade manufactured by ISF and designed by Rachel Tomlinson, University of Cambridge in 2005. The striated surface is a desirable feature of the product.

The influences of vertical pitch, tool radius, wall angle, lubrication, tool design and tool rotation speed on surface finish in ISF have been measured. Leach et al [36], Junk et al [74] and Allwood et al [32] each have demonstrated qualitatively that surface waviness increases as vertical pitch increases. Hagan and Jeswiet [59] showed that roughness increases exponentially with vertical pitch in SPIF, and an average roughness of $0.5\mu\text{m}$ with an average peak to valley height of $4\mu\text{m}$ was recorded with a vertical pitch of 0.05 mm . Jeswiet et al [6] later reported that it is more effective to fix the tangential distance between tool passes on an inclined surface rather than the vertical pitch to achieve a uniform surface finish. Junk et al [74] found that surface roughness increases as tool radius and wall angle increase, and measured roughness between $0.9\mu\text{m}$ and $21.3\mu\text{m}$ on 1.5 mm aluminium formed by TPIF with a single tool pass. Kim and Park [38] found that lubrication improved surface finish, as well as using a rolling ball tool instead of a hemispherical-headed tool. Hagan and Jeswiet [59] found that there is an optimum tool rotation speed to minimise the surface roughness at a given vertical pitch, which was

approximately 1500 rev/min for a 45° pyramid formed by SPIF with a tool of 12.7 mm diameter. In addition to these factors which have been measured, it is likely that surface finish will also depend on the sheet material and the sheet thickness, and hence the influence of these factors on surface finish should also be investigated.

2.4.3 Deformation Mechanics

The deformation mechanics is one of the most fundamental areas of research of ISF, describing how the sheet moves under the indenter and the strains associated with it. An understanding of the deformation mechanism is important to allow accurate numerical models of the process to be developed for tool path design and process control, and to develop an understanding of the increased forming limits of ISF in comparison to pressing. Previous research into the deformation mechanics has focused on two approaches: experimental measurement of strains and displacements of the surfaces of sheets; and the use of the finite element (FE) method for prediction of strains through the thickness. Although this work has provided valuable insights, the work is limited and sometimes contradictory, and hence the deformation is not fully understood.

Measurements and numerical simulations of both SPIF and TPIF have shown that, for a conventional spiral tool path along straight or gently curved sides, material does not move significantly in the direction parallel to the plane of the undeformed sheet, but moves mainly normal to this plane. Hence, strains on the surface of the sheet are zero or negligible parallel to the tool direction and positive perpendicular to the tool direction, and these directions correspond to the minor and major directions of surface strain respectively. This was first measured for SPIF of circular and elliptical frustums by Iseki in 1993 [75]. Shim and Park [53] later used a FE analysis to predict that strains are approximately uniaxial along straight sides formed by SPIF, and Kim and Park [38] predicted a similar result for an indenter moving back and forth along a straight line. The same result was later measured experimentally by Park and Kim [76] for pyramids formed by both SPIF and TPIF with a central support post. Near to uniaxial strains have subsequently been measured for a straight sided pyramid formed by TPIF by Bambach et al [61], a truncated cone formed by SPIF from various materials by Fratini et al [47], and for various shapes formed by SPIF by Jeswiet and Young [77].

Although near to uniaxial surface strains have been most commonly observed in ISF, non-zero minor surface strains can be achieved under certain conditions, and this has been of particular interest for plotting forming limit diagrams over a range of ratios of major to minor surface strain, which are reviewed later in Section 2.4.5. Iseki [75] first used a cross-shape and a straight line to generate a range of strain states from uniaxial to biaxial in 1993. Shim and Park [53] found that near to equi-biaxial strains occurred at the corners of shapes with various angles, whilst uniaxial strains occurred along the flat sides. Kim and Park [38] used a straight line test to generate a range of ratios of major to minor strain, and reported that the strain state at the start and end points of the line was biaxial, whilst the strain in the middle was uniaxial. Filice et al [45] reported that reducing the radius of curvature of the tool path increases the minor strain, and that near to biaxial strains could be achieved with a diameter of the tool path of 24 mm. A cross-shape was used by the same authors to create biaxial strain conditions at the intersection of perpendicular lines. A dome, hyperbola, cone, pyramid and five-lobe shape were used by Jeswiet et al [46] to create non-zero minor strains on forming limit diagrams for SPIF. However, the minor strains achieved on these shapes were small in comparison to the major strains, and hence strains were close to uniaxial.

Following from the above result that strains along straight sides are uniaxial and that material mainly displaces normal to the plane of the undeformed sheet, strains on the sheet surface perpendicular to the tool direction (i.e. along the direction of steepest descent on the sheet surface) increase with increasing wall angle. Due to conservation of volume, the result brings about a relationship between the wall thickness after forming (t_1) with the wall angle (α) and the original wall thickness (t_0) known as the *sine law* (2.1).

$$t_1 = t_0 \sin \alpha \quad (2.1)$$

The accuracy of the sine law for prediction of wall thickness in SPIF or TPIF has been found to be variable across the profile of a formed product. Matsubara [78] first found in 1994 that the sine law gives an accurate prediction of wall thickness at the mid-point of walls of various angles formed by TPIF. A detailed investigation of the accuracy of the sine law across the profile of cones of various wall angles formed by SPIF was

carried out by Young and Jeswiet in 2004 [79], which showed that the wall thickness is higher than the sine law prediction over the first 10-15 mm and reduces to approximately 0.05-0.2 mm thinner than the sine law prediction over the remainder of the profile. It was suggested that this can be likened to an overspinning condition in shear forming, in which the thickness of the product is less than the sine law thickness, as described by Sortais in 1963 [80]. In 2005, Ambrogio et al [58] similarly found that the wall thickness across a cone of constant wall angle formed by SPIF is higher than the sine law prediction close to the perimeter of the sheet and approximately 0.2 mm lower than the sine law prediction over the remainder of the profile.

A deformation mechanism that is sometimes associated with ISF but has not been experimentally verified is one of pure shear through the thickness of the sheet with plane strain in the plane parallel to the undeformed sheet. This mechanism is drawn in a cylindrical-polar co-ordinate set (r, z, θ) with tooling configurations for SPIF and TPIF in Fig. 11a and Fig. 11b respectively. However, in the literature usually only one element of material is shown before and after deformation, see for example Bambach et al [61]. The mechanism was originally derived from experimental measurements of shear spinning by Kalpakcioglu [81] in 1961 as shown in Fig. 11c. Shear spinning is a rotary forming process in which a rotating blank is formed against a mandrel to produce a product with a thickness in the axial direction that is equal to the original sheet thickness, as described by Wong et al [12]. Literature in which the deformation mechanism of ISF has been described as pure shear as in shear spinning include an investigation of ISF of preformed sheets by Shankar et al [82], an investigation of wall thickness variations in SPIF by Young and Jeswiet [79] and experiments on formability by Kim and Yang [83]. Matsubara [37] also proposed that the fact that the sheet thickness in TPIF closely matches sine law thickness suggests that there are no movements of material particles in a horizontal plane during forming. Making a less direct link to the idealised mechanism of pure shear, Jeswiet et al [46, 77, 84, 85] have drawn the idealised deformation mechanism of shear spinning as the basis from which the sine law equation is derived in several papers, although they have stated that the sine law is not always applicable in ISF. Hirt et al [40, 67, 74] have also drawn this mechanism as the basis for the derivation of the sine law in several papers on TPIF and SPIF, stating that close to plane strain conditions and volume constancy lead to this

direct relation between wall thickness and the angle of the component surface, although they have also provided detailed FE simulations of the actual deformation mechanism. It is possible that these frequent references to the deformation mechanism of shear spinning in ISF literature due to the derivation of the sine law have led to the above interpretations that this mechanism also occurs in ISF.

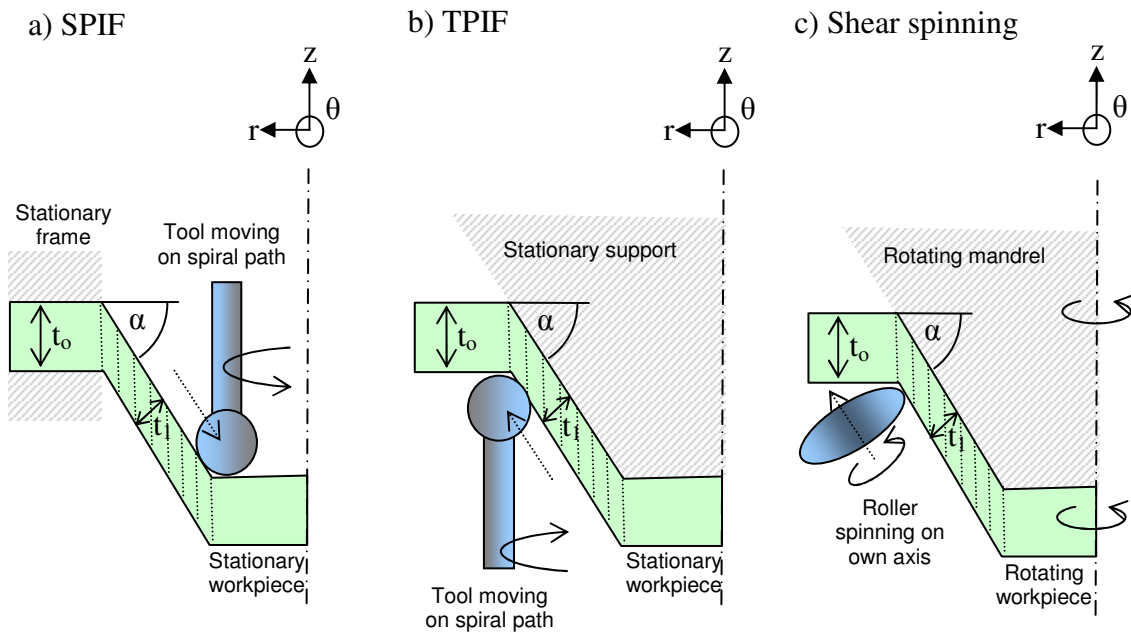


Fig. 11. Idealised deformation mechanism of pure shear that has sometimes been associated with ISF drawn for various tooling configurations: a) SPIF; b) TPIF; and c) shear spinning, for which this mechanism was originally measured by Kalpakcioglu [81].

Although the sine law applies for shear spinning as well as ISF and the idealised pure shear mechanism has been experimentally verified for shear spinning by Avitzur in 1960 [86] and in greater detail by Kalpakcioglu in 1961 [81], this idealised mechanism does not necessarily also apply for ISF. This is because the sine law is applicable for a wide range of alternative mechanisms which are also consistent with the experimental observations of deformation. For example, the sine law applies for pure bending and stretching in the (r,z) plane which requires only minimal displacement of the upper and lower surfaces of the sheet in the plane perpendicular to the tool direction. Kalpakcioglu [81] described this in his original paper and Emmens [87] reiterated it in 2007, when he also showed that the principal strains achieved by forming by shear are greater than those achieved by forming by stretch. Furthermore, the idealised

mechanism for shear spinning was derived from two approximations made to the real deformation measured by Kalpakcioglu [81]. Firstly, distortion of the plate close to the mandrel surface was neglected such that axial gridlines were approximated as remaining perfectly axial, on the basis that the distorted region was small in comparison to the thickness of the sheet. Secondly, circumferential flow that occurred in the direction of the roller was approximated as plane strain. The original deformation mechanism measured by Kalpakcioglu [81] for shear spinning, which was obtained by gridding the cross-section of a half-inch (12.7 mm) thick copper plate, is shown in Fig. 12. The surface which was in contact with the mandrel is highlighted.

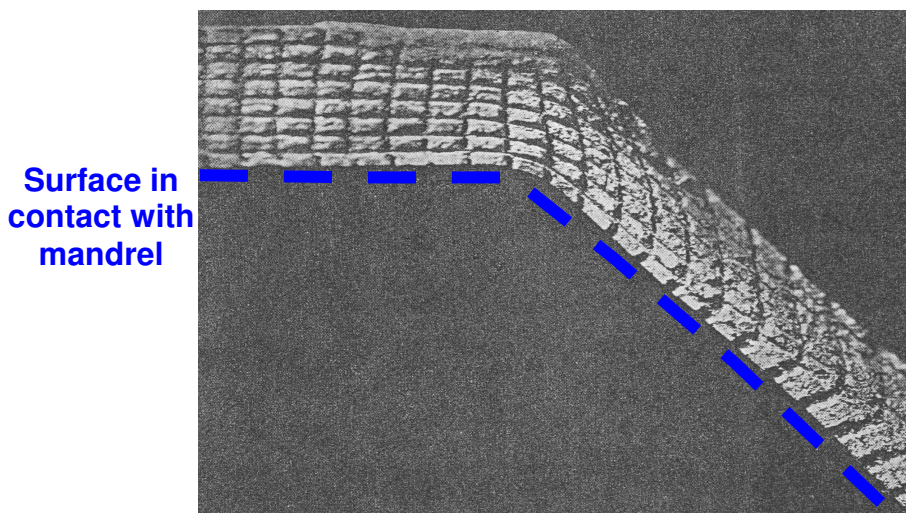


Fig. 12. Deformed grid on cross-section of a half-inch (12.7 mm) thick copper plate formed by shear spinning (Kalpakcioglu, 1961 [81]). It was from this that the idealised mechanism of pure shear associated with shear spinning was derived.

Further consideration of the sine law concedes that the sine law applies for any deformation mechanism that obeys the following conditions: (1) on average there is no radial displacement of any through-thickness element of material; and (2) at any given radius, the displacement in the tangential direction is the same at any tangential position. The first condition prevents material from accumulating in the radial direction and dictates that the wall thickness will decrease as the wall angle increases in accordance with the sine law. The second condition dictates that material does not accumulate at any point in the tangential direction. Hence, pure shear is not the only mechanism for which the sine law applies, and plane strain is also not a necessary condition. Some examples of alternative mechanisms for which the sine law applies are illustrated in Fig.

13. In each example the tangential strain is not shown. However, as described above, this can be anything as long as it is the same at any tangential position for a given radius.

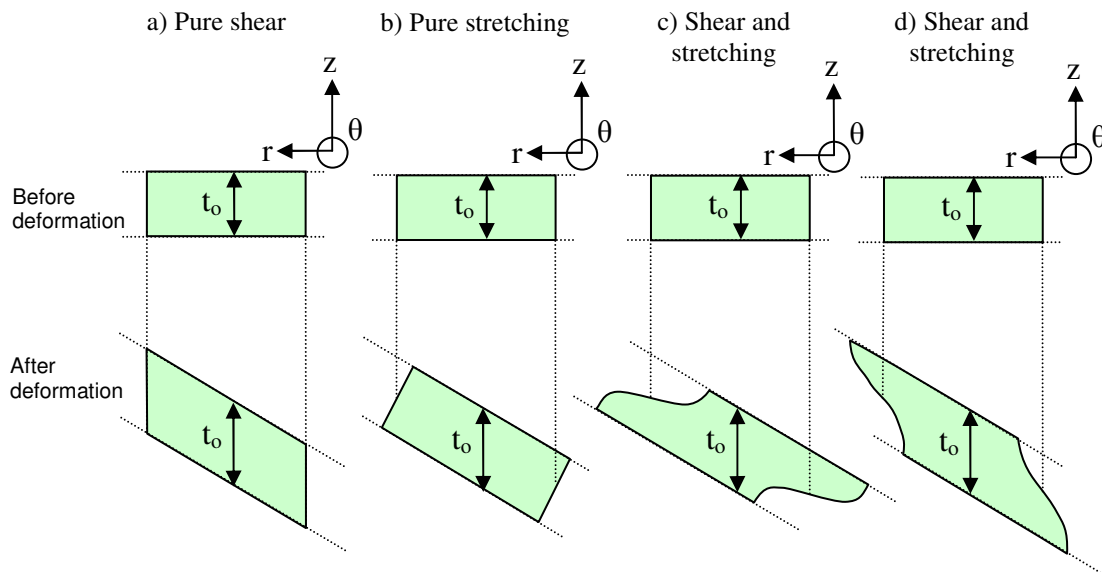


Fig. 13. Examples of deformation mechanisms of through-thickness elements in the r - z plane for which the sine law applies: a) pure shear (idealised mechanism of shear spinning [81]; b) pure stretching; c) and d) combinations of shear and stretching with non-linear through-thickness strain.

Experimental and numerical investigations have provided some evidence for the deformation mechanics through the thickness of the sheet. Contrary to the idealised deformation mechanism described above, Allwood et al [88] have recently shown by experimental measurement that straight vectors adjoining corresponding points on the upper and lower surfaces of sheet formed by SPIF remain almost normal to the surface in the plane perpendicular to the tool direction, suggesting that the deformation in this plane is almost pure bending and stretching. Meanwhile, there is relative movement between corresponding points parallel to the tool direction, indicating that shear occurs in this direction. Consistent with these experimental observations, Sawada et al [89] also predicted bending and stretching as opposed to shear in the plane perpendicular to the tool direction for TPIF with a central support post using a simplified 2D numerical model. Conversely, Bambach et al [61] used a 3D finite element model with four elements over the thickness to predict that shear dominates whilst stretching is also significant in the plane perpendicular to the tool direction in SPIF against a backing plate. In contrast to the findings of Allwood et al [88], Bambach et al [61] predicted that shear in the plane perpendicular to the tool direction is negative, suggesting that the

lower surface of the sheet is displaced further towards the centre of the geometry than the upper surface. The same model predicted that all components of strain are negligible in the direction parallel to tool travel. However, this is not necessarily a contradiction to the experimental measurements of Allwood et al [88] because the tool path used by Bambach et al [61] alternated in direction which would tend to cancel out any shear on successive laps as a result of friction, whereas the tool always moved in the same direction in the experiment by Allwood et al [88].

FE simulations have provided further insight into the evolution of strains throughout the process, which is of particular interest because experimental measurements of surface strains taken after deformation do not show the strain path through the process, and it is unlikely that this strain path is linear. FE simulations have predicted that the evolution of the strain components at any given position through the thickness of the sheet follows a step-wise trend, with each step corresponding to one lap of the tool. The pitch of the steps is greatest when the indenter is closest to the position where strains are predicted. This shows that the indenter forms a local region of the sheet, doing most work on the area that it is in contact with and less work on the surrounding region in any given tool lap. Kitazawa [29] first demonstrated this trend in 1993 by pasting strain gauges onto the surface of a sheet of metal formed into an ellipse by SPIF. Bambach et al [61] later numerically predicted that direct and shear strains parallel and perpendicular to the tool direction follow this step-wise trend, and that the pitch of the steps increases as tool diameter decreases because the deformation is more localised around the smaller tool. Ambrogio et al [90] showed that the pitch of the step-wise increments in major strains increases as wall angle and vertical pitch increases. The Von Mises equivalent plastic strain for a fixed element in a sheet formed by SPIF has been plotted by Bambach et al [61] and by Qin et al [91], which follows a similar step-wise trend.

Overall the above experiments have provided useful insight into the deformation mechanics. However, there are some gaps in the knowledge. In particular, there are contradictory results for the through-thickness deformation both parallel and perpendicular to the tool direction, the deformation mechanisms of SPIF and TPIF have not been distinguished, and FE models which have provided the most detailed insights so far have not yet been experimentally verified through the thickness of the sheet.

2.4.4 Tool Forces

Tool forces are a topic of growing interest in ISF, particularly due to the problem of excessive wear on the bearings of adapted CNC milling machines used for ISF that were originally designed for machining and because of the requirement for knowledge of maximum forming forces for new machine designs. The forces have been investigated through three approaches: numerical prediction; analytical prediction; and experimental measurement. The first two approaches offer the possibility of predicting whether forming a given product will exceed a machine's strength, whilst the latter has provided experimental verification of these models. In addition, experimental research has provided empirical insights in three main areas: (1) trends in tool forces throughout ISF processes; (2) the influences of various process parameters on tool forces; and (3) comparison of the magnitudes of perpendicular tool force components. The findings of this research are reviewed below.

Simple numerical and analytical models have been used to predict a safe maximum tool force for machine design. Allwood et al [32] used a simple model based on equilibrium of 1.6 mm mild steel at yield along a line around an indenter to predict horizontal and vertical tool force components of 5.3 kN and 13.2 kN respectively for safe design of a new ISF machine. The predictions were experimentally verified by torque measurements on an early hand-driven prototype of the machine. Ceretti et al [16] estimated a much lower value of maximum vertical and horizontal tool forces in TPIF against a positive die of 1 kN using effective stresses obtained in a simplified FE model multiplied by a safety factor. However, neither the sheet material nor the thickness used for this estimation have been specified and therefore the predictions cannot be compared.

Analytical and numerical models have been developed for prediction of the influence of process parameters on tool force throughout the process, although further development is required to achieve a high accuracy. Iseki [39] developed a simple approximate deformation analysis of SPIF based on equilibrium of a sheet of metal at yield stretched over an indenter and simple support for prediction of tool force as well as strains and geometry. Horizontal and vertical tool forces compared accurately to tool forces predicted by the FE model up to a product height of 3 mm but were not experimentally verified. For a more detailed prediction of the vector sum of tool force throughout a

SPIF process, He et al [92] used a 3D FE model of a 40° segment of a cone assuming symmetry boundary conditions. Experimental verification showed that the predicted force followed the correct trend throughout the process but the magnitude was approximately 30% too large. Possible reasons were suggested as the assumption of isotropic Von Mises yield criterion, the assumption of isotropic work-hardening and inaccuracy in the description of friction between the tool and workpiece. Duflou et al [93] carried out a set of experiments from which regression equations were derived for prediction of tool forces as a function of four parameters: vertical pitch; wall angle; tool diameter; and thickness. The equations gave an accurate prediction of tool force for a part with an initially shallow wall angle, but were not accurate for a part with an initially steep angle. The authors attributed this to excessive thinning causing a drop in tool force at steep angles.

Trends in tool forces throughout a process have been measured experimentally for two simple geometries: square-based pyramids and cone shapes. For a square-based pyramid formed in 0.3mm annealed aluminium by SPIF, Iseki [39] showed three main results: a steep rise in horizontal and vertical forces occurs as the tool approaches a corner; there is a peak in force as the tool increments downwards; and tool force is higher on the second lap than the first. Duflou et al [54] measured similar trends for square-based pyramids formed in 1.2mm AA3003-O by SPIF. However, Duflou et al showed that the average of the vector sum of tool force on each lap only increases over the first few laps of the tool path before stabilising to a steady-state value for pyramids of wall angles 30° and 40° . For steeper wall angles of 50° and 60° , Duflou et al [54] found that the force increases to a maximum over the first few contours before decreasing to an approximately steady-state value. Similar trends in tool forces have been measured for the same material formed to square-based pyramids by TPIF by Jeswiet et al [56]. The authors found that a peak in tool force occurred over the first few laps of a pyramid with a 60° wall angle, whilst peaks were not distinct for shallower angles of 30° and 45° . The authors suggested that the peak in force could be due to excessive thinning by steep wall angles causing the material to approach necking. The trend of increasing tool force to a steady-state value has also been measured for cone shapes formed by SPIF by Duflou et al [13, 54]. Similar to square-based pyramids, a peak in tool force was found to occur over the first few laps for cones with wall angles

from 50° to 73° , whilst levelling-off of tool force without passing through a maximum occurred for shallower angles of 20° , 30° and 40° . Duflou et al [54] also suggested that the peak in force was a result of necking, and claimed that a FE model and experimental measurement had verified that the minimum wall thickness occurred on the lap with the maximum tool force. Hence it was suggested that the gradient of the force curve between the peak and minimum values could be used to predict failure in ISF.

Quantitative comparison of perpendicular tool force components in SPIF has shown that the vertical (axial) tool force is the largest component. Jeswiet et al [56] found that the maximum axial force component in SPIF of a square pyramid of 1.2mm AA3003-O was approximately 500N, whilst the components parallel and perpendicular to the tool direction were approximately 50N and 100N respectively. Bologna et al [55] also found that vertical force was greater than the vector sum of tool forces in the horizontal plane. The maximum vertical force measured was 10.9kN for a 1mm DC03 deep drawing steel plate formed with a punch diameter of 20mm.

The influences of process parameters on tool force in SPIF have been measured. Duflou et al [13, 54] found that the steady-state value of the average total tool force vector increases linearly with tool diameter and vertical pitch, and by a quadratic relationship with wall angle and sheet thickness. The peak force was found to increase linearly with tool diameter, vertical pitch and wall angle, whilst it follows a quadratic relationship with sheet thickness. It was found that vertical pitch has the least influence on tool force, and hence can be increased without great penalty to reduce production times. Bologna et al [55] investigated the influence of tool pitch, sheet thickness and tool diameter on the horizontal and vertical components of tool force in SPIF in order to derive equations for tool force as a function of these process parameters. The authors found that all components of tool force follow increasing trends with these parameters, and that sheet thickness had the strongest influence on tool force.

Although the trends in tool forces measured throughout ISF and the influence of process parameters on tool forces have been measured and discussed qualitatively, a detailed knowledge of the trends in tool forces in terms of the process mechanics is still lacking. The tool forces result from elastic and plastic work done on the sheet in addition to

work against friction, and hence there is the potential for a quantitative explanation of change in tool forces throughout the process as a result of these factors. Furthermore, tool forces have so far only been measured or predicted as a function of time through the process rather than position in the sheet. Hence forces have not yet been correlated to changes in the geometry and wall thickness, which are likely to affect tool force.

2.4.5 Forming Limits

Forming limits are receiving particular attention in ISF because it has been widely reported that higher forming limits are achieved in ISF than in tests used to characterise the forming limits in pressing. A range of theories have been presented for why this may be the case. However, the validity of the result has recently been questioned due to inconsistencies in the tool paths used and the way that the limits are defined, as well as the non-linearity of strain paths.

The forming limits in ISF are commonly represented on forming limit diagrams, where the horizontal axis represents the minor strain and the vertical axis represents the major surface strain at failure. Minor strain and major strain are the lowest and highest strains respectively measured on the sheet surface as close as possible to a crack formed by ISF. Because the surface strains in SPIF and TPIF are approximately uniaxial along straight sides with the direction of major strain along the direction of steepest descent (perpendicular to the tool direction), an alternative measure of forming limit that is commonly used is the maximum major strain at zero minor strain (FLD_0) or the maximum wall angle at failure. The forming limits, according to any of the above definitions, depend on the design of the tool path, the material being formed and the design of the tooling that is used to form it. A review by Jeswiet et al [10] reported maximum wall angles for various process conditions between 40° (brass of initial thickness 1 mm) and 78° (AA3003-O initial thickness 2.1 mm). The forming limits that have been measured and the factors that influence them are reviewed below.

Iseki [75] in 1993 first measured the forming limit curve of SPIF by creating various ratios of major to minor strain using a straight line and a cross shape. The forming limit curve followed a straight line with a slope of -1 and hence Iseki concluded that fracture

occurred at a constant thickness strain, which for 0.3 mm thick annealed aluminium with a vertical pitch of 0.5 mm was 0.7. Shim and Park [53] later used various tool paths to create a range of strain states on a material similar to that used by Iseki which were formed until failure occurred. Although a linear regression line of negative slope was imposed on the forming limits, the scatter of the results was significant and hence it cannot be assumed that the forming limits follow a linear trend or that the gradient can be accurately measured. Filice et al [45] provided further experimental results that showed a stronger similarity to Iseki's original work. Forming limits were measured over a range of ratios of major to minor strain generated by a spiral tool path in SPIF on 0.3 mm AA1050. The forming limits followed a linear trend with a slope of -1.04 in the positive quadrant of strain space.

The forming limits of SPIF and TPIF are influenced by a wide range of factors including lubrication, sliding between the tool and sheet, sheet thickness, tool radius, vertical pitch, tool speed, tool path design and the properties of the sheet material. Kim and Park [38] found that using no lubrication as opposed to lubrication and a rotating ball rather than a hemispherical-headed tool increased the formability in SPIF. Jeswiet et al [84] found that the maximum achievable wall angle follows a linear relationship with sheet thickness. Park et al [76] found that formability across a range of ratios of major to minor strain increases as the tool radius increases, whereas Kim and Park [38] found that there is an optimum tool diameter for formability. Kitazawa [29], Kim and Park [38] and Ambrogio et al [58] all showed that formability increases as vertical pitch decreases resulting from a more homogenous wall thickness distribution. Kim and Park [38] also found that the formability increases as the tool linear speed decreases. The effects of the properties of the material formed, including anisotropy, grain orientation, strain hardening exponent and annealing, have been researched with varying results. Bambach et al [61] found that anisotropy had little effect on a FE prediction of strains in SPIF of mild steel DC04, whereas Ceretti et al [16] found that the orientation of the rolling direction had a strong influence on what geometric features could be obtained for Cu DHP in TPIF against a positive die support. Kim and Park [38] also found that formability depends on the orientation of the rolling direction, but the preferable direction ultimately depended on the tool diameter. In an investigation of the influence

of the mechanical properties of the sheet on formability, Fratini et al [47] found that strain hardening coefficient had the strongest influence.

The forming limits of ISF have been compared to theoretical predictions and measurements of conventional forming limit tests and it has, until recently, been widely accepted that higher forming limits are achieved in ISF. Iseki [75] first found in 1993 that forming limits of SPIF of annealed aluminium in the positive quadrant of strain space exceeded the limits predicted by Hill's and Swift's theories of plastic instability. Kitazawa [29] also showed by experimental measurement that the limit strains in plane strain of hard aluminium were higher for SPIF than for press forming. Lamminen [34] experimentally verified that forming limits in TPIF with a central support post of two cold rolled steels and one austenitic stainless steel were greater than those obtained by a hydraulic bulge test; major strains of up to approximately 200% were achieved by TPIF of the cold rolled steels, whilst only approximately 50% was achieved by the hydraulic bulge test. Hirt et al [67] also experimentally verified that the forming limits of TPIF with a central support post of mild steel DC04 are near to uniaxial and approximately two to four times greater than the conventional forming limits for that material. Shim and Park [53] found that higher strains were achieved in SPIF than a dome stretch test over a range of strain ratios for annealed aluminium AA1050-O.

Theories have been proposed for the higher forming limits observed in ISF than in the conventional tests. The first theory presented for the increased forming limits observed in ISF was by Kitazawa [29] in 1993, who proposed that the forming limits are dictated by low-cycle fatigue and can be predicted by a modified Coffin-Manson fatigue law. In 2003, Bambach et al [61] used a 3D FE model to predict that the triaxiality ratio (ratio of hydrostatic pressure to Von Mises equivalent stress) is negative in the region of the sheet that the indenter is instantaneously in contact with, which is the area where most plastic work is being done. Hence it was proposed that the increased forming limits observed in ISF are a result of the hydrostatic pressure suppressing damage. Hirt et al [67] subsequently used a Gurson-Tveergard-Needleman (GTN) constitutive theory for prediction of volume fraction of voids to numerically confirm the experimentally observed tendency that forming limits increase as tool diameter decreases and vertical pitch increases. Ambrogio et al [90] similarly predicted a negative mean stress in the

active area under immediate contact of the tool which is subject to plastic deformation, and also proposed that this allows for larger forming limits to be achieved in ISF than traditional pressing by delaying the nucleation and growth of voids. A similar result was reiterated by Micari [94], who proposed that a further contributing factor to the increased forming limits in ISF is that the maximum principal stress is low in the actively yielding region, typically 50-200 MPa for vertical pitches of 0.5 to 2 mm. Most recently, Allwood et al [95] proposed a model based on a modified Marciniak and Kuczyński analysis incorporating shear which predicted that through-thickness shear can increase the forming limits in comparison to pure stretching. Through-thickness shear was measured experimentally in SPIF by measuring the relative displacement of points marked on the upper and lower surfaces of sheets. Hence it was proposed that through-thickness shear may account for the increased forming limits of ISF in comparison to pressing. The modified Marciniak and Kuczyński analysis was experimentally verified for a simplified ISF process called *paddle-forming*, where it was shown that a dimple in a sheet of metal could be formed to a greater depth with a rotating paddle causing shear than by a pure stretching process under a punch.

The validity of making a straight forwards comparison of forming limits measured by ISF to those of the bulge formability test has recently been questioned, as well as the suitability of the forming limit curve for predicting forming limits in ISF. In 2006, Landert [68] showed how failure is defined at different stages for the two tests; for ISF it is defined where the sheet cracks, whereas for the bulge test it is defined where necking first occurs because this is regarded as failure for some manufacturing processes. Significantly, cracking exceeds the necking stage in the bulge formability test, and bulge formability tests where cracking is used as the failure criterion follow a similar shape as the ISF forming limit diagrams. Hence, Landert has questioned whether increased forming limits are actually achieved in ISF than pressing at all. Bambach et al [96] more recently measured the limit strains at rupture and necking for various tool paths in ISF and concluded that the necking limits vary considerably depending on the tool path whereas the rupture limits follow more consistently a linear trend of negative gradient in the positive quadrant of strain space. The authors also demonstrated using FE that the strain paths in ISF are not linear, whereas linear is assumed in conventional stretch formability tests, and therefore concluded that the

forming limit curve is not an appropriate tool for predicting the feasibility of a given part design in ISF. Emmens [87] recently discussed how the major and minor surface strains in ISF are not the principal strains due to through-thickness shear, whereas they are the principal strains in stretching. Allwood et al [88] proposed that the conventional Marciniak-Kuczyński analysis used to predict forming limits in pressing is not applicable to ISF because it assumes that strain paths are proportional throughout the process and hence can be integrated. The authors showed by numerical simulation that the strain path in paddle-forming is non-linear, and suggested that the strain path is also likely to be non-linear in ISF. This builds on the idea presented by Emmens [87] that the surface strains should be treated with caution; if the strain path is non-proportional throughout the deformation then the strains measured on the surface after deformation do not represent the components of the strain tensor used in the Marciniak-Kuczyński analysis because the strains cannot be integrated.

From the research in forming limits of ISF reviewed above, three main areas for future research can be identified. Firstly, a consistent standard for measuring and reporting forming limits in ISF has not yet been established, and hence the forming limits measured in different tests cannot yet be accurately compared to each other or to previous results of formability tests in pressing. Secondly, the reason for the increased forming limits of ISF is not yet fully understood and cannot yet be predicted. Further work should be carried out to experimentally verify and numerically predict the cause of increased forming limits in ISF. Thirdly, if the reason for increased forming limits is established, the process could be designed to take advantage of this to improve the forming limits. For example, if through-thickness shear is the cause, the tool path could be designed to increase shear possibly by modifying the tool size or friction coefficient.

2.4.6 Geometric Accuracy

A high geometric accuracy that meets product design requirements in ISF requires careful tool path design or process control. This is because the deformation caused by the indenter is not entirely localised or entirely plastic; deformation occurs outside the contact area of the indenter that is partly elastic and can be difficult to predict. Hence, a tool path such as a contour or spiral that follows the profile of the required shape will

not result in a product of that shape, and the tool path needs to be adjusted to compensate for this. The geometric accuracy of any given ISF process depends on the design of the product and the process. For SPIF processes based on a simple contour or spiral tool path following the product geometry, the error is typically of the order of millimetres; Leach et al [36] found that asymmetric products could be incrementally formed to an accuracy of ± 2 mm, Ambrogio et al [1] achieved an accuracy of less than 1 mm for an ankle support, and Duflou et al [5] measured errors between -1.8 mm and 5.4 mm on a scaled down model of a solar oven cavity with flat sides. For TPIF using non-optimised spiral or contour tool paths the accuracy is of similar magnitude; Hirt et al [67] reported a geometric error of up to 3 mm for asymmetric demonstration products formed against a positive die. These geometric accuracies are inadequate for some applications; Allwood et al [70] reported that the accuracy requirements for a range of 28 sheet metal products is between 0.1 mm (cap for mass-produced car) and 5 mm (cowling panel for an historic plane). Hence, there is a motivation for developing methods for correcting the tool path to compensate for this error to improve geometric accuracy without compromising the flexibility of the process.

Geometric accuracy has been improved by three basic approaches: the iterative application of a correction algorithm to the tool path based on geometric error that is measured or numerically predicted for a product formed with a first guess of the tool path; the use of simple rules to modify the tool path; or the use of multiple passes. Hirt et al [50] have developed an iterative tool-path correction algorithm based a finite element prediction of the product geometry which reduced geometry error from 1.7 mm to less than 0.2 mm with two iterations for a four-sided pyramid formed by TPIF. In order to achieve a lower computation time than the finite element approach, Ambrogio et al [97] have developed a tool path correction algorithm based on a neural network applied to a simplified numerical prediction of the product geometry to reduce the maximum error from 0.6 to 0.02 mm. Ambrogio et al [51] also showed how a simple strategy for reducing the deflection of bending zones in unsupported SPIF is to increase the wall angle of the first few laps, where the required wall angle can be predicted by FEM. Duflou et al [5] showed how using a double pass schedule with a reverse finishing pass can reduce the average geometric error from 1.3 to 0.4 mm for a scaled-down solar cooker cavity and from 0.3 to 0.1 mm for a cranial plate. Leach et al [36]

showed that unwanted bending could be removed by simply reversing the workpiece and forming the opposite side. Although all of the above techniques have been used to successfully reduce the geometric error of products formed by ISF to a range that is acceptable for most design requirements, a challenge that remains is to automate the implementation of the above methods to enable manufacture of bespoke products to the required standard. To achieve this goal, it is desirable to incorporate tool path modification into automated tool path design software that can be widely used without skilled operator intervention.

2.4.7 Uniformity of Wall Thickness

The uniformity of wall thickness achievable in ISF is important to meet product design specifications as well as allowing high forming limits to be achieved by avoiding excessive thinning. As described in Section 2.4.3, a simple spiral or contour tool path of constant wall angle does not produce a wall of constant thickness as would be predicted by the sine law (Equation 2.1), and this may be unacceptable for some products due to structural weaknesses. Also, the deformation mechanics of a conventional spiral or contour tool path dictates that the wall thickness decreases as the wall angle increases, which has been found in a range of experiments to limit the maximum wall angle to between 40° (brass of initial thickness 1 mm) and 78° (AA3003-O initial thickness 2.1 mm) (reviewed by Jeswiet et al [10]). There is therefore a motivation for developing alternative tool path designs that overcome these limitations.

Modifications to the shape of the tool path or multipass schedules have been developed for improving uniformity of wall thickness. Young and Jeswiet [79] showed that the thinning band which occurs on the first few laps of the outer perimeter of a shape formed by SPIF can be reduced by using multiple tool passes of scaled vertical increment. Ambrogio et al [58] found that the homogeneity of wall thickness distribution can be improved by reducing the vertical pitch, and hence formability is improved. Bambach et al [57] investigated alternative tool pass schedules for conical frustums formed by SPIF with the aim of achieving a more uniform wall thickness distribution and found that a radial in-plane strategy gave the best results. Dai et al [98] designed a tool path that achieves uniform wall thickness for a dome by investigating

the relationship between the undeformed blank and the deformed specimen with the ideal uniform strain distribution. Kim and Yang [83] used a double-pass tool path to improve uniformity of wall thickness on several products where the geometry of the first pass was based on a prediction of the thickness found with the sine law. Although these alternative tool path designs have all been used successfully to improve the uniformity of the wall thickness distribution in ISF, further development of tool path design software is required to automate this process and hence to make these methods practical to implement on an industrial basis.

2.4.8 Economic and Ecological Implications

ISF is likely to be cheaper and faster for production of small batch-sizes or customised one-offs of formed sheet metal parts than processes such as pressing and deep drawing because these processes require specialised tooling which is time consuming and expensive to develop. Specialised die sets are expensive because they are usually machined from hardened steel to withstand repeated forming processes and the design needs to be carefully calculated and precision machined to compensate for elastic springback to achieve high geometric accuracy. Where steep wall angles are required, several forming stages are necessary because a draw angle of up to only approximately 30° can be achieved with a single press; Waller [99] gives an example of a simple funnel that requires 13 deep drawing stages to form, where each stage uses a separate male and female die set. This increases the tooling cost further. A growing interest in customisation as opposed to mass production, which has been the dominant production model since the early 20th century, has motivated advances in conventional sheet forming processes to reduce tooling cost and improve flexibility as well as the development of ISF as an entirely alternative forming method. This is a principle motivation for development of the process.

The maximum batch size for which ISF is cheaper than alternative processes requiring specialised tooling depends on the machine cost, tooling cost, product design, size of product and production costs such as labour and electricity. A break-even analysis by Ambrogio et al [100] estimated that ISF is cheaper than stamping for batch sizes of up to 600 to 1100 parts depending on the complexity of the product. An economic model by Micari et al [101] which considered die cost and cycle time predicted that ISF is

cheaper than stamping for batch sizes up to between 100 to 1200 parts. Hirt et al [102] considered two products of different sizes and complexity to predict that ISF is cheaper and faster than deep drawing for batch sizes of up to between 220 and 650 parts. A wider range of 28 products was considered in a structured search for applications of ISF by Allwood et al [70], in which it was estimated that ISF is cheaper than alternative processes for batch sizes between approximately 10 and 2500 parts depending on the product. This analysis also showed that the lead time of ISF increases more rapidly with batch size than the alternative processes, but there are still a large number of products for which ISF is faster. Overall, these analyses have shown that ISF is likely to offer significant economic savings in comparison to deep drawing for small batches.

The ecological implications of ISF are a popular topic for discussion, but detailed analyses are currently lacking. An ecological evaluation of ISF by Hirt et al [102] showed that it has strong ecological benefits compared to deep drawing and manual sheet working, including reductions in energy and materials for the die, noise emissions, safety precautions and chemical fillers. Petek et al [44] also discussed the ecological implications of using liquid lubricants in ISF and suggested that the use of hard lubricants such as tungsten carbide and molybdenum disulphide is more ecologically favourable. However, it is likely that the full ecological benefits of ISF have not yet been explored. For example, ISF has the potential to be used for localised production that has strong ecological advantages in comparison to high-volume mass production by reducing transportation distances, allowing customised products to be produced where and when they are required and allowing sheet metal to be recycled by re-forming. These potential benefits suggest that future research in this area could be highly beneficial to industrial production.

2.5 Sandwich Panel Forming

Sandwich panels are composite materials consisting of two stiff outer faceplates separated by a core of low density material which are joined by a strong bond. The principal advantage of a sandwich panel in comparison to a monolithic sheet is that it has a higher flexural rigidity per unit weight. This is because the faceplates, which are the main components for resisting bending, are separated by the core which

significantly increases the second moment of area per unit width without adding considerably to the weight. Sandwich panels can be compared to I-beams for bending in 2D (Fig. 14), in which the central rib serves a similar function to the core of the sandwich panel for separating the end faces. Further advantages of sandwich panels include sound-deadening, buoyancy, thermal insulation, vibration damping and blast protection. Applications include panels in aircraft, cars or marine craft where weight reduction to reduce fuel consumption is desirable. However, sandwich panels are also prone to complications which are not such a concern for monolithic materials, including recycling (separation of core and faceplate materials), fatigue (particularly at core-faceplate interface), joining (stresses at joints can lead to delamination failure) and degradation by corrosion.

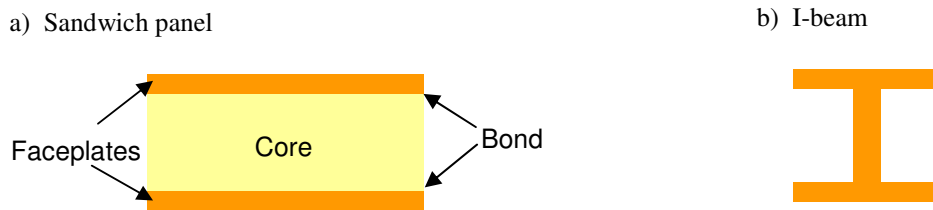


Fig. 14. Structure of a sandwich panel and an equivalent I-beam: (a) sandwich panel; (b) I-beam.

A common measure of the effectiveness of a sandwich panel is the equivalent flexural rigidity $(EI)_{eq}$. This is a measure of resistance to bending in the elastic regime. The details of the calculation of $(EI)_{eq}$ are explained in text books on sandwich panels such as by Zenkert [103]. The calculation of $(EI)_{eq}$ can be simplified to Equation 2.2, where E_f is the stiffness of the faceplates, t_f is the thickness of the faceplates, and d is the separation of the faceplates, as shown in Fig. 15. The principal result is that the faceplates make the greatest contribution to stiffness and that the stiffness is strongly dependent on the separation of the faceplates. This is known as the *sandwich effect*.

$$(EI)_{eq} \approx \frac{E_f t_f d^2}{2} \quad (2.2)$$

Fig. 15. Calculation of the equivalent flexural rigidity of a sandwich panel.

For many applications such as vehicle body panels, sandwich panels are required as a 3D shell as opposed to a 2D flat sheet. The methods of manufacturing 3D sandwich shells can be broadly divided into two categories: (1) building the sandwich shell from its component parts; and (2) forming the sandwich panel directly. Methods for building a 3D sandwich shell directly from its component parts include lay-up techniques for fibre and foam or wood layers such as used in boat hulls. These methods are reviewed by Karlsson and Åström [104]. Where it is mechanically feasible, there are practical advantages of the second approach because it allows for separation of the manufacturing and forming stages, the possibility to use existing tooling used for sheet metal forming and avoidance of time consuming and labour-intensive lay-up techniques. Hence, there is growing interest in development of sandwich panels that are formable with conventional sheet forming processes to similar limits as sheet metals, particularly for substitution of sheet metal body panels in vehicles. The most successful designs developed for this purpose are metal/polymer/metal sandwich panels and metal/metal fibre/metal sandwich panels, and the properties of these materials in forming are reviewed below. A third sandwich panel which can be formed to a limited extent as a complete material but can be formed successfully as a precursor material is metal/metal foam/metal sandwich panels, and this is also reviewed below.

2.5.1 Metal/Polymer/Metal Sandwich Panels

Metal/polymer/metal sandwich panels were first developed in the early 1980 s. Aluminium and stainless steel are the most common metals used for the faceplates, with polypropylene, polyethylene or nylon as the core materials. There have been several studies of their deformation by conventional forming methods. Miller [105] found that the formability of mild steel/polypropylene/mild steel sandwich panels is comparable to automotive aluminium alloy sheets but less than low carbon steel. DiCello [106] measured the forming limit diagram of a range of steel/polypropylene/steel sandwich panels and found that the formability was greater than AA5182 for all those tested, but all but one had a formability less than AK steel which is typically used for car body panels. McKenna et al [107] found that the limiting draw ratio for aluminium/nylon/aluminium sandwich panels is greater than or equal to that of auto body panel materials and drawing quality steels. However, in deep drawing of

metal/polymer/metal sandwich panels, DiCello [106] reports more severe problems with wrinkling than in metal sheets. Somoyajulu [108] found that the forming limit of aluminium-polymer sandwich panels strongly depends on skin thickness. Landert [68] recently carried out the first investigations of the applicability of ISF to sandwich panels with mild steel faceplates and polypropylene cores. Experimental work was done on the Cambridge ISF rig and tool paths for testing the forming limits of the faceplates were developed in collaboration with the author. Landert observed that whilst the outer surface of the sandwich panels remains completely smooth, the inner surface becomes wavy due to the contact of the indenter. Landert also reported that the forming limits of this sandwich panel follow the characteristic straight line of slope -1 in the positive quadrant of strain space as has been similarly reported for several monolithic sheet metals (reviewed in Section 2.4.5), and that the forming limits in ISF exceed the limits of the conventional punch stretch test. However, the deformation mechanism of this material in ISF has not yet been measured and the characteristics have not been compared to sheet metals.

2.5.2 Metal/Metal Fibre/Metal Sandwich Panels

Metal/metal fibre/metal sandwich panels include HSSA (Hybrid Stainless Steel Assembly) patented by Gustafsson [109] and sandwich panels with a core of sintered metal fibres developed at the University of Cambridge [110]. HSSA (now named Hybrix® produced by Lamera in Sweden) has a core of fibres oriented almost perpendicular to the faceplates, whereas the core of the sandwich panels made at Cambridge is a sintered mat where the fibres are mainly oriented at an acute angle to the faceplates. In Hybrix® the core is bonded to the faceplates by epoxy or resin bonding (as a continuous layer or discreet blobs), whilst the core of the Cambridge sandwich panels is bonded by brazing or adhesive [111, 112]. In both materials, both core and faceplates are usually made of stainless steel. Wrinkling, core crushing and surface waviness limit the deformation of these panels in pressing or deep drawing. Landert [68] observed wrinkling of the inner faceplates in deep drawing of Hybrix® with both continuous epoxy bonding and discontinuous resin bonding and for the Cambridge sandwich panel with a brazed core. However, wrinkling was reduced by using a flange, and a hydraulic counter-pressure resulted in a more uniform through-thickness strain.

Mohr [113] found that core shear failure was the dominant failure mechanism in draw bending of the Cambridge sandwich panel and recommended that the shear strength should be at least one order of magnitude higher to prevent core shear failure in forming operations. Landert [68] also observed that the formability of this material is limited due to failure in fibre-faceplate bonds. Landert [68] recently investigated the applicability of ISF to Hybrix® sandwich panels with continuous bonding and discrete regions of bonding with epoxy or resin adhesive and the Cambridge sandwich panel with a sintered metal fibre core. This work was carried out on the Cambridge ISF rig and tool paths were developed in collaboration with the author. Landert found that wrinkling, which was a problem in deep drawing, did not occur in ISF of these materials. However, the inner surfaces of the Hybrix® panels were roughened due to compaction of the porous core against the faceplates. The fibre-fibre and fibre-faceplate interfaces failed along the sloping sides and flat bottoms of truncated pyramids formed in these materials because the interfaces were too weak to withstand unwanted deformation. Through-thickness strains were evaluated at four positions along cross-sections formed by ISF, although the accuracy was likely to be significantly reduced by delamination which occurred when the samples were cut with a bandsaw. Unlike the metal/polymer/metal sandwich panel which was also investigated, the forming limits were found to be of similar magnitude to those of the conventional punch stretch test for these materials. However, measurement of the forming limits focused on failure of the sandwich panels and did not consider whether or not the core had already failed.

2.5.3 Metal/Metal Foam/ Metal Sandwich Panels

Metal foam core sandwich panels are typically available in total thickness of greater than 10 mm, and hence are thicker than sheet metal parts. The most common core material is aluminium. Methods for manufacturing metal foams and their mechanical properties are reviewed by Ashby et al [114]. Metal foam core sandwich panels are not usually formed to intricate geometries due to the high compressibility of the core, and hence the forming characteristics in conventional metal forming processes have not been extensively researched. However, a recent study by Contorno et al [115] showed that an aluminium/aluminium foam/aluminium sandwich panel (Alulight®) of thickness 13.5 mm could be formed by draw bending to depth of 13 mm without damage.

Bending tests have given further insight into the mechanical deformation, where strips of the sandwich panels have been bent until failure against a cylinder of specified radius and failure mechanisms have been plotted against dimensionless ratios of core thickness to span length and faceplate thickness to span length. Failure mode maps for three point bending were plotted by McCormack et al [116], where failure modes were face yielding, face wrinkling, core failure or indentation. Bart-Smith [117] measured failure modes of face yielding, core shear or indentation of thin metal foam core sandwich panels in three point bending. Chen et al [118] measured collapse mechanisms in four point bending as core shear, indentation or face yield. A more successful way of creating an intricate 3D sandwich shell of this material is to use conventional sheet metal forming methods to form a compacted precursor material which can later be inflated into a metal foam core sandwich panel by heating, as explained by Banhart [119]. An example of an application given by Stöbener et al [120] is a frontal crash energy absorber for a suburban railcar.

2.6 Scope of Present Research

ISF could potentially facilitate localised and customised sheet metal forming with benefits for the customer as well as the environment. However, the process is still not widely applied in industry, its application being mainly limited to experimental prototyping at car companies or prototyping companies. Hence there is a motivation for developing the process by addressing some of the gaps in the present knowledge and expanding the process capabilities. From the findings of the above review, the main gaps in the present knowledge or limitations in the process capabilities can be summarised as follows:

- Techniques to improve geometric accuracy generally involve time consuming numerical analyses that are complicated to implement
- The process is not fully automated; a skilled operator is required to program at least a first guess of the tool path and to select process variables such as tool size and vertical pitch
- Machine designs are often restricted to single indenters which can move on only three axes, hence the range of feasible geometries is limited

- ISF machines are expensive and not widely available; the only manufacturer is currently Amino in Japan
- Surface finish resulting from ISF is wavy, which is regarded as unacceptable for some applications
- An understanding of the process mechanics is limited
- The process has so far mainly been applied to monolithic sheet metals; the application to composites and sandwich panels is not well understood

This thesis presents new insights into the last two in the above list of gaps in the knowledge of ISF by researching deformation mechanics of ISF of sheet metals and sandwich panels. Deformation mechanics is one of the most fundamental areas of research of ISF and is of particular interest to allow accurate numerical models of the process to be developed for tool path design and process control, as well as to develop an understanding of the increased forming limits observed in ISF in comparison to pressing. Crucially, numerical simulations of the deformation mechanics have not yet been experimentally verified, some results are contradictory and the mechanisms of TPIF and SPIF have not been clearly distinguished. The deformation mechanics of sheet metals will be investigated by the first experimental verification of through-thickness deformation of SPIF and TPIF with a comparison to pressing, as well as a comparison of tool forces in SPIF and TPIF to the deformation mechanics. The deformation mechanics of sandwich panels will be investigated by two approaches. Firstly, the mechanical feasibility of ISF of various sandwich panel designs will be evaluated through failure modes, surface damage and thickness reduction. Secondly, the deformation, tool forces and the applicability of the sine law for prediction of wall thickness for ISF of a suitable sandwich panel will be compared to that of a mechanically similar monolithic sheet metal to evaluate to what extent existing knowledge of ISF of sheet metals is also applicable to sandwich panels. This will build on the previous work of Landert [68] by investigating a wider range of failure modes other than faceplate fracture, presenting the first work on the relative movement of upper and lower surfaces in ISF and making the first comparison to sheet metals. The research will be carried out on the newly-built ISF rig at Cambridge University, and preparatory work will involve commissioning a new system for measuring tool forces.

3. Commissioning of a Tool Force Measuring System

ISF experiments presented in this thesis were carried out on a new ISF rig designed and built at Cambridge University Engineering Department by Julian Allwood and Neil Houghton [32]. The rig is the only custom built ISF machine to include an in-built tool force measuring system, which offers the potential of providing new insights into the deformation mechanics through analysis of tool force as well as real-time process control based on force feedback. Preparatory work for the tool force experiments presented later in this thesis and for the benefit of future users of the machine involved designing the circuitry for the tool force system and measuring uncertainty due to calibration error, drift and noise. This work is reported in this chapter.

3.1 Tool Force System Design

The literature review has identified two methods previously used to measure tool forces in ISF: strain gauges on the tool post; and a force dynamometer table to support the workpiece and measure the reaction on the tool. Although these systems have provided insightful tool force results, the former method has the disadvantage of inaccuracy due to lateral forces being measured by the bending moment on the tool post rather than measuring directly, and neither system allows simultaneous reading of tool force with tool position, and hence the tool force cannot be compared accurately to position in the sheet or resolved relative to the instantaneous tool direction. In 2004, Allwood et al [32] designed a tool force system for the new Cambridge ISF rig with the aim of overcoming these problems based on the principle that the force on the tool can be found by measuring the equal and opposite reactions on the workpiece frame which is in equilibrium with the tool. The system, illustrated in Fig. 16, consists of six tension/compression loadcells (Novatech type F256UBROKN, range -5 kN to 5 kN) which each constrain one degree of freedom of the workpiece frame such that the frame is fully constrained without redundancy. The six voltage signals from the loadcells (in the range of approximately -20mV to 20mV) are amplified in a unit containing six amplifiers (Novatech type SY018) which increases the amplitude of the signals to the range of -10V to 10V. These amplified signals are then read by a PCI card (APCI-ADADIOCS) in the desktop PC which is connected to the amplifier unit via a 50-way cable. The loadcells are arranged such that there are three on the z -axis (vertical) and 2 on the x -axis and 1 on the y -axis in the horizontal plane. The total tool force on each axis can then be found by the sum of the forces measured by each loadcell on that axis.

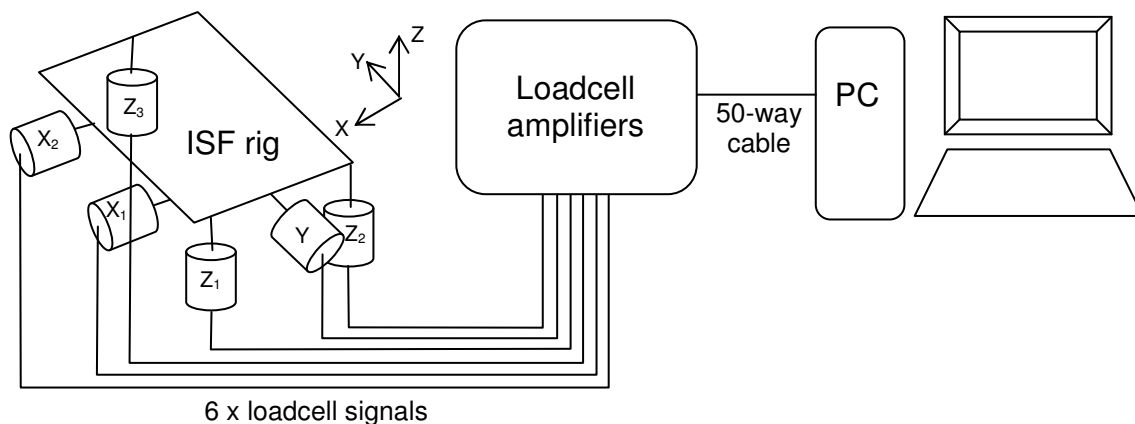


Fig. 16. Schematic diagram of main components of tool force system on ISF machine.

Although the tool force system was designed and in place at the start of work for this thesis, it did not give accurate or stable measurements of tool force therefore further work was required to commission it. This involved careful re-design of the amplifier circuit, wiring of a 50-way D-type connector to the ADC card, developing software to read the tool force in real-time and sectional calibration. The accuracy of the system was then measured by combining errors due to noise, drift and calibration to validate whether it was suitable for its intended purpose of measuring tool forces in ISF. The commissioning process of the tool force system is described below. The details of the system operation, in addition to tool path design procedures and machine operation, have been recorded in a separate manual to be kept next to the machine for future users of the system (Jackson [121]).

3.1.1 Design of Amplifier Circuit

The amplifier circuit consists of six amplifiers (Novatech type SY018), one for each loadcell, a power supply unit which transforms a 240V AC input into 24V DC output required for the amplifier supply, and a 50-way D-type connector to output the amplified signals to the ADC card. The circuit was re-wired according to the manufacturers' instructions. Testing showed that the minimisation of noise was essential for accurate readings, and therefore the following features were incorporated into the design:

- Screened signal wires with twisted cores
- Earthing of the screens at the end at which the signals are measured only
- Enclosure of the power supply unit in an aluminium box
- Enclosure of the amplifier system in a steel box
- Earthing of pins on the D-type connector for single-ended inputs

The circuit diagram, which was designed by the author and built by Simon Smith, is shown in Fig. 17.

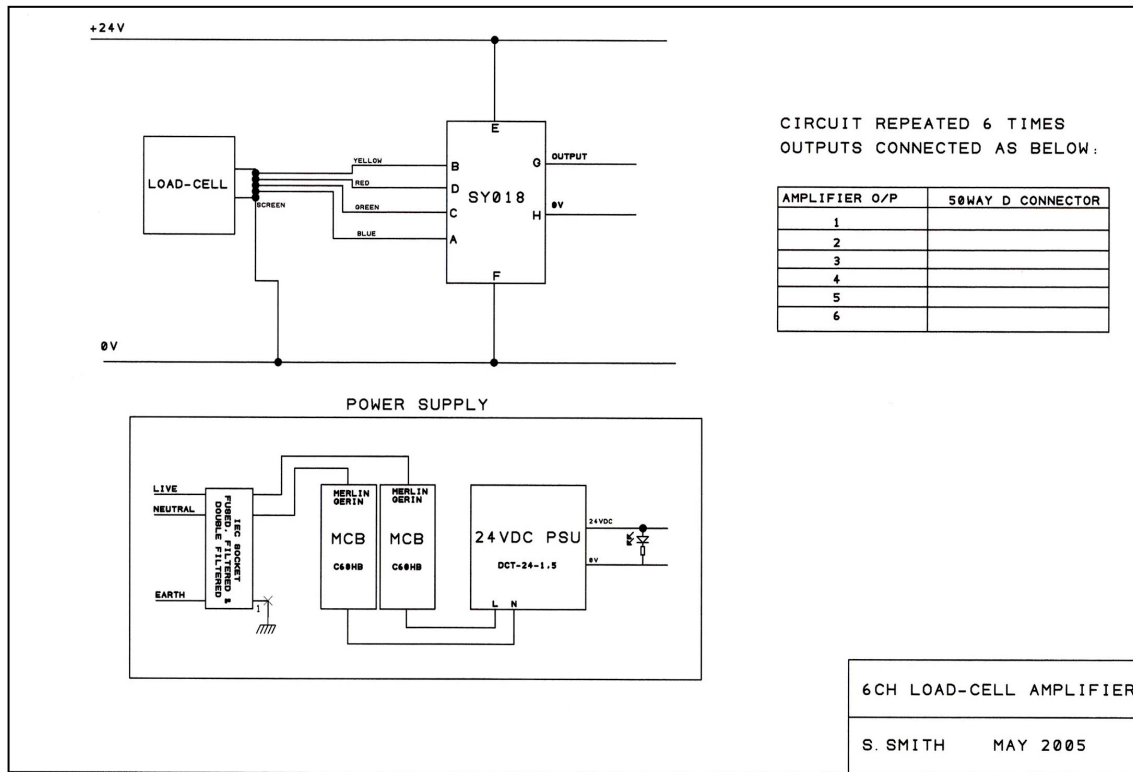


Fig. 17. Circuit diagram for amplifier unit (drawn by Simon Smith, May 2005)

3.1.2 Design of Software for Reading Tool Force and Position

Software for recording tool forces simultaneously with tool position was designed in the programming language Visual Basic.NET, which enabled simple software with the minimum necessary functionality to be developed in a relatively short time. The software, which has an intuitive graphical user interface, is able to record tool force on each of the six loadcells from the APCIADADIO-CS card simultaneously with tool position in the x , y and z directions from the Trio Motion PCI208 motion controller card in real-time at a sample period defined by the user. The readings are recorded in a table which can be saved to a .txt file for importing later into Matlab or other software for analysis. The software contains an additional interface for recording the experiment details such as the tool path file, the indenter size, the sheet material, thickness, etc. These details are recorded as a heading to the data file. The software also contains functions for driving the machine and a sample program has been written, although this feature has not been used extensively because the machine is driven through Motion Perfect 2 software, supplied by Trio Motion. Visual Basic.NET was chosen as the programming language because the Trio Motion PCI208 motion controller card and the

Arcom APCI-ADADIOCS card were supplied with ActiveX controls or dynamic-link libraries (DLLs) for accessing the cards which could easily be imported into the program. The minimum sample period of the software is approximately 0.4 s, and hence for a tool speed of 20 mm/s as is typically used in the experiments on this rig this will allow a minimum spacing between readings of approximately 8 mm. This spacing is likely to be adequate for most ISF experiments which are carried out on an area of size 140 x 140 mm. However, a slower tool speed should be used to allow a shorter distance between successive readings if necessary. A function structure diagram of the software is shown in Fig. 18.

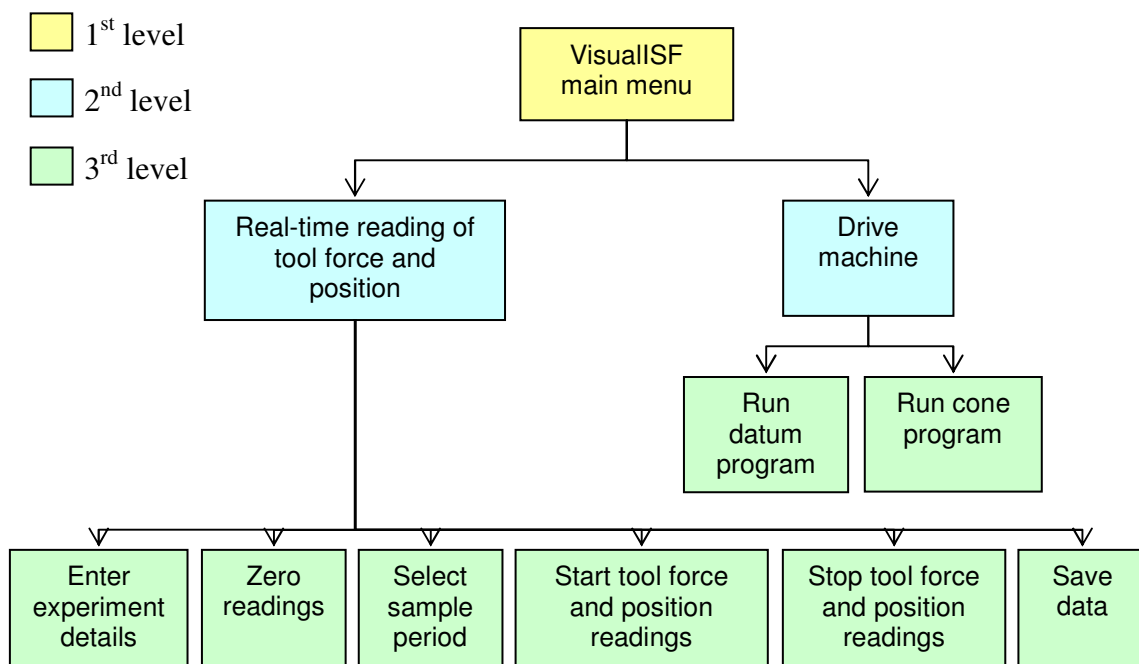


Fig. 18. Function structure of Visual Basic software

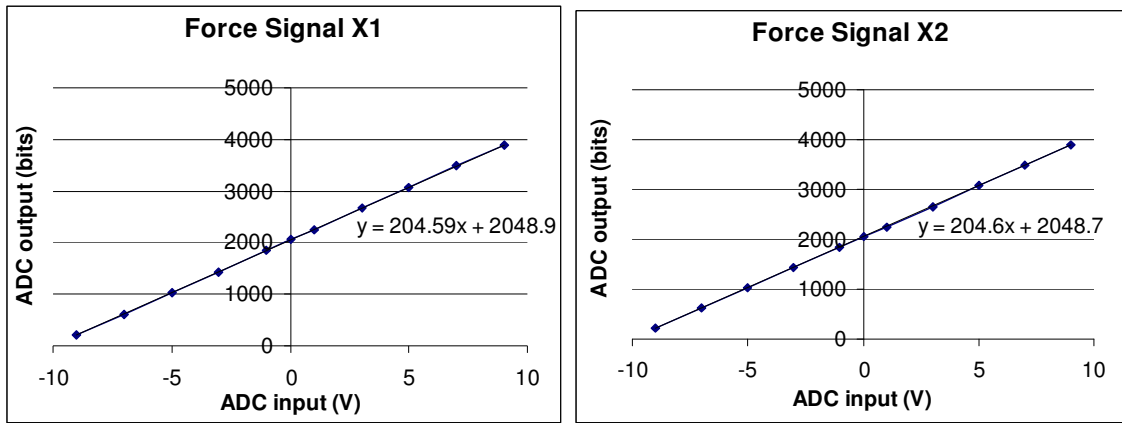
3.2 Calibration of Tool Force System

Calibration of the tool force system was required to ensure that measured forces correspond accurately to applied forces. A decision was made not to calibrate the completed system due to difficulties associated with applying a known weight of suitable magnitude (up to ± 5 kN) on each loadcell. This is because applying a known force to each loadcell separately and measuring the output would involve dismantling the mounting for the loadcell frame which is unstable and difficult to assemble because

the z -axis loadcells support the frame in compression from underneath. Instead a sectional calibration of each separate component of the system was performed, which enabled output force to be calculated from the linear functions describing each section of the system. Calibration of the loadcells and amplifiers was carried out by the manufacturers who supplied certificates, and therefore the only component that was required to be calibrated in-house was the ADC card, which is described in Section 3.2.1 below. The sectional calibrations carried out by the manufacturers and the in-house calibration of the ADC card were combined to give the overall output signal as a function of input force, described in Section 3.2.2.

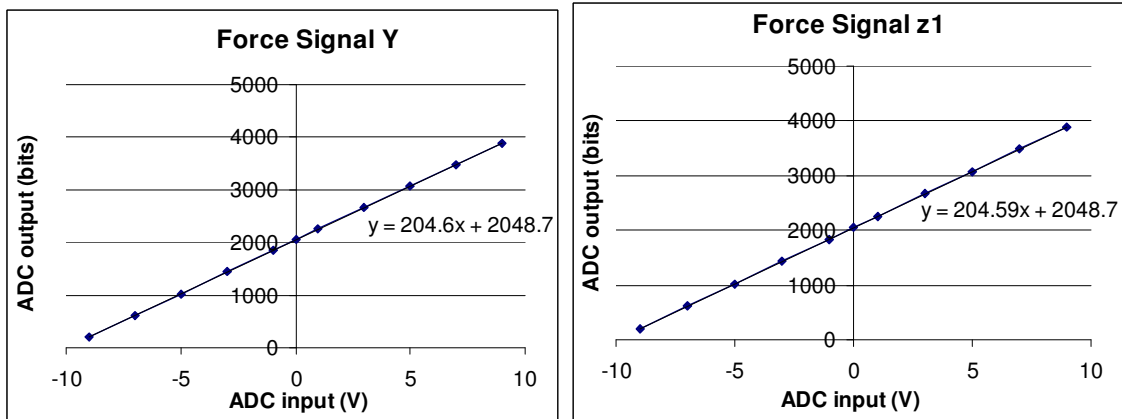
3.2.1 Calibration of APCI-ADADIOCS Card

Calibration of the APCI-ADADIOCS card accurately established the linear function relating the six analogue input signals (amplified tool force signals in the range of approximately -10V to 10V) to the output signals of the card in bits (range approximately 0 to 4095 bits). This was carried out by supplying a range of accurately measured stable voltages to the signal channels on the APCI-ADADIOCS card whilst keeping the necessary pins earthed (1, 21 and 34), recording the output from each channel in bits, and fitting a linear regression line to output as a function of input. The signal was supplied from a 12V car battery, adjusted using a $5\text{M}\Omega$ potential divider and measured with a digital voltmeter to an accuracy of 1mV. The output signal, sampled at a frequency of approximately 1Hz for duration of approximately two minutes in each test, was averaged and the results of output in bits as a linear function of input in Volts are displayed in Fig. 19.



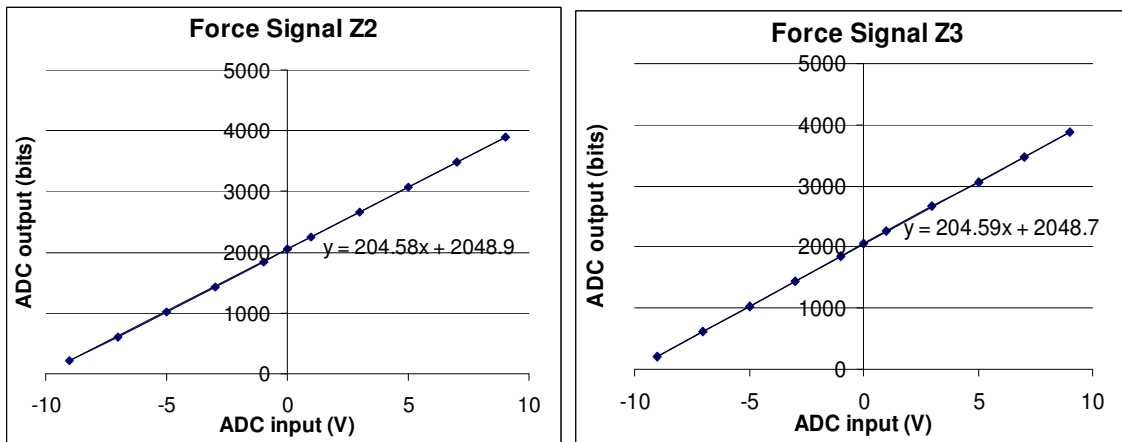
a) Force signal X₁

b) Force signal X₂



c) Force signal Y

d) Force signal Z₁



e) Force signal Z₂

f) Force signal Z₃

Fig. 19. Averaged outputs in bits for a range of input voltages on each channel on APCI-ADADIO card

3.2.2 Combination of Sectional Calibrations

A signal flow diagram summarising the approximate ranges of the input and output signals at each component of the tool force system is shown in Fig. 20. The linear functions describing output as a function of input labelled on the diagram, obtained by calibration of each of the components of the system, are summarised in Table 1. Function B(A), describing the loadcell output voltage as a function of applied force A was provided by the manufacturer, Novatech. Similarly, function C(B), describing the output voltage of the amplifiers as a function of input voltage was supplied by the manufacturer. Function D(C) describing the output in bits as a function of input voltage of the ADC card was found by in-house calibration (described above). The final function E(D) was found by re-arranging the previous equations and converts the output of the ADC card in bits to a reading of tool force in Newtons.

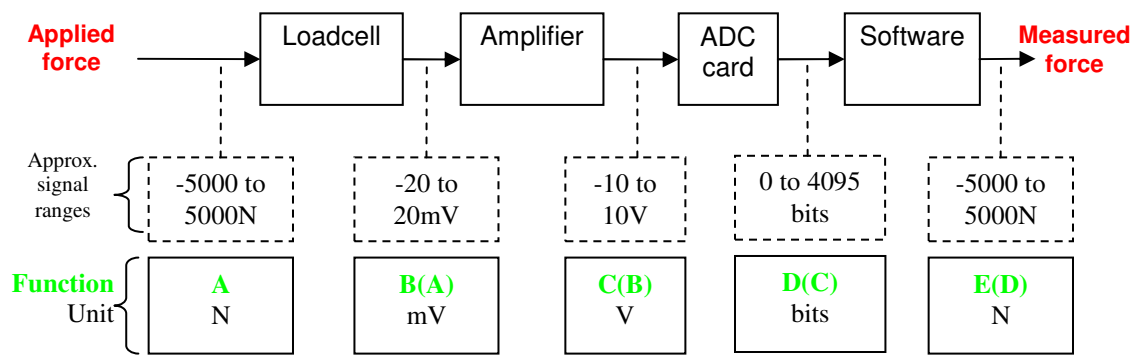


Fig. 20. Approximate ranges of signals at each stage in the signal flow diagram

Signal	B(A)	C(B)	D(C)	E(D)
X_1	$B = \frac{A \times 19.9845}{5000}$	$C = \frac{B \times 10}{20}$	$D = 204.59C + 2048.9$	$E = \frac{10000(D - 2048.9)}{204.59 \times 19.9845}$
X_2	$B = \frac{A \times 20.024}{5000}$	$C = \frac{B \times 10}{20}$	$D = 204.6C + 2048.7$	$E = \frac{10000(D - 2048.7)}{204.6 \times 20.024}$
Y	$B = \frac{A \times 20.0285}{5000}$	$C = \frac{B \times 10}{20}$	$D = 204.6C + 2048.7$	$E = \frac{10000(D - 2048.7)}{204.6 \times 20.0285}$
Z_1	$B = \frac{A \times 20.0065}{5000}$	$C = \frac{B \times 10}{20}$	$D = 204.59C + 2048.7$	$E = \frac{10000(D - 2048.7)}{204.59 \times 20.0065}$
Z_2	$B = \frac{A \times 20.0015}{5000}$	$C = \frac{B \times 10}{20}$	$D = 204.58C + 2048.9$	$E = \frac{10000(D - 2048.9)}{204.58 \times 20.0015}$
Z_3	$B = \frac{A \times 20.0085}{5000}$	$C = \frac{B \times 10}{20}$	$D = 204.59C + 2048.7$	$E = \frac{10000(D - 2048.7)}{204.59 \times 20.0085}$

Table 1. Functions obtained at each stage in the system from sectional calibration

3.3 Accuracy of Tool Force System

The aim of this section is to find the accuracy of the forces measured by the tool force system, i.e. how close tool forces measured by the system are to the true values of the tool force applied. Three possible sources of error in the tool force measurements have been identified: calibration error; drift; and noise. Calibration error could exist as a result of inaccurate sectional calibration, i.e. if readings measured by the system in a stable condition are not equal to the applied load. Drift occurs if there is a warm-up period of the tool force system, and hence should be measured so it can be avoided in future experiments. Noise on the tool force signal is a result of electrical interference and will also have a statistical influence on the accuracy of a single tool force measurement. The total error of the system is the sum of all three of these errors, and ideally this should be small in comparison to the magnitude of readings that are expected to be taken. The magnitude of tool force readings are expected to be of the order of hundreds of Newtons in the horizontal and vertical directions based on previous works by Duflou et al [13], Jeswiet et al [56] and Bologna et al [55]. The measurement of each of the sources of error is described in Sections 3.3.1 to 3.3.3 below. The errors are combined in Section 3.3.4.

3.3.1 Calibration Accuracy

The sectional calibration of the tool force system carried out in Section 3.2 should allow for accurate tool force measurements, i.e. measurements that are close to the true value of force that is applied. However, it is necessary to measure the calibration accuracy of the complete system to verify if this is a source of error. The calibration accuracy of the tool force system can be measured by comparing applied force to measured force for each of the loadcells under a range of forces, where the measured force is calculated from the ADC card reading according to function $E(D)$ shown in Table 1. However, it was not practical to test each of the six loadcells individually because this would require disassembly of the loadcell frame which is unstable and difficult to assemble because the z -axis loadcells support the frame in compression from underneath. An alternative approach would be to test the combined calibration accuracy of the x -axis loadcells (X_1 and X_2), the single y -axis loadcell (Y) and the three z -axis loadcells (Z_1 , Z_2 and Z_3) working in parallel by hanging weights from the machine. However, testing of the

horizontal axes (x and y) in combination was also not possible because it would be dangerous to hang substantial weights of up to 5 kN over the side of the machine due to a risk of toppling, the routing of electrical cables and lack of space. Measurement of the calibration accuracy was therefore only carried out on the z -axis with all three z -axis loadcells (Z_1 , Z_2 and Z_3) working in parallel by hanging known weights under the machine. It is likely that the calibration accuracy of the z -axis is similar to that of all six loadcells because the components and circuitry of each tool force signal are the same and the same procedure for sectional calibration was followed.

The calibration accuracy of the z -axis tool force measurements was measured by suspending a range of known weights between approximately 100 and 740 N underneath the workpiece frame. Although the maximum weight applied is a small fraction of the maximum range that the loadcells can each measure (5 kN), it is anticipated that most ISF experiments will have vertical tool forces within this range and it was not practical to suspend any heavier weights under the machine. The applied weights were buckets of shot peen, measured with a spring balance to a resolution error of $\pm 0.5\text{kg} = \pm 5\text{ N}$. The experimental set-up, which involved supporting the weights on the spring balance hung from a bar resting across the workpiece frame, is illustrated in Fig. 21.

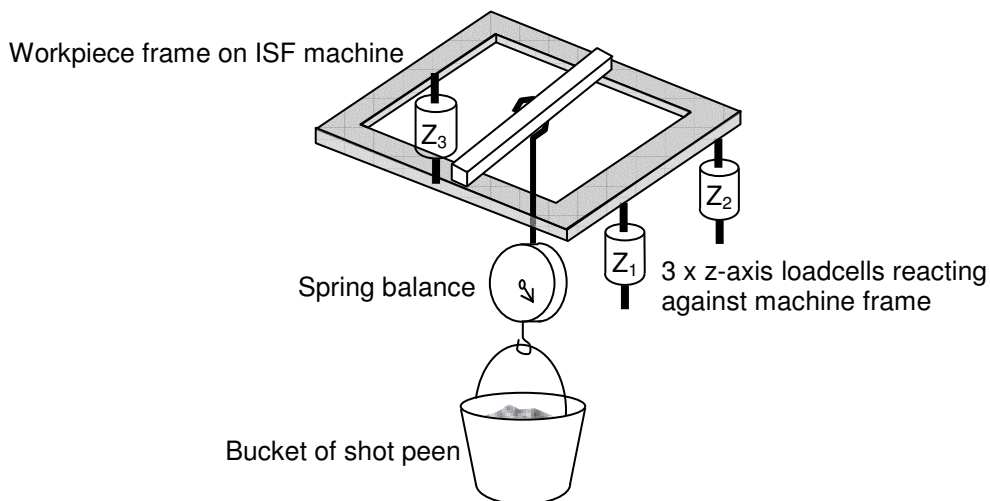


Fig. 21. Experimental set-up used for measurement of calibration accuracy of z -axis by suspending weights from the workpiece frame on the ISF machine

The measured weight under each applied load was calculated by finding the average output signal of tool force measured at a frequency of 1Hz for duration of approximately one minute. The readings were averaged over a period of time instead of taking just one reading to eliminate error due to noise to give a precise estimation of the calibration accuracy by ensuring a low *standard error in the mean*. The higher the number of readings in the set, the lower the standard error in the mean, σ_x , which is found by dividing the standard deviation, σ , by the square root of the number of readings, n (Equation 3.1) (Kirkup [122]). The standard error in the mean was approximately only 0.6 N for each of the weights measured, and therefore the mean of readings taken for one minute duration is a precise representation of the reading of the system.

$$\sigma_x = \frac{\sigma}{\sqrt{n}} \quad (3.1)$$

The results for measurements of calibration accuracy are shown on Fig. 22, where average total vertical force is plotted against applied force as blue markers. The red line shows the case where measured load equals the applied load, i.e. for a perfect system with zero calibration error of the tool force system and zero error of the spring balances used to measure the applied load. On each of the blue markers, horizontal error bars show the resolution error of the applied load measured by the spring balance. Vertical error bars indicating the uncertainties in the mean of the measured load are not shown because they would be too small on these axes.

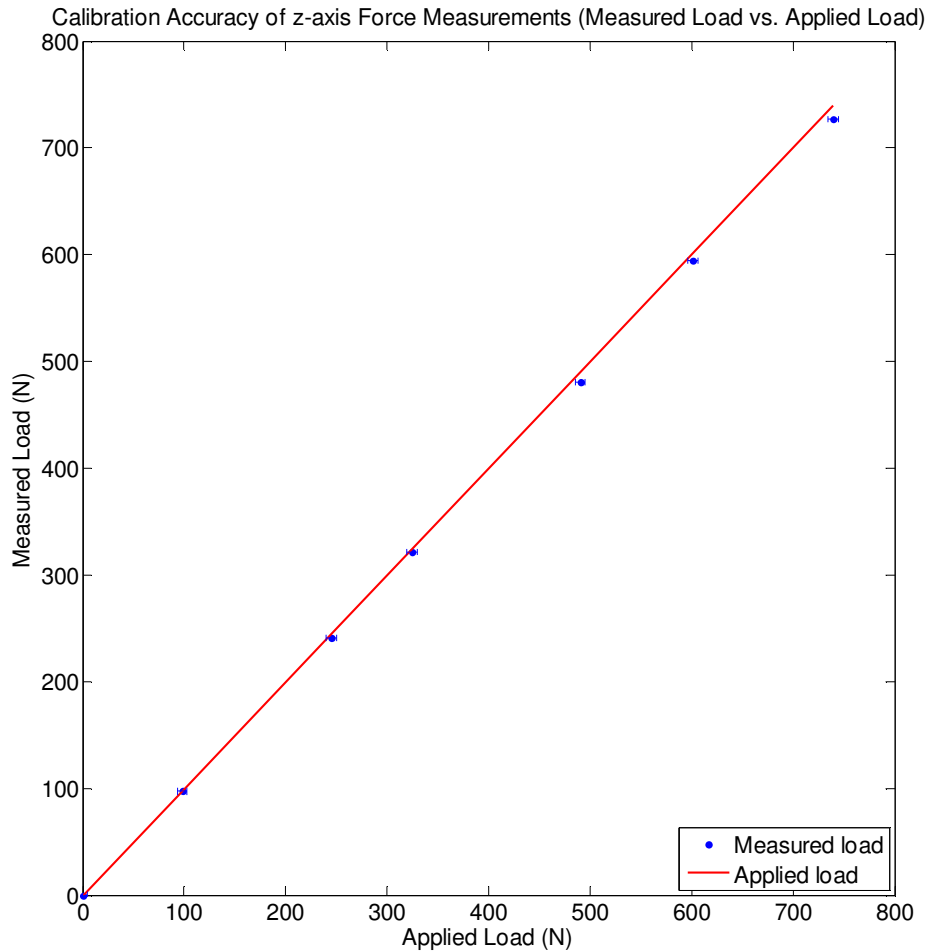


Fig. 22. Measured force vs. applied force for z-axis loadcells loaded in parallel for a range of known compressive weights

It can be seen from Fig. 22 that measured force is close to applied force for the tool force system across the range of forces that were tested. The average calibration error measured across the force range of 100 to 740 N for the z-axis in parallel was 5.5N, with a maximum error of 13 N for an applied load of 740 N (percentage error 1.8%). Most of this error can be accounted for by the resolution error of the spring balances that were used to measure the applied load. The calibration error of each individual z-axis loadcell can be estimated by dividing the average calibration error of the three axes in parallel by three ($\pm 5.5 \text{ N} \div 3 = \pm 1.8 \text{ N}$) (Kirkup [122]). It will be assumed that the same calibration error occurs on all six loadcells.

3.3.2 Drift

Drift in the tool force system has been investigated as a potential source of error to determine whether or not a ‘warm-up’ period is required to allow readings to stabilise, and if so the duration of this period. The two sections of the system that have power supplies and therefore may require warm-up periods are the amplifier unit and the PC. In order to isolate the contribution of each of these components to a warm-up period, drift has been measured for the following scenarios:

- Amplifiers and PC just switched on
- Amplifier has been left on for several hours and PC just switched on
- PC has been left on for several hours and amplifiers just switched on.

The results for all six channels for the above three scenarios are shown in Fig. 23.

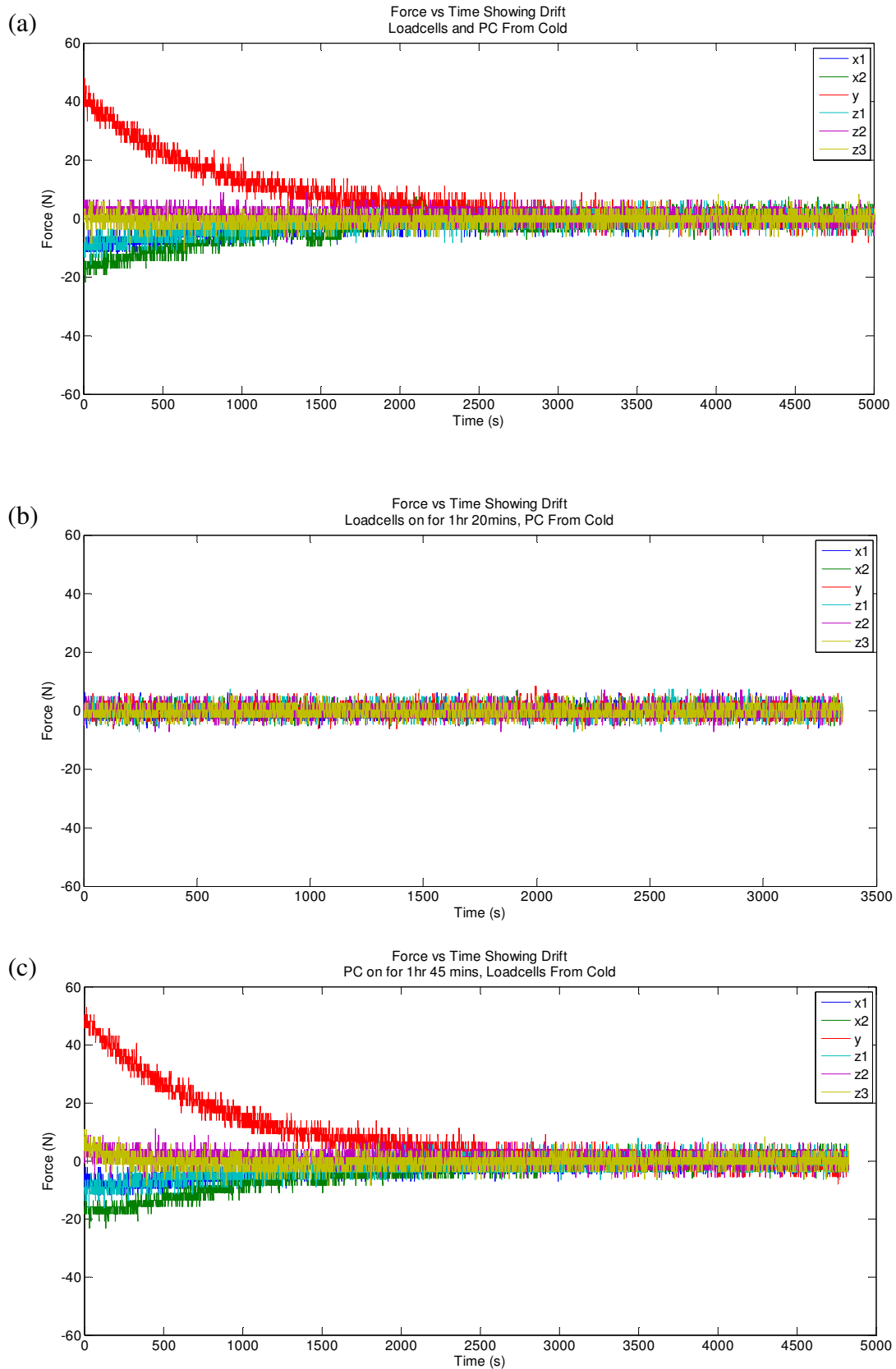


Fig. 23. Measurements of drift under various conditions: a) amplifier unit and PC switched on from cold; b) amplifier left on for 1hr 20 mins, PC switched on from cold; c) PC left on for 1hr 45 mins, amplifiers switched on from cold.

The measurements of drift show that only the loadcell amplifiers have a warm-up period; the PC can be started from cold with no effect on the tool force readings. The warm-up period is approximately 3600 s (≈ 1 hr), and therefore the loadcell amplifiers should be switched on for this period of time before tool force measurements are taken. Provided the loadcells have been allowed to warm-up properly before readings are taken, drift should provide no contribution to experimental error of the system.

3.3.3 Noise

Noise in the tool force measurement system has been investigated as a potential source of error. The error in a single tool force reading as a result of noise is equal to the standard deviation of a set of readings taken at that force (Kirkup [122]). Possible sources of electrical noise include electrical mains, lighting, equipment in the surrounding laboratory, power supplies to the motors and transformers in the machine supply unit, although precautions were taken to minimise noise in the system as described in Section 3.2.1. Noise was measured under the following three conditions which might occur at different stages during a typical ISF experiment:

- Machine turned off
- Machine turned on but not moving
- Machine turned on and moving

The error due to noise under each of the above conditions was calculated by finding the standard deviation of tool force on each channel for readings taken with no load on the machine at a frequency of 1Hz for duration of approximately 1 hr. The results for the three conditions are represented as force versus time plots and histograms of noise on each channel in Fig. 24. The standard deviations of noise on all six channels are given to two significant figures in Table 2.

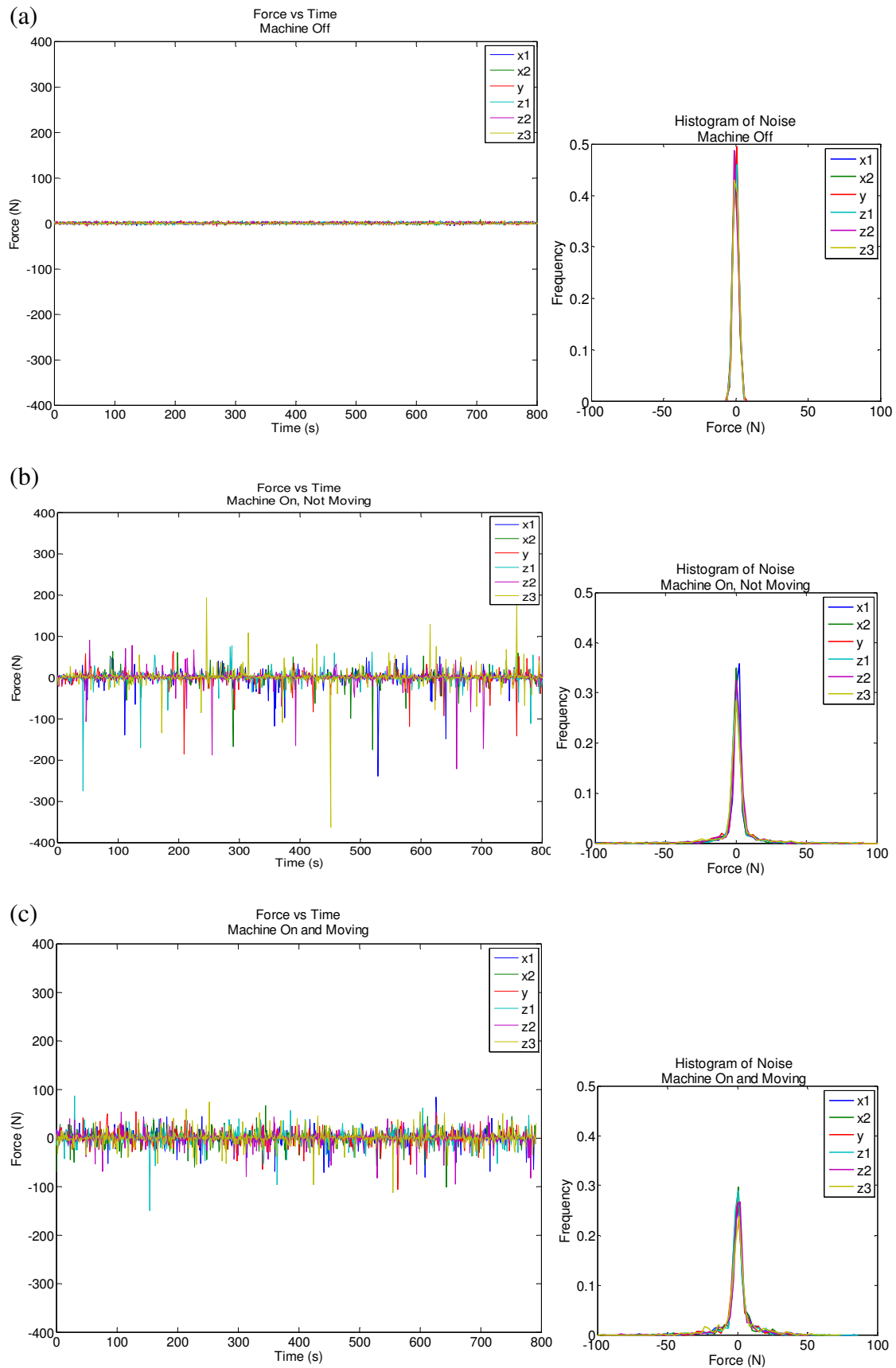


Fig. 24. Noise on all six channels for a range of operating conditions: a) machine turned off; b) machine turned on but not moving; c) machine turned on and moving.

<i>Channel</i>	<i>Standard Deviations (N)</i>		
	<i>Machine Off</i>	<i>Machine On, Not Moving</i>	<i>Machine On and Moving</i>
X ₁	2.0	17	12
X ₂	1.8	14	12
Y	1.9	16	11
Z ₁	1.8	16	13
Z ₂	1.9	17	13
Z ₃	1.9	21	14
Average	1.9	17	12

Table 2. Standard deviations of noise for all six channels in a range of operating conditions

The results show that a different level of noise occurs in each scenario, and that the greatest noise occurs when the machine is turned on and not moving. When the machine is on and moving, as would be the case throughout most tool force experiments, the error due to noise for a single reading of tool force is ± 12 N.

3.3.4 Combination of Errors

The accuracy of the tool force system can be found by combining the errors due to noise and calibration error. (The error due to drift should be zero provided that the loadcells have been allowed to warm up sufficiently.) The total error in tool force measured on each channel for the scenario when the machine is on and moving, as would be the case throughout most tool force experiments, is summarised in Table 3.

<i>Channel</i>	<i>Calibration Error (N)</i>	<i>Error Due to Noise (N)</i>	<i>Total Error (N)</i>
X ₁	± 1.8	± 12	± 14
X ₂	± 1.8	± 12	± 14
Y	± 1.8	± 11	± 13
Z ₁	± 1.8	± 13	± 15
Z ₂	± 1.8	± 13	± 15
Z ₃	± 1.8	± 14	± 16
Average	± 1.8	± 12	± 15

Table 3. Combination of errors due to noise and calibration on all channels of tool force system

3.4 Summarising Comments

A system has been developed for measuring tool forces simultaneously with tool position on the ISF rig, for use in the experiments presented later in this thesis. The software for reading tool force and tool position has a minimum sample period of 0.4 s, which allows an adequate distance between successive readings of approximately 8 mm for a typical tool speed of 20 mm/s. The loadcells should be switched on for approximately 1hr before readings are taken to warm up. Provided the loadcells have warmed up properly, the error of tool force readings is the combination of error due to calibration and error due to noise. When the machine is on and moving, this is on average ± 15 N for a single tool force reading on each force signal. The error is likely to be small in comparison to the tool forces measured in ISF experiments, which are expected to be of the order of hundreds of Newtons.

4. The Mechanics of Incremental Forming of Sheet Metals

Despite extensive research in ISF over the last decade, the deformation mechanics is not fully understood and has never been experimentally verified through the thickness of the sheet. An understanding of the deformation mechanism is important to allow accurate numerical models to be developed for tool path design and process control, and to develop an understanding of the increased forming limits observed in ISF in comparison to pressing. The aims of this chapter are therefore to provide new insights into the deformation mechanics of sheet metals in ISF. This is achieved through two approaches: (1) experimental measurement of the through-thickness deformation in SPIF and TPIF; and (2) comparison of the tool forces throughout a simple tool path in SPIF and TPIF. It is shown that the deformation mechanisms of both SPIF and TPIF are increasing shear and stretching perpendicular to the tool direction, with shear parallel to the tool direction as the most significant component. The measured strains follow similar trends to the tool forces, which suggests that shear in the tool direction is a result of friction between the tool and workpiece.

4.1 Through-thickness deformation in SPIF and TPIF

Until now, research on the deformation mechanics of ISF has focussed on measurement of the strains and displacements of the surfaces of sheets or FE predictions of strains through the thickness. However, experimental measurement of the full through-thickness deformation, which would serve to validate the FE models and give further insight than surface measurements, has not been carried out. The aim of this section is therefore to provide the first experimental measurements of deformation through the thickness of plates formed by the two most common forms of ISF: SPIF and TPIF against a positive die support. A comparison will also be made to pressing with the aim of distinguishing the key differences which may account for the observed increased forming limits in ISF, as were discussed in Chapter 2, Section 2.4.5.

The first four parts of this section (4.1.1 to 4.1.4) describe the method used to measure the through-thickness deformation of SPIF, TPIF and pressing. This is based on a visioelastic technique similar to that developed by Kalpakcioglu in 1961 [81]. A grid pattern is machined on to the cross-sections of two half-plates which are subsequently brazed together then formed before separating by heating. The principal advantage of this technique is that brazing allows a strong and thin joint to be formed which can subsequently be easily destroyed by heating. The method used to analyse the deformation and calculate strains is described in Section 4.1.5. Experimental error is calculated in Section 4.1.6. The results are presented in Section 4.1.7, and the section ends with a brief summary of the results (Section 4.1.8). A full discussion of the results has been left to Section 4.3 at the end of the chapter to allow a comparison to the tool force results which are to follow in Section 4.2.

4.1.1 Selection and Characterisation of Materials

Copper C101 was selected as the sheet material for this experiment because it can be readily cold-worked and effectively brazed. The sheet was received in a work-hardened condition. A sheet of thickness 3.2 mm was selected because this is sufficiently thick to allow one longitudinal centreline in the cross-sectional grid pattern and hence to allow the variation of strains through the thickness of the sheet to be measured. This thickness

is towards the upper end of the range of sheet thickness that is commonly used in ISF. As discussed in Chapter 2, sheets for ISF are usually between 0.5 and 1.5 mm.

The selected sheet metal has been characterised by tensile testing to show how the heating cycle involved in brazing has affected the mechanical properties, as well as to provide a basis for a discussion of how the deformation measured in this experiment might transfer to other materials more commonly used in ISF. In-house characterisation was required as opposed to relying on databook values for two reasons. Firstly, there is potential for wide variability in mechanical properties depending on manufacturer, batch, etc. Secondly, the heat-treatment undertaken to braze the copper plates was not typical of annealing processes and therefore was not characterised in the databooks. C101 can be annealed by heating to 370-650°C followed by rapid cooling. However, the thermal cycle undertaken for brazing involved heating the sheet to 900°C for a period of 20 minutes and then cooling slowly in air to avoid disturbance of the braze. Tensile testing was carried out on sub-size tensile specimens in the rolling and transverse directions as specified by American standard ASTM E8M-01. An Instron 5500 machine was used at a rate of 0.5 mm/s. The results are shown in Fig. 25.

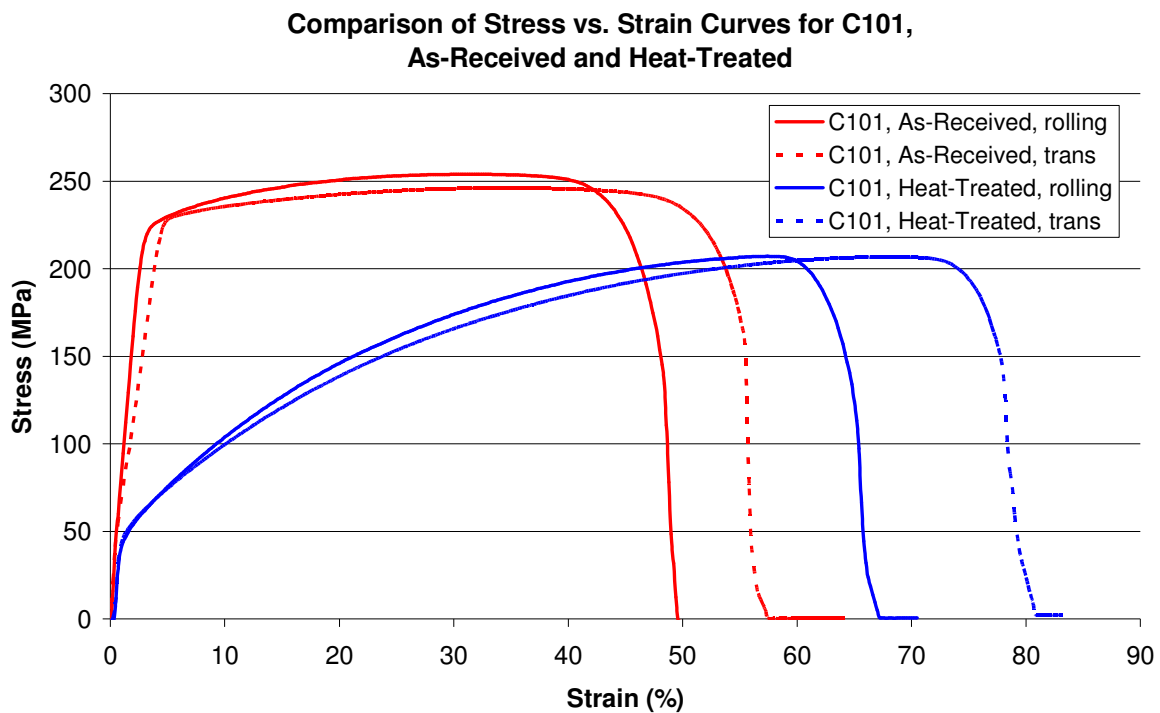


Fig. 25. A comparison of stress vs. strain curves for C101 in the as-received and heat-treated conditions, showing characteristics in the rolling and transverse directions.

Tensile testing provided three interesting insights into the mechanical properties of the formed plate. Firstly, a significantly lower yield stress was observed for the heat-treated material than the as-received material. This suggests that annealing had taken place, relieving some of the work-hardening that would have existed in the original material as a result of rolling. The high initial rate of work-hardening of the annealed material is a typical characteristic of copper. Secondly, rumpling of the surface of the heat-treated material was observed on a small scale (1-2 mm), indicating that the recovered grain size was larger than the original. Finally, the heat-treated material was anisotropic in terms of elongation; elongation of approximately 75% was measured in the transverse direction whilst only 60% was measured in the rolling direction. However, because the plates will not be formed to failure in these experiments, it is safe to assume that the copper will behave isotropically throughout the elastic and plastic regime. Although the stress versus strain curve of the C101 used in this experiment is likely to differ from those of mild steel and aluminium alloys that are more commonly used in ISF, it is likely that the deformation mechanism will show similarities to these materials when they are formed by the same process. The extent to which the results of this experiment may be transferable to other materials will be discussed at the end of this chapter.

4.1.2 Preparation of Sheets

To minimise variation in mechanical properties between the sheets used for SPIF, TPIF and pressing, each sheet was cut from a single sheet of C101. The three plates of initial size 175 x 175 mm were cut in half in the thickness direction. One of the cross-sections of each plate was machined flat and then marked with a 1.5 x 1.5 mm grid pattern using a V-shaped cutter of internal angle 90°. This was achieved accurately using a milling machine by making one longitudinal cut and many intersecting transverse cuts at a spacing of 1.5 mm. The plates were joined back together by brazing such that the gridded surface was on the inside of the brazed joint. Johnson Matthey Silver Flo 55 hard solder (melting point 630-660°C) was used for brazing to form a hard but ductile joint that could withstand forming without failure. This was purchased as rods of diameter 2 mm which were rolled into a flat and straight strip of width approximately 3 mm and thickness 0.5 mm using small rollers. The strip was then cut to the length of the joint using scissors. The joint and the solder were cleaned with an abrasive and rinsed thoroughly with acetone and water to remove oxidation and grease immediately

before applying high temperature flux (activation temperature 750–1000°C) neatly to the areas to be joined. The wetting of the flux was improved by adding soap. The solder strip and pieces of the copper plate were then carefully aligned and pushed together whilst resting on support blocks above a heat resistant plate. The assembly was then lifted carefully into a furnace that was preheated to the required temperature of 900°C and left for 20 minutes. This was sufficient time to fully melt the solder without exhausting the flux. The brazed plate was then removed from the furnace and left to cool in air to avoid disturbance of the joint. Oxidation was then removed from the cooled plate using a bead blaster. The plate used for pressing was cut into a circle of diameter 145 mm using a water jet cutter in order to fit within the die set. The plates used for SPIF and TPIF were left in their original square shape because this was required to fit in the square clamping frame used on the ISF machine.

4.1.3 Forming

A truncated cone with a wall angle of 30°, outer diameter of 100 mm and inner diameter of 20 mm with a corner radius at the top and bottom of 10 mm was formed in the brazed plate using each of SPIF, TPIF and pressing. Although 30° is a shallow wall angle that is likely to be well within the forming limits of the sheets formed by ISF, this angle was chosen because preliminary trials suggested that it was the maximum wall angle at which the brazed joint did not fail in SPIF. The configurations of tooling for the three forming processes are shown in Fig. 26. The forming machine which was used for SPIF and TPIF was the specialised rig developed by Allwood et al [32]. For SPIF and TPIF, a contour path was used with a vertical pitch between successive laps of 0.5 mm and a tool of radius 7.5 mm. The step-down point between each contour was along a radius at 90° to the brazed joint, therefore the deformation along the brazed joint should not be affected by the change in speed and direction of the tool at the step-down point. The tool speed was 20 mm/s with an acceleration and deceleration into the step-down point of 10 mm/s². Lubrication was Castrol Spherol extreme pressure grease L-EP2. Because the workpiece frame is fixed on the ISF machine, the TPIF shape was formed by raising the positive die from underneath after each lap by turning four leadscrews on a mounted support whilst keeping the vertical position of the indenter constant and increasing the diameter on successive laps. For pressing, the blank holder was a flat ring of width 30 mm and thickness 12 mm, loosely fastened to the female (lower) die by

six M8 bolts so the bolt heads just made contact with the blank holder surface. The male and female dies were machined out of mild steel. Sheets of polythene were placed on either side of the blank to reduce friction between the blank and dies or blank holder without using grease. The male die descended slowly into the blank at a rate of approximately 0.03 mm/s using an Avery 1000 kN hydraulic universal testing machine.

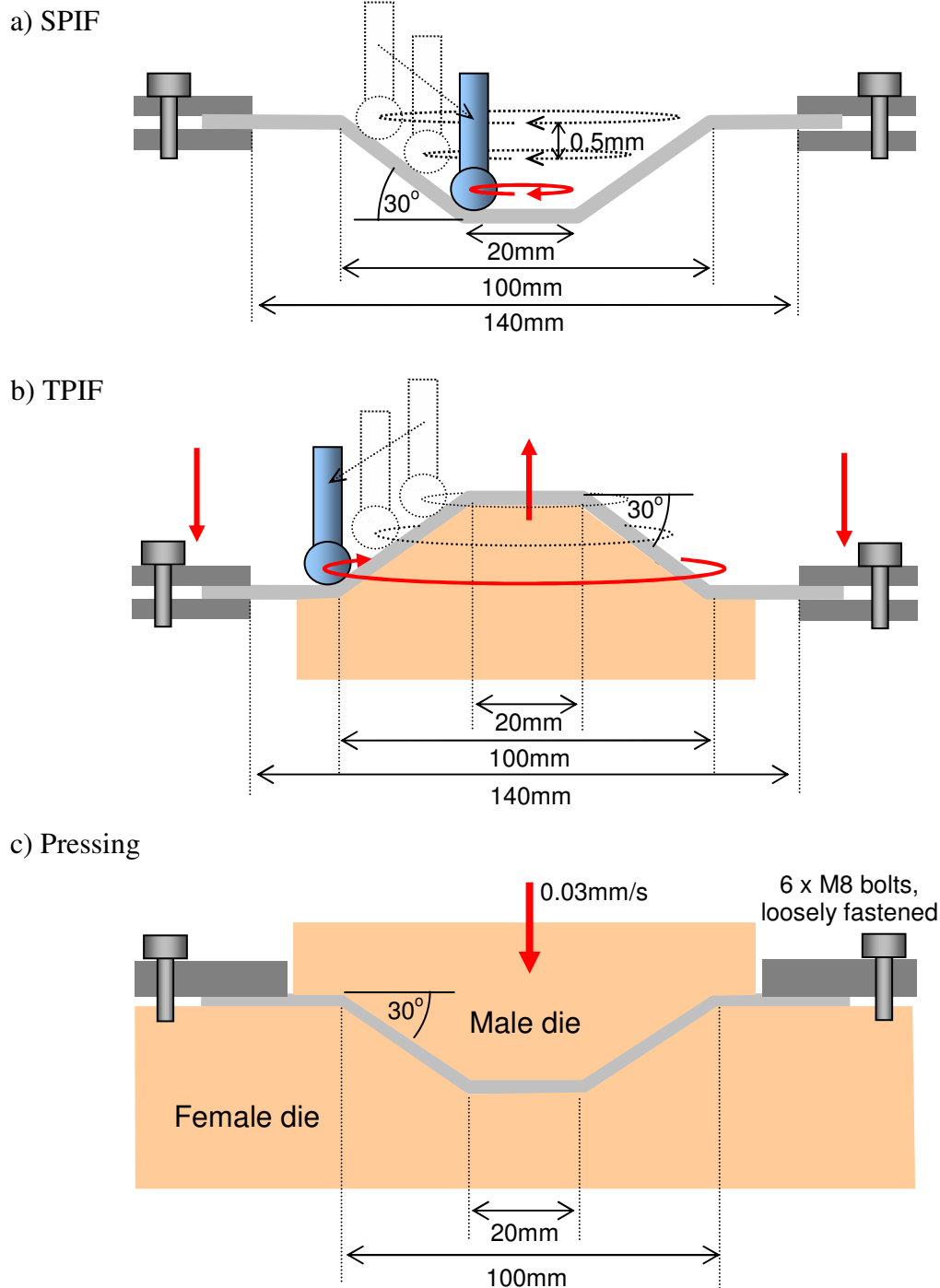


Fig. 26. Forming processes used to form copper plates: a) SPIF, b) TPIF and c) pressing.

4.1.4 Separation of Plates and Measurement of Deformation

After forming, the plates were separated by heating in the furnace to 900°C for approximately 20 minutes until the solder had melted. The remains of solder on the gridded surface were removed by heating the plate again with the gridded surface placed against a clean fluxed sacrificial copper plate onto which the solder was drawn. The plates were quenched on removal from the furnace to remove most of the oxidation by differential thermal contraction. The remaining oxidation was then removed with the bead blaster. A schematic diagram of the method, from flat gridded plate to formed and separated plates, is shown in Fig. 27.

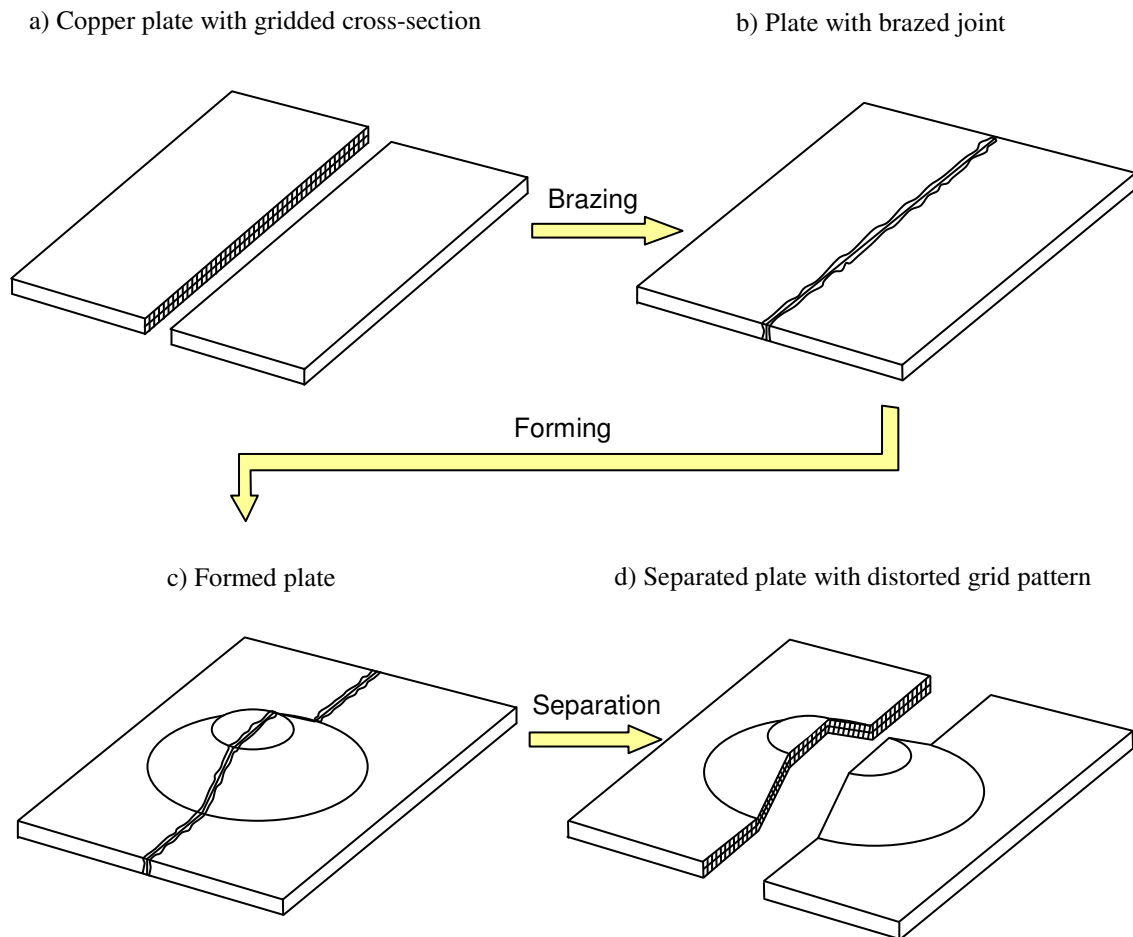


Fig. 27. Schematic diagram of method for measuring through-thickness deformation: a) copper plate with gridded cross-section; b) plate with brazed joint; c) formed plate and d) separated plate with distorted grid pattern.

The deformation of the cross-sections was photographed digitally along the cross-sections to a high resolution. The intersections of the gridlines and surface points were then measured in three dimensions using an OMICRON co-ordinate measuring machine (CMM) with x10 magnification microscopic eyepiece. The accuracy of the deformation measurements are evaluated later in Section 4.1.6. The thickness was measured across the cross-sections using vernier callipers to an accuracy of ± 0.005 mm.

4.1.5 Analysis of Deformation

The deformation will be analysed by plotting graphs of geometry, engineering strains and thickness variation for the copper plates. It is important to note that, because it is only possible to take measurements of geometry before forming and after forming, only strains at the end of the process can be calculated; the evolution of strains throughout the process cannot be found. Hence, the results of this experiment cannot be used to validate the step-wise evolution of strains that has been predicted by several finite element models; it is only the final strain components that can be compared. Furthermore, it is unlikely that the final strains at any point are the result of proportional growth of strain throughout the process. The strains are simply a representation of final geometry in comparison to initial geometry.

Deformation, engineering strains and thickness are plotted against global axes (r, θ, z) . The strains are calculated in a local co-ordinate set $(1, 2, 3)$. The right-handed global co-ordinate set (r, θ, z) is defined such that r is radial in the plane of the undeformed sheet and perpendicular to the tool direction, θ is circumferential in the plane of the undeformed sheet and parallel to the tool direction, and z is axial and perpendicular to the plane of the undeformed sheet. The origin of the global co-ordinate set is in the centre of the top surface of the plate before deformation, as shown in Fig. 28. The right-handed local co-ordinate set $(1, 2, 3)$ is defined such that the 1-direction is parallel to a projection of the longitudinal gridlines in the r - z plane, the 2-direction is parallel to the θ -direction and the 3-direction is perpendicular to the 1-direction in the r - z plane, as illustrated in Fig. 28. Strains were calculated over one half of the cross-section, as highlighted in Fig. 28. The local co-ordinate set $(1, 2, 3)$ has been chosen as the orientation in which to calculate strains because it is easiest to interpret strains that are aligned with the deformed gridlines and parallel or perpendicular to the tool direction.

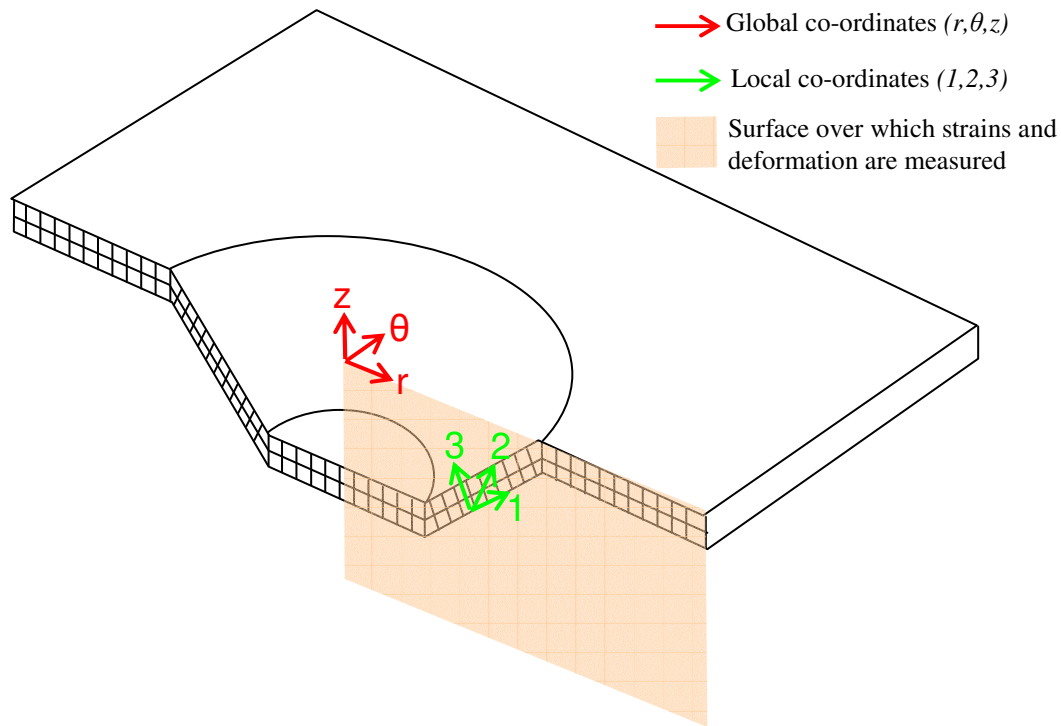
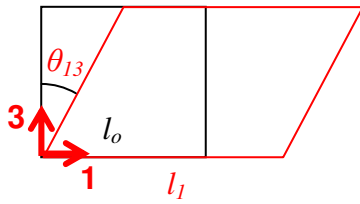


Fig. 28. A 3-dimensional representation of the global and local co-ordinate sets used to interpret strains in SPIF, TPIF and pressing.

Strains have been calculated from the relative movement before and after deformation of the points of intersection of the gridlines in the local co-ordinate set as shown in Fig. 29. Engineering strains perpendicular to the tool direction, ε_{11} , were found from the ratio of extension to original length of the longitudinal gridlines projected into the 1-direction (Equ 4.1). It is justified to use engineering strains instead of true (logarithmic) strains because the strains are small. The maximum ratio of extension to original length is approximately 0.2 due to the shallow wall angle of the formed plates, which gives an engineering strain that is greater than true strain by only 1.8%. Strain ε_{11} is plotted against r as the average of ε_{11} at each of the lower, middle and upper surfaces of the grid pattern. This is because there is negligible variation of ε_{11} through the thickness of the sheet because there is negligible curvature of the cross-section. The cross-section is approximately straight along the base, inclined side and truncated apex of the cone, and the most highly curved regions are the intersections between the inclined side and the base or apex of the cone. Here the radius of curvature is approximately 10 mm, which is large in comparison to the original segment length of 1.5 mm.

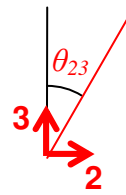
In plane of grid:



$$\epsilon_{11} = \frac{l_1 - l_0}{l_0} \quad (4.1)$$

$$\gamma_{13} = \tan \theta_{13} \quad (4.2)$$

Perpendicular to plane of grid:



$$\gamma_{23} = \tan \theta_{23} \quad (4.3)$$

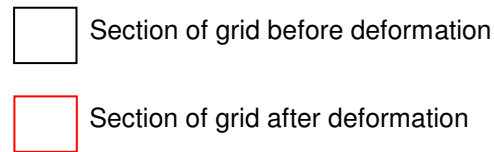


Fig. 29. Calculation of engineering strains from deformation

Engineering shear strains perpendicular and parallel to the tool direction in the through-thickness plane of the sheet have been calculated from the tangents of the angle of rotation of initially perpendicular gridlines in the $I,3$ plane (γ_{13}) and $2,3$ plane (γ_{23}). These are shown in Equ (4.2) and Equ (4.3) respectively, and follow a common definition of engineering shear strain found in text books such as Hertzberg [123]. Due to a measurable variation in shear strains through the thickness of the sheet, both components of shear strain were calculated along the r -direction at two layers through the thickness: between the lower and middle surfaces; and between the middle and upper surfaces. In order to reduce experimental error, shear strain γ_{13} was plotted as the average of the shear in each corner of each grid element. According to the definition of the local co-ordinate set $(1,2,3)$, a positive value of shear γ_{13} corresponds to a shearing towards the outside of the plate, whilst a negative value corresponds to shearing towards the inside of the plate. Because the indenter contacts the lower surface of the plate in TPIF and the upper surface of the plate in SPIF and in both cases runs anticlockwise, a positive γ_{23} corresponds to material being sheared in the tool direction in SPIF, whilst a negative γ_{23} corresponds to material being sheared in the tool direction in TPIF.

The final quantity that has been calculated to analyse the deformation of the sheets is the variation in thickness across the cross-section. Three graphs of thickness have been plotted against r : the average original thickness; the thickness that was measured after deformation with vernier callipers; and the thickness predicted from the sine law. The sine law used the average wall angle of the lower, middle and upper surfaces at each r -position because the variation in the wall angle of the sheet through its thickness was negligible. The average original thickness has been used to represent the original thickness across the entire cross-section of the sheet because preliminary measurements showed that the original thickness varied negligibly by approximately ± 0.02 mm.

4.1.6 Experimental Error

It is important to give careful consideration to experimental error in the present experiments because small errors in displacement measured on a small grid can equate to large errors in strains. Similarly, small errors in measured displacement on a plate with a shallow wall angle can equate to large errors in the sine law prediction of wall thickness. Three possible sources of experimental error have been identified: (1) measurement error; (2) possible changes in the mechanical properties of the sheet material across the brazed joint causing a change in the deformation mechanics; and (3) possible cracking of the brazed joint causing the cross-section not to distort in the same way as the rest of the sheet. The magnitudes of each of these errors and the resulting errors of calculations of strains are evaluated below.

The first source of error, measurement error, has been assessed for the OMICRON CMM by repeatedly measuring the same point six times and finding the range of positions recorded. The absolute errors in the r , z and θ directions which were obtained by these tests are summarised in Table 4 to one significant figure. The same accuracy is assumed everywhere on the cross-sections of each of the SPIF, TPIF and pressing plates.

<i>Dimension</i>	<i>Absolute Error (mm)</i>
r	± 0.02
z	± 0.01
θ	± 0.06

Table 4. Measurement errors of the Omicron CMM

The second source of experimental error to consider is any possible difference in the deformation of the brazed joint in comparison to the bulk material as a result of changes in mechanical properties across the joint. The measured deformation of the joint is only accurate if the joint has similar mechanical properties to the rest of the copper plate. Hard silver solder was used for the brazing of the copper plates with the aim of providing a strong joint that will not fail under the stresses applied by the indenter. It is possible that this joint may be harder or softer than the host material, and therefore that it may deform differently to the rest of the material. Because the deformation is mainly plastic, a simple hardness test will give a first insight into the variation in mechanical properties across the joint. Unlike welding, a heat affected zone does not form in furnace brazing because the whole plate undergoes the same heating cycle; the joint is formed by the filler forming a thin alloy layer at the interface with the host material [124]. This interface layer is highlighted on Fig. 30a, which is a micrograph of a cross-section which was polished then etched with dilute ferric chloride solution. Hence it is only necessary to consider the hardness of the filler material itself and the surrounding copper material. Microhardness measurements using a Shimadzu machine showed that the hardness of the filler was 90Hv whilst that of the copper plate was approximately 73.8Hv. The effect of this variation in hardness on the deformation mechanics is difficult to predict accurately. However, because the filler band is narrow ($\sim 120\mu\text{m}$) and because the difference in hardness is relatively small ($\sim 22\%$), it shall be assumed that any variation in the deformation mechanics resulting from the increased hardness of the filler band is negligible.

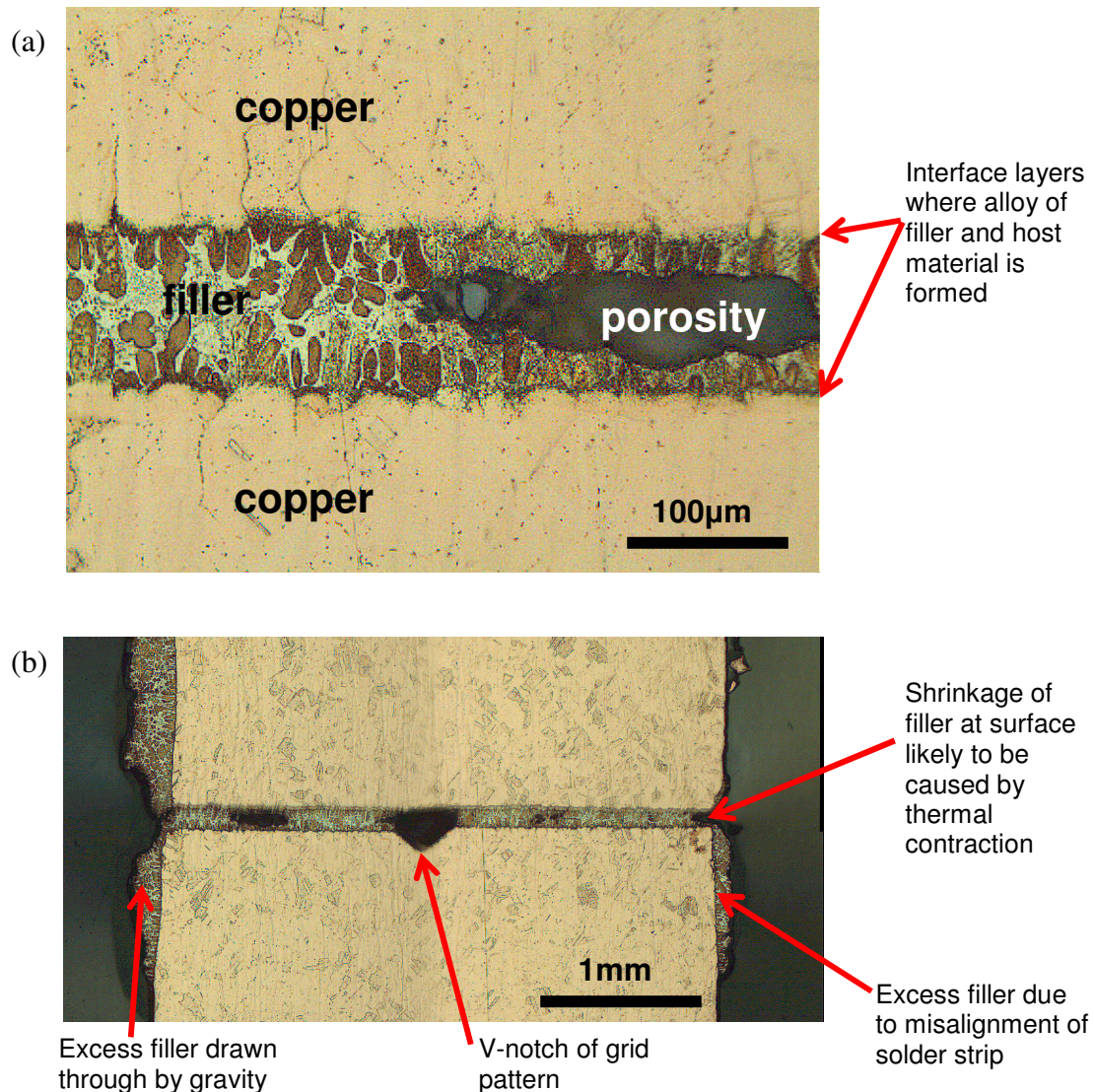


Fig. 30. Micrograph of a typical section of the braze before forming: (a) detail of porosity and filler layer; (b) full cross-section.

The third possible contributory factor to experimental error is cracks opening up along the brazed joint causing the joint to deform dissimilarly to the host material. Cracking was observed in SPIF although the joint did not fail, and smaller cracks were observed in TPIF. It is therefore necessary to consider the effects of cracking on the accuracy of the deformation measurements and strain calculations. Cracking could result from three factors: (1) porosity in the joint providing stress concentrations from which cracks can nucleate; (2) shrinkage of the filler material causing recessions at the surface of the joint from which cracks can nucleate (as described by Roberts [125]); (3) a filler material with a lower ductility than the host material which will fail before the copper plate in plastic deformation.

The first possible source of cracking, porosity, has been investigated by microscopy and X-ray tomography. A region of porosity is evident in the micrograph of the joint before deformation shown in Fig. 30a, which has length approximately 0.3 mm whilst the total width of the joint is 3.27 mm. Larger porosity as a result of the V-notch of the grid pattern is evident on the cross-section of Fig. 30b. X-ray tomography through a cross-section of the sheet of depth 4 mm before deformation showed that a similar volume of porosity was observed along the length of the braze (Fig. 31a). The porosity may be a result of inadequate contact between the solder and host material during heating or because of inadequate fluxing allowing oxidation which prevents bonding. This porosity is likely to act as a stress concentrator from which cracks can propagate.

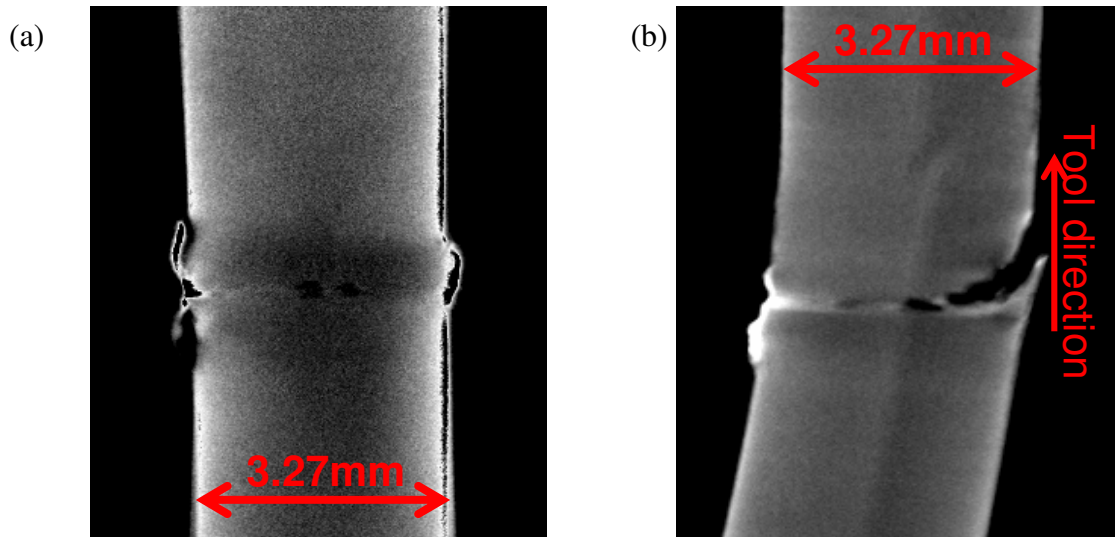


Fig. 31. X-ray tomography of cross-sections of braze: (a) before deformation; (b) after deformation.

The second possible source of cracking is shrinkage of the filler material due to thermal contraction, causing a notch along the surfaces of the joint which can act as a stress concentration from which cracks can propagate. Fig. 30b shows that on one side of the joint the filler has shrunk, whereas on the opposite side excess filler has coated the plate surface. This is due to misalignment of the strip of solder with the joint or gravity causing the filler to flow downwards in the furnace whilst it is molten.

Thirdly, the filler material may crack in preference to the copper plate if it has a lower ductility. It was not possible to measure the ductility of the braze material alone because the area in question is too small. However, tensile testing of the brazed copper

plate and the parent copper material was carried out to test whether the joint was a point of weakness in the plate as a combination of all three of the above factors. The results are shown in Fig. 32. This demonstrated that the brazed material had a ductility of approximately 40% whilst that of the parent copper plate was approximately 60% in the rolling direction and 75% in the transverse direction. Up to the point of failure, the brazed specimen followed a similar stress vs. strain curve to the parent material, and failure occurred along the brazed joint. This shows that the brazed joint was indeed a point of weakness in the material, and hence that cracking was likely to occur along the brazed joint as the material was strained.

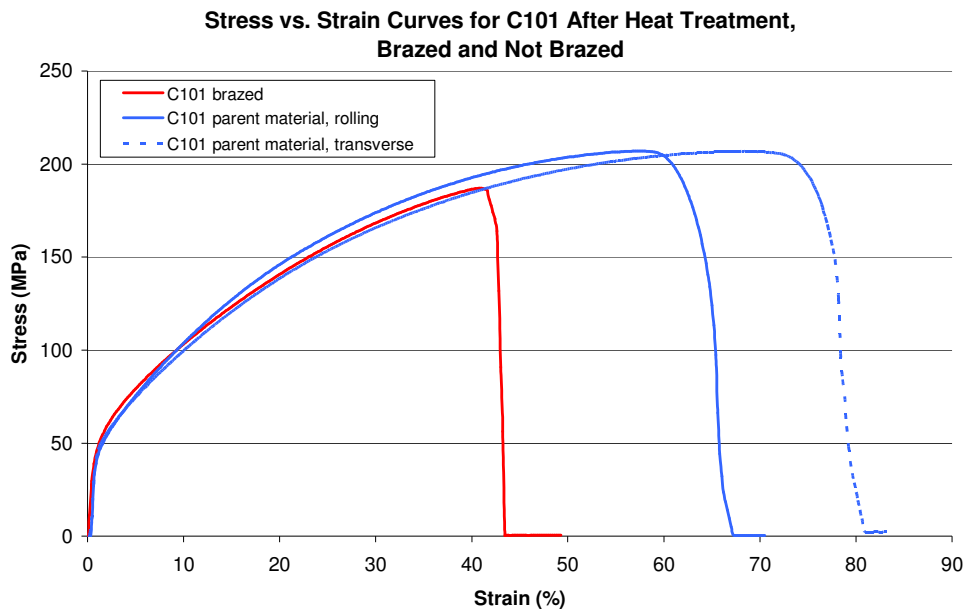


Fig. 32. Tensile tests of C101 after heat treatment, comparing the characteristics of the parent material with the properties across the brazed joint.

The extent of cracking in TPIF has been measured by taking a micrograph of a cross-section in the most severely deformed region of the formed plate (close to the base of the cone) (Fig. 33). This shows that a crack has propagated from the formed surface along the joint or through the host material close to the joint. Similar was shown by the X-ray tomograph in Fig. 31b. It is therefore evident that the brazed joint has not deformed exactly as the host material would have; the crack has opened up by up to approximately 0.2 mm. More severe cracking of up to approximately 0.8 mm was observed in SPIF, measured with vernier callipers on the formed sheet before separation. No cracking was observed in pressing.

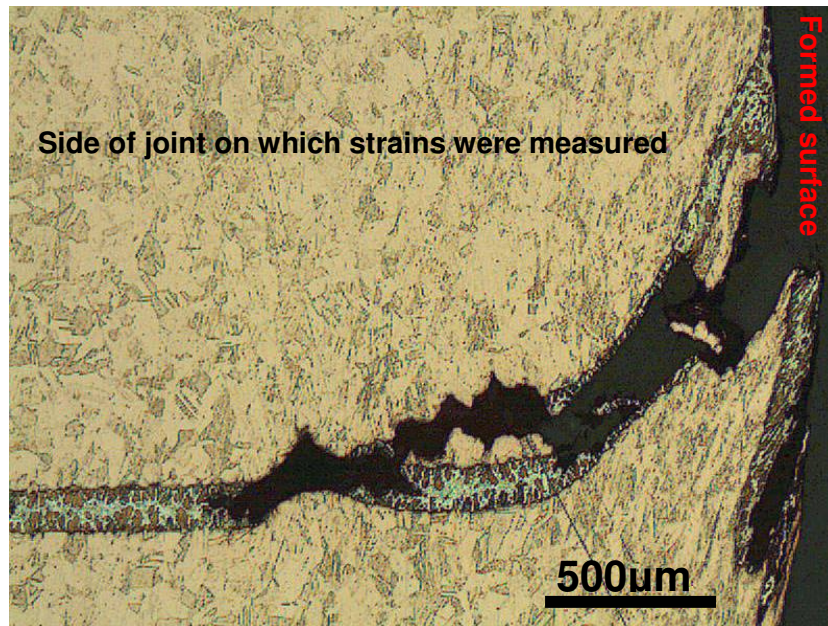


Fig. 33. Micrograph of crack through cross-section of TPIF sample showing propagation along braze from the formed surface.

In order to calculate the error in the calculations of strains from the measurement error and cracking reported above, the following assumptions have been made:

- The total position error in each of the r , z and θ direction is the sum of errors from measurement and cracking.
- The measurement error for each of r , z and θ is the same at any position.
- The position error resulting from cracking affects the measurements of θ only, and this error is greatest at the tool contacted surface, half of this value at the middle surface and zero at the surface not contacted by the tool. This is based on the observation that the tool-contact surface opened up the widest, whilst the surface not contacted by the tool did not open up at all.
- The position error of θ along each gridline due to cracking is proportional to the strain γ_{23} . This is based on the observation that the crack opened up the most where the shear γ_{23} was greatest and did not open up at all in the sections with no shear.
- The maximum position error of θ due to cracking (which is on the tool contact surface at the point with maximum γ_{23}) is ± 0.4 mm for SPIF, ± 0.1 mm for TPIF and 0 mm for pressing.

Following from the above assumptions, the absolute values of error in each dimension r , z and θ (Err_r , Err_z and Err_θ respectively) are summarised in Table 5, each to one significant figure.

		Err_r	Err_z	Err_θ		
				Upper surface $Err_{\theta upper}$	Middle surface $Err_{\theta middle}$	Lower surface $Err_{\theta lower}$
Error due to Measurement (mm)	SPIF	± 0.02	± 0.01	± 0.06	± 0.06	± 0.06
	TPIF	± 0.02	± 0.01	± 0.06	± 0.06	± 0.06
	Pressing	± 0.02	± 0.01	± 0.06	± 0.06	± 0.06
Error due to Cracking (mm)	SPIF	0	0	$\pm \left(0.4 \times \frac{\gamma_{23 upper}}{\gamma_{23 max upper}} \right)$	$\pm \left(0.2 \times \frac{\gamma_{23 middle}}{\gamma_{23 max middle}} \right)$	0
	TPIF	0	0	$\pm \left(0.1 \times \frac{\gamma_{23 upper}}{\gamma_{23 max upper}} \right)$	$\pm \left(0.05 \times \frac{\gamma_{23 middle}}{\gamma_{23 max middle}} \right)$	0
	Pressing	0	0	0	0	0
Total Error (mm)	SPIF	± 0.02	± 0.01	$\pm \left(0.06 + 0.4 \times \frac{\gamma_{23 upper}}{\gamma_{23 max upper}} \right)$	$\pm \left(0.06 + 0.2 \times \frac{\gamma_{23 middle}}{\gamma_{23 max middle}} \right)$	± 0.06
	TPIF	± 0.02	± 0.01	$\pm \left(0.06 + 0.1 \times \frac{\gamma_{23 upper}}{\gamma_{23 max upper}} \right)$	$\pm \left(0.06 + 0.05 \times \frac{\gamma_{23 middle}}{\gamma_{23 max middle}} \right)$	± 0.06
	Pressing	± 0.02	± 0.01	± 0.06	± 0.06	± 0.06

Table 5. Summary of errors in each dimension r , z and θ for SPIF, TPIF and pressing.

The absolute errors of r , θ and z in Table 5 can be used to calculate the absolute errors of the strains and the sine law prediction of wall thickness by partial differentiation of the strain equations with respect to these values (Kirkup [122]). This is shown for a general function $X(x_1, x_2 \dots x_i)$ in Equation 4.4. The absolute error in X , ΔX , is found by the sum of the magnitudes of the partial differentials of X with respect to each of the variables $x_1, x_2 \dots x_i$, multiplied by the absolute errors of each of these variables: $\Delta x_1, \Delta x_2 \dots \Delta x_3$.

$$\text{For } X = X(x_1, x_2 \dots x_i), \quad \Delta X = \left| \frac{\partial X}{\partial x_1} \right| \Delta x_1 + \left| \frac{\partial X}{\partial x_2} \right| \Delta x_2 + \dots + \left| \frac{\partial X}{\partial x_i} \right| \Delta x_i \quad (4.4)$$

The partial differentiation of the strain equations and sine law to find the absolute errors of these values is lengthy, and therefore this is detailed in the Appendix.

4.1.7 Results and Observations

Photographs of half of the cross-sections of each of the formed sheets, from the middle of the plate (left) to the outer edge (right), are shown in Fig. 34. An arrow indicates the direction of successive laps on the plates formed by SPIF and TPIF, which is positioned along the surface that the tool made contact with. Measurements of these cross-sections are shown in the (r,z) , (r,θ) and (θ,z) planes for SPIF (Fig. 35a-c), TPIF (Fig. 36a-c) and pressing (Fig. 37a-c). The z and r axes are shown to equal scales but the θ axis has been expanded for clarity. The surfaces of the sheets that contacted the tool in ISF (upper surface in TPIF and lower surface in SPIF) are highlighted in each plane. In each of Fig. 35, Fig. 36 and Fig. 37, direct strains ε_{11} versus r are shown in (d), shear strains γ_{13} versus r are shown in (e), shear strains γ_{23} versus r are shown in (f), and thickness versus r , measured and predicted by the sine law, are shown in (g). Error bars have been drawn on the plots of strains and the sine law wall thickness according to the calculations described in Section 4.1.6. However, error bars are omitted on the plots of displacement and measured wall thickness because they are negligible on the scale of these axes. Axes of the same scale have been used on equivalent plots on Fig. 35, Fig. 36 and Fig. 37 in order to allow for an easy visual comparison of the magnitudes of strains and deformation measured in the three processes.

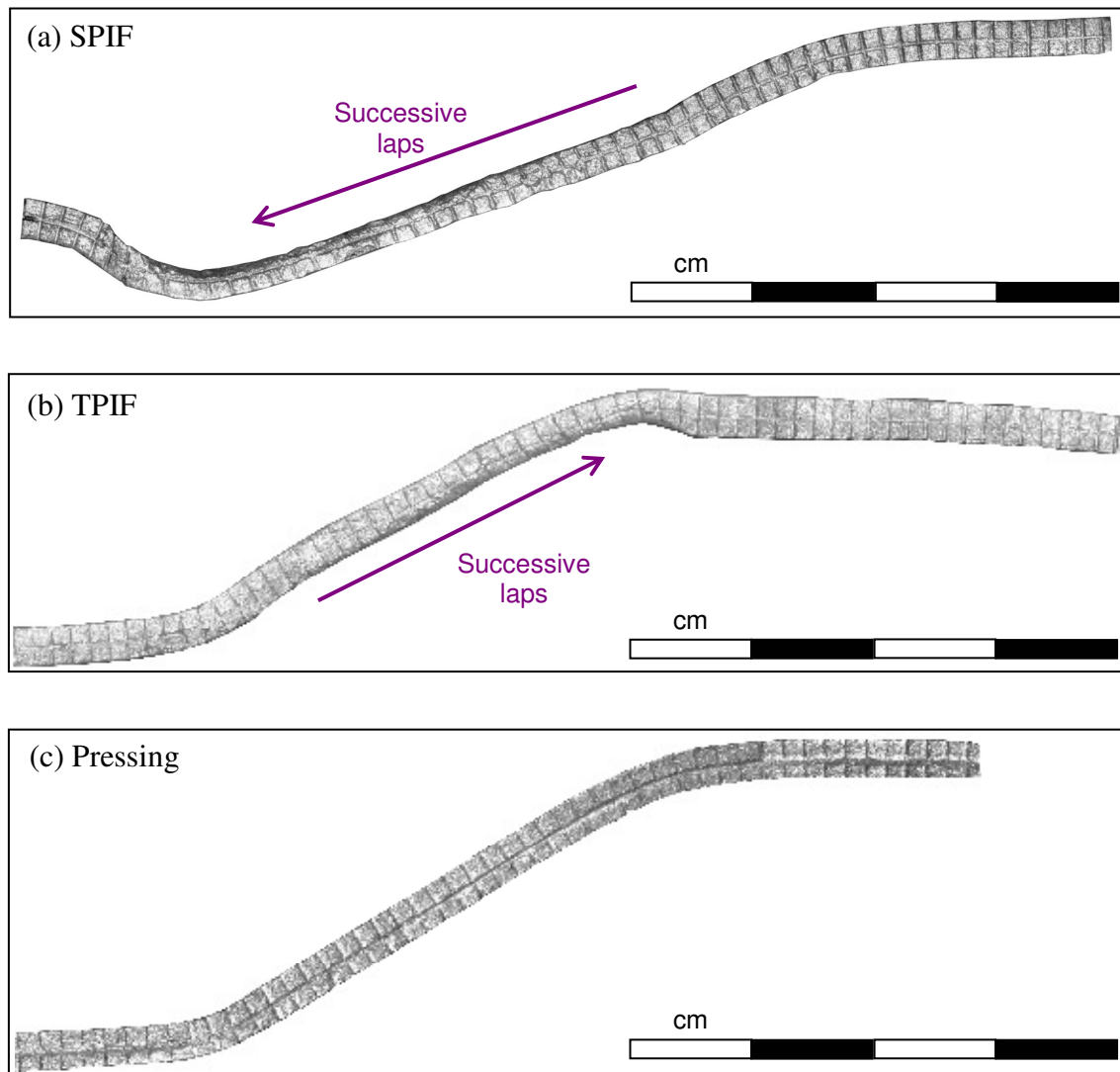


Fig. 34. Photographs of half of the cross-sections of the copper plates in the (r,z) plane after deformation, from centre (left) to outside edge (right): a) SPIF; b) TPIF; and c) pressing. The direction of successive laps is shown next to the surface contacted by the tool on the images for SPIF and TPIF.

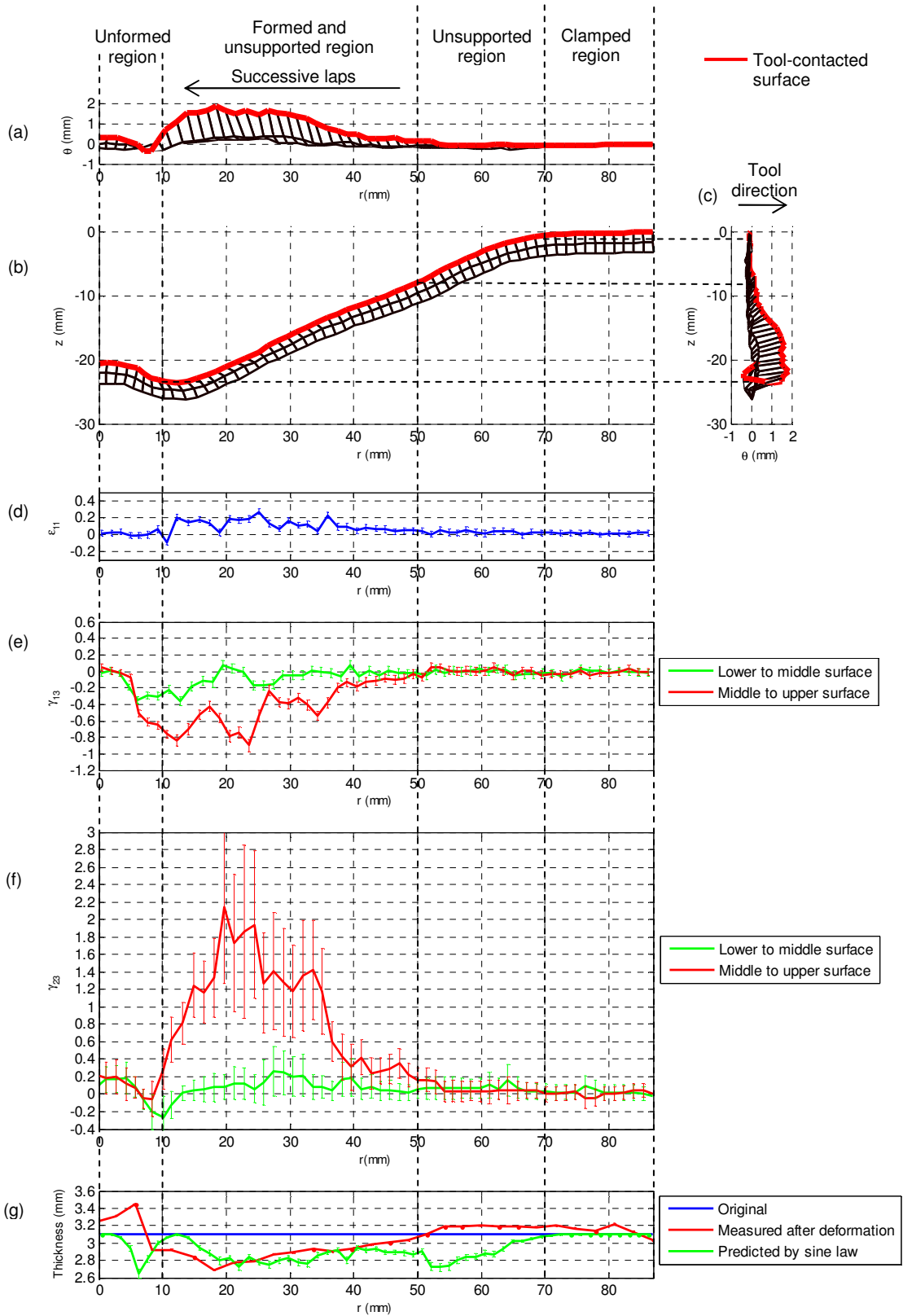


Fig. 35. Measurements of plate formed by SPIF: a) geometry in (r, θ) plane; b) geometry in (r, z) plane; c) geometry in (θ, z) plane; d) ϵ_{11} versus r ; e) γ_{13} versus r ; f) γ_{23} versus r ; g) thickness versus r (original, measured after deformation and predicted from wall angle using sine law).

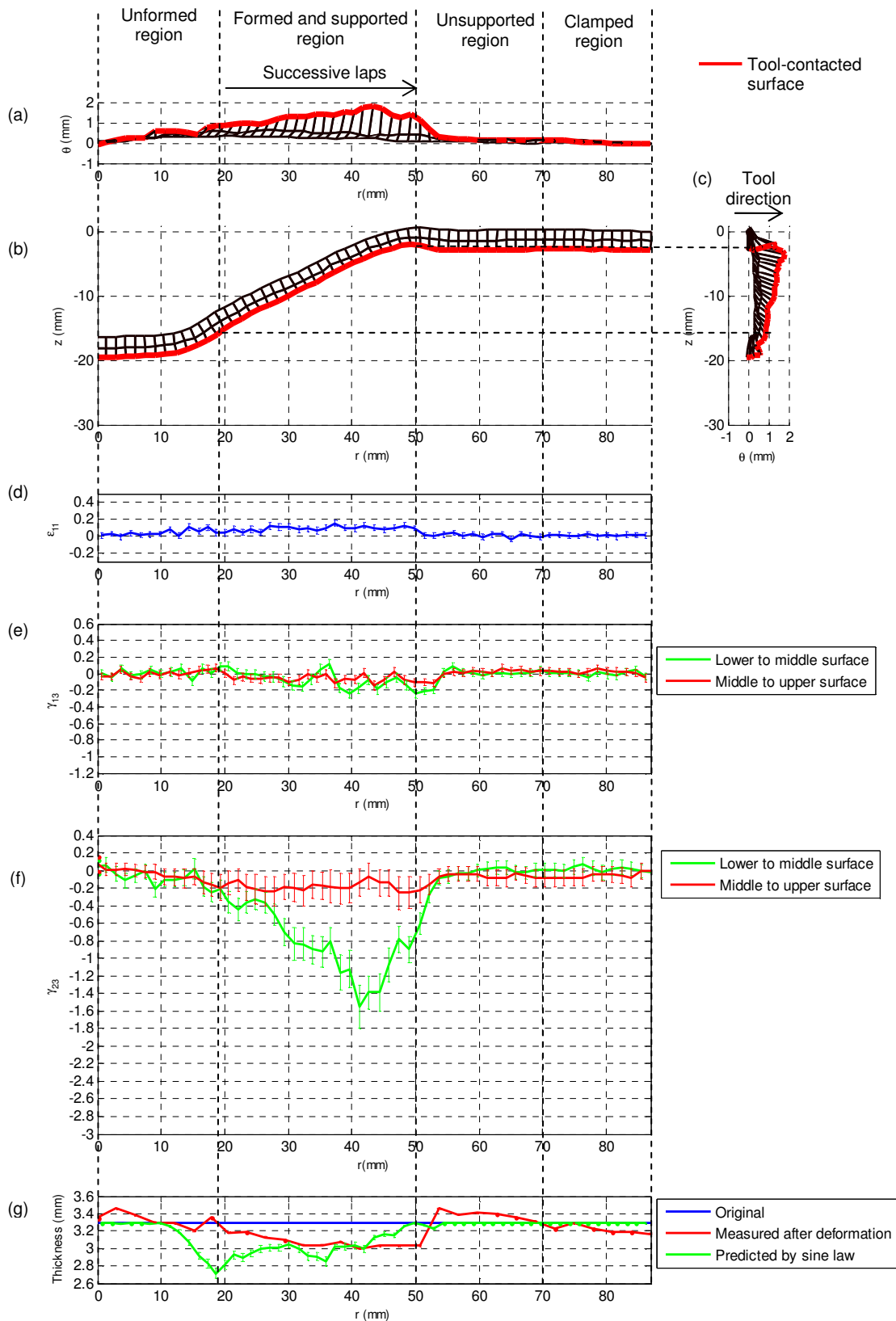


Fig. 36. Measurements of plate formed by TPIF: a) geometry in (r, θ) plane; b) geometry in (r, z) plane; c) geometry in (θ, z) plane; d) ϵ_{11} versus r ; e) γ_{13} versus r ; f) γ_{23} versus r ; g) thickness versus r (original, measured after deformation and predicted from wall angle using sine law).

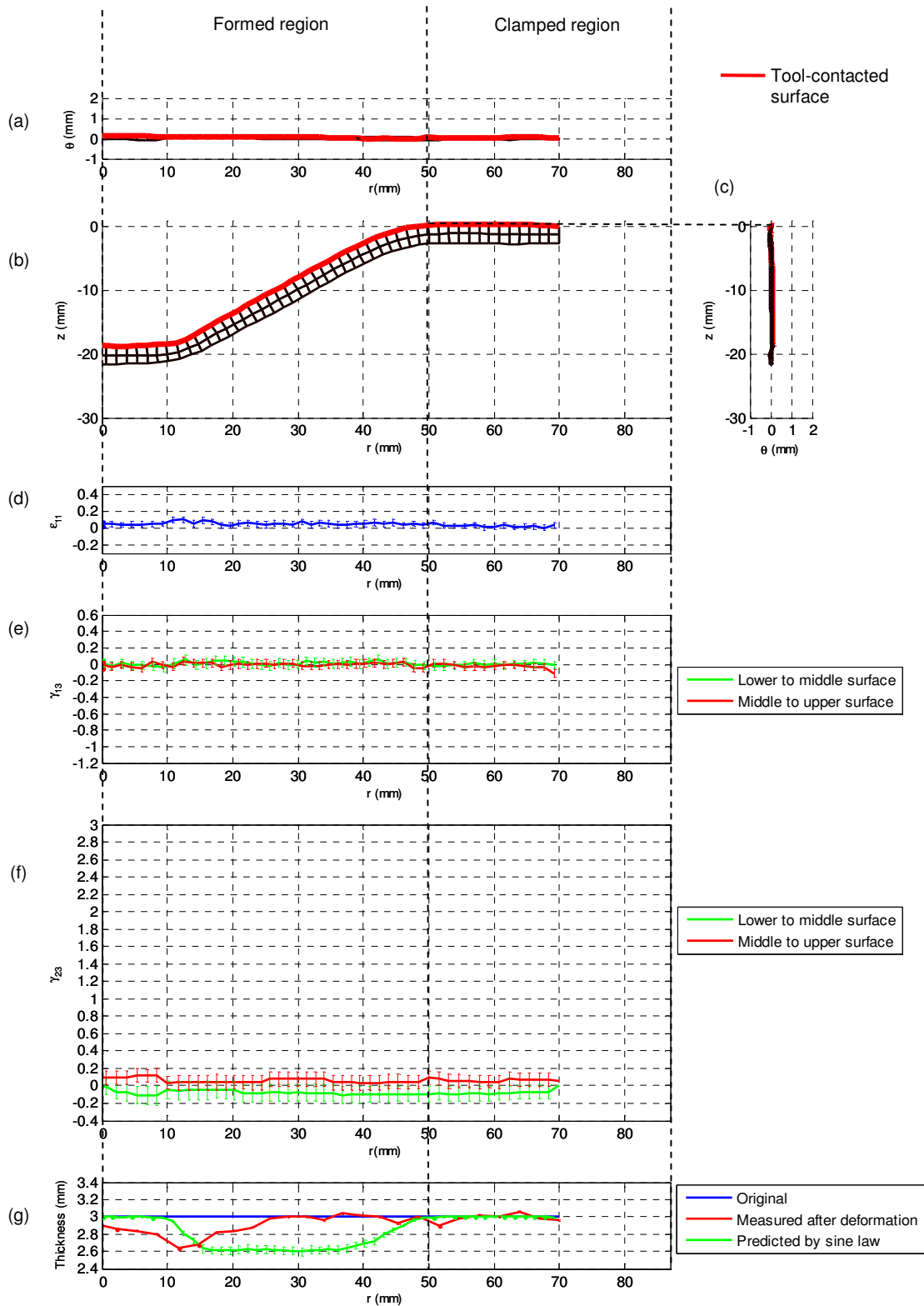


Fig. 37. Measurements of plate formed by pressing: a) geometry in (r, θ) plane; b) geometry in (r, z) plane; c) geometry in (θ, z) plane; d) ϵ_{11} versus r ; e) γ_{13} versus r ; f) γ_{23} versus r ; g) thickness versus r (original, measured after deformation and predicted from wall angle using sine law).

A comparison of the lengths of the error bars to the magnitude of strain measurements on the plots for SPIF, TPIF and pressing shows that everywhere the experimental error is sufficiently low for trends in strains to be observed across the cross-sections and for the calculated strains to accurately represent the deformation of the sheet. The component of strain with the highest relative error is shear γ_{23} , which reaches a maximum of 50% for the middle to upper surface layer of the plate formed by SPIF. For this strain component, cracking made the most significant contribution to the error. Otherwise the relative errors are small for ϵ_{11} and γ_{13} because these were a result of the relatively small measurement error of the CMM only.

The measurements show that the deformation mechanism of the copper plate formed into a truncated cone is a combination of bending, stretching and shear for both SPIF and TPIF, whilst the deformation of the pressed plate is purely stretching and bending. Overall, the greatest strain component for both ISF processes is shear in the tool direction (γ_{23}), whilst perpendicular to the tool direction both stretching (ϵ_{11}) and shear (γ_{13}) are of similar magnitudes. The details of the deformation mechanisms are compared below.

The amount of stretching (ϵ_{11}) is different for each process and varies across the cross-sections. For SPIF, ϵ_{11} increases with decreasing r in the direction of progressive tool laps (Fig. 35d). For TPIF, it is not possible to determine a clear trend in ϵ_{11} (Fig. 36d). However, ϵ_{11} is positive across the cross-section and on average lower than for SPIF. ϵ_{11} is everywhere approximately zero across the pressed plate (Fig. 37d). This is because material is drawn in under the blank holder to minimise stretching in pressing, whereas localised stretching occurs under the indenter in both ISF processes because draw-in of material from the sides is prevented by the rigid clamping.

Shear in the $(1,3)$ plane (γ_{13}) occurs in both SPIF and TPIF as the tool-contacted surface is pushed in the direction of successive laps; towards the centre of the sheet in SPIF (Fig. 35e) and towards the outside of the sheet in TPIF (Fig. 36e). For SPIF, two clear trends are evident: γ_{13} increases with successive laps; and γ_{13} increases towards the tool-contacted surface through the thickness of the sheet. For TPIF, although it is not possible to determine trends in γ_{13} with any certainty from Fig. 36e, it can be judged from the photograph in Fig. 34b that γ_{13} follows the same qualitative trends as SPIF in

the through-thickness and radial directions. For SPIF, these trends in γ_{13} result in an upwards bulge at the centre of the plate where the thickness is greater than the original thickness (Fig. 35g). A thickness greater than the original thickness is also observed at the outside lap for TPIF (Fig. 36g), but is less significant than for SPIF because the strains are smaller and the displaced material is accommodated over a wider circumference. This effect has never previously been reported in ISF, and may be because the thickness of the plate used in the present experiments (3.1-3.3 mm) is thicker than plates typically used in ISF experiments (approximately 1-1.5 mm).

Shear in the (2,3) plane (γ_{23}) can be directly attributed to the movement of the tool over the workpiece in the ISF experiments as the sheet is dragged in the tool direction. Shear γ_{23} is the largest strain component for both SPIF and TPIF (Fig. 35f and Fig. 36f), but does not occur in pressing (Fig. 37f). Shear γ_{23} has three qualitative similarities with γ_{13} for both SPIF and TPIF: it increases on successive laps; there is a variation through the thickness such that the shear is greatest at the tool-contacted surface of the sheet; and it is greater for SPIF than TPIF. The above findings are discussed in more detail and compared to other previous results in Section 4.3.

4.1.8 Summary of Findings

Overall, three significant results can be drawn from the above observations for the C101 plate formed to a truncated cone: (1) in both SPIF and TPIF the deformation is a combination of stretching and shear that increases on successive laps, with the greatest strain component being shear in the tool direction; (2) shear occurs perpendicular to the tool direction in both SPIF and TPIF, which is more significant in SPIF resulting in a piling up of the material at the centre of the plate; (3) the deformation mechanism is inherently different for SPIF and TPIF, and therefore the two processes should be distinguished in future discussions of their deformation mechanics.

4.2 Comparison of Tool Forces in SPIF and TPIF

In order to build on the results of the previous section and to provide further insight into the deformation mechanisms of SPIF and TPIF of sheet metals, in this section the deformation mechanics will be investigated by an alternative approach: measurement of tool forces. Tool force is insightful to the deformation mechanisms of ISF because it can be considered as a combination of two effects: reaction against friction in the direction parallel to the tool path; and work done as the indenter causes elastic and plastic deformation as it moves across the sheet. Measurements of tool force throughout a given ISF process may therefore be used to indicate changes in the deformation mechanics, specifically the degree of stretching, shear and contact friction.

So far investigations of tool forces in SPIF and TPIF have focussed on measuring the trends in tool forces throughout a range of experiments and measuring the influence of process variables on tool force, as reviewed in Section 2.4.4. Although some suggestions for changes in the deformation mechanics throughout the process have been made on the basis of this evidence, this has not been backed up by strong experimental data. The aim of this section is therefore to provide the first detailed comparison of measured tool forces to strains in SPIF and TPIF by comparing tool forces measured parallel and perpendicular to the tool direction to strains measured for the copper plates formed in Section 4.1. The method used to measure the tool force is described in Section 4.2.1 and the results are presented in Section 4.2.2. A detailed discussion of the results has been left to Section 4.3 to allow a full comparison to the results of Section 4.1 and previous published work to be made.

4.2.1 Method

Tool forces have been measured throughout SPIF and TPIF of the copper plates that were formed in Section 4.1 using the system described in Chapter 3. The tool forces were not measured on the actual plates that were used to measure the deformation in Section 4.1 because it was initially anticipated that small changes in the tool force may be observed as the tool traversed the brazed joint due to either slight misalignment of the two half-plates, cracking of the brazed joint or an uneven surface finish caused by

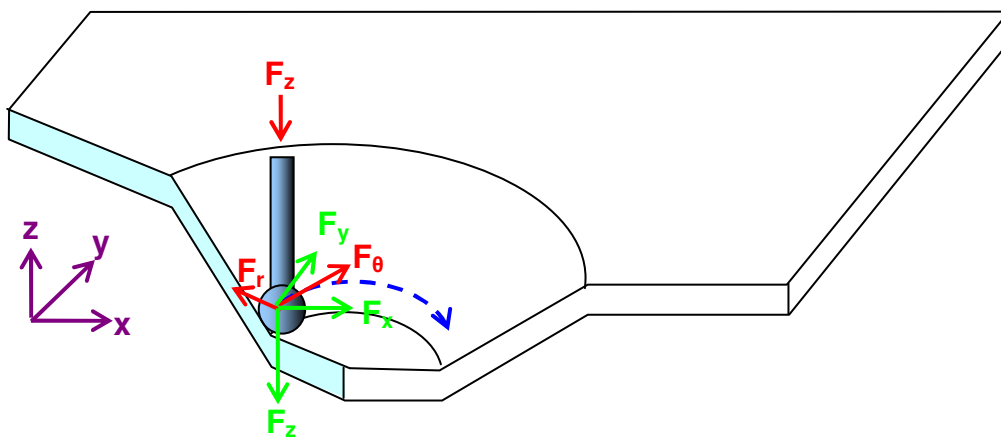
leakage of the filler material. This could potentially cause irregularities in what was otherwise expected to be axisymmetric tool force measurements. Instead, plates without a braze from the same batch as that used in Section 4.1 were subjected to the same heat treatment conditions as described in Section 4.1.1 then formed using the same tool paths for SPIF and TPIF as described in Section 4.1.3.

A sample period of approximately 400ms, which is the maximum that the tool force system will allow, was used to record tool force throughout the SPIF and TPIF experiments. The tool was travelling at a speed of 20 mm/s with an acceleration and deceleration into the step-down point between the contour laps of 10 mm/s^2 , and hence tool force readings were expected at least every 8 mm of tool travel.

Tool force components were measured by the system in the global x , y and z directions (F_x , F_y and F_z respectively), which are aligned with the three perpendicular axes of the machine (horizontal left to right, horizontal front to back and vertical respectively). In order to provide tool force components that are easy to compare to the deformation mechanics measured in Section 4.1, these tool force components were resolved into polar components F_r , F_θ and F_z that are aligned parallel and perpendicular to the conical tool path. The directions of the global and polar tool force components are illustrated in Fig. 38a and b for SPIF and TPIF respectively. The polar force components are defined such that a positive force represents the tool pushing onto the sheet, and hence F_r is positive outwards for SPIF and positive inwards for TPIF. In both cases, F_z is positive downwards whilst F_θ is positive in the clockwise direction.

- Machine axes (x, y, z)
- Force components F_x, F_y and F_z aligned parallel to axes of machine measured by tool force system
- Force components F_r, F_θ and F_z in polar coordinate set aligned relative to the instantaneous direction of the tool (directions defined so force is positive when acting towards the sheet)

(a) SPIF



(b) TPIF

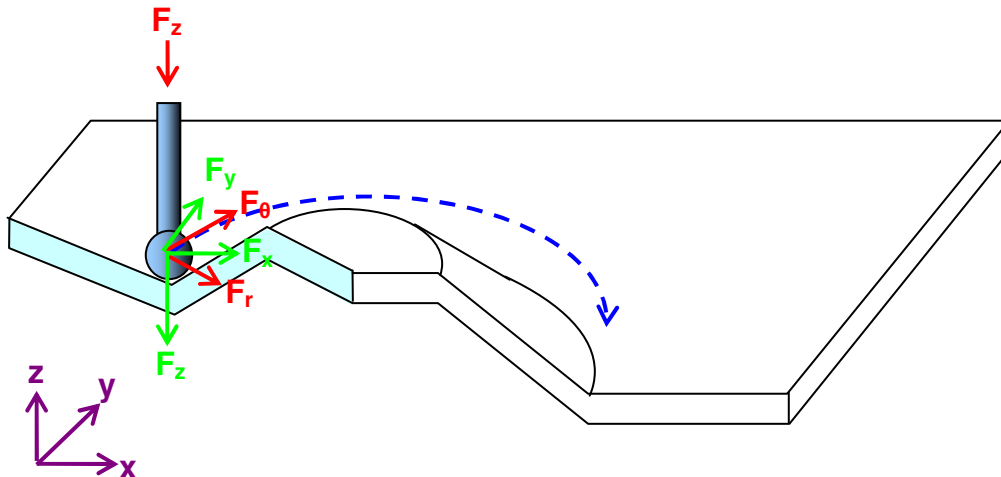


Fig. 38. Diagram showing the directions of the global tool force components (F_x, F_y and F_z) and the polar tool force components F_r, F_θ, F_z that are aligned relative to the instantaneous tool direction: (a) SPIF; (b) TPIF.

The global components of tool force (F_x and F_y) were resolved into polar components (F_r and F_θ) by finding the dot product of the global components with the \underline{e}_r and \underline{e}_θ directions that are perpendicular and parallel to the instantaneous tool direction respectively (4.8 and 4.9). At any time t_i , the instantaneous direction was found by drawing a tangent between the previous point measured at t_{i-1} and the next point measured at t_{i+1} , as illustrated in Fig. 39.

$$F_r = F_x \cdot \underline{e}_r + F_y \cdot \underline{e}_r \quad (4.8)$$

$$F_\theta = F_x \cdot \underline{e}_\theta + F_y \cdot \underline{e}_\theta \quad (4.9)$$

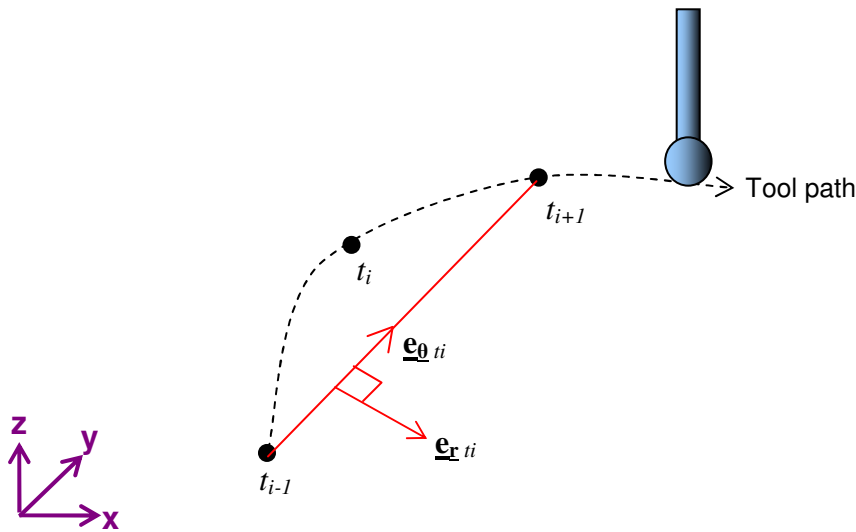


Fig. 39. Calculation of the instantaneous direction of the tool at time t_i by drawing a tangent between the position at t_{i-1} and the position at t_{i+1} .

4.2.2 Results and Observations

The measurements of the polar tool force components versus radius throughout the SPIF and TPIF processes are shown by two types of graphical representations: Fig. 40 shows maps of tool force versus tool position in the x,y plane for SPIF and TPIF; whilst Fig. 41 shows data points of tool force vs. radial position for each reading taken. Both of the figures demonstrate that tool force components F_r , F_z and F_θ follow trends with radius r , but also that variation of what was expected to be axisymmetric tool force components occurs on each lap.

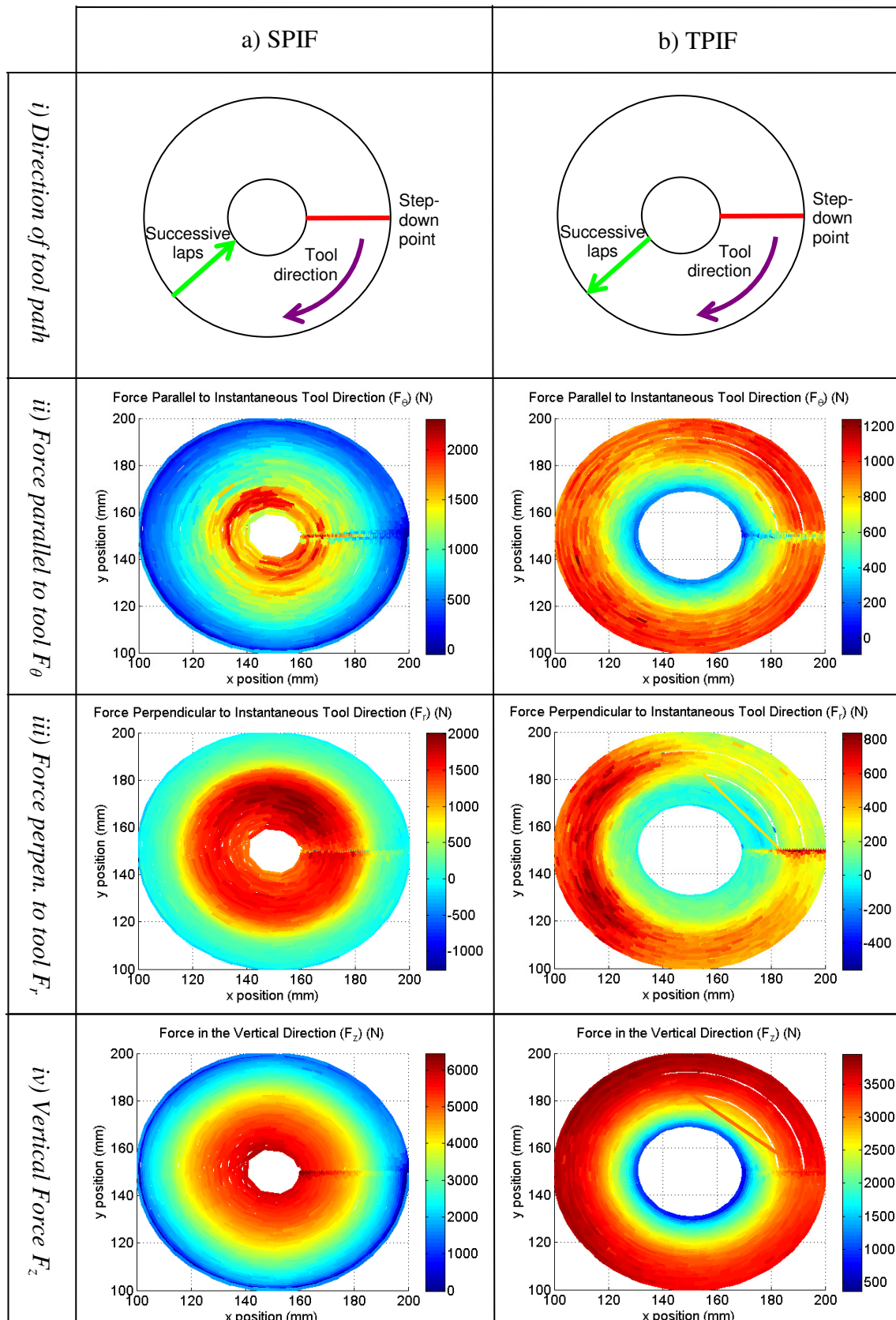
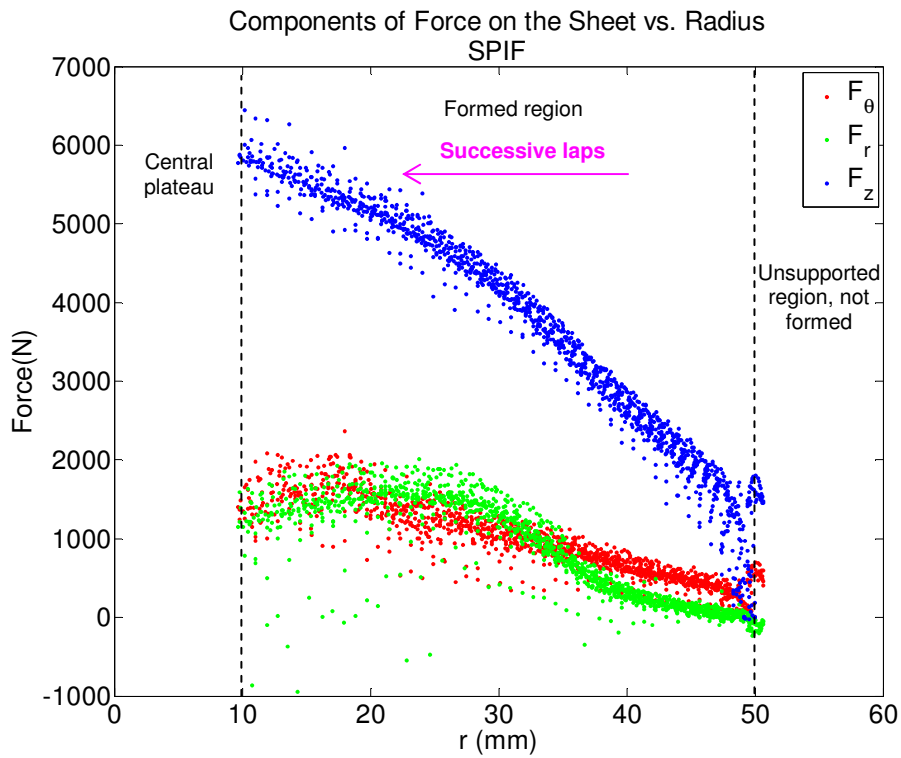


Fig. 40. Tool force components vs. tool position in the x,y plane for (a) SPIF and (b) TPIF: (i) diagram showing the direction of the tool path; (ii) force parallel to the tool direction (F_r); (iii) force perpendicular to the tool direction (F_{θ}); and (iv) axial tool force component (F_z).

(a)



(b)

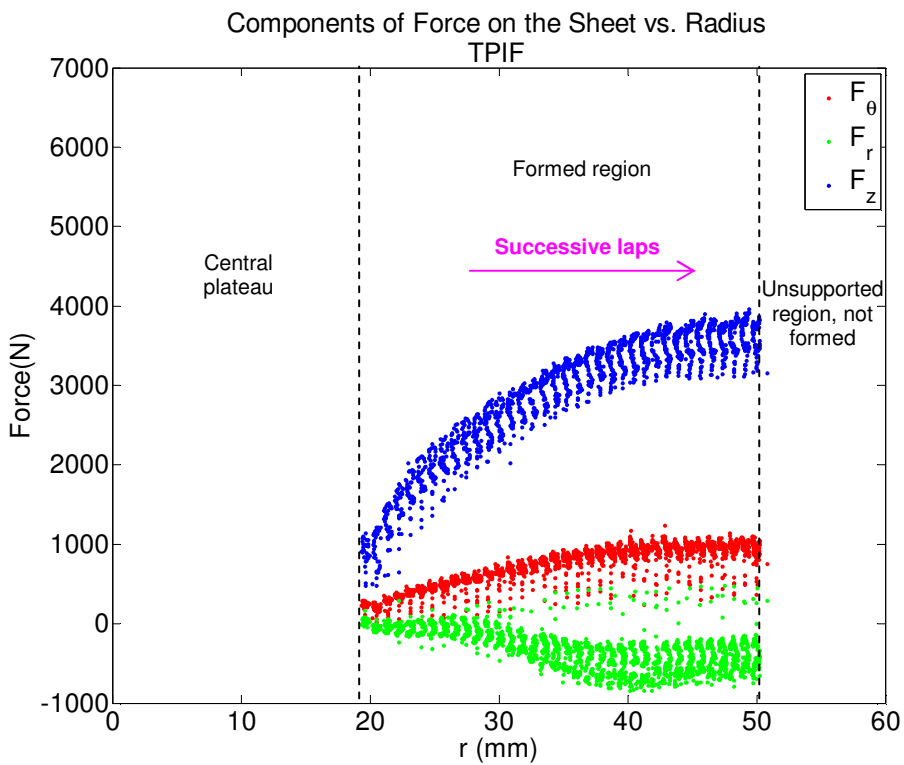


Fig. 41. Components of force on sheet vs. radius: (a) SPIF; (b) TPIF.

The variation in tool force on each lap is the cause of scatter of the data points in Fig. 41. If the tool force was perfectly axisymmetric then any tool force reading at a given radius would have the same value of tool force. The scatter in tool force readings has a range of approximately ± 500 N for F_z and increases from approximately ± 50 to ± 500 N in the direction of successive laps for F_r and F_θ for both SPIF and TPIF. This scatter cannot be fully accounted for by uncertainty due to noise and calibration of the tool force system, which was measured in Chapter 3 to be approximately ± 15 N for each loadcell when the machine is on and moving. Fig. 40 shows that some of this scatter is periodic depending on the position of the tool in any given lap. This explains the periodic grouping of readings in the plots of Fig. 41 a and b, which is more significant for TPIF than SPIF.

From the graphs in Fig. 40, three reasons can be suggested for both the periodic grouping of data points and the scatter observed on the graphs. Firstly, for both SPIF and TPIF all of the components of tool force exhibit a change around the step-down point that is not characteristic of the forces measured elsewhere on a given lap. The force parallel to the tool, F_θ , decreases whilst the other components, F_r and F_z , increase. This is likely to be because the tool is instantaneously moving away from the formed surface in the x,y plane, and hence the force parallel to the tool direction in the x,y plane will decrease, whilst it is pushing downwards into the sheet therefore the vertical force increases. In addition, the tool force parallel to the tool direction could be affected by friction which may depend on the tool speed. Secondly, all components of tool force are higher on the left-hand side of the cone formed by TPIF than on the right (Fig. 40b). This is likely to be caused by misalignment between the conical path of the indenter and the positive die support that was positioned underneath the worksheet. The die and the indenter were aligned as well as possible before forming by making a visual inspection, but it is likely that this could have allowed for misalignment of up to 1-2 mm in any direction. This asymmetry explains why the periodic grouping of the TPIF data points in Fig. 41b is more noticeable than any grouping of data points for SPIF in Fig. 41a. The third reason that is suggested for the grouping of data points and the scatter of data is the varying speed of the indenter as it accelerates and decelerates to the step-down point. The varying speed will allow for an uneven spacing between any given data point with the previous point and the next point, and hence could allow for an error in the calculation of the instantaneous tool direction. Resolution of the tool force into

components parallel and perpendicular to the instantaneous tool direction could therefore be inaccurate in a region where the tool is accelerating or decelerating. For the same reason, grouping of data points will occur around the step-down point because the tool speed is slower in this region and hence the tool travels a shorter distance between successive force readings. Note that for the tool force measurements of TPIF shown in Fig. 40b there is a diagonal line across the top right corner. This represents a software error in the tool force readings where several readings were missed. The number of data points missed is small in comparison to the overall length of the tool path, and therefore the scatter plot in Fig. 41 would not have been noticeably affected.

Despite the scatter in tool force readings that is described above, the scatter is overall small in comparison to the total range of forces that are measured, and hence general trends in the tool forces with radius can be deduced from Fig. 41 for SPIF and TPIF. Although experimental error in the strain measurements prevents an accurate comparison of trends in tool forces to trends in strains, the plots of tool force components versus radius for SPIF and TPIF show two qualitative trends that can be correlated to the deformation mechanics reported in Fig. 35 and Fig. 36. Firstly, it is evident that all components of tool force increase with successive laps in both SPIF and TPIF, as do strain components. Hence, increasing tool force on successive laps is a result of the increasing rate of work on successive laps due to increasing shear and increasing stretching. The rate of increase of tool force is likely to be further increased by work-hardening of the copper as it is strained, which was shown in Fig. 25 to increase throughout the plastic regime. The second trend in tool forces that can be correlated to the deformation mechanics is that tool forces and strains are greater for SPIF than for TPIF. Hence, the higher tool forces observed for SPIF than TPIF are a result of greater strains in forming (compare Fig. 41a and b with Fig. 35 and Fig. 36). These trends in tool forces are compared to previous works and the results of Section 4.1 in more detail in Section 4.3.

4.2.3 Summary of Findings

The observations of the tool force measurements for the C101 plate formed into a truncated cone can be summarised as two principal results: (1) all components of tool force increase on successive laps in both TPIF and SPIF, which is an indication of increasing work and is consistent with the measurements of increasing strains; (2) tool forces are greater for SPIF than TPIF, which is also consistent with the measurements of strains for the two processes.

4.3 Discussion

From the observations of deformation mechanics and tool forces in SPIF and TPIF reported above, six points for discussion have been raised. Firstly, the trends observed in strains will be compared to previous experimental and numerical results. Secondly, the measured deformation mechanisms of SPIF and TPIF will be compared to the idealised mechanism of pure shear previously measured for shear spinning by Kalpakcioglu [81]. Thirdly, the accuracy of the sine law for prediction of wall thickness will be evaluated by comparing the wall thickness to deformation mechanics. The results will also be compared to previous investigations of wall thickness variations in ISF. Fourthly, trends in tool forces observed for SPIF and TPIF will be compared to the measured strains and previous investigations of tool force. Fifthly, the trends observed in strains for SPIF and TPIF will be discussed and possible reasons for the observed trends will be suggested. Finally, the transferability of the results of the experiments to other ISF processes will be evaluated.

4.3.1 Comparison of Strains to Previously Published Results

The results for strains in SPIF and TPIF presented in Section 4.1.7 cannot be used to verify the findings of previous works because they are based on a different material, sheet thickness and geometry to those used in previous experimental or numerical investigations (as reviewed in Section 2.4.3). Furthermore, the results are more detailed than previous experimental investigations which reported measurements of the sheet surface without measuring the through-thickness deformation. However, a comparison

to previously published results will be made in this section because this indicates the extent to which the findings of this research may be transferable to other materials.

Comparison of the results of Section 4.1.7 with the findings of previous research of the deformation mechanics reviewed in Section 2.4.3 has highlighted three similarities and one difference. The first similarity is that stretching perpendicular to the tool direction, ε_{11} , which was measured for SPIF in Fig. 35d, was similarly predicted numerically for SPIF by Bambach et al [61]. Secondly, stretching perpendicular to the tool direction, measured for TPIF in Fig. 36d, was predicted in a simplified numerical model of TPIF with a central support post by Sawada et al [89]. The third similarity is that shear measured parallel to the tool direction, γ_{23} , in SPIF (Fig. 35f) is consistent with the experimental measurements of displacement for a 1 mm aluminium sheet in SPIF by Allwood et al [88]. In the same paper it was numerically predicted that shear would also occur in this direction in *paddle-forming*, and that this shear would be greater towards the tool-contacted surface, as was measured in the present experiment for SPIF. The results of the present experiments differ to previous work published by Bambach et al [61] in one respect. Bambach et al [61] numerically predicted that shear perpendicular to the tool direction, γ_{13} , occurred in SPIF in the opposite direction to what was measured in these experiments (Fig. 35e). This was predicted for two values of vertical pitch, 1 mm and 0.5 mm, and three values of tool diameter, 6 mm, 10 mm and 30 mm, at a wall angle of 65° . The sheet material was Al99.5 and thickness was 1.5 mm. Possible reasons for the discrepancy in shear γ_{13} therefore include differences in the material properties, sheet thickness and wall angle used in the Bambach experiment to the present experiment. Note that, although Bambach et al [61] also predicted that shear parallel to the tool direction, γ_{23} , was not significant, this is not necessarily a contradiction to the results of this research because the direction of the tool in the previous work was alternating which may cancel out any shear due to friction on successive laps, whereas the tool always moved clockwise in the present experiments. Although the results of the present experiments cannot be used to experimentally verify Bambach's finite element model because the processes investigated are different, a feature of this research that is potentially valuable in future is that the experimental method developed in this chapter could be used in future for carrying out this task.

Similarities between the results of deformation and strains in the present experiment to previous works on different materials and geometries suggests that some of the results may be transferable to other sheet materials, thicknesses and wall angles used more typically in ISF. The results for wall thickness variation and tool forces will also be compared to previous works later in this discussion, leading to a full evaluation of the transferability of the results to other set-ups of ISF in Section 4.3.6.

4.3.2 Comparison of Mechanisms of SPIF and TPIF to the Idealised Mechanism

The results of Section 4.1 show that the deformation mechanisms of both SPIF and TPIF are significantly different to the idealised mechanism of shear spinning illustrated in Fig. 11, page 34. As was described earlier in Chapter 2, this idealised mechanism was derived by Kalpakcioglu [81] by simplification of experimental measurements of deformation in shear spinning, which was shown in Fig. 12, page 35. Although it is not surprising that the deformation mechanism is different for SPIF because the support of the workpiece is different, it is more surprising for TPIF because the support of the workpiece is almost equivalent to shear spinning, but in a rotating frame of reference. There are two principal differences between the TPIF mechanism (Fig. 34 page 92) and the idealised pure shear mechanism: (1) through-thickness gridlines that remain axial in the idealised mechanism do not remain axial in TPIF; and (2) circumferential shear occurs in TPIF whilst the idealised mechanism has plane strain. Two possible reasons are suggested for why the first of these differences might occur. Firstly, the formed plate used in Kalpakcioglu's original paper from which the idealised mechanism was derived was 12.5 mm thick [81], whereas those used in these experiments were 3.2 mm thick. The deformation was approximated by Kalpakcioglu such that through-thickness gridlines remained axial because the distorted region next to the mandrel surface was a small portion of the overall thickness, whereas this distance is significant in comparison to the thickness of the sheets used in this experiment. It is therefore possible that if a thinner plate had been used by Kalpakcioglu that it would not be possible to assume that through-thickness gridlines remain axial, as is the case for TPIF. Secondly, the vertex between the inclined wall and the central face of the support tool used in the present experiment was rounded to a radius of 10 mm, whereas a vertex that was not rounded

was used in the original work by Kalpakcioglu. Bending and stretching as opposed to shear may be more likely to occur as the tool pushes the sheet over a rounded corner. This is likely to be promoted by the positive die that was continually pushing into the sheet, and therefore stretching it. This could therefore also account for the observation that through-thickness gridlines remain axial in the Kalpakcioglu experiment whilst not in the TPIF experiment. The second principal difference, that circumferential flow was measured for TPIF but not for the idealised mechanism of shear spinning, is actually consistent with Kalpakcioglu's experimental measurements. The reason for omitting this in the idealised mechanism was not given.

4.3.3 The Accuracy of the Sine Law Prediction of Thickness

Fig. 35g and Fig. 36g show that there is a continual variation in measured wall thickness across the profiles formed by SPIF and TPIF and that the sine law prediction is generally lower than the measured thickness. For the first time, the accuracy of the sine law and the variation in the measured wall thickness is explained below by referring to the measured deformation mechanics. The variation in wall thickness measured and predicted in the present experiments is also compared to the previous results of Young and Jeswiet [79] and Ambrogio et al [58] to highlight some interesting discrepancies.

For both SPIF and TPIF of the C101 plate formed in the present experiments, the error between the sine law prediction and measured thickness results from a variation in strains across the cross-sections that causes radial displacement of material. As described in Section 2.4.3, the sine law can only apply when on average there is no radial displacement of any through-thickness element of material. For SPIF, the measured thickness decreases in the direction of successive laps across the formed region whilst the sine law prediction remains approximately constant because the wall angle is uniform (Fig. 35g). The decreasing measured wall thickness is a result of increasing shear, γ_{13} , and stretching, ϵ_{11} , causing material to be pushed towards the centre of the cone. Similar to SPIF, the measured wall thickness in TPIF decreases in the direction of successive laps (Fig. 36g). This is also likely to be a result of increasing ϵ_{11} and γ_{13} , although the trends cannot be clearly identified from these measurements. Unlike SPIF, the sine law prediction of thickness in TPIF is not constant but increases in the direction of successive laps. This is because the wall angle decreases due to the

release of elastic stresses on removal of the support tool, and hence the error in the sine law is greater for TPIF than SPIF. The maximum error of the sine law prediction relative to the measured thickness in the formed region is approximately 0.2 mm for SPIF and -0.6 mm for TPIF, which corresponds to percentage errors of 7% and -18% respectively.

Two interesting discrepancies have been identified between the present results for the accuracy of the sine law in SPIF and the previous works of Young and Jeswiet [79] and Ambrogio et al [58]. (The accuracy of the sine law for the TPIF experiment cannot be compared to previous experiments because no detailed studies of the wall thickness distribution in TPIF against a positive die have previously been carried out.) Young and Jeswiet [79] showed that, for a cone of 30° wall angle formed in 1.21 mm thick AA3003-O, the wall thickness continually decreases over the first 20 mm of the radial direction and then stabilises to a constant value that is slightly less than the sine law prediction for the remainder of the cross-section. For a steeper cone in the same material of 70° wall angle, the wall thickness decreases to a minimum at approximately 20 mm from the perimeter of the product, then increases to a constant value across the rest of the profile. Similarly Ambrogio et al [58] found that, for truncated pyramids of 50° and 55° formed by SPIF in 1 mm AA1050-O, the wall thickness decreased continually for up to approximately 15 mm in the radial direction, and then stabilised to a constant value. The two discrepancies of these previous results to the present SPIF experiment are as follows: (1) the measured wall thickness decreases continually across the entire cross-section in the present experiment whereas it stabilised to a constant value in the previous experiments; and (2) the measured wall thickness in the present experiment does not pass through a minimum.

The first of the above discrepancies suggests that, whilst the measurements of deformation in the present experiments have shown that strains ε_{11} and γ_{13} are continually increasing across the cross-section of the SPIF plate, the strains may be constant across the steady-state region of the plates investigated by Ambrogio et al [58] and Young and Jeswiet [79]. Although this point cannot be verified without experimental measurement of the through-thickness deformation of the plates studied by Ambrogio et al [58] and Young and Jeswiet [79], it is likely that this is the case because if the strains were to continually increase along the radial direction in these previous

experiments this would have resulted in radial displacement of material, and hence a continually decreasing wall thickness. Further research is required to find out why the strains may have reached a constant value in the previous experiments whilst they did not in the present experiment. This may be because the plate was thicker in the present experiments (3.1-3.3 mm) than the previous experiments (1 mm or 1.21 mm), or because a different material was used (C101 versus AA3003-O or AA1050-O). However, it cannot be because the wall angle of the present experiments was a shallow 30° ; Young and Jeswiet [79] found that the wall thickness stabilised for an aluminium cone of the same wall angle. It is possible that the strains that were measured in the present experiment represent the transition region which occurred over the first 15 to 20 mm from the outer edge of the cone in the previous experiments by Young and Jeswiet [79] and Ambrogio et al [58]. In this small transition region in the previous experiments, the wall thickness followed a similar trend to that which was observed over the entire cross-section in the present experiments; it started at the original sheet thickness and reduced to a value that was slightly lower than the sine law prediction of wall thickness. This could be verified by forming a tool path in the copper plates with a greater number of laps, i.e. a cone with a wider diameter, and measuring whether the strains attain a constant value further down the tool path. Likewise, it would be insightful to verify whether a transition in strain occurred over the first 15 to 20 mm of the tool path in the previous experiments performed by Young and Jeswiet [79] and Ambrogio et al [58] that is similar to the transition in strains measured across the cross-section of the copper plate in the present experiments. If the strains measured in the present experiments on the copper plates do represent a transition region in wall thickness, it would be expected that some 'levelling-off' of strains perpendicular to the tool direction would be observed. However, it is not possible to accurately verify this trend due to experimental error.

The second discrepancy between the wall thickness distribution in the present experiments to that of the previous experiments is that a thinning band was not observed for the present SPIF experiment whilst one was observed at approximately 20 mm from the perimeter for the 70° cone formed by Young and Jeswiet [79]. Young and Jeswiet [79] suggested that the thinning band for steep cones coincided with necking as the material was stretched close to its limits. Hence it is likely that the thinning band was avoided in the present experiments because the shallow 30° angle was not sufficient for the material to approach necking. The fact that a thinning band was not observed in the

present experiments suggests that the deformation mechanism that was observed was not representative of all ISF processes; thinning bands may be more likely to occur in thinner sheets formed to steeper wall angles, and hence further investigation is required to verify this.

Overall, the above discussion of the accuracy of the sine law for prediction of wall thickness and comparisons to previous experiments provide four key observations: (1) the sine law prediction of wall thickness is not equal to the actual wall thickness in SPIF or TPIF because, unlike shear spinning, the deformation mechanics allows for radial displacement of material; (2) the distribution of wall thickness, and hence the accuracy of the sine law, is likely to depend on the sheet thickness; (3) the deformation mechanics observed in the present experiment for SPIF may represent a transition region in strains; and (4) the deformation mechanism which was measured for the copper plate is not representative of all SPIF processes because a thinning band, which has sometimes previously been measured, did not occur.

4.3.4 Comparison of Tool Forces to Deformation Mechanics

In Section 4.2.2 it was observed that tool forces in SPIF and TPIF increased with successive laps, and that tool forces are higher for SPIF than for TPIF. For the first time it was possible to offer an explanation for the trends in tool forces in terms of the deformation mechanics throughout the processes. Increasing tool forces were attributed to increasing work in the sheet as a result of increasing strains and work-hardening, and the higher forces in SPIF than TPIF were attributed to higher strains. These observations require further discussion for four reasons: (1) to compare trends in tool forces in these experiments to previous experiments and to the deformation mechanics; (2) to suggest reasons for the lower strains and tool forces observed in TPIF than SPIF; (3) to discuss the influence of friction on shear strains; and (4) to discuss the possible influence of tool force on forming limits.

It is evident from Fig. 41 that, although the magnitudes of tool force components in SPIF and TPIF are increasing with successive laps, the gradient is following a decreasing trend for F_z and F_θ , whilst F_r has a maximum gradient when r is approximately 35 mm for both processes. This suggests that tool forces may be

approaching a steady value. This observation further supports the idea suggested above (Section 4.3.3) that the strains measured may represent a transition region that could eventually stabilise if further laps were completed. It has been observed that the increase in tool forces in Fig. 41 is a result of increasing work in the sheet that is likely to be both a combination of increasing strains (measured on Fig. 35 and Fig. 36) in addition to work-hardening of the copper plate (shown in Fig. 25). If work-hardening does contribute to the increasing tool forces, this would be expected to cause a steeper rate of increase of tool forces with successive laps than a non-work-hardening material. This could be verified by comparing the trends in tool forces and strains measured in this experiment to tool forces and strains measured for a material that maintains approximately constant yield stress throughout the plastic regime.

Comparison of the tool forces (Fig. 41) with the variations in wall thickness measured in the experiments on SPIF and TPIF (Fig. 35g and Fig. 36g) shows that tool forces increase as wall thickness decreases on successive laps. Significantly, trends in tool forces measured in previous published work are also directly comparable to measurements of wall thickness in SPIF. (A similar comparison cannot be made for TPIF against a positive die because there have been no previous studies of wall thickness for this process.) An increasing trend followed by levelling-off to a steady-state value was observed for both horizontal and vertical tool force components for 1.2 mm thick AA3003-O formed to a wall angle of 30° by Duflou et al [93]. Young and Jeswiet [79] measured the same trend in wall thickness for the same material formed to the same geometry; wall thickness decreased over the first 20 mm from the perimeter of the product and then stabilised to a constant value. A trend of increasing horizontal and vertical tool force components to a maximum followed by a small decrease to steady-state values was observed for a cone with a steeper 70° wall angle also formed in 1.2 mm AA3003-O by Duflou et al [93]. Young and Jeswiet [79] measured the same trend in wall thickness for this material formed to the same geometry; wall thickness decreased to a minimum at approximately 20 mm from the perimeter of the product and then increased slightly to a constant thickness that was maintained across the rest of the cross-section. However, although similar trends in tool forces and wall thickness can be observed in these previous experiments, the two characteristics cannot be accurately compared because tool forces measured by Duflou et al [93] were reported as a function of time during the process whereas wall thickness was reported by Young and Jeswiet

[79] as a function of distance from the perimeter. Further work is required to verify the *position* at which the tool forces stabilised, and hence whether this corresponds to the position of the stabilisation of wall thickness measurements. However, the comparison of these previous works along with the results of the present experiments suggests that there is a correlation between tool force and wall thickness in SPIF. This is likely to be because tool forces increase as stretching and shear perpendicular to the tool direction increase and hence wall thickness decreases. There is a practical application to the above observation: measurement of tool force could provide a real-time prediction of wall thickness distribution throughout the process, and hence indicate if excessive thinning and failure is imminent. Similar was recently suggested by Duflou et al [93], who claimed that it may be possible to use the gradient of the force curve between the peak and steady-state values to predict failure.

The observation that lower tool forces occur for TPIF than SPIF requires further discussion because the reasons are not immediately obvious as the same geometries are formed in each process. Reaction of the tool against the positive die support might have suggested that the tool forces would actually be *higher* in TPIF than SPIF, but the opposite is the case. It is suggested that the lower tool forces observed in TPIF than SPIF are likely to be because the positive die support is providing an additional stretching force across the workpiece. This stretching force is not measured by the tool force system because it is reacted against within the workpiece frame. Any additional force applied by the indenter to the tensioned sheet in TPIF will therefore bring the material closer to its yield point than the same force applied to an equivalent unstretched sheet in SPIF, and hence higher tool forces are required in SPIF to make the sheet yield in tension than in TPIF. A two-dimensional drawing illustrating the additional stretching force on the workpiece applied by the positive die support in TPIF is shown in Fig. 42, where forces that are reacted within the workpiece frame are shown as red arrows and the forces measured by the tool force system are shown as green arrows.

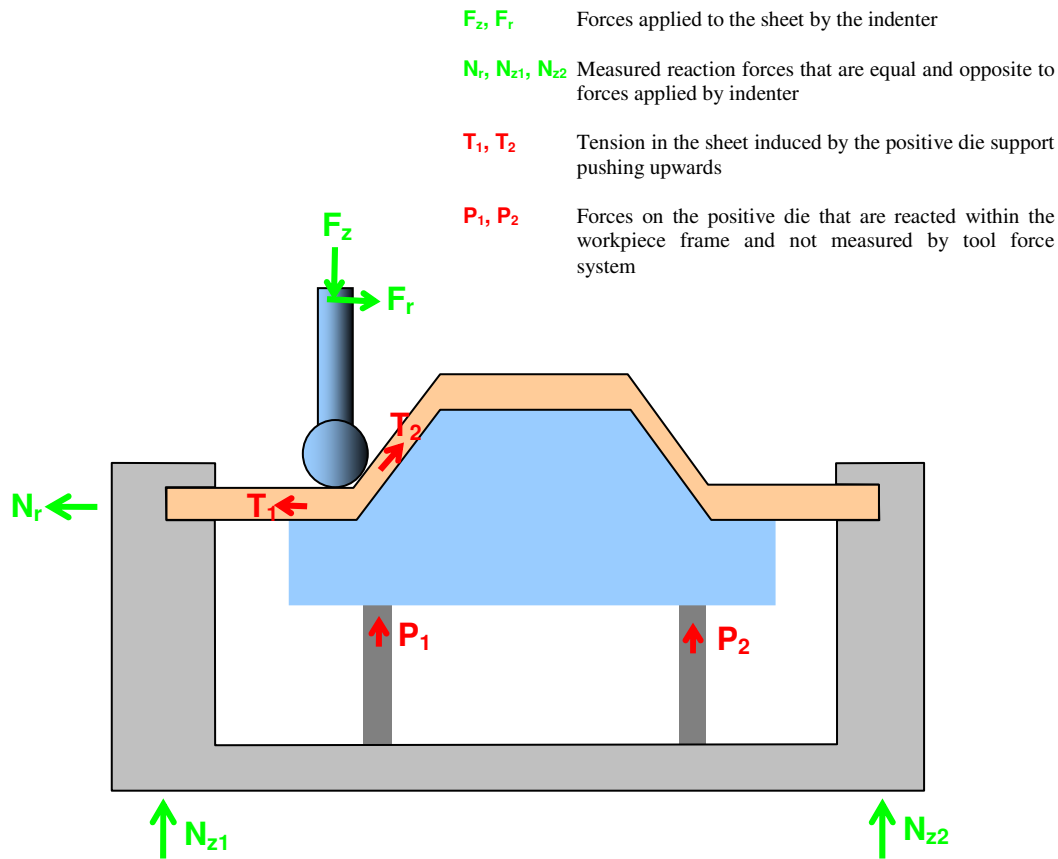


Fig. 42. 2D drawing showing directions of forces acting within and on the workpiece frame in TPIF

The third point for discussion is the influence of friction on shear strains. Friction between the tool and workpiece is likely to increase as the normal reaction force between the two increases. The normal reaction force is approximately equal to the vertical tool force because the wall angle of the formed plates is shallow. Shear in the tool direction, γ_{23} , is likely to be a direct result of friction between the tool and workpiece because it is shear parallel to the tool direction. Hence, as vertical tool force increases, shear in the tool direction γ_{23} will also increase. This idea is supported by the experimental observations; shear strains γ_{23} are up to approximately 40% greater for SPIF than TPIF (compare Fig. 35f and Fig. 36f), whilst vertical tool forces are approximately 50% greater for SPIF than TPIF (compare Fig. 41a and b), where the reason for the higher vertical force in SPIF was explained in the previous paragraph.

Finally, the possible influence of tool force on forming limits is discussed. Allwood et al [95] recently predicted that through-thickness shear increases the forming limits predicted by the Marciniak-Kuczyński analysis, and therefore suggested that through-

thickness shear may account for the increased forming limits observed in ISF in comparison to pressing. If this is the case, SPIF is likely to achieve higher forming limits than TPIF due to increased through-thickness shear. However, an alternative hypothesis was proposed by Hirt et al [61] in 2003 that the increased forming limits in ISF in comparison to pressing may be due to hydrostatic compressive stresses under the indenter suppressing the nucleation and growth of voids. In contrast to the hypothesis proposed by Allwood et al [95], this might allow TPIF to achieve higher forming limits than SPIF because the sheet is pushed against the positive die support. The forming limits of SPIF and TPIF have so far not been compared, and for the above reasons this could be an interesting area of research.

4.3.5 Discussion of Trends in Strains

The discussions of tool forces and the applicability of the sine law for prediction of wall thickness have highlighted three interesting observations of the trends in strains in SPIF and TPIF: (1) the strains are not constant throughout the process but in general they increase on successive laps; (2) the increasing strains may represent a transition region that is approaching a steady-state; and (3) the increasing shear parallel to the tool direction, γ_{23} , correlates to an increasing vertical tool force throughout the process. These observations raise two further interesting questions that have not yet been answered: (1) ‘Why should the strains not be constant throughout the process despite a uniform tool path?’ and (2) ‘Why does shear occur *perpendicular* to the tool direction (Fig. 35e and Fig. 36e)?’ To complete the discussion of the deformation mechanics of ISF, these two questions will be discussed below.

It is suggested that the reason why the strains are not constant throughout the process despite a uniform tool path is due to an evolution of the contact area as the forming progresses. This is based on experimental observations; as the process progresses, the deformation seems to transform from a widely distributed deformation across the sheet to a highly localised deformation under the contact area of the tool. The reason for this may be because as the sheet becomes more three-dimensional it is more rigid and hence resists widely spread deformation, restricting the deforming area to around the contact area of the tool. The transition from a widely distributed to a highly localised deformation is likely to cause the vertical tool force to increase because for a given

penetration depth the strains and hence stresses are higher in the localised area than when widely distributed. The increasing vertical tool force combined with a likely increase in the contact area of the tool will cause the friction under the tool to increase, and therefore increases the shear parallel to the tool direction, γ_{23} . Stretching, ϵ_{11} , also increases as the indenter penetrates further into the local area under the tool. If the increasing strains do represent a transition region that is approaching a steady-state, the attainment of steady-state strains may represent the condition where the deformation has become highly localised.

The possible localisation of deformation due to the increasing rigidity of the sheet would suggest that the deformation should inherently be more localised for TPIF than SPIF because the sheet is always partly constrained by the contact of the positive die support. This would suggest that the forces and strains would be higher at any given stage in the process for the TPIF plate than the SPIF plate. However, this is not the case (Fig. 41). It is possible that stretching of the sheet over the positive die (as described in Section 4.3.4) is the dominant factor that reduces the forces of TPIF in comparison to pressing, but that the localisation of the deformation still applies to explain the progressive increase in tool forces in TPIF as well as SPIF. The effect of localisation of the deformation on tool force could be investigated in TPIF by removing the clamping fixture. This process would resemble spinning but in a frame of reference fixed to the workpiece. It would be expected that any effect of localisation of the deformation or reduction of forces due to stretching applied by the outer frame would be removed.

An alternative explanation for the progressively increasing strains could have been the accumulation of strains caused by the overlapping contact area of the tool on successive passes. However, any transition region as a result of overlapping passes would be expected to be approximately the size of the contact area of the tool, which must be less than the tool radius of 7.5 mm. It is evident that the strains increase over most of the formed region of the sheet (approximately 30 mm) in SPIF and TPIF, and therefore the overlapping tool passes cannot be the explanation. However, shear strain parallel to the tool direction, γ_{23} , shows a sharp drop-off from the maximum value to approximately zero over the final approximately 10 mm of the formed region for both SPIF and TPIF. The transition region approximately corresponds to the size of the contact region of the

tool, and hence the drop-off in shear is likely to be a result of the material not having sustained as many passes as the rest of the formed region.

The transition from a widely distributed to a highly localised deformation may also explain the transition in tool forces over the first few laps measured for cones of various wall angles formed by Jeswiet et al [56] and Duflou et al [93], as well as the transition in wall thickness measured by Young and Jeswiet [79] and Ambrogio et al [58]. The observation that tool forces and wall thickness reach a steady-state value after approximately 20 mm for these cones formed in 1.2 mm AA3003-O whereas no steady-state values were reached in the present experiments suggests that the progression from widely distributed to highly localised deformation may require fewer laps for the thinner aluminium. This hypothesis could be tested by measuring the change in geometry around the indenter with a stereovision camera as sheets of various materials are formed.

Shear perpendicular to the tool direction, γ_{13} , cannot be explained directly by friction due to the direction of the tool path. Two alternative explanations are proposed: (1) rotation of the tool; and (2) the tool pushing material downwards as it moves in descending contours over the inclined wall. The tool was designed to rotate freely on low friction bearings in order to minimise surface damage, tool wear and horizontal force by minimising sliding friction. Across most of the formed region in SPIF, γ_{13} is negative which shows that the upper surface of the sheet is pushed more towards the centre of the cone than the lower surface (Fig. 35e). If γ_{13} occurs as a result of rotation of the tool, this would suggest that γ_{13} is accumulated in the wake of the tool path; an anti-clockwise tool path would cause clockwise rotation of the tool, which could only push material towards the centre of the plate under the trailing hemisphere of the tool, rather than the leading hemisphere. However, it is expected that the pressure would be higher under the leading hemisphere of the tool rather than the trailing hemisphere, and therefore rotation of the tool is unlikely to be the full explanation for shear perpendicular to the tool direction. Alternatively, shear γ_{13} may be due to the indenter pushing material downwards as it pushes against the inclined surface of the metal sheet. The cause of shear γ_{13} could be investigated by locking off the rotation of the indenter, so the effect of rotation of the tool is eliminated.

The significance of the above observations of the deformation mechanics of ISF is twofold. Firstly, the strains sustained by any given element of material in SPIF or TPIF are not the same at any position, and hence finite element modelling must involve a simulation of the full tool path to predict the final strain on any element. Secondly, if forming limits are increased by through-thickness shear as Allwood et al [88] have suggested they may be, then the forming limits may increase as the process progresses as a result of increasing shear.

4.3.6 Transferability of the Results to Other ISF Processes

The objective of this section is to provide an evaluation of the transferability of the results of the present experiments to other more typical ISF experiments. This is important because the material, sheet thickness and geometry used in this experiment are not typical of those widely used in ISF research. These atypical choices were imposed by experimental constraints as described in Section 4.1.1. Copper, used in this experiment because it can be brazed, is not common in ISF due to its cost. High ductility steels or annealed aluminium alloys are more commonly used. The 3.1-3.3 mm thick plates, used to allow a longitudinal gridline to be machined along the cross-section, were thicker than the 1.0-1.5 mm sheets typically used in ISF. The wall angle used in the present experiment was a shallow 30° to avoid failure of the brazed joint, whilst steeper wall angles of 40° to 60° are more typical of ISF experiments.

The transferability of the results of the present experiments to other more typical ISF experiments will be evaluated by summarising the main similarities and differences that were highlighted throughout the discussion in three main areas: deformation and strains; tool force variation; and wall thickness variation. Reasons will be suggested for the differences in terms of the material properties, sheet thickness and geometry. The material properties of the heat-treated C101 used in the present experiments and aluminium alloys used in previous experiments are summarised in Table 6. The properties of the heat-treated C101 were obtained from the tensile test shown in Fig. 25, whilst all other properties were obtained from Smithells Metal Reference Book [126].

<i>Material</i>	<i>Experiments Where Used</i>	<i>Yield Strength (MPa)</i>	<i>Ultimate Tensile Strength (MPa)</i>	<i>Percentage Elongation at Failure</i>
Heat-treated C101	Present Work	40	205	60-80%
Annealed aluminium AA1050-O (DIN A199.5)	Bambach et al [61] Sawada et al [89] Ambrogio et al [58]	35	80	47%
Quarter-hard aluminium 5251-H22	Allwood et al [88]	130	220	8%
Annealed aluminium AA3003-O	Duflo et al [13] Jeswiet et al [56] Duflo et al [93] Young and Jeswiet [79]	41	110	30%

Table 6. Material properties for heat-treated C101 used in this chapter, along with three other aluminium alloys used in previous ISF research.

The main similarities of the results in Section 4.1.7 to the results of previous experiments are summarised as follows:

- Stretching (ϵ_{11}) observed in the plane perpendicular to the tool direction across the copper plates in SPIF and TPIF was similarly observed in finite element simulations of TPIF of 0.9 mm Al5050-O by Sawada et al [89] and SPIF of a 47° 1.5 mm thickness Al99.5 pyramid by Bambach et al [61]. Similar was found by experimental measurements of the relative movement of surfaces of 1 mm aluminium 5251-H22 formed to 45° by SPIF by Allwood et al [88]. This suggests that stretching perpendicular to the tool direction may be a feature of the deformation mechanics that always occurs irrespective of the material, thickness or wall angle. However, further work is required to investigate how the variation of stretching across the cross-section depends on these characteristics.
- Shear parallel to the tool direction (γ_{23}) was found to increase along the cross-section in the copper plates. Similar was found to occur in an experimental investigation of the relative movement of the surfaces of plates formed by SPIF of 1 mm aluminium 5251-H22 formed to 45° by Allwood et al [88]. This suggests that the result of increasing shear γ_{23} may be broadly transferable to more typical ISF processes. However, the degree of shear is likely to be greater for the copper plate as a result of increased friction due to the higher vertical tool force caused by the greater thickness of the copper in comparison to aluminium.

- The wall thickness was found to be initially greater than the sine law thickness then reduced to less than the sine law thickness across the formed region of the copper plates. Similar was observed in a study of 1 mm AA1050-O formed by SPIF to an angle of 55° by Ambrogio et al [58] and for 1.2 mm AA3003-O formed to an angle of 30° by Young and Jeswiet [79]. This suggests that thinning beyond the sine law prediction as a result of material being pushed towards the centre of the geometry may occur in ISF irrespective of wall angle, thickness or material.
- Tool forces followed an increasing trend with decreasing gradient in the present experiment. Increasing force to a steady-state value was similarly observed over the first few laps for SPIF of 1.2 mm AA3003-O formed to angles of 20° , 30° , 40° and 50° by Duflou et al [13] and for TPIF of the same material formed to 30° , 45° and 60° against a central support post by Jeswiet et al [56]. The increasing tool force with decreasing gradient is likely to be a result of increasing strains under the indenter due to progressive localisation of the deformation. Hence, evolution of the contact area and therefore strains and tool forces observed in the present experiments is likely to be representative of more typical ISF processes.

The main differences of the results in Section 4.1.7 to the results of previous experiments, and possible reasons for these differences, are summarised as follows:

- Tool force increased continually throughout the present experiments on the copper plates formed to a wall angle of 30° . In contrast, tool forces reached a steady-state value in previous experiments of SPIF of 1.2 mm AA3003-O formed to a wall angle of 30° by Duflou et al [13, 93] and TPIF of the same material formed to the same wall angle by Jeswiet et al [56]. Similarly, wall thickness followed a decreasing trend over the first 20 mm followed by levelling-off to a steady-state value in a previous experiment by Young and Jeswiet [79] for a 30° cone of 1.2 mm AA3003-O, whereas the wall thickness continually decreased and did not level-off in the present experiments. Although a similarity that has already been drawn between the experiments is that tool forces and strains are likely to increase as a result of localisation of the deformation, it is likely that the number of laps over which the deformation localises is higher in the present experiments both as a result of the thicker sheet

used and possibly the higher rate of work hardening of the copper. Hence, it is likely that the continual increase in strain observed in the present experiments would not transfer to thinner aluminium sheets, which are likely to have uniform strains across most of the cross-sections.

- Vertical tool force was found to reach a maximum of approximately 6000 N in SPIF and 4000 N in TPIF of the copper plates in the present experiments. In contrast, a significantly lower maximum value of vertical tool force of approximately 350 N was reached for 1.2 mm AA3003-O formed to 30° by TPIF by Jeswiet et al [56], whilst a maximum vertical tool force of only approximately 420 N was measured in SPIF of the same material formed to the same wall angle by Duflou et al [93]. This is likely to be a result of both the lower thickness of the sheets and the lower work hardening of the aluminium in comparison to copper.
- Young and Jeswiet [79] previously showed that a thinning band occurred close to the perimeter of 1.21 mm AA3003-O sheet formed by SPIF to a truncated cone of angle 70°. Similarly, a peak in tool force was observed to occur over the first few laps of the same material formed to the same wall angle in SPIF by Duflou et al [54]. The peak in tool force and thinning band were not observed in the present experiments, possibly because the plate was thicker, the material was C101 instead of aluminium, the wall angle of 30° was shallower or because a backing plate was used to support the perimeter. Hence, the deformation mechanics observed close to the perimeter of the formed region in the present experiments is unlikely to be a good representation of the deformation mechanics in processes similar to those studied by Young and Jeswiet [79] and Duflou et al [54].
- In a numerical simulation of SPIF of a 0.9 mm Al99.5 plate formed to an angle of 47° by Bambach et al [61], the shear strain perpendicular to the tool direction (γ_{13}) was found to occur in the opposite sense to the shear strain measured in SPIF of the copper plates. This may be a result of the different wall angle, sheet thickness or material used in the simulation, or as a result of numerical inaccuracies. Hence the results for shear perpendicular to the tool direction measured for the copper plates may not be broadly transferable to other ISF processes.

Consideration of all of the above factors shows that the unusual choice of material, sheet thickness and wall angle used in the present experiments is likely to have resulted in strains that have some differences to more typical ISF experiments. ISF experiments typically use thinner sheets of annealed aluminium alloys formed to steeper wall angles than the copper plates used in these experiments. However, some similarities are likely to have occurred, and hence some aspects of the results may be transferable to these more typical processes. Specifically, it is likely that through-thickness shear would have been greater for the copper plate than thinner sheets, whilst it is likely that a similar evolution in strains on successive laps occurred in the present experiments to past experiments on thinner sheets.

4.4 Concluding Remarks

The findings of Chapter 4, ‘The Mechanics of Incremental Forming of Sheet Metals’, can be concluded as follows:

- The deformation mechanisms of both SPIF and TPIF are increasing stretching and shear in the radial-axial plane (perpendicular to tool direction) and shear in the tool direction.
- Shear in the tool direction is the most significant strain component.
- Increasing stretching and shear perpendicular to the tool direction account for differences between the sine law and measured wall thickness for SPIF and TPIF.
- Shear both parallel and perpendicular to the tool direction is the main distinction between the deformation mechanisms of SPIF or TPIF and pressing.
- Tool forces correlate to shear parallel to the tool direction which suggests that the shear is primarily a result of friction between the tool and workpiece.

5. The Mechanics of Incremental Forming of Sandwich Panels

ISF has so far mainly been applied to monolithic sheet metals. However, the economic advantages of the process for customised production may be transferable to alternative groups of materials which are otherwise formed by dies. A group of materials of particular interest is sandwich panels, which offer weight savings or increased stiffness in comparison to monolithic sheets. The application of ISF to sandwich panels with metal faceplates was first investigated by Landert [68] of Cambridge University Department of Materials Science and Metallurgy in collaboration with the author. This chapter presents the author's own contribution to this new area of research, focusing on the mechanics of ISF of sandwich panels. The starting point is an investigation of the mechanical feasibility of ISF of various sandwich panel designs. This is achieved by examination of failure modes, thinning and surface quality of various formable sandwich panel designs in ISF. It is shown that ISF is applicable to sandwich panels with ductile and largely incompressible cores which are able to sustain the local deformation under the indenter. Secondly, the influence of ISF on a suitable formable sandwich panel has been compared to that of a monolithic sheet metal through comparison of tool forces, the accuracy of the sine law and the relative movement of upper and lower surfaces. It is shown that ISF has a similar influence on both materials, and hence established knowledge derived for ISF of monolithic sheet metals may be used in future to apply ISF to sandwich panels.

5.1 The Mechanical Feasibility of ISF of Various Sandwich Panel Designs

Having investigated the deformation mechanics of sheet metals in Chapter 4 through investigation of the through-thickness deformation and measurement of tool forces, this chapter presents a new starting point for research into the deformation mechanics of an alternative class of materials: sandwich panels. Unlike monolithic sheet metals, various sandwich panel designs that can be formed by pressing cannot necessarily be formed by ISF due to localised damage that could be sustained during the process. This is because, as described by Zenkert [103], sandwich panels are particularly susceptible to failure by local indentation. Failure modes can occur that are internal to the sandwich panel such as damage to the core or core-faceplate bonding, hence an external inspection of the faceplates as is commonly used for monolithic sheet metals will not suffice. Furthermore, reduction in thickness should be considered as damage because this significantly reduces the stiffness of the sandwich panel, in addition to surface damage which is important for some applications. Hence an approach that is entirely different to that followed in Chapter 4 for monolithic sheet metals has been adopted in this chapter to investigate the mechanics of sandwich panels, starting in this section with an investigation of the mechanical feasibility of ISF of various sandwich panel designs. This will be carried out by inspection of failure modes and damage occurring under appropriately designed tool paths. This research builds on the earlier research carried out by Landert [68] in three respects: (1) a wider range of failure modes and damage sustained during ISF other than faceplate fracture are considered; (2) more accurate measurements of through-thickness strains are taken to evaluate reduction in thickness by avoiding delamination when cross-sections are cut; and (3) the deformation of sandwich panels is investigated under tool paths that simulate the first contact of the tool in ISF.

5.1.1 *Selection of Materials*

Four sandwich panels representing the key formable sandwich panel designs reviewed in Chapter 2 have been selected on which to evaluate the mechanical feasibility of ISF. Two panels with metal faceplates and polymer cores have been selected: mild steel

faceplates with a polypropylene core (MS/PP/MS) (Sollight® manufactured by Arcelor); and aluminium faceplates with a polypropylene core (Al/PP/Al) (Hylite® manufactured by Corus). One sandwich panel with stainless steel faceplates and a stainless steel fibre core (SS/SS fibre/SS) (Hybrix® manufactured by Lamera) has been selected. The fourth sandwich panel has aluminium faceplates and an aluminium foam core manufactured by Alulight (Al/Al foam/Al). The specifications of the sandwich panels are given in Table 7. As described in Chapter 2, formability comparable to that of sheet metals has been measured for all of the above sandwich panels in conventional formability tests, with the exception of the Al/Al foam/Al sandwich panel which has demonstrated limited ability to be formed in a draw bending test and is not usually formed directly. This material is tested here in order to provide insights into the effects of ISF applied to a broad range of sandwich panels, to highlight important considerations and to suggest directions for future work.

<i>Sandwich Panel</i>	<i>Product Name (Manufacturer)</i>	<i>Total thickness [mm]</i>	<i>Core thickness [mm]</i>	<i>Core Material</i>	<i>Faceplate thickness [mm]</i>	<i>Faceplate Material</i>	<i>Core-Faceplate Bonding</i>
MS/PP/MS	Sollight® (Arcelor)	2.0	1.44	Polypropylene	0.28	Mild steel	Hot co-laminating
Al/PP/Al	Hylite® (Corus)	1.2	0.8	Polypropylene	0.2	AA5182	Not available
SS/SS fibre/SS	Hybrix® (Lamera)	1.2	0.8	Stainless steel fibre	0.2	Stainless steel	Epoxy resin
Al/Al foam/Al	Alulight® (Alulight)	13.5	9.5	Al alloy foam AlMg1Si0.6	2	AA5251-H22	Epoxy adhesive

Table 7. Specifications of sandwich panels tested

5.1.2 Design of Tool Paths

As a starting point for research into the effects of ISF on sandwich panels, two simple tool paths have been chosen to represent the least mechanically demanding deformation that could occur in SPIF. These have been chosen because if the sandwich panels fail under these conditions they will also fail under the more demanding descending contour or spiral tool paths that are typical of ISF. The first tool path is a straight line (Fig. 43a), representing the local indentation which occurs in the first deformation of any ISF process. The length of the line is 100 mm and tool speed is 10 mm/s. The second tool path is a spiral in a horizontal plane with overlapping passes (Fig. 43b). This subjects

the material to repeated passes as well as local indentation which occurs in the typical spiral or contour tool paths of ISF, but the wall angle is zero and hence the material is not subjected to thinning by a non-zero wall angle. The pitch between successive laps is 0.1 mm, tool speed is 40 mm/s, and the outer diameter of the spiral is 40 mm for all sandwich panels apart from Al/Al foam/Al, for which a wider diameter of 80 mm was used. In both the line and spiral tests the tool radius is 7.5 mm, the size of the unsupported region of the sheet is 140 x 140 mm and lubrication is Castrol SpheroL grease L-EP2. The depth of the path below the initial plane of the sheet is 8 mm because initial trials showed that this is sufficient to cause a localised plastic deformation under the indenter head in the first pass in all of the materials tested.

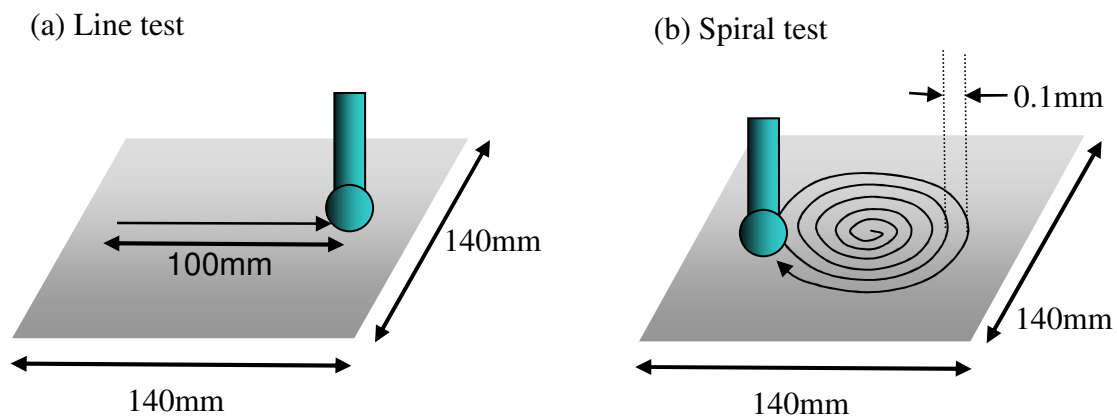


Fig. 43. Tool paths to test mechanical feasibility of ISF of sandwich panels: (a) line and (b) spiral.

5.1.3 Failure Modes and Damage

Three factors will be considered to evaluate the mechanical feasibility of ISF of sandwich panels: mechanical failure; reduction in thickness; and surface finish degradation. The first factor, mechanical failure, occurs when damage is sustained to the core, faceplates or core-faceplate bonding such that the faceplates and core are no longer able to co-operate therefore bending stiffness or strength is reduced. There are several ways in which this can occur, as described below. Thickness reduction results in a significant loss in bending stiffness called the *sandwich effect* as described by Zenkert [103], although the core and faceplates can still co-operate. Surface quality degradation has no structural significance, but is of critical importance for applications such as car body panels.

Eight possible modes of mechanical failure of sandwich panels have been described by Zenkert [103] under various types of loading. These are faceplate fracture, core shear failure, face wrinkling (inwards or outwards), buckling, shear crimping, face dimpling and local indentation. Assuming that shear, in-plane tension or local indentation are the only loadings that occur in ISF due to the direction of applied loading, Zenkert's original list may be reduced to three modes most likely occur in ISF: (a) faceplate fracture; (b) core shear failure; and (c) local indentation. In addition, delamination (d) may occur. These four failure modes are illustrated in Fig. 44.

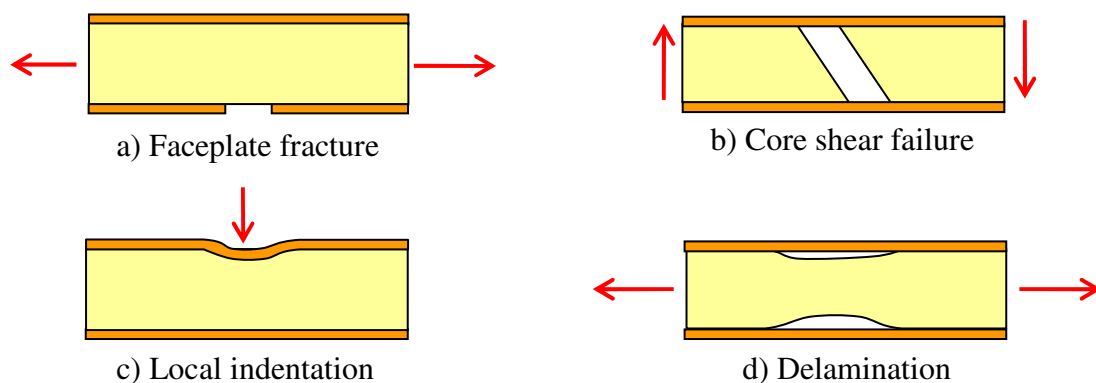


Fig. 44. Four failure modes of sandwich panels which may occur in ISF and associated loading: a) faceplate fracture, b) core shear failure, c) local indentation and d) delamination.

In contrast to sheet metals, it is not sufficient to inspect only the surfaces of the sandwich panels to identify failure modes because two of the above four failure modes are internal. An internal inspection is therefore necessary and for these preliminary tests has been carried out by cutting a strip of material from the centre of the sheet, mounting this strip in resin, mechanically polishing the surface then inspecting under a microscope. To avoid delamination of the strip of material during the cutting process to allow accurate thickness measurements, a waterjet cutter was used as opposed to a band saw which would tend to pull the sandwich panel apart. An electron microscope Stereoscan 430 was used to inspect the thin sandwich panels (MS/PP/MS, Al/PP/Al and SS/SS fibre/SS), and a 5 mega pixel digital camera Canon Ixus i5 Zoom was used to photograph the Al/Al foam/Al which was too wide for the microscope.

The reduction in thickness of the sandwich panels has been reported in terms of engineering strain at three positions: the core; the average strain of both faceplates; and the strain of overall sandwich panel. Engineering strain was calculated from ratio of change in thickness to original thickness of each layer. Thickness was measured with the Olympus BX51M optical microscope using ANALYSISauto software to an accuracy of $\pm 0.005\mu\text{m}$ for MS/PP/MS, SS/SS fibre/SS and Al/PP/Al. Vernier callipers were used to measure the thickness of Al/Al foam/Al to an accuracy ± 0.01 mm because this was too wide to observe under the microscope. To give a qualitative indication of the effect of ISF on surface finish, the upper and lower surfaces of each sandwich panel have been photographed after the area test with a digital camera Canon Ixus i5 Zoom.

5.1.4 Results and Observations

Fig. 45 shows the cross-sections of the sandwich panels before deformation and after forming with the line and spiral tool paths, from which failure modes can be identified. In each micrograph, the surface which the tool contacted is at the top and the direction of tool travel is normal to the plane of the micrograph. The centreline of the tool path is in the centre of each image for the line path, and the centre of the spiral is in the centre of each image for the spiral path, apart from for the Al/Al foam/Al sandwich panel which was taken at the most highly compressed region. Fig. 46 is a photograph of the full cross-section of the Al/Al foam/Al sandwich panel formed by the spiral tool path, showing distortion of the upper surface. Fig. 47 shows through-thickness strain from the line and spiral tool paths. The strain was measured at the centreline of the tool path for the line path (Fig. 47a). For the spiral path the strain was measured at the centre for the MS/PP/MS, Al/PP/Al and SS/SS fibre/SS sandwich panels because uniform compression was observed over the formed area, whereas for the Al/Al foam/Al sandwich panel the strain was measured at the most highly compressed point close to the outer edge of the spiral because the strain was non-uniform (Fig. 47b). The upper and lower surfaces of each sandwich panel after the spiral test showing changes in the surface finish are shown in Fig. 48.

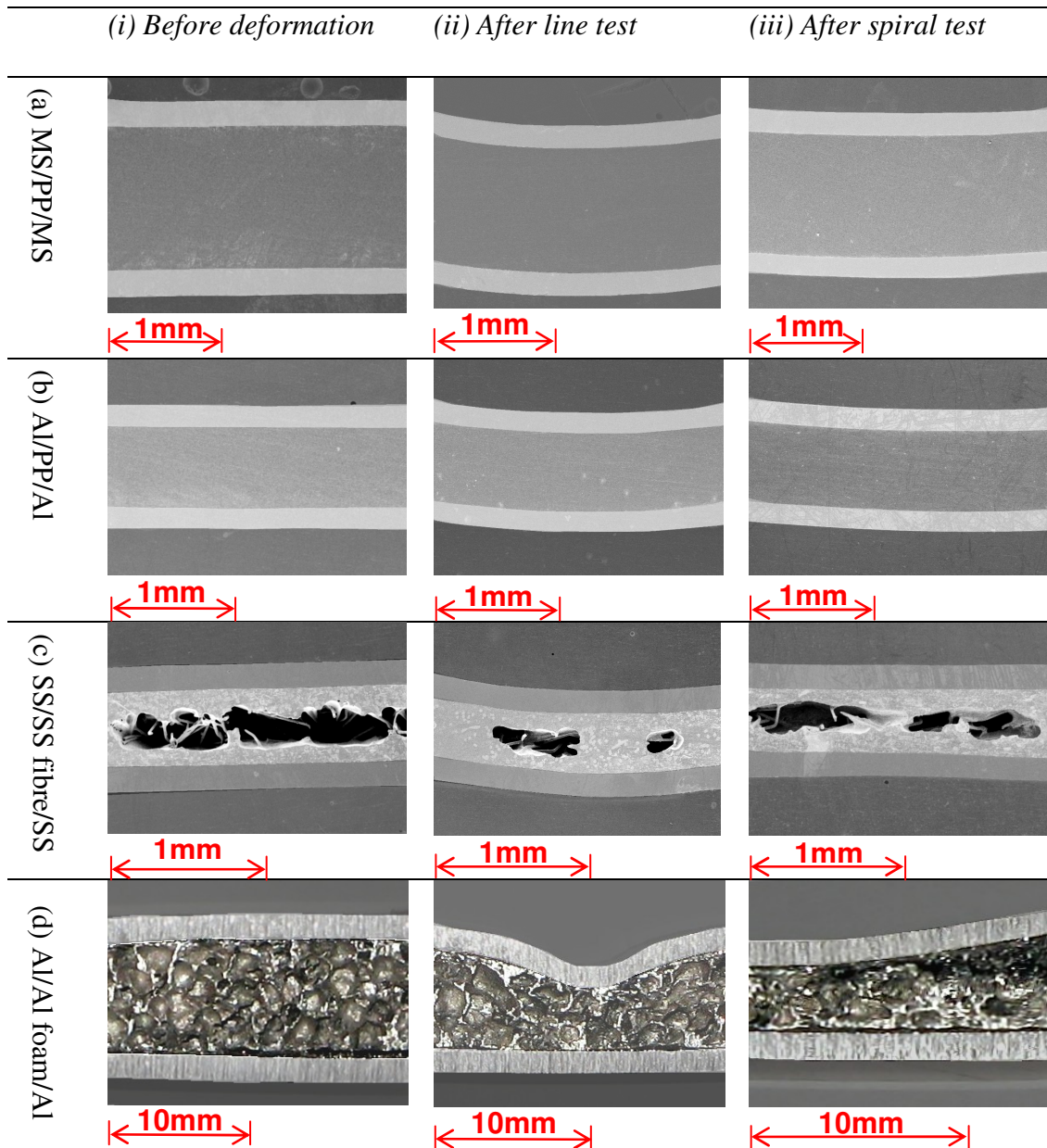


Fig. 45. Cross-sections of sandwich panels before and after deformation: (a) MS/PP/MS, (b) Al/PP/Al, (c) SS/SS fibre/SS and (d) Al/Al foam/Al.

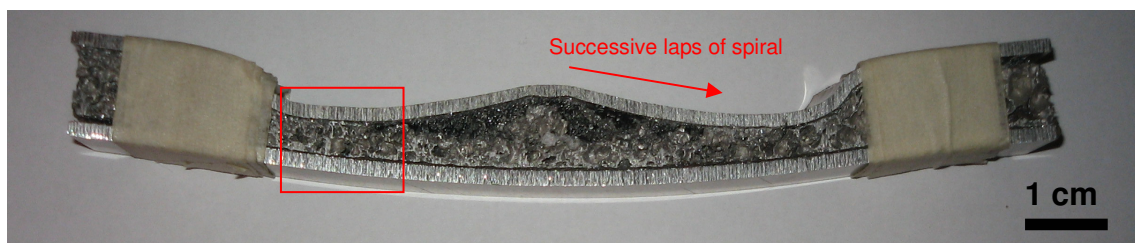
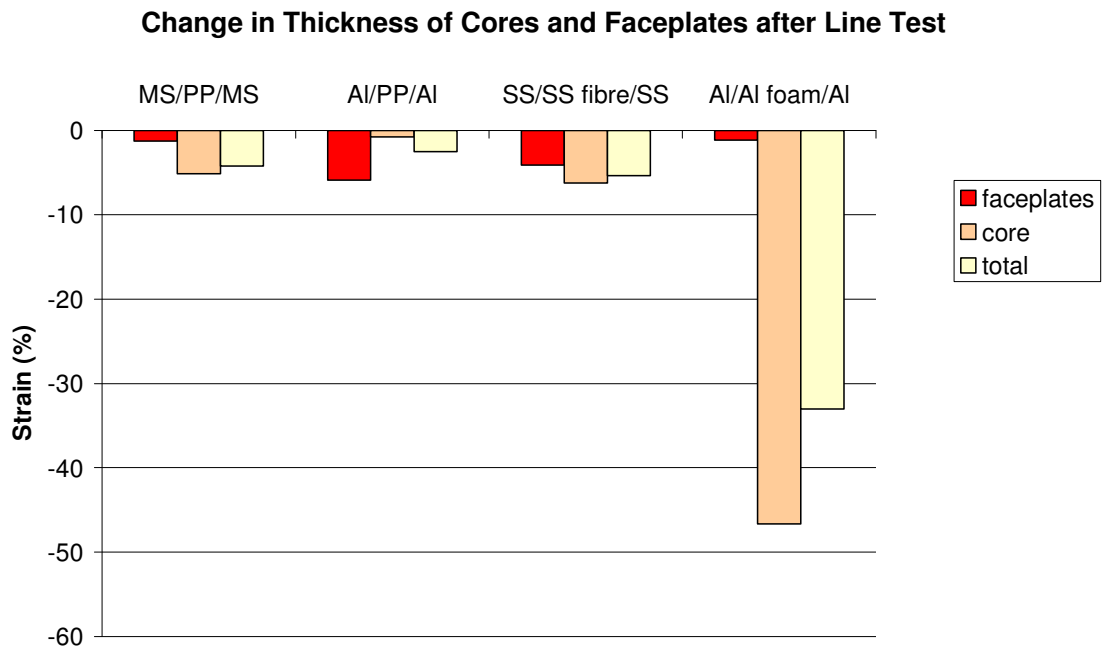


Fig. 46. Photograph of full cross-section of Al/Al foam/Al sandwich panel formed by the spiral tool path showing distortion of the upper surface. The ends have been taped together due to delamination which occurred during the process. The direction of successive laps of the spiral is shown and the red rectangle marks the position of Fig. 45d)iii.

a)



b)

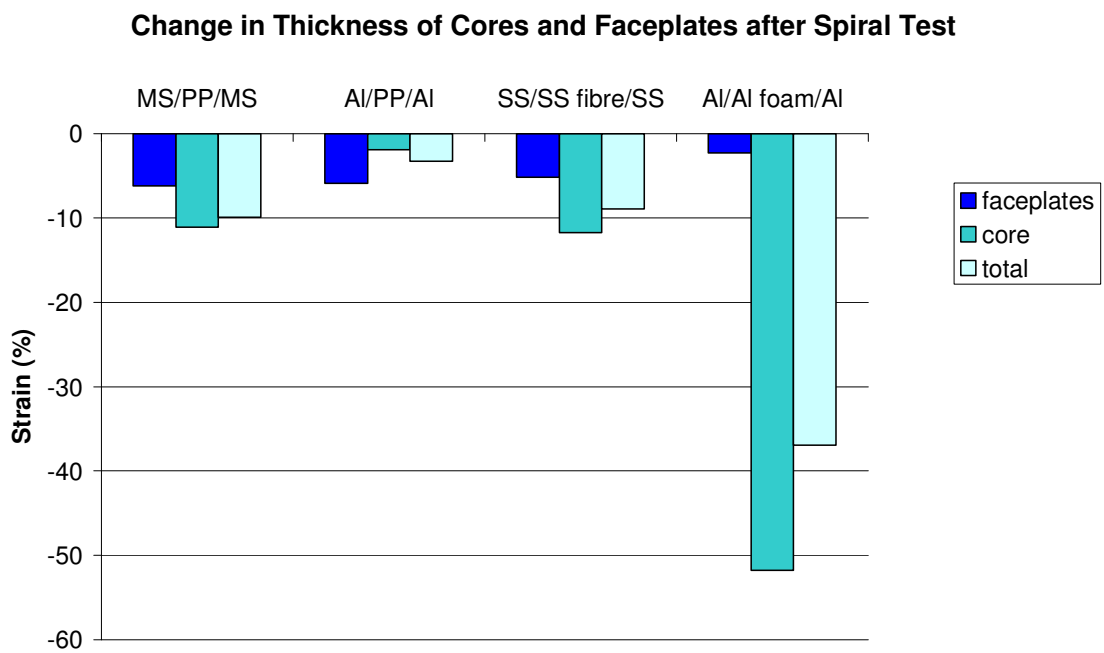


Fig. 47. Through-thickness strain of sandwich panels at the position showing the most severe reduction in thickness: a) after line test; b) after spiral test.

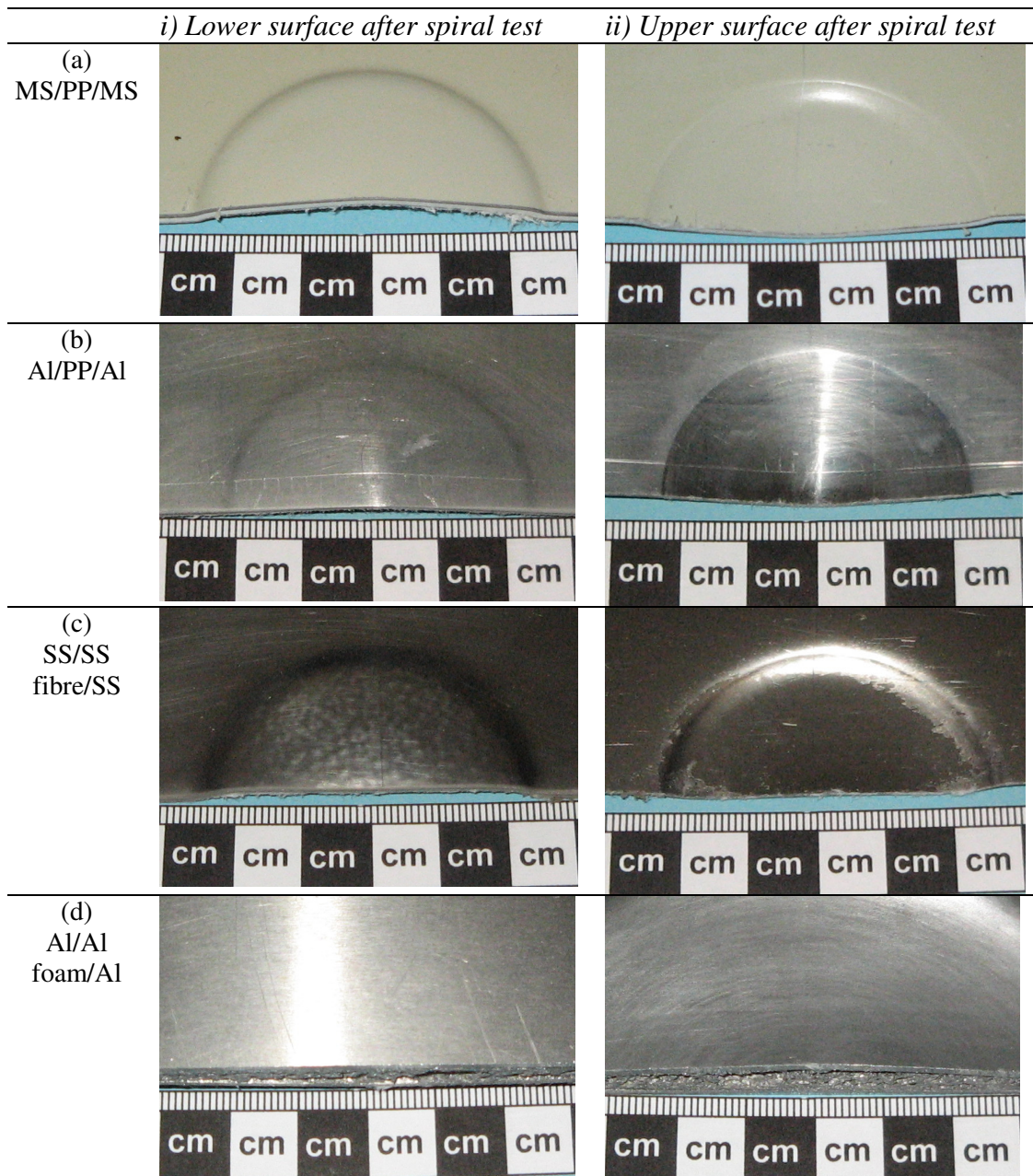


Fig. 48. Lower and upper surface of sandwich panels after spiral test: (a) MS/PP/MS, (b) Al/PP/Al, (c) SS/SS fibre/SS and (d) Al/Al foam/Al. For the Al/Al foam/Al sandwich panel no distortion of the lower surface is visible because the deformation of the upper surface was entirely absorbed by the compressible metal foam core. The diameter of the spiral formed on the Al/Al foam sandwich panel was larger than on the other materials (80 mm and 40 mm respectively).

The results show that the MS/PP/MS, Al/PP/Al and SS/SS fibre/SS sandwich panels have been formed successfully in the line and spiral tests. Micrographs of the cross-sections show that no failure modes occur (Fig. 45a, b and c), and hence the faceplates are still able to co-operate as the original sandwich panel structure. The core fibres of the SS/SS fibre/SS sandwich panel have been bent, but it is not possible to determine from these images whether a loss in core shear strength has occurred as a result of breakage of the fibres in the forming process. Only small negative strains of the core and faceplates occurred in the line and spiral tests for these three materials (Fig. 47), indicating that bending stiffness provided by the co-operating faceplates is largely maintained. The small strains may be attributed primarily to in-plane stretching causing a reduction in thickness as a result of volume constancy. However, different strains are observed for the core and faceplates for all three materials, whereas equal strains would be expected if volume constancy and uniform stretching was observed throughout. The core of SS/SS fibre/SS has been strained by a greater amount than the faceplates, which is because the core is compressible and hence volume constancy was not maintained. However, greater strain also occurred in the core than the faceplates of the MS/PP/MS sandwich panel, whilst for the Al/PP/Al sandwich panel the opposite occurred. This may be due to variations in the original thickness of the cores across the panels.

The images of the surfaces of MS/PP/MS, Al/PP/Al and SS/SS fibre/SS show that negligible or minor surface finish degradation is sustained for the first two, but more severe degradation is sustained by SS/SS fibre/SS, and hence this material may not be suitable for forming by ISF. The surfaces of MS/PP/MS remain smooth because the coating prevents damage caused by the tool moving across the surface, whilst the surfaces remain flat because the core is continuous and largely incompressible (Fig. 48a). This is advantageous for applications with high aesthetic requirements. The upper surface of Al/PP/Al shows scratching due to movement of the tool over the surface (Fig. 48b). This is comparable to scratching of sheet metals in ISF and it is likely that this can be reduced by careful selection of process variables as it is for sheet metals, such as tool pitch (Hagan and Jeswiet [59]), and lubrication and tool design (Kim and Park [38]). In contrast, Fig. 48ci shows that the lower surface of the SS/SS fibre/SS sandwich panel exhibits large-scale waviness as a result of the fibrous core being compacted against the lower surface under the action of the indenter. Similar was observed by Landert [68] when this material was formed to a steeper wall angle by ISF. The upper surface of this

material also exhibits waviness but to a lesser extent. Small-scale scratching of this material is less severe than the faceplates of Al/PP/Al, possibly because the SS is harder and therefore more resistant to damage by abrasion. Surface waviness observed on the SS/SS fibre/SS sandwich panel is likely to be unacceptable for some applications and may be less severe in pressing where the tool force is distributed over a larger area.

In contrast to the materials described above, the Al/Al foam/Al sandwich panel sustained severe damage in the first pass of the indenter, and therefore is not suitable for forming into 3D shells by ISF. Fig. 45d shows that the porous and brittle core is compressed severely under the indenter. This reduction in thickness is greater than the other core materials (Fig. 47) and is likely to lead to a loss of bending stiffness due to both reduction in faceplate separation and reduction in shear strength in the core due to fracture of the metal foam cell walls. Delamination between the core and faceplates occurred, which was more apparent for the spiral test (Fig. 45diii) than the line test (Fig. 45dii). This is probably because the spiral test caused out-of-plane distortion of the upper surface (Fig. 46), which may be a result of local stretching under the indenter causing compressive stresses to build up in the upper faceplate. The epoxy resin core-faceplate bonding used on this sandwich panel was made in-house and stronger bonding is made by the manufacturer which may have avoided delamination. Fig. 48ci shows that scratching of the upper surface occurs due to movement of the tool. However, this is comparable to that of sheet metals and could be removed by post-forming finishing operations and therefore is not necessarily a disadvantage for this process.

5.1.5 Summary of Findings

Unlike ISF of sheet metals, it is not sufficient to consider fracture of the surfaces of sandwich panels to indicate failure; other failure modes such as core crushing and delamination that are internal to the panel should be considered. For ISF to be applicable to sandwich panels, the panels must be able to sustain ductile deformation under the localised action of the indenter without collapse of the core or failure of the faceplates. Preliminary trials under some simple tool paths have suggested that suitable core and faceplate materials are polymers and metals respectively. Porous cores such as metal fibres and metal foams sustain compression and local damage in ISF which could lead to a loss of core shear strength, loss of bending stiffness and surface waviness.

5.2 Comparison of the Influence of ISF on a Sandwich Panel and Sheet Metal

The influence of ISF on monolithic sheet metals has been widely researched and the principle results so far, as reviewed in Chapter 2, include the influence of process variables on tool forces, the strains on the surface of the sheet and the applicability of the sine law for prediction of wall thickness. Chapter 4 presented some new results for the deformation mechanics, including the through-thickness deformation of a monolithic plate. Having established the sandwich panel designs to which ISF is applicable in section 5.1, the next stage of research into the mechanics of ISF of sandwich panels will involve investigating the extent to which these previous results for monolithic sheet metals are applicable to sandwich panels. This will be achieved by measuring and comparing three factors for a mechanically similar monolithic sheet metal and sandwich panel in ISF: (1) the influence of tool radius and vertical pitch on tool force; (2) the relative movement of upper and lower surfaces of the sheets; and (3) the accuracy of the sine law for prediction of wall thickness. The methods and results for each comparison are reported below, where the latter two experiments have been combined to enable the accuracy of the sine law to be directly compared to the movement of the upper and lower surfaces. The results are discussed and compared to previous works and the findings of Chapter 4 in Section 5.3.

5.2.1 Selection of Materials

The sandwich panel selected for testing is 2 mm thick MS/PP/MS, as described in Table 7, because it was demonstrated in Section 5.1 that it can be formed successfully by ISF. The sheet metal selected for comparison is 2 mm thick 5251-H22 aluminium because it has a similar plastic bending moment per unit width to MS/PP/MS. This was established by a 3-point bend test to be 325Nm/m, whilst that for MS/PP/MS was 300Nm/m (Fig. 49). Tensile tests in the rolling and transverse directions (Fig. 50) were carried out to characterise Young's modulus, 0.2% proof stress, percentage elongation and tensile strength from the average in each direction (Table 8). Although the materials show similar behaviour in 3-point bending due to the distribution of strength about the neutral axis, the sandwich panel has a lower tensile strength than the monolithic sheet due to the properties of the component materials in tension. The

aluminium, which is a quarter-hard wrought magnesium alloy, has a lower percentage elongation than the sandwich panel. These measured properties will be used to provide a basis for comparison of the results for the sandwich panel and monolithic sheet metal.

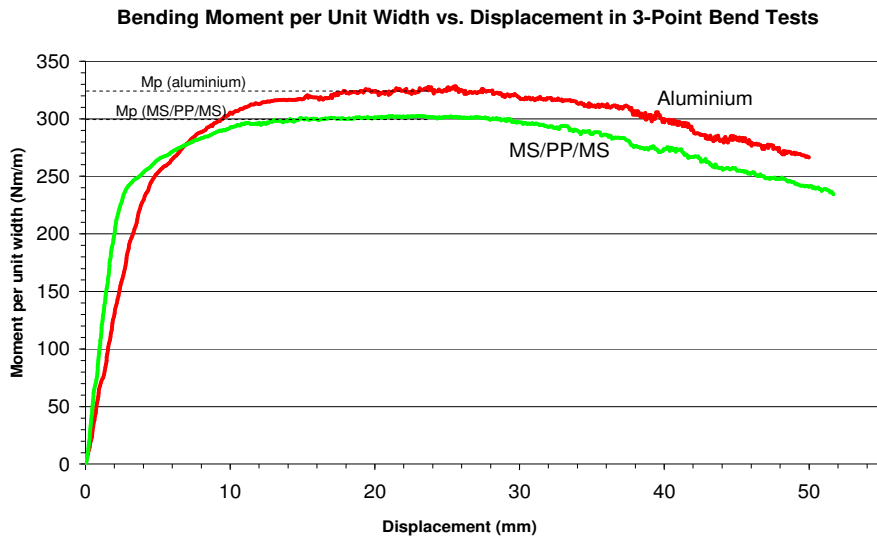


Fig. 49. Bending moment per unit width vs. displacement in three point bend tests.

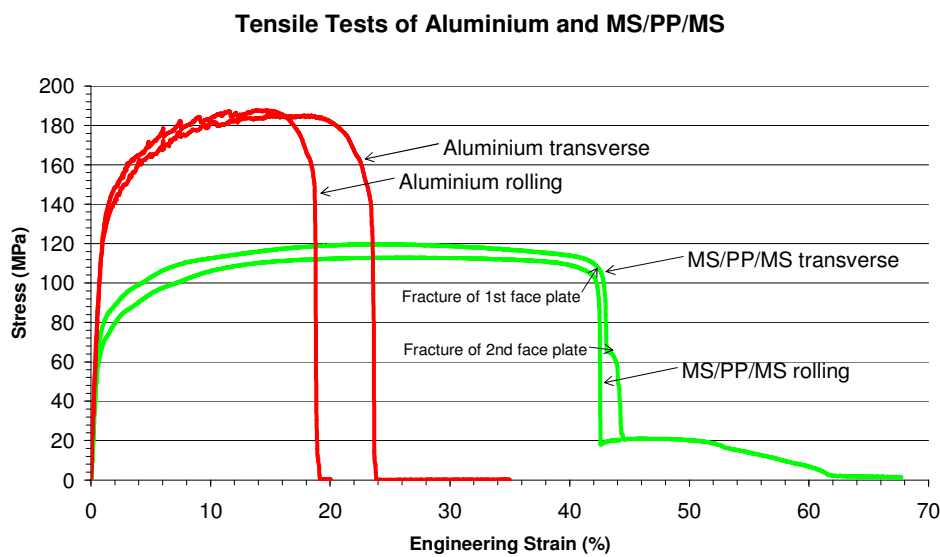


Fig. 50. Stress vs. strain in tensile tests for MS/PP/MS and aluminium.

Property	MS/PP/MS	Aluminium
Young's Modulus (GPa)	9.4	12.4
0.2% Proof stress (MPa)	77	137
% Elongation	67	21
Ultimate tensile strength (MPa)	117	187

Table 8. Mechanical properties of MS/PP/MS and aluminium, established from tensile test.

5.2.2 Influence of Tool Radius and Vertical Pitch on Tool Force

The influence of tool radius and vertical pitch on tool force in ISF of the monolithic sheet metal and the sandwich panel have been compared to establish whether similar trends are observed for the two materials. This has been achieved according to the following procedure: (1) perpendicular components of tool force have been measured throughout similar ISF experiments using a range of tool radii and vertical pitches on both materials; (2) the variation in tool forces throughout the processes have been analysed in order to define a suitable measure of tool force for comparison between processes; and (3) this measure of tool force has been plotted against tool radius and vertical pitch to compare trends for the two materials. In addition to providing data for comparison of the two materials in ISF, the tool force measurements provide further insight into the deformation mechanics which will be discussed and compared to the findings of Chapter 4 and previous works on sheet metals in Section 5.3.

5.2.2.1 Method

The tool path that has been designed on which to measure tool force for a range of vertical pitches and tool diameters is a four-sided pyramid because it was expected that uniform strains could be achieved on successive laps. The pyramids were formed to a wall angle of 40° because preliminary trials showed that this was close to but did not exceed the forming limits of either material. The tool paths, illustrated in Fig. 51, had a base area of 100 x 100 mm centred upon an unsupported area of 140 x 140 mm on a sheet of total size 175 x 175 mm. Fig. 51 shows the machine axes (x, y, z) where x and y are in the plane parallel to the undeformed sheet and z is the normal direction upwards (parallel to the tool axis). Lubrication was Castrol Spheerol L-EP2 extreme pressure grease and tool speed was 40 mm/s for each experiment.

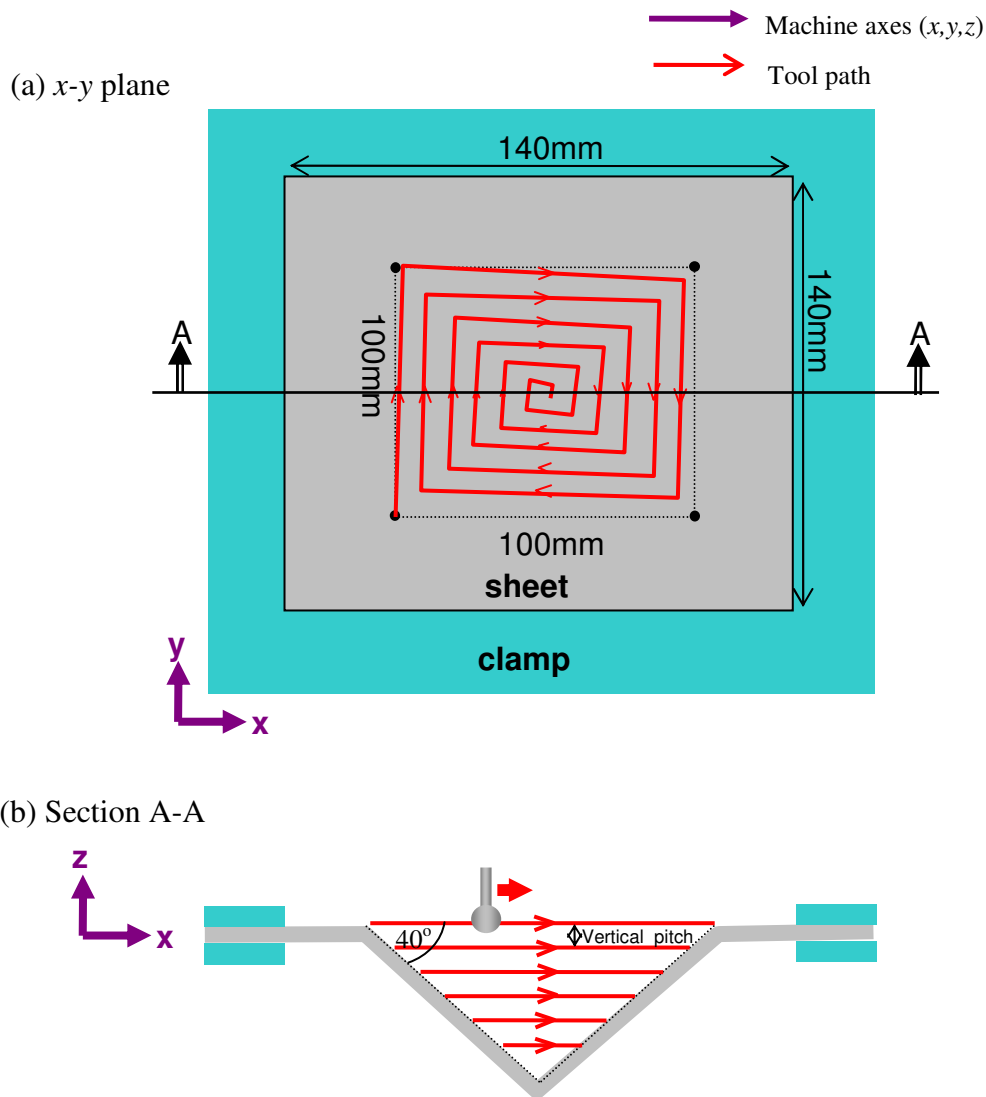


Fig. 51. Tool path used in comparison of vertical tool forces: (a) in x-y plane and (b) cross-section A-A in x-z plane through apex.

Due to the constraint of available tool radii and the amount of the sandwich panel available, nine combinations of three tool radii (5, 7.5 and 15 mm) with three vertical pitches (0.1, 0.5 and 2 mm) were used. Although this gives insufficient data points to accurately measure trends relating tool force to these parameters, sufficient data is available to give a useful quantitative comparison. Tool force was measured in the x , y and z directions throughout the experiments using the tool force system described in Chapter 3, with a sample period of one second. The components of tool force were then resolved into four components relative to the instantaneous tool direction: force parallel to the tool direction (F_{para}); force perpendicular to the tool direction (F_{perp}); vertical tool force (F_{axial}); and total tool force (F_{total}). The instantaneous tool direction at any

recorded point t_i was taken as the direction of the vector adjoining the previous point at time t_{i-1} to the next point at time t_{i+1} . Because the tool followed an approximately square path, the instantaneous direction was almost always approximately aligned with one of the axes x or y . The force components are defined to be positive in the directions acting on the sheet, as shown in Fig. 52.

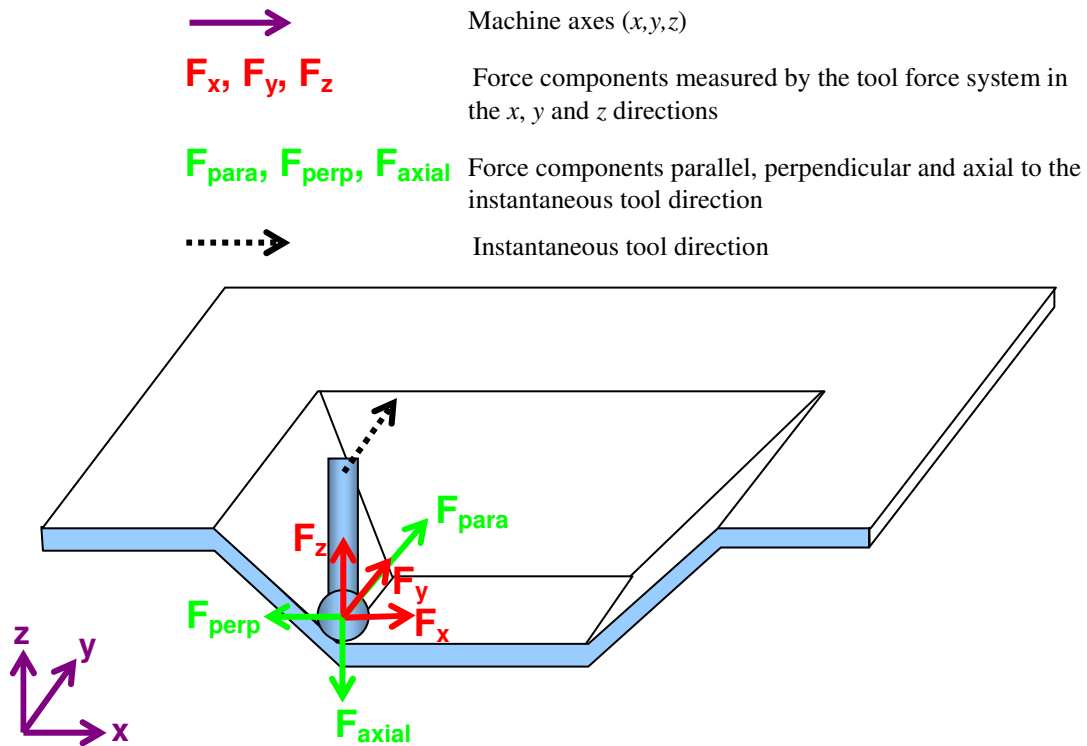


Fig. 52. Resolution of tool force components in (x,y,z) directions to components parallel, perpendicular and axial to the instantaneous tool direction.

5.2.2.2. Results and Observations

Tool force components F_{para} , F_{perp} , F_{axial} and F_{total} are plotted across the formed area in the x - y plane for the experiment with a vertical pitch of 2 mm and tool radius of 7.5 mm for MS/PP/MS and aluminium in Fig. 53. On each plot, the tool direction is clockwise. Colour bars with equal scales have been used on equivalent figures for each material to allow an easy visual comparison of the magnitude of the tool forces. The other eight experiments with different values of vertical pitch and tool radius showed similar trends in tool forces. This experiment has been chosen as an example from which to derive a suitable single measure of tool force that can be used to interpret the influence of tool radius and vertical pitch on tool force.

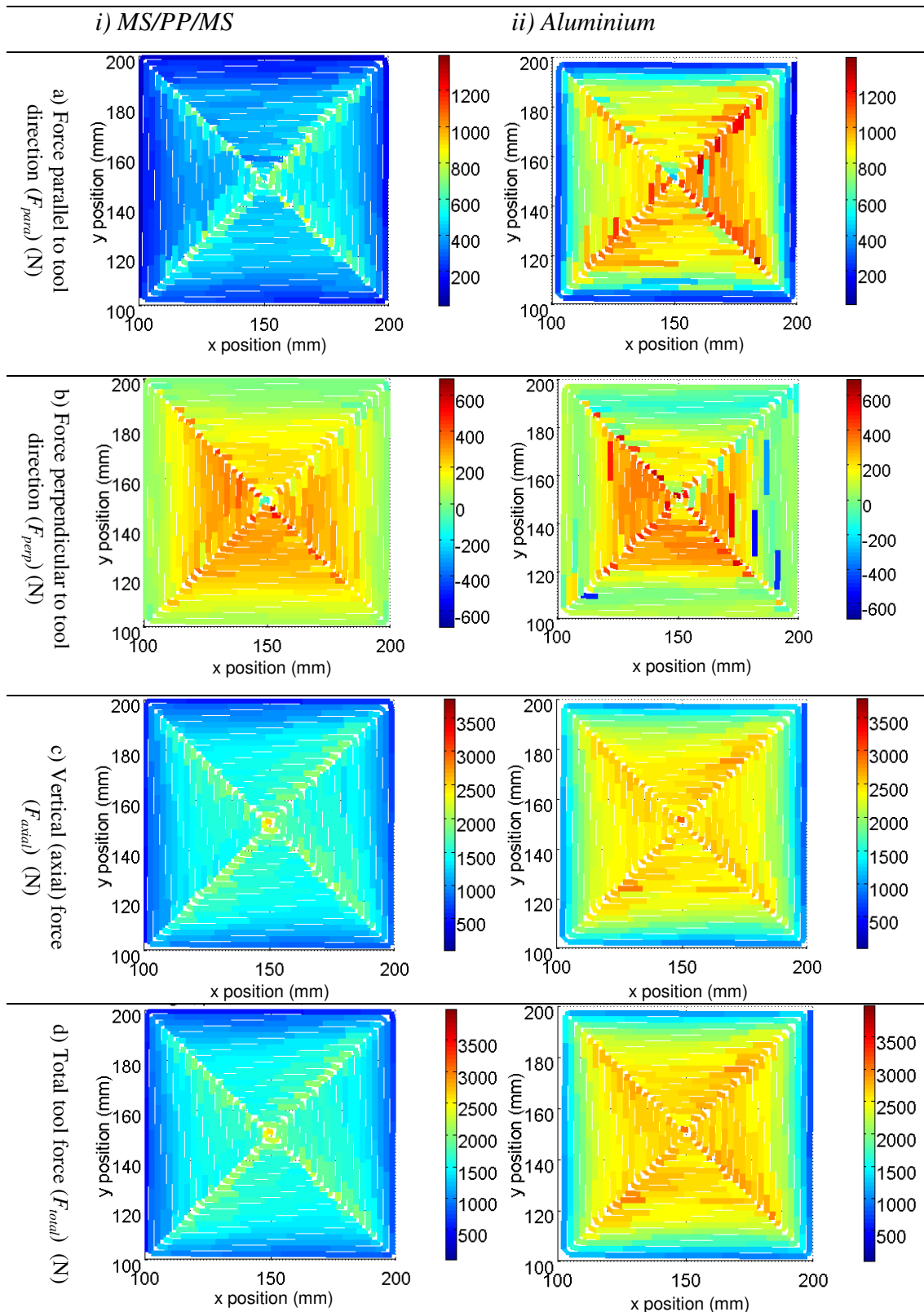


Fig. 53. Tool forces shown in x - y plane in SPIF of MS/PP/MS and aluminium with vertical pitch of 2 mm and tool radius of 7.5 mm: (a) force parallel to tool direction (F_{para}); (b) force perpendicular to tool direction (F_{perp}); (c) axial (vertical) tool force (F_{axial}); and (d) total tool force vector (F_{total}). On each plot the tool direction is clockwise.

From Fig. 53, four observations of the trends in tool force components can be made: (1) each tool force component is rotationally symmetric; (2) on average each component of tool force increases on successive laps and stabilises to a steady-state value towards the apex of the pyramid; (3) each component of tool force increases towards the corners of the pyramid; and (4) tool forces are higher for aluminium than MS/PP/MS. Similar trends were observed for all nine experiments, and these are discussed further and compared to previous works in Section 5.3.3.

A suitable measure of tool force for comparison of each component in each process is the average minimum force on each side of the pyramid during the steady-state phase (F_{ss}). This has been selected for 2 reasons: (1) the initial transition region does not provide a stable single measure of tool force from which the processes can be compared; and (2) the sample period of 1 s was too low to capture the sharp peak of tool force in each corner whilst it was sufficiently fast to capture the smooth minimum in tool force at the centre of each lap more accurately. The position of F_{ss} for each of the tool force components for the experiment with a vertical pitch of 2 mm and a tool radius of 7.5 mm on MS/PP/MS and aluminium is shown in Fig. 54a and b respectively. Similar graphs were plotted for all nine experiments on both materials to allow all components of F_{ss} to be measured. F_{ss} of each tool force component is plotted against tool radius and vertical pitch for MS/PP/MS and aluminium in Fig. 55. On each graph the vertical axis has the same scale to allow a visual comparison of the magnitude of tool forces to be made easily.

The plots of F_{ss} versus tool radius and vertical pitch for each of the components of tool force in Fig. 55 follow similar trends for both the sandwich panel and monolithic sheet metal. In general, every component of tool force follows an increasing trend with tool radius and vertical pitch, although it is not possible to establish the exact relationship of this trend with only three data points for each variable. These trends will be discussed further and compared to previously published results in Section 5.3.3.

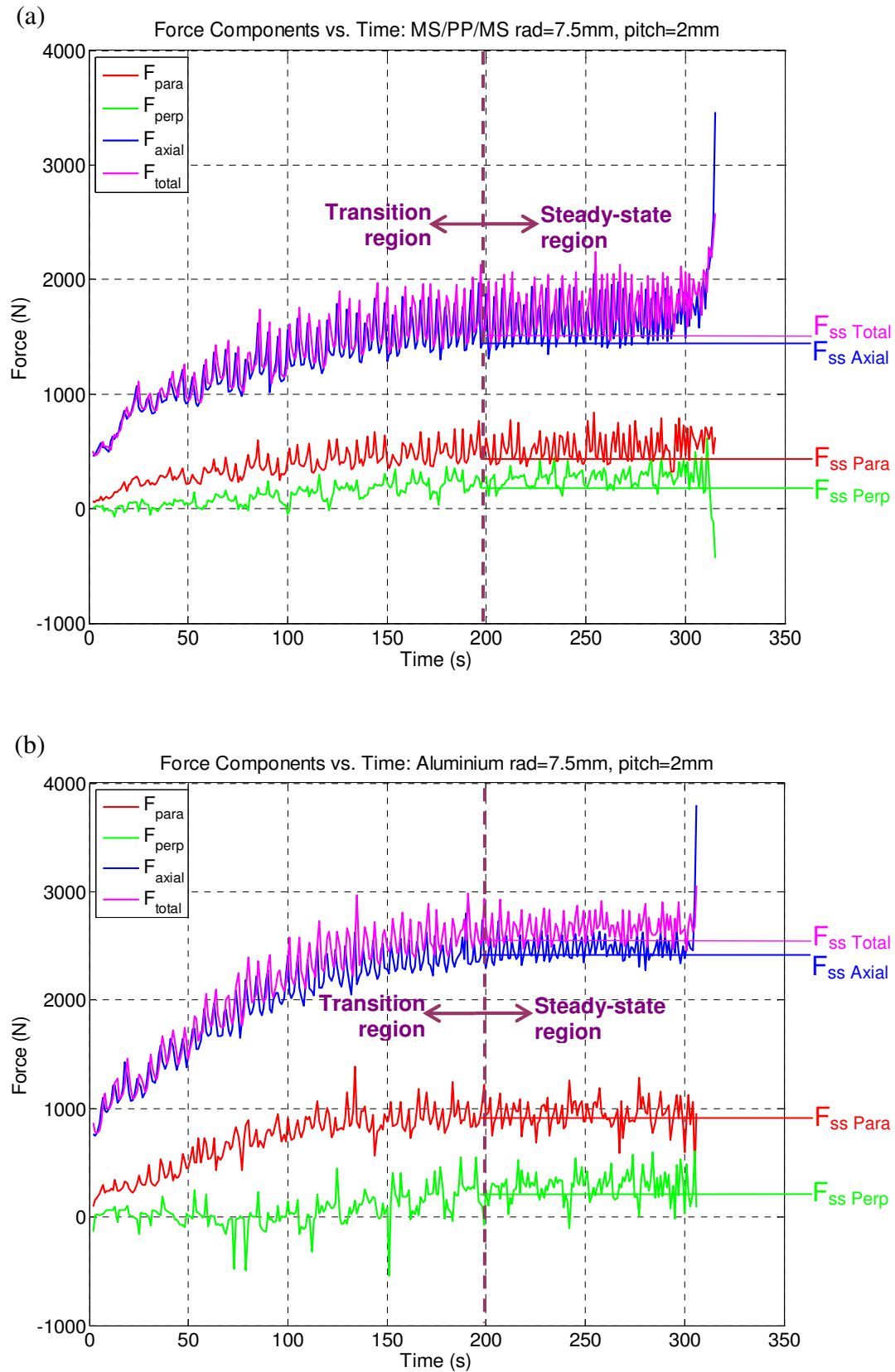


Fig. 54. Tool force components vs. time through forming pyramid with vertical pitch of 2 mm and tool radius of 7.5 mm showing steady-state forces: a) MS/PP/MS; b) aluminium.

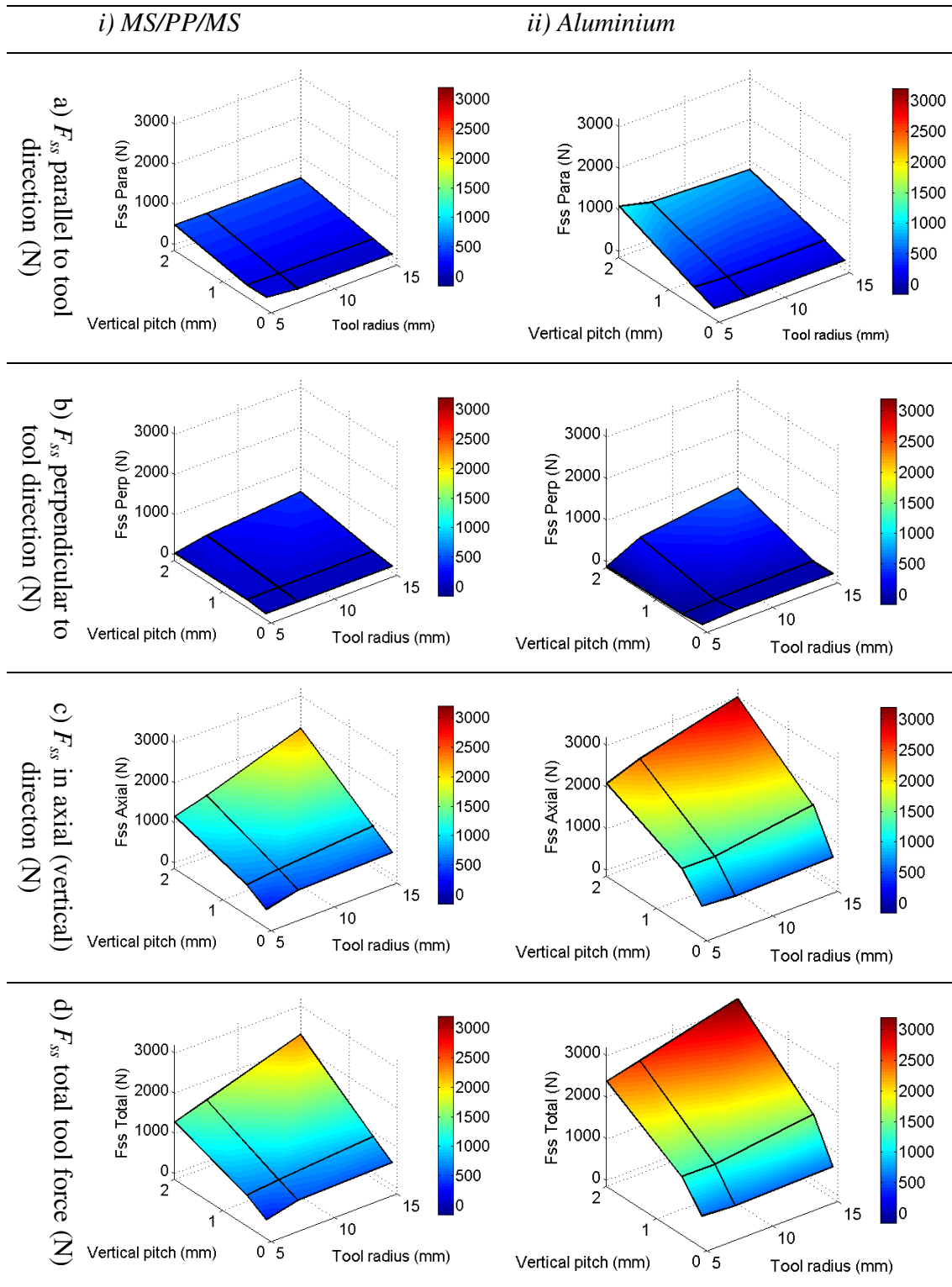


Fig. 55. Steady-state tool force components vs. tool radius and vertical pitch: (a) F_{ss} parallel to tool direction; (b) F_{ss} perpendicular to tool direction; (c) F_{ss} in vertical (axial) direction; and (d) F_{ss} total tool force vector.

5.2.3 Displacement of Upper and Lower Surfaces and Accuracy of the Sine Law

The displacements of the upper and lower surfaces of the monolithic sheet metal and the sandwich panel have been measured and compared to provide the first insights into the deformation mechanism of sandwich panels in ISF as well as to show whether the mechanics of the two materials are similar. The accuracy of the sine law for prediction of wall thickness has been evaluated and compared to the measurements of deformation to show whether it is applicable with similar accuracy to sandwich panels as for monolithic sheet metals. The method and results of this experiment are described below.

5.2.3.1 Method

Unlike the copper plate which was observed for SPIF and TPIF in Chapter 4, it was not possible to braze the MS/PP/MS sandwich panel due to the polymer core and an alternative joining technique was not found. It was therefore not possible to obtain measurements of the strains at different positions through the thickness. However, the relative movement of the upper and lower surfaces was measured to give a first insight into the deformation mechanics of MS/PP/MS and aluminium.

The displacement of the upper and lower surfaces of each material was measured by mechanically marking the surfaces at intervals of 5 mm along the centreline before deformation using a scribe. The positions of the scribe marks on the upper and lower surfaces were measured before and after deformation using a Mitutoyo co-ordinate measuring machine (CMM) with a pointed stylus. The points on the upper and lower surfaces were then translated using code written in Matlab so they were correctly spatially aligned with each other in order to interpret the relative movement of corresponding points on the upper and lower surfaces as a result of the deformation. This translation was achieved by aligning a set of reference points measured in the corners of each of the plates. Through-thickness lines adjoining corresponding points on the upper and lower surfaces were corrected for initial misalignment by subtracting the angle to the vertical before deformation from the angle after deformation.

The most significant source of error in the CMM measurements was reading error due to interpretation of the position of the stylus above the point to be measured. This error

was evaluated by repeatedly measuring the same point, which gave an absolute error in each of the x , y and z directions of approximately ± 0.15 mm. Because the reading error of the CMM with the solid stylus used in this experiment is up to 10 times that of the optical CMM used in Chapter 4, it has not been possible to calculate strains for the sandwich panel and monolithic sheet metal. The absolute error in strains would be approximately ± 0.06 for stretching and ± 0.15 for shear, and a rule-of-thumb calculation using the principles developed in Chapter 4 predicts that the *minimum* relative error will be approximately 14% for stretching strains and 43% for shear strains. Although the measurement technique used in this experiment is less accurate than the optical CMM used in Chapter 4, an advantage is that there is no error due to cracking because the plates have remained intact. The accuracy of the sine law for prediction of wall thickness has been evaluated using the equation developed in the Appendix.

The formed geometry on which deformation was measured for each material was a four-sided pyramid, similar to that of Fig. 51, with the only difference being that the pyramid was truncated to leave a plateau of width 20 mm at the top. The pyramids were truncated with the aim of observing how deformation is accumulated throughout the process. The vertical pitch was 0.5 mm, tool radius was 7.5 mm, tool speed was 40 mm/s and Castrol Spheerol L-EP2 grease was used for lubrication.

The accuracy of the sine law for prediction of wall thickness has been evaluated by comparing wall thickness predicted by the sine law (Equation 2.1) to the measured wall thickness, which was found with vernier callipers to an accuracy of ± 0.01 mm across each of the corresponding pairs of marked points. The measured wall angle rather than the wall angle of the tool path has been used in the sine law prediction of wall thickness to ensure that the accuracy of the results is not affected by any deviation between the profile of the product and the profile of the tool path.

5.2.3.2. Results and Observations

Fig. 56 and Fig. 57 show the deformation and wall thickness distributions for the sandwich panel and the monolithic sheet metal respectively. The deformation is shown for one half of the cross-sections, from the centre (left) to the outside edge (right), in three planes: (a) y - x ; (b) y - z ; and (c) x - z . The measured points have been joined by

straight lines along the top surface, bottom surface and through the thickness. The upper surface of the sheet which the tool contacted has been highlighted in red. Error bars due to reading error on the CMM are shown in the x -direction, whilst those in the y and z directions are not shown because they are negligible on the scales used for these axes. The clamped, unsupported, formed and unformed (central plateau) regions of the sheets are indicated. Wall thickness measured with vernier callipers before and after deformation is compared to the sine law prediction on Fig. 56d and Fig. 57d. Error bars are shown for the measured thickness due to the resolution of the vernier callipers as well as error bars for the sine law prediction of wall thickness.

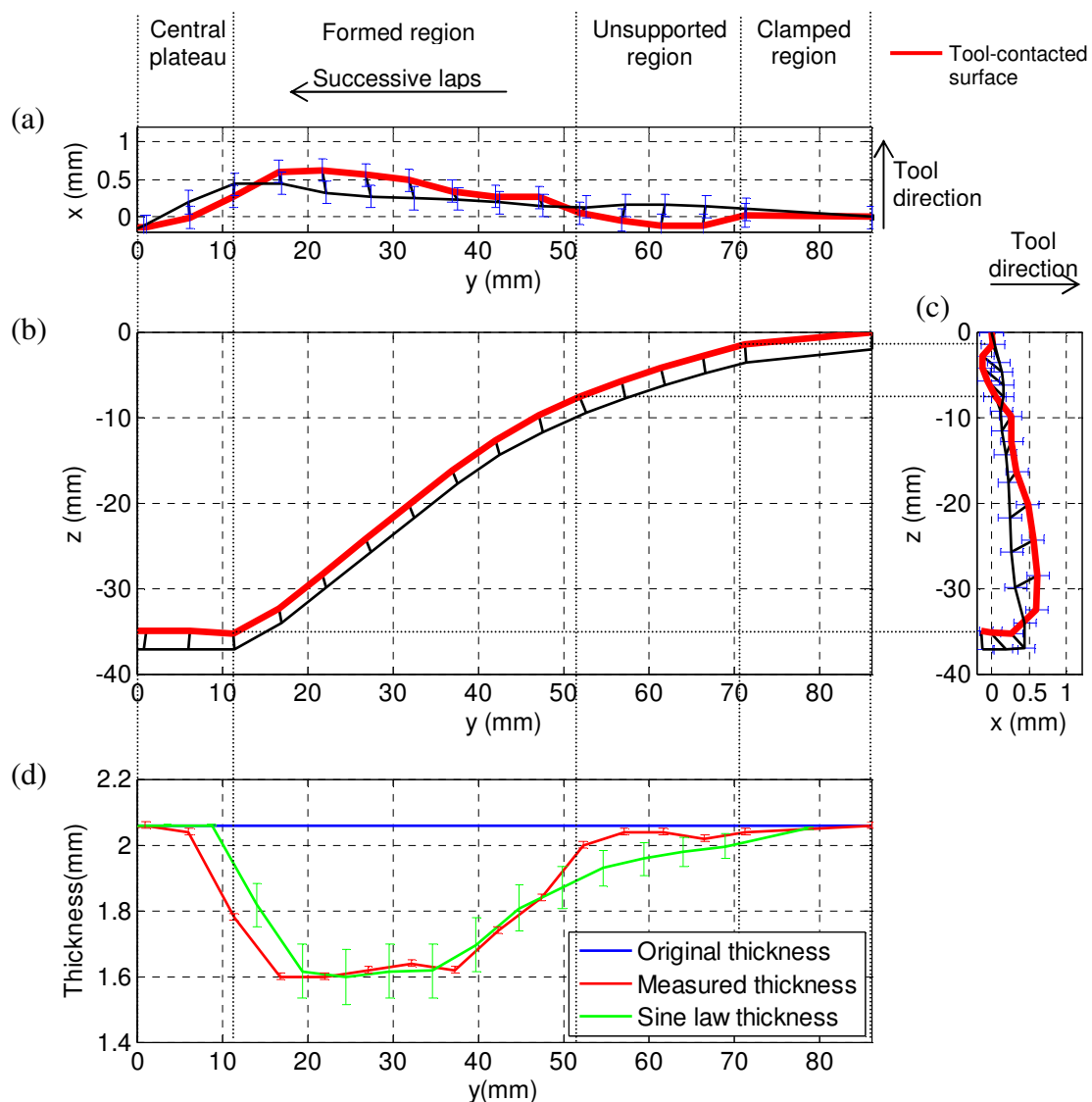


Fig. 56. Measurements of deformation and thickness of MS/PP/MS: (a) deformation in y - x plane; (b) deformation in y - z plane; (c) deformation in x - z plane; (d) comparison of original thickness, measured thickness and sine law thickness.

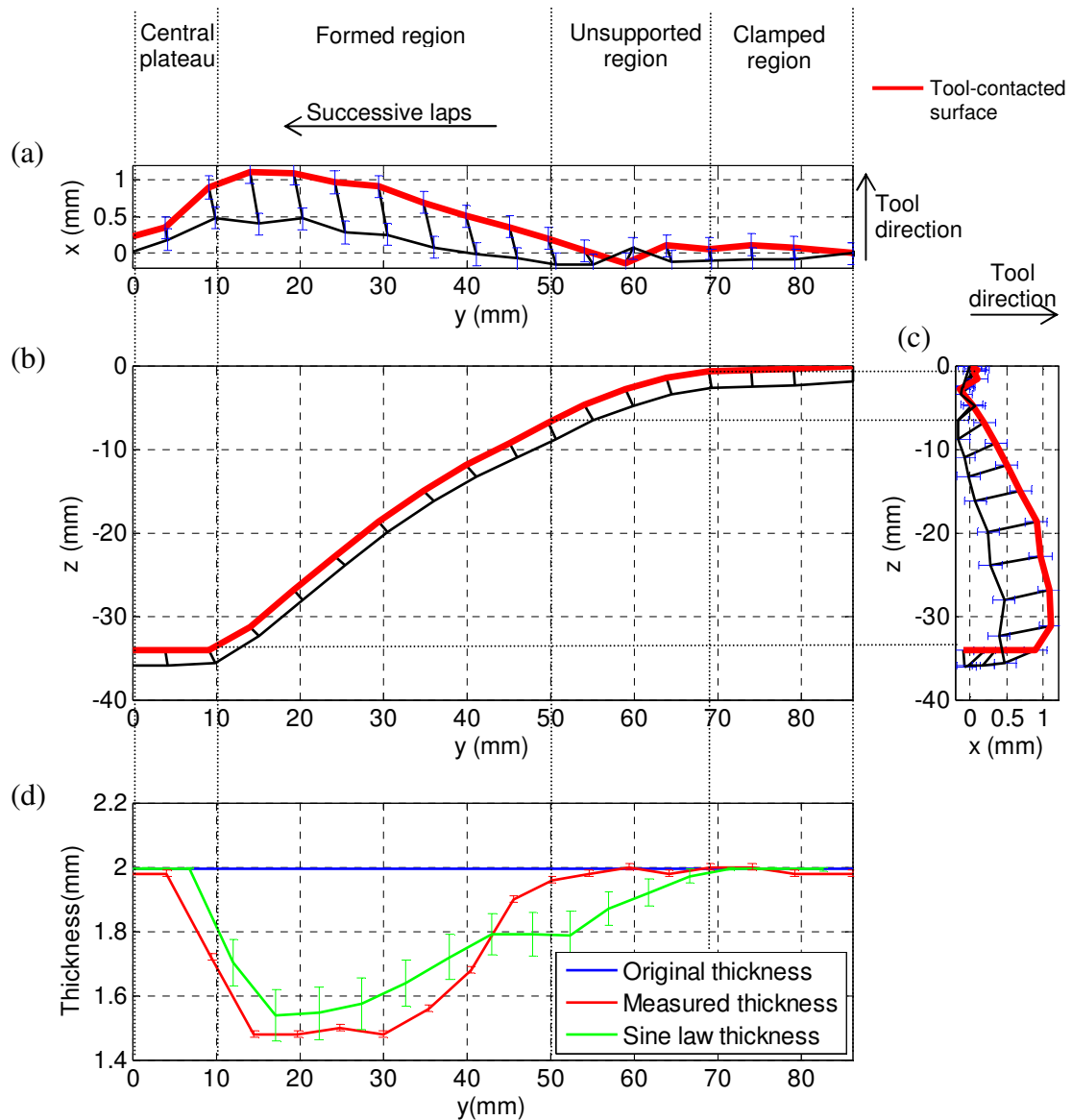


Fig. 57. Measurements of deformation and thickness of Aluminium: (a) deformation in y - x plane; (b) deformation in y - z plane; (c) deformation in x - z plane; (d) comparison of original thickness, measured thickness and sine law thickness.

Fig. 56 and Fig. 57 show that the deformation of MS/PP/MS and monolithic aluminium are similar in the x - y , z - y and z - x planes. For both materials the deformation mechanism is predominantly stretching in the y - z plane, with shear in the y - x plane. The sine law is shown to give a prediction of wall thickness which follows the measured wall thickness to within ± 0.2 mm across the cross-sections of both materials. The average errors are similar in both cases; ± 0.06 mm and ± 0.09 mm for the sandwich panel and monolithic sheet metal respectively. Hence the sine law is applicable to both materials to a similar accuracy. These observations will be discussed further in Section 5.3.

5.2.4 Summary of Findings

Vertical pitch and tool radius have a similar influence on the trends in tool force components in SPIF of a MS/PP/MS sandwich panel and a monolithic aluminium sheet metal. The movements of the upper and lower surfaces of both materials are similar and the accuracy of the sine law for predictions of wall thickness is comparable. Hence, ISF of suitable sandwich panels could be an easy step forwards applying knowledge and equipment used for ISF of sheet metals.

5.3 Discussion

The evaluation of the mechanical feasibility of ISF of sandwich panels and the comparison of the influence of ISF on a sandwich panel and monolithic sheet metal have raised four areas for further discussion. Firstly, it is discussed how the findings of Section 5.1 could be built on in future to evaluate the mechanical feasibility of ISF of sandwich panels under a wider range of process conditions. Secondly, trends in the deformation of MS/PP/MS and aluminium will be compared to previous results to evaluate to what extent the measured deformation represents typical ISF processes. Thirdly, the trends in tool forces measured throughout ISF of MS/PP/MS and aluminium will be discussed because this provides further insights into the deformation mechanics. Fourthly, the movement of the upper and lower surfaces and the accuracy of the sine law for prediction of wall thickness will be discussed in more detail and compared to previous results as well as the copper plate measured in Chapter 4.

5.3.1 Mapping of the Mechanical Feasibility of ISF of Sandwich Panels

The research in Section 5.1 demonstrated that ISF of two sandwich panels (MS/PP/MS and Al/PP/Al) is possible using two simple tool paths. The tool paths were chosen as a starting point because they demonstrate the least mechanically demanding deformation that constitutes ISF. If the materials fail under these paths they will fail under the more demanding spiral or contour tool paths that are more commonly used in ISF. However, the research leaves open questions concerning the limits of forming sandwich panels under a wider range of process conditions.

In order to determine whether the sandwich panels which were formed successfully in Section 5.1 could also be formed with more typical tool paths, samples of the materials were formed into four-sided pyramids of increasing wall angle until failure occurred. The tests showed that, for a vertical pitch of 0.5 mm with a tool radius of 7.5 mm, the maximum wall angles were approximately 50° and 40° for MS/PP/MS and Al/PP/Al respectively. The limiting failure mechanism in each case was faceplate fracture, as shown in Fig. 58b. This indicates that the range of geometries that can be formed in these materials is only slightly more limited than that of sheet metals, for which the limiting wall angle reported by Jeswiet et al [10] for various process conditions was between 40° (brass of initial thickness 1 mm) and 78° (AA3003-O initial thickness 2.1 mm). However, it cannot be assumed that these are the limiting wall angles and failure mode under all process conditions of ISF; different conditions may cause other failure mechanisms to dominate whilst reaching different values of limiting wall angles.

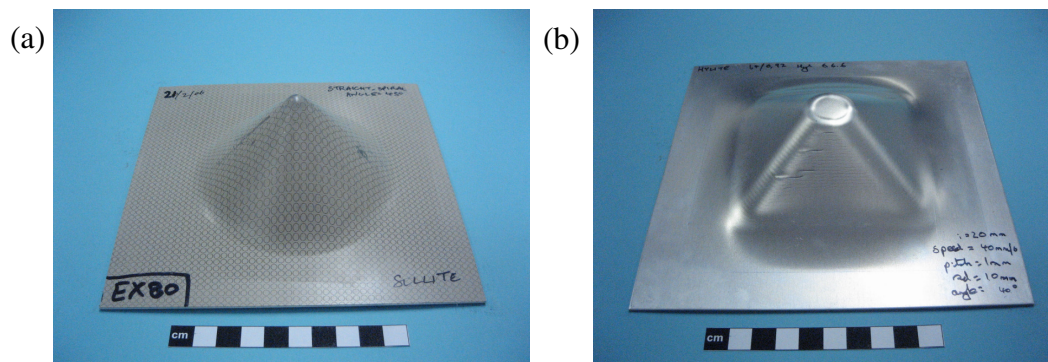


Fig. 58. Sandwich panels formed to non-zero wall angles: (a) MS/PP/MS (45° angle without failure) and (b) Al/PP/Al (40° angle showing faceplate fracture).

It is suggested that failure mode maps may be a useful way of representing the forming limits and failure modes of sandwich panels under various forming conditions in future. Failure mode maps have been used extensively to characterise behaviour of sandwich panels in previous research, some examples of which were reviewed in Section 2.5. The concept of a failure mode map is presented for an imaginary soft-core sandwich panel under the influence of two parameters (wall angle and tool radius) in Fig. 59.

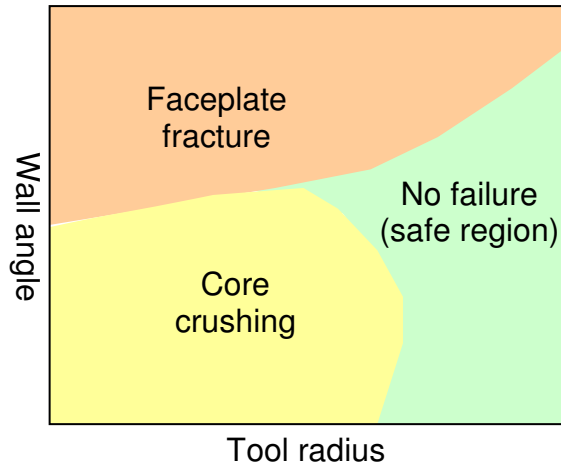


Fig. 59. Concept for a failure mode map which could be used in future for representing the safe forming conditions and failure modes for a sandwich panel in ISF. The horizontal and vertical axes show two process parameters (in this case wall angle and tool radius) whilst the shaded regions show the failure modes or successful condition.

5.3.2 Trends in Deformation of MS/PP/MS and Aluminium

The measurements of deformation in the z - y plane of MS/PP/MS and aluminium shown in Fig. 56b and Fig. 57b respectively are largely consistent with previous predictions of FE models and experimental measurements for sheet metals. This suggests that the deformation of MS/PP/MS and aluminium may be a good representation of typical ISF experiments. For both materials, lines adjoining the upper and lower surfaces remain approximately perpendicular to the sheet surface across most of the cross-section and there is negligible translation of the surfaces in the y -direction. This shows that stretching is the dominant mechanism in this plane, whilst shear and bending are less significant. This is consistent with the previous experimental measurements of relative movement of the upper and lower surfaces of an aluminium sheet formed by SPIF by Allwood et al [88], as well as the simplified FE model developed by Sawada et al [89] and FE through-thickness strain predictions in this plane by Bambach et al [61]. Stretching in this plane was similarly observed for the copper plate in Chapter 4 (Fig. 35d page 93). However, shear towards the centre was also measured in this plane for the copper plate (Fig. 35e). From the measurements of deformation shown in Fig. 56b and Fig. 57b, aluminium appears to have negligible shear in the y - z plane, whilst MS/PP/MS appears to have strain that occurs in the opposite sense to that in the copper plate, i.e. the tool-contacted surface is sheared towards the outside of the plate. This

resembles more closely the idealised mechanism of shear spinning shown in Fig. 11, page 34. These differences between the deformation mechanisms of the copper plate and the sandwich panel or aluminium may be a result of the different thickness, mechanical properties, wall angle or curvature of the formed geometries. However, it is not possible to verify the differences without more accurate measurements of through-thickness strains of the aluminium sheet and MS/PP/MS sandwich panel.

For both the MS/PP/MS and aluminium, the measurements in the x - y and z - x planes show that there is translation of both upper and lower surfaces in the direction of tool movement. Greater translation of the upper surface results in shear between the two surfaces. This may be attributed to friction of the tool moving across the upper surface, and is consistent with the analysis of through-thickness shear in SPIF and paddle-forming reported by Allwood et al [88], as well as shear measured for the copper plate in Fig. 35f. The monolithic aluminium shows greater through-thickness shear than the MS/PP/MS sandwich panel. If shear in the tool direction is a result of friction between the tool and workpiece, the lower shear for the sandwich panel is likely to be a result of two factors. Firstly, the coating on the MS/PP/MS sandwich panel is likely to reduce the coefficient of friction between the tool and workpiece. Secondly, vertical tool force is lower and hence further reduces friction (Fig. 55c). This is likely to be because the tensile strength of the sandwich panel is lower than the sheet metal. The observation of shear in the tool direction for all three of the materials tested (copper plate, MS/PP/MS and aluminium) suggests that this is likely to be a generic characteristic of ISF. This is a key distinction from the deformation mechanics of pressing.

5.3.3 Trends in Tool Forces of MS/PP/MS and Aluminium

Four trends were observed in the components of tool force throughout SPIF of MS/PP/MS and aluminium in Fig. 53 and Fig. 55 (page 140 and page 143): (1) each tool force component increases towards a steady-state value on successive laps; (2) the tool force components peak in the corners of the pyramids; (3) tool forces for MS/PP/MS are approximately 60% that of the aluminium sheet; and (4) tool force increases with vertical pitch and tool radius. These observations are discussed below.

The trend that tool force increases towards a steady-state value was similarly observed for the copper plates formed by both SPIF and TPIF in Chapter 4 (Fig. 41, page 103). However, in contrast to the results of Chapter 4, a steady-state tool force was actually reached in these experiments on the MS/PP/MS sandwich panel and aluminium, whereas a steady-state was not reached for the copper plate. The trends measured in the present experiments therefore have more similarity to trends previously measured by Duflou et al [93] and Jeswiet et al [56], which similarly levelled-off to a steady-state value. These measurements were performed on 1.2 mm AA3003-O sheets. Hence the deformation of the aluminium sheet and MS/PP/MS sandwich panel may be more representative of typical ISF processes than the copper plate investigated in Chapter 4.

In Section 4.3.5 it was suggested that the tool force increases as strains increase, and hence that a steady-state in tool force is reached when strains across the material on successive laps become constant. It is therefore likely that constant strains were attained in these experiments on the MS/PP/MS sandwich panel and the monolithic aluminium sheet after an initial transition period. For the experiments with a tool radius of 7.5 mm and vertical pitch of 2 mm shown in Fig. 53 (page 140), this is at approximately 25 mm from the perimeter. However, it is not possible to verify whether constant strains were achieved from the deformation measurements in Fig. 56 and Fig. 57 without more accurate measurement of the through-thickness deformation.

The measurements of deformation of the MS/PP/MS sandwich panel and the aluminium sheet (Fig. 56 and Fig. 57 respectively) show an interesting feature which is not evident for the copper plate formed by SPIF in Chapter 4 (Fig. 35) and correlates to the levelling-off of tool force in Fig. 53. This is that the wall angle of the formed region increases progressively over the first 20-25 mm of the formed region (from $y=50$ mm to approximately $y=30$ mm). This observation supports the idea proposed in Section 4.3.5 that the deformation may evolve from a widely distributed to a highly localised deformation over the first few laps of the tool path. Localisation of the deformation would correspond to the wall angle of the formed region increasing until it equals the wall angle of the tool path. A practical application of this observation is that measurement of tool forces may be used to indicate progression to higher geometric accuracy. A possible future area of research is therefore to investigate whether geometric accuracy does indeed improve as further laps are completed. If this is the

case, additional laps could be added to the perimeter of a product to accommodate this transition region. This material could later be removed to leave a product of higher geometric accuracy.

The second trend, that tool force increases towards the corners of the sheet, was previously observed for SPIF of sheet metal by Iseki [39]. It is possible that the peak in tool force results from the deformation becoming localised in the corners because it is constrained by the surrounding geometry of the sheet, and hence more plastic work is done as the indenter moves forwards. It was observed in the experiments that the flat sides of pyramids tend to curve inwards in the x - y plane, whilst the corners retain their position. This suggests that the corners may constrain elastic springback. Hence, it may be possible that in future corners or ridges could be used to improve the geometric accuracy of products of ISF by increasing in stiffness to react against springback.

The third observed trend in tool force, that the steady-state magnitudes of tool force components for SPIF of MS/PP/MS are approximately 60% that of the aluminium sheet, may be attributed to three factors. Firstly, the tensile strength of MS/PP/MS is lower than aluminium which will cause less work in stretching. The UTS of MS/PP/MS is 117 MPa whilst that of aluminium is 187 MPa. Secondly, it is likely that the shear strength of MS/PP/MS is lower than that of the aluminium sheet due to the compliant polypropylene core, which will reduce work done in shear. Thirdly, the coefficient of friction between the tool and the workpiece is likely to be lower for MS/PP/MS than aluminium due to the protective coating which was shown in the earlier experiments of Section 5.1 to remain intact. However, without further analysis of the contact area, the material properties and the friction characteristics of the sheet-indenter interface it is not possible to uncouple the contribution of elastic and plastic work and friction to each of the tool force components. The effects of the distribution of material strengths around the neutral axis in MS/PP/MS combined with the deformation mechanics of ISF are highly advantageous. It is possible to form the sandwich panel which has higher elastic bending stiffness and equivalent plastic bending moment to the monolithic sheet metal using lower tool forces, whilst producing a product that has a higher stiffness to weight ratio than the monolithic sheet. The lower tool force is advantageous because it will reduce tool wear and allow a lighter machine design for equivalent precision.

The fourth observation, that the components of tool force increase as tool radius and vertical pitch increase, can be attributed to an increasing rate of work in each case. In the first case, the contact area of the tool has increased, and in the latter case the degree of stretching under the tool has increased. Trends in steady-state tool force components resulting from tool radius and vertical pitch cannot be accurately ascertained from the present experiments because only three data points were measured. However, the trends are similar to previously reported results for sheet metals in two respects. Firstly, Fig. 55c shows that F_{ss} for vertical force increases with tool radius and vertical pitch for both materials. A statistical data analysis by Bologna et al [55] similarly showed that vertical tool force increases linearly with both tool radius and vertical pitch for sheet metals formed by SPIF. Secondly, Fig. 55 shows that F_{ss} for total tool force component increases with increasing vertical pitch and tool radius. Duflou et al [13] similarly found that the steady-state value of total tool force increases linearly with both vertical pitch and tool radius. A later study by Duflou et al [93] using a statistical data analysis found that steady-state vertical tool force follows a quadratic relation to tool radius whilst the relation to vertical pitch is linear and coupled with sheet thickness. However, the findings of Chapter 4 have shown that a steady-state tool force is not necessarily achieved during ISF, even for a product of a constant wall angle, and that tool force can vary throughout the process as the deformation mechanics evolve. Duflou et al [93] previously highlighted the limitations of steady-state force predictions for geometries with increasing wall angles because steady-state conditions may not be achieved. It is therefore likely that any trends ascertained by a statistical data analysis for the influence of process parameters on tool force may not be widely applicable to any geometry formed in a given product. In this respect, a full 3D numerical simulation may be more appropriate for prediction of tool force than a statistical analysis.

5.3.4 The Accuracy of the Sine Law Prediction of Thickness

Within the bounds of experimental error, the sine law prediction of wall thickness is lower than the measured wall thickness at the outside of the plate and higher than the measured thickness at the inside of the plate for both the sandwich panel and the monolithic sheet metal (Fig. 56d and Fig. 57d respectively). For both materials, this comparison of sine law wall thickness to measured wall thickness is similar to that of the copper plate in Chapter 4 as well as the previous results of Young and Jeswiet [79]

and Ambrogio et al [58]. This further supports the idea that the measured deformation is likely to be a good representation of typical ISF processes. The measurements of the copper plate formed by SPIF on Fig. 35 (page 93) showed that the measured thickness was lower than the sine law thickness at the inside of the formed region as a result of material being pushed towards the centre of the plate. This occurred due to increasing shear and stretching normal to the tool direction. The same figure showed that the measured thickness is initially higher than the sine law thickness at the start of the formed region because here the strains in the material are low and hence the thickness is close to the original thickness. It is likely that similar trends in strains occurred in the present experiments.

Within the formed region, the sine law prediction is approximately equal to the measured thickness for the sandwich panel but is greater than the measured thickness for the monolithic aluminium sheet. This may be a result of reduced shear normal to the tool direction for the sandwich panel, and hence radial displacement of material is reduced. This may be because of reduced friction due to lower forces due to the reduced tensile strength of the material as well as the smooth surface coating. If the effect of reducing friction by surface coating or using a material of lower tensile strength is to reduce through-thickness shear normal to the tool direction, it is possible that this could be controlled to improve uniformity of wall thickness across the formed region. However, this could have the negative effect of reducing forming limits due to through-thickness shear according to the model proposed by Allwood et al [95].

5.4 Concluding Remarks

The findings of Chapter 5, ‘The Mechanics of Incremental Forming of Sandwich Panels’, can be concluded as follows:

- It is not sufficient to consider fracture of the surfaces of sandwich panels to indicate failure; other failure modes such as core crushing and delamination that are internal to the panel should be considered.
- ISF can be used to deform MS/PP/MS and Al/PP/Al sandwich panels. This is because these panels have ductile and largely incompressible cores and faceplates which survive the local indentation in ISF without collapse or fracture.

- A MS/PP/MS sandwich panel and a monolithic aluminium sheet are formed with similar trends in tool forces in ISF, whilst the movements of the upper and lower surfaces and the accuracy of the sine law prediction of wall thickness are similar in both cases. Hence ISF of some sandwich panels may be an easy step forwards applying existing knowledge of ISF of monolithic sheet metals.
- The deformation mechanisms of a MS/PP/MS sandwich panel and a monolithic aluminium sheet formed by SPIF are predominantly stretching perpendicular to the tool direction with through-thickness shear parallel to the tool direction.

6. Summary and Outlook

6.1 Summary

This thesis has provided new insights into the mechanics of ISF of sheet metals and sandwich panels. The findings are summarised below.

For a copper plate of thickness 3.1-3.3 mm formed by SPIF and TPIF to a wall angle of 30°:

- The deformation mechanisms of both SPIF and TPIF are shear parallel to the tool direction with both stretching and shear perpendicular to tool direction.
- All components of strain generally increase on successive laps. This is likely to be a result of localisation of the actively deforming area throughout the process.
- Increasing stretching and shear perpendicular to the tool direction account for differences between the sine law and measured wall thickness for SPIF and TPIF.
- Shear, both parallel and perpendicular to the tool direction, is the main distinction between the deformation mechanisms of SPIF or TPIF and pressing.
- Tool forces correlate to shear parallel to the tool direction, suggesting that the shear is primarily a result of friction between the tool and the workpiece.

The new insights into the mechanics of ISF of sandwich panels can be summarised as follows:

- ISF can be used to deform MS/PP/MS and Al/PP/Al sandwich panels. This is because the cores and faceplates are ductile and largely incompressible and therefore survive the local indentation applied in ISF without collapse or fracture.
- The main mechanical results established for ISF of sheet metals transfer closely to sandwich panels. Tool force components show similar variations with vertical pitch and tool radius, the sine law describes sheet thinning with wall angle, and the through-thickness strains experienced by both materials are similar. Hence established knowledge and process implementation procedures derived for ISF of monolithic sheet metals may be used in future to apply ISF to sandwich panels.

6.2 Outlook

Despite extensive research over the last decade and strong potential economic, mechanical and ecological benefits, ISF is still not widely applied in industry. The outlook for future research into ISF should be focussed on developing the process in the most advantageous ways to make it suitable for wide industrial application. The main shortcomings of the process or gaps in the present knowledge were highlighted in the review in Chapter 2, Section 2.6, and this thesis addresses two of these shortcomings by researching the deformation mechanics of sheet metals and sandwich panels. To build on the research that has been presented in this thesis, some directions for future research are suggested below.

6.2.1 *Further Research for the Mechanics of ISF*

Three suggestions for future work can be raised from the observations of deformation mechanics and tool forces in SPIF and TPIF which were presented in Chapter 4. Although the measurements of the copper plates were insightful as the first experimental measurements of deformation in ISF, the results are known to apply only to the material, thickness, geometry and process conditions that were used in these experiments. The results should not be assumed to be applicable to other ISF processes without further research. The first suggestion for future work is therefore to investigate the deformation mechanics under a wider range of process variables such as tool diameter, tool speed, lubrication, vertical pitch, wall angle, sheet material and sheet thickness. The main reason why a plate that is thicker than those typically used in ISF was used for this experiment was to allow space for a longitudinal gridline to be machined along the cross-section. An alternative method for marking finer longitudinal gridlines in future experiments on thinner plates is to use laser etching. Copper was chosen as the sheet material because it is a suitable material for brazing. However, it is also possible to braze alternative materials including aluminium and titanium using appropriate fillers. Improvement of the brazing process by reduction of porosity may be possible by heating in a vacuum furnace to avoid oxidation. This may reduce the error in deformation measurements due to cracking. Further reduction of the experimental error could be achieved in future experiments by repeating the experiments several times and averaging the strains on each plate at each radial position, or by averaging the

strains on both halves of the cross-section. Hence, there are several possibilities for improving the experimental technique developed in Chapter 4 to enable a wider range of materials and sheet thickness more typical of those used in ISF to be researched to a greater accuracy.

The second suggestion for future research is to carry out an investigation of the evolution of deformation during the process, and hence to determine why the tool forces and strains follow an increasing trend. It was suggested in Section 4.3.5 that the increasing trend in strains and tool forces measured in the copper plates may be a result of the progressive localisation of the deformation as the sheet becomes more rigid as it is formed, and that a similar transition may have occurred over a shorter distance in previously published studies of wall thickness variation and tool forces. Verification of the reason for increasing forces and strains has two potential practical applications: (1) localisation of the deformation could correspond to increasing geometric accuracy, and hence it is possible that measurement of tool forces could give some indication of the geometric accuracy of a product as it is formed; and (2) increasing tool forces could be correlated to thinning in the sheet, and therefore may be used to indicate and avoid rupture during forming. Hence, it is suggested that the evolution of deformation during the process should be measured for a range of materials, sheet thickness, wall angles, vertical pitches, geometries, etc. This could be done by measuring the geometry of the sheet using a stereovision camera throughout the process.

Thirdly, a suggestion for future work on the deformation mechanics is an experimental investigation of the influence of through-thickness shear on forming limits. Allwood et al [88] have recently proposed a model based on a modified Marciniak-Kuczyński analysis incorporating shear which predicted that through-thickness shear can increase the forming limits in comparison to pure stretching. This could account for the increased forming limits of ISF in comparison to pressing. Future experiments could verify this theoretically predicted trend, as well as show which process design factors (such as tool radius, vertical pitch, lubrication, etc.) may be effective for increasing the through-thickness shear in ISF by increasing friction, and therefore increasing the forming limits. Hence, in future it is possible that the degree of shear in ISF could be influenced through careful process design in order to achieve the forming limits required by the product design.

6.2.2 Alternative Techniques for ISF of Metal Foam Sandwich Panels

Although it was shown in Chapter 5 that it is not possible to use ISF to form an Al/Al foam/Al sandwich panel into a 3D shell directly without crushing of the core, an alternative approach that is successful is to form a compact precursor sandwich sheet prior to subsequent expansion to create a foamed sandwich shell. A precursor material (manufactured by Alulight International) consists of a core of aluminium and TiH_2 powder roll bonded between two aluminium faceplates, as described in detail by Banhart [119]. The material can be formed in this compacted state, and later heated causing the core to inflate whilst the formed faceplates retain their shape. A trial has demonstrated that this material can be formed by ISF to a square based pyramid with a wall angle of 40° and then heated to allow foaming (Fig. 60). Although the figure shows distortion of the upper and lower faceplates, this is a result of heating and not the forming process because the foaming temperature was high in comparison to the melting temperature of the sheet.

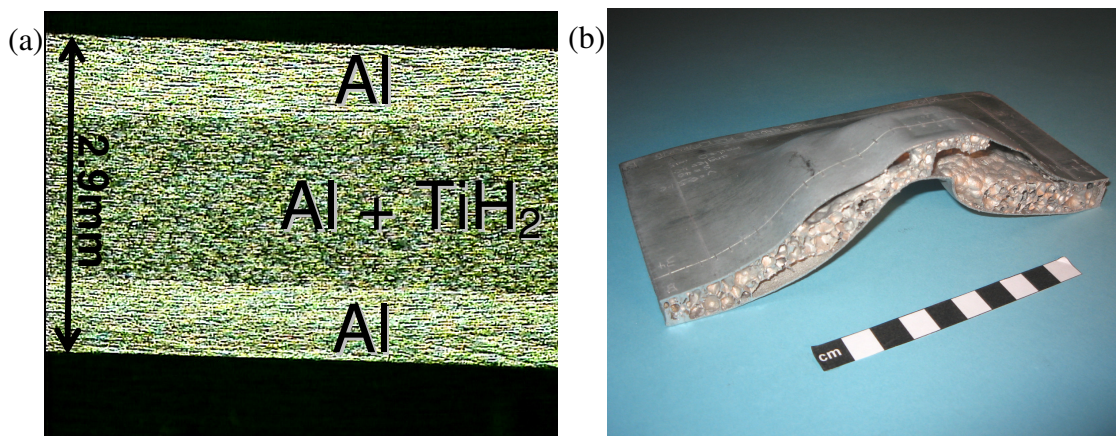


Fig. 60. ISF of an inflatable Al/Al foam/Al sandwich panel: (a) cross-section of precursor material before ISF and (b) an inflated 3D sandwich shell from a precursor formed by ISF.

ISF could be used in future to form impressions in one surface of metal/metal foam/metal sandwich panels whilst the other surface remains flat, as shown in Fig. 61. This is possible because the core is highly compressible and therefore collapses in a localised area under the indenter whilst the overall sandwich structure is sufficiently stiff to resist bending, even when only supported around the edges. Possible applications include channels in heat exchangers and features on insulating panels.

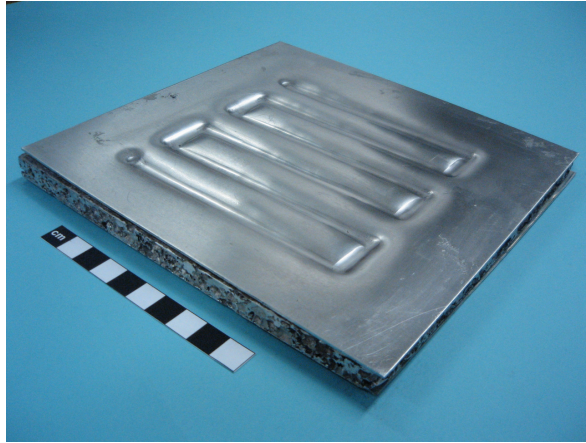


Fig. 61. Impressions formed by ISF in upper surface of an Al/Al foam/Al sandwich panel

6.2.3 Real-Time Process Control

Two of the main difficulties of implementing ISF are poor geometric accuracy resulting from non-localised deformation occurring outside the tool contact area that is difficult to predict, and rupture of the sheet as a result of excessive thinning. Furthermore, surface waviness as a result of the indenter passing over the surface has been identified as a disadvantage in comparison to pressing. It is recommended that in the future real-time process control of ISF could be developed to address these difficulties.

Currently, techniques for improving geometric accuracy are often based on applying a correction algorithm to a first guess of the tool path using predictions of the geometric error before forming. Although advances have been made in reducing the completion time of numerical models, this approach is still not satisfactory. Inaccuracies will inevitably result from any model due to approximation of the real mechanics, and simulations are inherently time consuming due to a long tool path and a high number of elements. Furthermore, variables such as vertical pitch, tool rotation speed and tool radius are rarely optimised in process design to improve the product quality but are instead selected based on user experience or the limitations of the available equipment. Real-time process control is proposed as an alternative to pre-process design to achieve a high product quality because it avoids these difficulties.

The method of real-time process control can be considered as automation of what would be the job of a skilled craftsman in traditional metal forming processes, who uses

feedback from all his senses to modify a tool path in real-time to produce the required product. Craft-based processes are successful because the craftsman learns how to control the process over time based on experience as well as taught knowledge, and because he can apply his knowledge to any product. This is particularly successful for customised production where the skill of a craftsman is more effective in producing a one-off than lengthy computer simulations. Hence real-time process control could be particularly suitable for ISF. It is proposed that a successful automated real-time process control system in ISF should implement computer-based learning as it forms in addition to programmed control algorithms to simulate the learning process that is undertaken in a craft-based process. Feedback could be based on computer vision of the sheet's geometry and surface texture (which could indicate necking), as well as tool forces and possibly sound. It has already been suggested above that trends in tool forces may be used to indicate a progression from a widely distributed to highly localised deformation, and hence improvement in geometric accuracy. In addition, tool forces could be used to indicate strains and hence thinning.

Development of a fully automated control system is likely to be a challenging area of research requiring knowledge from many disciplines. This is because, despite extensive automation of spinning over the last 50 years due to CNC technology [127], spinning still requires user input; usually a skilled programmer will program a first guess of the tool path, and this will be corrected in trial runs before the tool path is used to manufacture a batch. However, the benefits of a real-time process control system for ISF could be significant, enabling customised one-offs to be produced on a localised scale without skilled operator intervention.

6.2.4 Future Machine Designs

Finally, the innovation of machine designs is suggested as an important area for future research to optimise the range of geometries which it is possible to make. The ideal configuration of tooling and equipment for ISF is one which allows the widest possible range of geometries to be formed to the highest possible quality. Factors that should be considered include the size of workpiece that is possible to form, the orientation of the workpiece, whether the workpiece is moved instead of the indenter, the axes and range of movement of the indenter, the strength and stiffness of the indenter support, the

number of indenters and the design of the workpiece clamping. For example, it is more energy efficient to move the workpiece instead of the indenter if the workpiece is small, although this requires more space than keeping the workpiece stationary and moving the indenter. Mounting the workpiece vertically requires less floor space if the blank is a flat sheet, but if the product is a three-dimensional volume of equal dimensions then this has no advantage. Indenters on ISF machines are often restricted to movement on three axes without rotation, and therefore the range of feasible geometries can be immediately expanded by increasing the range of movement of the indenters, e.g. by using a mobile robot arm. Workpiece support is often restricted to two-dimensional clamping frames, hence wastage around the perimeter of the formed shape could be reduced and the range of feasible shapes of starting blanks could be expanded by using a flexible 3D clamp. The capabilities of the machine could be further expanded by allowing interchangeable tooling to perform finishing operations such as laser cutting, polishing or painting. Furthermore, small and lightweight machines are particularly suitable to localised production, and hence there may be a future for ISF in the localised production of customised products, avoiding the long transportation distances and overcoming the monotony of designs in mass production. It is possible that the combination of a small, lightweight and versatile machine with a sophisticated real-time process control system would be sufficient for ISF to become a widely used sheet metal forming process used in industry.

Appendix – Calculation of Experimental Errors

The absolute errors of the strains and the sine law prediction of wall thickness calculated in Section 4.1 are derived in this section. As described in Section 4.1.6, the absolute error ΔX of a function $X(x_1, x_2, \dots, x_i)$ can be derived from the magnitudes of the partial derivatives multiplied by the absolute errors of the variables, $\Delta x_1, \Delta x_2, \dots, \Delta x_i$, according to Equation 4.4 (Kirkup [122]). This equation is re-written below.

$$\text{For } X = X(x_1, x_2, \dots, x_i), \quad \Delta X = \left| \frac{\partial X}{\partial x_1} \right| \Delta x_1 + \left| \frac{\partial X}{\partial x_2} \right| \Delta x_2 + \dots + \left| \frac{\partial X}{\partial x_i} \right| \Delta x_i \quad (4.4)$$

Similarly, where an average value of a function \bar{X} is calculated from functions X_1, X_2, \dots, X_n , then the absolute error $\Delta \bar{X}$ can be found from the average of the absolute errors of the functions $\Delta X_1, \Delta X_2, \dots, \Delta X_n$ according to (7.1).

$$\text{For } \bar{X} = \frac{X_1 + X_2 + \dots + X_n}{n}, \quad \Delta \bar{X} = \left| \frac{\partial \bar{X}}{\partial X_1} \right| \Delta X_1 + \left| \frac{\partial \bar{X}}{\partial X_2} \right| \Delta X_2 + \dots + \left| \frac{\partial \bar{X}}{\partial X_n} \right| \Delta X_n$$

$$\therefore \Delta \bar{X} = \frac{\Delta X_1 + \Delta X_2 + \dots + \Delta X_n}{n} \quad (7.1)$$

Strains ε_{11} , γ_{13} and γ_{23} and the sine law prediction of wall thickness t_l have been calculated from the positions of the corner points of each section of the grid that was machined onto the cross-sections of the copper plates according to Equations 4.1, 4.2, 4.3 and 2.1 respectively. The geometry of a deformed section of the grid, showing the directions of the local and global co-ordinate sets, the absolute errors of each of the corner points in the r , θ and z directions, and angles θ_{13} and θ_{23} , is shown in Fig. 62. The corner points of the grid section are labelled a, b, c and d. The absolute errors of the corner points are labelled Err_r , Err_z and Err_θ , as defined in Table 5, page 90. The wall angle, α , is defined as the angle between the vector **ab** and the vertical z in the r - z plane. Angle ω_{13} is defined as the angle between vectors **ab** and **ac** in the r - z plane. Each of the equations for strain and wall thickness can therefore be defined in terms of the positions of the corner points of the grid sections by variables $r_a, r_b, r_c, r_d, z_a, z_b, z_c, z_d, \theta_a, \theta_b, \theta_c$ and θ_d . The absolute error of each equation can then be found by partial differentiation with respect to each of these variables according to (4.4).

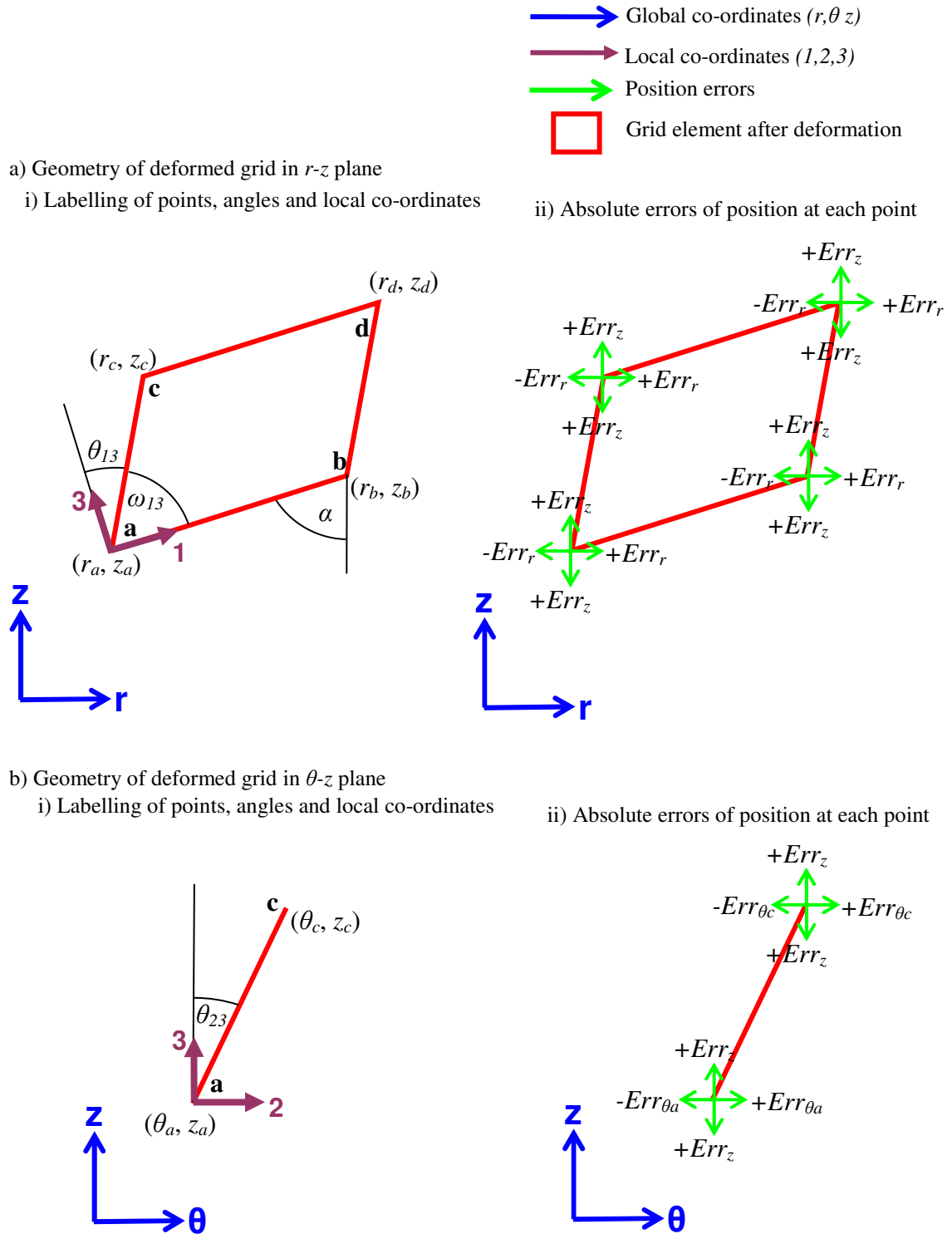


Fig. 62. Geometry of a section of the deformed grid on the cross-section of a copper plate used in Section 4.1 showing absolute errors of each of the corner points: a) geometry in the r - z plane; b) geometry in the θ - z plane.

A.1 Derivation of Absolute Error in Strain ε_{11}

The absolute error in strain ε_{11} , $Err_{\varepsilon_{11}}$, is derived below.

Strain ε_{11} was defined in (4.1) as

$$\varepsilon_{11} = \frac{l_1 - l_0}{l_0}, \quad (4.1)$$

where l_0 is the original longitudinal length of an element and l_1 is the length after deformation. It is assumed that l_0 is a constant equal to 1.5 mm. According to Fig. 62, l_1 can be defined in terms of the positions of the corner points in r - z co-ordinates according to (7.2) below.

$$l_1 = \sqrt{(r_b - r_a)^2 + (z_b - z_a)^2} \quad (7.2)$$

Applying (4.4), the absolute error in ε_{11} is given by (7.3):

$$Err_{\varepsilon_{11}} = \left| \frac{\partial \varepsilon_{11}}{\partial r_a} \right| \Delta r_a + \left| \frac{\partial \varepsilon_{11}}{\partial r_b} \right| \Delta r_b + \left| \frac{\partial \varepsilon_{11}}{\partial z_a} \right| \Delta z_a + \left| \frac{\partial \varepsilon_{11}}{\partial z_b} \right| \Delta z_b \quad (7.3)$$

Completing the partial differentiation gives:

$$Err_{\varepsilon_{11}} = \frac{1}{l_0} \left\{ \frac{|r_b - r_a|(\Delta r_b + \Delta r_a) + |z_b - z_a|(\Delta z_b + \Delta z_a)}{\sqrt{(r_b - r_a)^2 + (z_b - z_a)^2}} \right\} \quad (7.4)$$

Where $\Delta r_a = \Delta r_b = Err_r$, and $\Delta z_a = \Delta z_b = Err_z$. Substitution into (7.4) gives $Err_{\varepsilon_{11}}$ in terms of the positions of the corner points and the absolute errors of the positions (7.5).

$$Err_{\varepsilon_{11}} = \frac{2}{l_0} \left\{ \frac{Err_r |r_b - r_a| + Err_z |z_b - z_c|}{(r_b - r_a)^2 + (z_b - z_a)^2} \right\} \quad (7.5)$$

As described in Section 4.1.5, the strain ε_{11} was plotted as the average of the lower, middle and upper surfaces ($\bar{\varepsilon}_{11}$). Hence the error of $\bar{\varepsilon}_{11}$ can be found by the average of the errors of each of the lower, middle and upper surfaces by applying (7.1).

$$Err_{\bar{\varepsilon}_{11}} = \frac{Err_{\varepsilon_{11,lower}} + Err_{\varepsilon_{11,middle}} + Err_{\varepsilon_{11,upper}}}{3} \quad (7.6)$$

A.2 Derivation of Absolute Error in Strain γ_{13}

The absolute error in strain γ_{13} , $Err_{\gamma_{13}}$, is derived below.

Strain γ_{13} was defined in (4.2) as

$$\gamma_{13} = \tan \theta_{13}, \quad (4.2)$$

where θ_{13} is the change in angle between initially perpendicular vectors **ab** and **bc** in the r - z plane as shown in Fig. 62. γ_{13} can be rewritten as (7.7).

$$\gamma_{13} = \frac{\pi}{2} - \omega_{13}. \quad (7.7)$$

Using vector notation gives (7.8).

$$\gamma_{13} = \tan \left(\frac{\pi}{2} - \cos^{-1} \left(\frac{\mathbf{ab} \cdot \mathbf{ac}}{|\mathbf{ab}| |\mathbf{ac}|} \right) \right) \quad (7.8)$$

Partial differentiation of the above function with respect to the positions of the corner points of the grid element is likely to be lengthy, and therefore a substitution will be used (7.9).

$$\gamma_{13} = \tan \left(\frac{\pi}{2} - \cos^{-1}(f) \right) \quad \text{where} \quad f = \frac{\mathbf{ab} \cdot \mathbf{ac}}{|\mathbf{ab}| |\mathbf{ac}|} \quad (7.9)$$

Expansion of the vector notation as a function of the co-ordinates of the corner points gives (7.10-7.12).

$$\underline{\mathbf{ab}} \cdot \underline{\mathbf{ac}} = (r_b - r_a)(r_c - r_a) + (z_b - z_a)(z_c - z_a) \quad (7.10)$$

$$|\underline{\mathbf{ab}}| = \sqrt{(r_b - r_a)^2 + (z_b - z_a)^2} \quad (7.11)$$

$$|\underline{\mathbf{ac}}| = \sqrt{(r_c - r_a)^2 + (z_c - z_a)^2} \quad (7.12)$$

To simplify the above notation, further substitutions will be used (7.13-7.16).

$$r_{ab} = r_b - r_a \quad (7.13)$$

$$z_{ab} = z_b - z_a \quad (7.14)$$

$$r_{ac} = r_c - r_a \quad (7.15)$$

$$z_{ac} = z_c - z_a \quad (7.16)$$

Substitution of (7.13-7.16) into (7.10-7.12) then (7.9) gives (7.17).

$$f = \frac{r_{ab}r_{ac} + z_{ab}z_{ac}}{\sqrt{r_{ab}^2 + z_{ab}^2} + \sqrt{r_{ac}^2 + z_{ac}^2}} \quad (7.17)$$

Applying (4.4), the absolute error in γ_{13} can be given by partial differentiation with respect to co-ordinates of the corner points in the r - z plane (7.18).

$$Err\gamma_{13} = \left| \frac{\partial \gamma_{13}}{\partial r_a} \right| \Delta r_a + \left| \frac{\partial \gamma_{13}}{\partial r_b} \right| \Delta r_b + \left| \frac{\partial \gamma_{13}}{\partial r_c} \right| \Delta r_c + \left| \frac{\partial \gamma_{13}}{\partial z_a} \right| \Delta z_a + \left| \frac{\partial \gamma_{13}}{\partial z_b} \right| \Delta z_b + \left| \frac{\partial \gamma_{13}}{\partial z_c} \right| \Delta z_c \quad (7.18)$$

The partial derivatives in (7.18) can be found by further partial differentiation of f with respect to the substituted variables.

$$\left| \frac{\partial \gamma_{13}}{\partial r_a} \right| = \left| \frac{\partial \gamma_{13}}{\partial f} \right| \left\| \frac{\partial f}{\partial r_{ab}} \frac{\partial r_{ab}}{\partial r_a} + \frac{\partial f}{\partial r_{ac}} \frac{\partial r_{ac}}{\partial r_a} \right\| \quad (7.19)$$

$$\left| \frac{\partial \gamma_{13}}{\partial r_b} \right| = \left| \frac{\partial \gamma_{13}}{\partial f} \right| \left\| \frac{\partial f}{\partial r_{ab}} \right\| \left| \frac{\partial r_{ab}}{\partial r_b} \right| \quad (7.20)$$

$$\left| \frac{\partial \gamma_{13}}{\partial r_c} \right| = \left| \frac{\partial \gamma_{13}}{\partial f} \right| \left| \frac{\partial f}{\partial r_{ac}} \right| \left| \frac{\partial r_{ac}}{\partial r_c} \right| \quad (7.21)$$

$$\left| \frac{\partial \gamma_{13}}{\partial z_a} \right| = \left| \frac{\partial \gamma_{13}}{\partial f} \right| \left| \frac{\partial f}{\partial z_{ab}} \frac{\partial z_{ab}}{\partial z_a} + \frac{\partial f}{\partial z_{ac}} \frac{\partial z_{ac}}{\partial z_a} \right| \quad (7.22)$$

$$\left| \frac{\partial \gamma_{13}}{\partial z_b} \right| = \left| \frac{\partial \gamma_{13}}{\partial f} \right| \left| \frac{\partial f}{\partial z_{ab}} \right| \left| \frac{\partial z_{ab}}{\partial z_b} \right| \quad (7.23)$$

$$\left| \frac{\partial \gamma_{13}}{\partial z_c} \right| = \left| \frac{\partial \gamma_{13}}{\partial f} \right| \left| \frac{\partial f}{\partial z_{ac}} \right| \left| \frac{\partial z_{ac}}{\partial z_c} \right| \quad (7.24)$$

The partial derivatives can be solved as follows:

$$\left| \frac{\partial \gamma_{13}}{\partial f} \right| = \sec^2 \left(\frac{\pi}{2} - \cos^{-1}(f) \right) \left(\frac{1}{\sqrt{1-f^2}} \right) \quad (7.25)$$

$$\frac{\partial f}{\partial r_{ab}} = \frac{r_{ac}}{\sqrt{r_{ab}^2 + z_{ab}^2} + \sqrt{r_{ac}^2 + z_{ac}^2}} - \frac{r_{ab}(r_{ab}r_{ac} + z_{ab}z_{ac})}{\sqrt{r_{ab}^2 + z_{ab}^2} \left(\sqrt{r_{ab}^2 + z_{ab}^2} + \sqrt{r_{ac}^2 + z_{ac}^2} \right)^2} \quad (7.26)$$

$$\frac{\partial f}{\partial r_{ac}} = \frac{r_{ab}}{\sqrt{r_{ab}^2 + z_{ab}^2} + \sqrt{r_{ac}^2 + z_{ac}^2}} - \frac{r_{ac}(r_{ab}r_{ac} + z_{ab}z_{ac})}{\sqrt{r_{ab}^2 + z_{ab}^2} \left(\sqrt{r_{ab}^2 + z_{ab}^2} + \sqrt{r_{ac}^2 + z_{ac}^2} \right)^2} \quad (7.27)$$

$$\frac{\partial f}{\partial z_{ab}} = \frac{z_{ac}}{\sqrt{r_{ab}^2 + z_{ab}^2} + \sqrt{r_{ac}^2 + z_{ac}^2}} - \frac{z_{ab}(r_{ab}r_{ac} + z_{ab}z_{ac})}{\sqrt{r_{ab}^2 + z_{ab}^2} \left(\sqrt{r_{ab}^2 + z_{ab}^2} + \sqrt{r_{ac}^2 + z_{ac}^2} \right)^2} \quad (7.28)$$

$$\frac{\partial f}{\partial z_{ac}} = \frac{z_{ab}}{\sqrt{r_{ab}^2 + z_{ab}^2} + \sqrt{r_{ac}^2 + z_{ac}^2}} - \frac{z_{ac}(r_{ab}r_{ac} + z_{ab}z_{ac})}{\sqrt{r_{ab}^2 + z_{ab}^2} \left(\sqrt{r_{ab}^2 + z_{ab}^2} + \sqrt{r_{ac}^2 + z_{ac}^2} \right)^2} \quad (7.29)$$

$$\frac{\partial r_{ab}}{\partial r_a} = -1 \quad (7.30)$$

$$\frac{\partial r_{ab}}{\partial r_b} = 1 \quad (7.31)$$

$$\frac{\partial r_{ac}}{\partial r_a} = -1 \quad (7.32)$$

$$\frac{\partial r_{ac}}{\partial r_c} = 1 \quad (7.33)$$

$$\frac{\partial z_{ab}}{\partial z_a} = -1 \quad (7.34)$$

$$\frac{\partial z_{ab}}{\partial z_b} = 1 \quad (7.35)$$

$$\frac{\partial z_{ac}}{\partial z_a} = -1 \quad (7.36)$$

$$\frac{\partial z_{ac}}{\partial z_c} = 1 \quad (7.37)$$

Substitution of (7.25) – (7.37) into (7.19) - (7.24) gives:

$$\left| \frac{\partial \gamma_{13}}{\partial r_a} \right| = \left| \frac{\partial \gamma_{13}}{\partial f} \right| \left\{ \frac{1}{\sqrt{r_{ab}^2 + z_{ab}^2} + \sqrt{r_{ac}^2 + z_{ac}^2}} \right\} \left| (r_{ac} + r_{ab}) - \frac{(r_{ab} + r_{ac})(r_{ab}r_{ac} + z_{ab}z_{ac})}{\sqrt{r_{ab}^2 + z_{ab}^2}(\sqrt{r_{ab}^2 + z_{ab}^2} + \sqrt{r_{ac}^2 + z_{ac}^2})} \right| \quad (7.38)$$

$$\left| \frac{\partial \gamma_{13}}{\partial r_b} \right| = \left| \frac{\partial \gamma_{13}}{\partial f} \right| \left\{ \frac{1}{\sqrt{r_{ab}^2 + z_{ab}^2} + \sqrt{r_{ac}^2 + z_{ac}^2}} \right\} \left| r_{ac} - \frac{r_{ab}(r_{ab}r_{ac} + z_{ab}z_{ac})}{\sqrt{r_{ab}^2 + z_{ab}^2}(\sqrt{r_{ab}^2 + z_{ab}^2} + \sqrt{r_{ac}^2 + z_{ac}^2})} \right| \quad (7.39)$$

$$\left| \frac{\partial \gamma_{13}}{\partial r_c} \right| = \left| \frac{\partial \gamma_{13}}{\partial f} \right| \left\{ \frac{1}{\sqrt{r_{ab}^2 + z_{ab}^2} + \sqrt{r_{ac}^2 + z_{ac}^2}} \right\} \left| r_{ab} - \frac{r_{ac}(r_{ab}r_{ac} + z_{ab}z_{ac})}{\sqrt{r_{ab}^2 + z_{ab}^2}(\sqrt{r_{ab}^2 + z_{ab}^2} + \sqrt{r_{ac}^2 + z_{ac}^2})} \right| \quad (7.40)$$

$$\left| \frac{\partial \gamma_{13}}{\partial z_a} \right| = \left| \frac{\partial \gamma_{13}}{\partial f} \right| \left\{ \frac{1}{\sqrt{r_{ab}^2 + z_{ab}^2} + \sqrt{r_{ac}^2 + z_{ac}^2}} \right\} \left| (z_{ac} + z_{ab}) - \frac{(z_{ac} + z_{ab})(r_{ab}r_{ac} + z_{ab}z_{ac})}{\sqrt{r_{ab}^2 + z_{ab}^2}(\sqrt{r_{ab}^2 + z_{ab}^2} + \sqrt{r_{ac}^2 + z_{ac}^2})} \right| \quad (7.41)$$

$$\left| \frac{\partial \gamma_{13}}{\partial z_b} \right| = \left| \frac{\partial \gamma_{13}}{\partial f} \right| \left\{ \frac{1}{\sqrt{r_{ab}^2 + z_{ab}^2} + \sqrt{r_{ac}^2 + z_{ac}^2}} \right\} \left| z_{ac} - \frac{z_{ab}(r_{ab}r_{ac} + z_{ab}z_{ac})}{\sqrt{r_{ab}^2 + z_{ab}^2}(\sqrt{r_{ab}^2 + z_{ab}^2} + \sqrt{r_{ac}^2 + z_{ac}^2})} \right| \quad (7.42)$$

$$\left| \frac{\partial \gamma_{13}}{\partial z_c} \right| = \left| \frac{\partial \gamma_{13}}{\partial f} \right| \left\{ \frac{1}{\sqrt{r_{ab}^2 + z_{ab}^2} + \sqrt{r_{ac}^2 + z_{ac}^2}} \right\} \left| z_{ab} - \frac{z_{ac}(r_{ab}r_{ac} + z_{ab}z_{ac})}{\sqrt{r_{ab}^2 + z_{ab}^2}(\sqrt{r_{ab}^2 + z_{ab}^2} + \sqrt{r_{ac}^2 + z_{ac}^2})} \right| \quad (7.43)$$

Substitution into (7.18), where $\Delta r_a = \Delta r_b = \Delta r_c = Err_r$ and $\Delta z_a = \Delta z_b = \Delta z_c = Err_z$ gives $Err_{\gamma_{13}}$ in terms of the errors of each of the corner positions (7.44).

$$Err_{\gamma_{13}} = \left| \frac{\partial \gamma_{13}}{\partial f} \right| \left| \frac{2[Err_r(r_{ac} + r_{ab}) + Err_z(z_{ac} + z_{ab})]}{\sqrt{r_{ab}^2 + z_{ab}^2} + \sqrt{r_{ac}^2 + z_{ac}^2}} \right| \left| 1 - \frac{(r_{ab}r_{ac} + z_{ab}z_{ac})}{\sqrt{r_{ab}^2 + z_{ab}^2}(\sqrt{r_{ab}^2 + z_{ab}^2} + \sqrt{r_{ac}^2 + z_{ac}^2})} \right| \quad (7.44)$$

As described in Section 4.1.5, the strain γ_{13} was plotted as the average of the values at each of the corners of the deformed element, $\bar{\gamma}_{13}$. Hence the error of $\bar{\gamma}_{13}$ can be found by the average of the errors of the strain in each corner (7.45). The error in shear strain in the other three corners of an element (γ_{13abd} , γ_{13bdc} and γ_{13dca}) can be found using Equation 7.44, but substituting r_{ab} , r_{ac} , z_{ab} and z_{ac} for the distances between the points subtending that corner.

$$Err_{\bar{\gamma}_{13}} = \frac{Err_{\gamma_{13cab}} + Err_{\gamma_{13abd}} + Err_{\gamma_{13bdc}} + Err_{\gamma_{13dca}}}{4} \quad (7.45)$$

A.3 Derivation of Absolute Error in Strain γ_{23}

The absolute error in strain γ_{23} , $Err_{\gamma_{23}}$, is derived below.

Strain γ_{23} was defined in (4.3) as

$$\gamma_{23} = \tan \theta_{23}, \quad (4.3)$$

where θ_{23} is the change in angle between **bc** and the vertical (z -direction) in the θ - z plane. This definition assumes that the surface of the plate that is normal to the r - z plane remains parallel to the θ -direction. According to Fig. 62, γ_{23} can be defined in terms of the positions of the corner points in θ - z co-ordinates according to (7.46) below.

$$\gamma_{23} = \frac{\theta_c - \theta_z}{z_c - z_a} \quad (7.46)$$

Applying (4.4), the absolute error in γ_{23} is given by (7.47):

$$Err_{\gamma_{23}} = \left| \frac{\partial \gamma_{23}}{\partial \theta_a} \right| \Delta \theta_a + \left| \frac{\partial \gamma_{23}}{\partial \theta_b} \right| \Delta \theta_b + \left| \frac{\partial \gamma_{23}}{\partial z_a} \right| \Delta z_a + \left| \frac{\partial \gamma_{23}}{\partial z_c} \right| \Delta z_c \quad (7.47)$$

Completing the partial differentiation gives

$$Err\gamma_{23} = \left| \frac{1}{z_c - z_a} \right| \left\{ \Delta\theta_c + \Delta\theta_a + \left| \frac{\theta_c - \theta_a}{z_c - z_a} \right| (\Delta z_a + \Delta z_c) \right\}, \quad (7.48)$$

where $\Delta z_a = \Delta z_c = Err_z$. Errors $\Delta\theta_c$ and $\Delta\theta_a$ are different depending on whether the lower to middle surface layer or the middle to upper surface layer is being considered according to (7.49) and (7.50):

Lower to middle surface:

$$\Delta\theta_a = Err_{\theta_{lower}} \quad \Delta\theta_c = Err_{\theta_{middle}} \quad (7.49)$$

Middle to upper surface:

$$\Delta\theta_a = Err_{\theta_{middle}} \quad \Delta\theta_c = Err_{\theta_{upper}} \quad (7.50)$$

Substitution into (7.48) gives two solutions for $Err\gamma_{23}$, one for each layer through the thickness:

Lower to middle surface:

$$Err\gamma_{23} = \left| \frac{1}{z_c - z_a} \right| \left\{ Err_{\theta_{middle}} + Err_{\theta_{lower}} + 2 \left| \frac{\theta_c - \theta_a}{z_c - z_a} \right| Err_z \right\} \quad (7.51)$$

Middle to upper surface:

$$Err\gamma_{23} = \left| \frac{1}{z_c - z_a} \right| \left\{ Err_{\theta_{upper}} + Err_{\theta_{middle}} + 2 \left| \frac{\theta_c - \theta_a}{z_c - z_a} \right| Err_z \right\} \quad (7.52)$$

A.4 Derivation of Absolute Error in Wall Thickness t_1

The absolute error in the sine law prediction of wall thickness, Err_{t1} , is derived below.

The sine law, was defined in (2.1) as

$$t_1 = t_0 \sin \alpha, \quad (2.1)$$

where t_l is the final wall thickness, t_0 is the original wall thickness and α is the wall angle. According to Fig. 62, t_l can be defined in terms of the positions of the corner points in r - z co-ordinates according to (7.53) below.

$$t_l = t_0 \frac{(r_b - r_a)}{\sqrt{(r_b - r_a)^2 + (z_b - z_a)^2}} \quad (7.53)$$

Applying (4.4), the absolute error in t_l is given by (7.54).

$$Err_{t_l} = \left| \frac{\partial t_l}{\partial r_a} \right| \Delta r_a + \left| \frac{\partial t_l}{\partial r_b} \right| \Delta r_b + \left| \frac{\partial t_l}{\partial z_a} \right| \Delta z_a + \left| \frac{\partial t_l}{\partial z_b} \right| \Delta z_b \quad (7.54)$$

Completing the partial differentiation gives

$$Err_{t_l} = \frac{t_0 \{ (\Delta r_b + \Delta r_a)(z_b - z_a)^2 + (\Delta z_b + \Delta z_a) |r_b - r_a| |z_b - z_a| \}}{\left((r_b - r_a)^2 + (z_b - z_a)^2 \right)^{3/2}}, \quad (7.55)$$

where $\Delta r_a = \Delta r_b = Err_r$, and $\Delta z_a = \Delta z_b = Err_z$. Substitution into (7.55) gives Err_{t_l} in terms of the positions of the corner points and the absolute errors of the positions (7.56).

$$Err_{t_l} = \frac{2t_0 \{ Err_r (z_b - z_a)^2 + Err_z |r_b - r_a| |z_b - z_a| \}}{\left((r_b - r_a)^2 + (z_b - z_a)^2 \right)^{3/2}} \quad (7.56)$$

As described in Section 4.1.5, the sine law wall thickness t_l was plotted as the average of the values at the lower, middle and upper surfaces (\bar{t}_l). Hence the absolute error of \bar{t}_l can be found by the average error of the wall thickness at the lower, middle and upper surfaces (7.57).

$$Err_{\bar{t}_l} = \frac{Err_{t_{l,lower}} + Err_{t_{l,middle}} + Err_{t_{l,upper}}}{3} \quad (7.57)$$

References

1. Ambrogio, G., Napoli, L.D., Filice, L., Gagliardi, F. and Muzzupappa, M., 2005. *Application of incremental forming process for high customised medical product manufacturing*. Journal of Materials Processing Technology. **162-163**: pp. 156-162.
2. Tanaka, S., Nakamura, T., Hayakawa, K., Nakamura, H., Motomura, I., Yamada, S. and Kasama, Y., 2002. *Dental prosthetic application of incremental forming process: Forming of titanium denture plate*. In: Proceedings of the 2002 Japanese Spring Conference for the Technology of Plasticity. pp. 229-230.
3. Tanaka, S., Nakamura, T., Hayakawa, K., Nakamura, H., Motomura, I., Yamada, S. and Kasama, Y., 2002. *Dental prosthetic application of incremental forming process: Forming for dental use; coping of porcelain fused to titanium and conical double-crown telescopic prosthesis or telescope dentures*. In: Proceedings of the 2002 Japanese Spring Conference for the Technology of Plasticity. pp. 231-232.
4. Allwood, J.M., Bramley, A.N., Ridgman, T.W. and Mileham, A.R., 2005. *A novel method for the rapid production of inexpensive dies and moulds with surfaces made by incremental sheet forming*. Proc. IMechE Part B: J. Engineering Manufacture. **220**: pp. 1-5.
5. Duflou, J., Lauwers, B., Verbert, J., Tunckol, Y. and De Baerdemaeker, H., 2005. *Achievable accuracy in single point incremental forming: Case studies*. In: 8th ESAFORM Conference. Cluj-Napoca, Romania. **Vol. II**: pp. 675-678.
6. Jeswiet, J., Duflou, J.R., Szekeres, A. and Lefebvre, P., 2005. *Custom manufacture of a solar cooker - A case study*. In: SheMet '05 International Conference on Sheet Metal. Erlangen, Germany. pp. 487-492.

7. Matsui, M. and Matsuda, H., 2001. *Incremental forming for automobile body panels*. Journal of the JSTP. **42(489)**: pp. 64-68.
8. Shima, S., 2001. *State of the art - Incremental forming*. In: The Third International Conference on Intelligent Processing and Manufacturing of Materials. Vancouver, Canada.
9. Hagan, E. and Jewsiet, J., 2003. *A review of conventional and modern single-point sheet metal forming methods*. J. Engineering Manufacture. **217 part B**: pp. 213-225.
10. Jeswiet, J., Micari, F., Hirt, G., Bramley, A., Duflou, J. and Allwood, J., 2005. *Asymmetric single point incremental forming of sheet metal*. Annals of the CIRP. **54(2)**: pp. 623-650.
11. Allwood, J.M. and Utsunomiya, H., 2006. *A survey of flexible forming processes in Japan*. International Journal of Machine Tools & Manufacture. **46(15)**: pp. 1939-1960.
12. Wong, C.C., Dean, T.A. and Lin, J., 2003. *A review of spinning, shear forming and flow forming processes*. International Journal of Machine Tools & Manufacture. **43**: pp. 1419-1435.
13. Duflou, J., Szekeres, A. and Vanherck, P., 2005. *Force measurements for single point incremental forming: An experimental study*. In: SheMet '05 International Conference on Sheet Metal. Erlangen, Germany. pp. 441-448.
14. Matsubara, S., 1994. *Computer numerical control incremental forming*. Journal Japan Society Technology of Plasticity. **35(406)**: pp. 1258-1263.
15. Hirt, G., Ames, J. and Bambach, M., 2006. *Validation of FEA for asymmetric incremental sheet forming by on-line measurements of deformation and tool forces*. Production Engineering. **XIII/1**: pp. 39-44.

16. Ceretti, E., Giardini, C. and Attanasio, A., 2004. *Experimental and simulative results in sheet incremental forming on CNC machines*. Journal of Materials Processing Technology. **152**: pp. 176-184.
17. Giardini, C., Ceretti, E., Attanasio, A. and Pasquali, M., 2004. *Analysis of the influence of working parameters on final part quality in sheet incremental forming*. In: 3rd International Conference and Exhibition on Design and Manufacturing of Dies and Molds, 7th International Symposium on Advances in Abrasive Technology. Bursa, Turkey. **DM 2004-13**.
18. Yoshikawa, T., Nakaruma, K., Ueno, K. and Shina, A., 1999. *Study of incremental sheet metal bulging using a pair of upper and lower tools - Study of incremental sheet metal bulging using tool bar (1)*. In: Proc. 1999 Spring Conf. Tech Plasticity. pp. 305-306.
19. Meier, H., Smukala, V., Dewald, O. and Zhang, J., 2007. *Two point incremental forming with two moving forming tools*. In: SheMet '07 International Conference on Sheet Metal. Palermo, Sicily. pp. 599-605.
20. Maidagan, E., Zettler, J., Bambach, M., Rodriguez, P.P. and Hirt, G., 2007. *A new incremental sheet forming process based on a flexible supporting die system*. In: SheMet '07 International Conference on Sheet Metal. Palermo, Sicily. pp. 607-614.
21. Powell, N.N. and Andrew, C., 1992. *Incremental forming of flanged sheet metal components without dedicated dies*. Proc IMechE. **206**: pp. 41-47.
22. Anon., 1991. *Flanged sheet metal components produced without dies*. Sheet Metal Ind. **68**: pp. 248.
23. Tanaka, S., Nakamura, T. and Hayakawa, K., 1999. *Incremental sheet metal forming using elastic tools*. In: Proceedings of the 6th ICTP. Advanced Technology of Plasticity. **Vol. II**: pp. 1477-1482.

-
24. Yoon, S.J. and Yang, D.Y., 2001. *Investigation into a new incremental forming process using an adjustable punch set for the manufacture of a doubly curved sheet metal*. Proc IMechE Part B. **215**: pp. 991-1004.
 25. Yoon, S.J. and Yang, D.Y., 2003. *Development of a highly flexible incremental roll forming process for the manufacturing of a doubly curved sheet metal*. Annals of the CIRP. **52/1/2003**: pp. 201-204.
 26. Saotome, Y. and Okamoto, T., 2001. *An in-situ incremental microforming system for three-dimensional shell structures of foil materials*. Journal of Materials Processing Technology. **113**: pp. 636-640.
 27. Muresan, I.C.-O., Brosius, A., Homberg, W. and Kleiner, M., 2005. *Finite element analysis of incremental sheet forming*. In: 8th ESAFORM Conference. Cluj-Napoca, Romania. **Vol. I**: pp. 105-108.
 28. Iseki, H. and Naganawa, T., 2002. *Vertical wall surface forming of rectangular shell using multistage incremental forming with spherical and cylindrical rollers*. Journal of Materials Processing Technology. **130-131**: pp. 675-679.
 29. Kitazawa, K., 1993. *Incremental sheet metal stretch-expanding with CNC machine tools*. In: Proceedings of the 4th International Conference on Technology of Plasticity. Advanced Technology of Plasticity. pp. 1899-1904.
 30. Iseki, H., Kato, K. and Sakamoto, S., 1992. *Flexible and incremental sheet metal bulging using a path-controlled spherical roller*. Trans. JSME Ser. C. **58 (554)**: pp. 279-287.
 31. Maki, T., 2006. Presentation: '*Dieless NC Forming*'. In: International Seminar on Novel Sheet Metal Forming Technologies, Jyväskylä, Finland.
 32. Allwood, J.M., Houghton, N.E. and Jackson, K.P., 2005. *The design of an incremental sheet forming machine*. In: SheMet '05 International Conference on Sheet Metal. Erlangen, Germany. pp. 471-478.

-
33. Meier, H., Dewald, O. and Zhang, J., 2005. *A new robot-based sheet metal forming process*. In: SheMet '05 International Conference on Sheet Metal. Erlangen, Germany. pp. 465-470.
 34. Lamminen, L., 2005. *Incremental sheet forming with an industrial robot - Forming limits and their effect on component design*. In: SheMet '05 International Conference on Sheet Metal. Erlangen, Germany. pp. 457-464.
 35. Schäfer, T. and Schraft, R.D., 2004. *Incremental sheet metal forming by industrial robots using a hammering tool*. In: 10èmes Assises Européennes de Prototypage Rapide. Association Française de Prototypage Rapide.
 36. Leach, D., Green, A.J. and Bramley, A.N., 2001. *A new incremental sheet forming process for small batch and prototype parts*. In: 9th Int. Conf. on Sheet Metal. Leuven. pp. 211-218.
 37. Matsubara, S., 2001. *A computer numerically controlled dieless incremental forming of a sheet metal*. Proc IMechE Part B. **215**: pp. 959-966.
 38. Kim, Y.H. and Park, J.J., 2002. *Effect of process parameters on formability in incremental forming of sheet metal*. Journal of Materials Processing Technology. **130-131**: pp. 42-46.
 39. Iseki, H., 2001. *An approximate deformation analysis and FEM analysis for the incremental bulging of sheet metal using a spherical roller*. J. Materials Processing Technology. **111**: pp. 150-154.
 40. Hirt, G., Junk, S., Bambach, M., Chouvalouva, I. and Ames, J., 2003. *Flexible CNC incremental sheet forming: Process evaluation and simulation*. In: VI Conferência Nacional de Conformação de Chapas. Porto Alegre/RS, Brasilien. pp. 30-38.
 41. Iseki, H., 2001. *Flexible and Incremental Bulging of Sheet Metal Using a High-Speed Water Jet*. JSME International Journal, Series C. **44(2)**: pp. 486-493.

-
42. Iseki, H. and Nara, T., 2007. *Incremental bulging of sheet metal using water jet and shots*. In: SheMet '07 International Conference on Sheet Metal. Palermo, Sicily. pp. 575-582.
 43. Emmens, W.C., 2007. *Detailed incremental forming of steel beverage cans by a high-pressure water jet*. In: SheMet '07 International Conference on Sheet Metal. Palermo, Sicily. pp. 567-574.
 44. Petek, A., Gantar, G., Pepelnjak, T. and Kuzman, K., 2007. *Economical and ecological aspects of single point incremental forming versus deep drawing technology*. In: SheMet '07 International Conference on Sheet Metal. Palermo, Sicily. pp. 931-938.
 45. Filice, L., Fratini, L. and Micari, F., 2002. *Analysis of material formability in incremental forming*. Annals of the CIRP. **51/1/2002**: pp. 199-202.
 46. Jeswiet, J., Young, D. and Ham, M., 2005. *Non-traditional forming limit diagrams for incremental forming*. In: SheMet '05 International Conference on Sheet Metal. Erlangen, Germany. pp. 409-416.
 47. Fratini, L., Ambrogio, G., Lorenzo, R.D., Filice, L. and Micari, F., 2004. *Influence of mechanical properties of the sheet material of formability in single point incremental forming*. Annals of the CIRP. **53/1**: pp. 207-210.
 48. Hirt, G., Ames, J. and Bambach, M., 2005. *A new forming strategy to realise parts designed for deep-drawing by incremental CNC sheet forming*. Steel Research. **76 (2005) no. 2/3**.
 49. Jeswiet, J. and Hagan, E., 2001. *Rapid proto-typing of a headlight with sheet metal*. In: 9th International Conference on Sheet Metal. Leuven.
 50. Hirt, G., Bambach, M., Junk, S. and Chouvalova, I., 2003. *FEM modelling and optimisation of geometric accuracy in incremental CNC sheet forming, Developments in Equipment Based Accuracy*. In: CIRP international conference on accuracy in forming technology (ICAFT/10). Chemnitz. pp. 293-304.

-
51. Ambrogio, G., Costantino, I., DeNapoli, L., Filice, L., Fratini, L. and Muzzupappa, M., 2004. *Influence of some relevant parameters on the dimensional accuracy in incremental forming: a numerical and experimental investigation*. Journal of Materials Processing Technology. **153-154**: pp. 501-507.
 52. Watzeels, K., Tunckol, Y., Henrard, C., Gu, J., Sol, H., Duflou, J. and Habraken, A.M., 2005. *Experimental validation of the finite element simulation of the first stroke in single point incremental forming*. In: 8th ESAFORM Conference. Cluj-Napoca, Romania. **Vol. II**: pp. 703-706.
 53. Shim, M.-S. and Park, J.J., 2001. *The formability of aluminium sheet in incremental forming*. Journal of Materials Processing Technology. **113**: pp. 654-658.
 54. Duflou, J., Tunckol, Y., Szekeres, A. and Vanherck, P., 2007. *Experimental study on force measurements for single point incremental forming*. Journal of Materials Processing Technology. **189**: pp. 65-72.
 55. Bologa, O., Oleksik, V. and Racz, G., 2005. *Experimental research for determining the forces on incremental sheet forming process*. In: 8th ESAFORM Conference. Cluj-Napoca, Romania. **Vol. I**: pp. 317-320.
 56. Jeswiet, J., Duflou, J.R. and Szekeres, A., 2005. *Forces in single point and two point incremental forming*. In: SheMet '05 International Conference on Sheet Metal. Erlangen, Germany. pp. 449-456.
 57. Bambach, M., Ames, J., Azaouzi, M., Campagne, L., Hirt, G. and Batoz, J.L., 2005. *Initial experimental and numerical investigations into a class of new strategies for single point incremental sheet forming (SPIF)*. In: 8th ESAFORM Conference. Cluj-Napoca, Romania. **Vol. II**: pp. 671-674.

-
58. Ambrogio, G., Filice, L., Gagliardi, F. and Micari, F., 2005. *Sheet thinning prediction in single point incremental forming*. In: SheMet '05 International Conference on Sheet Metal. Erlangen, Germany. pp. 479-486.
59. Hagan, E. and Jeswiet, J., 2004. *Analysis of surface roughness for parts formed by computer numerical controlled incremental forming*. J Engineering Manufacture Part B. **218**: pp. 1307-1312.
60. Belytschko, Liu and Moran, 2000. *Nonlinear finite elements for continua and structures*. Wiley.
61. Bambach, M., Hirt, G. and Junk, S., 2003. *Modeling and experimental evaluation of the incremental CNC sheet metal forming process*. VII Int. Conf. on Computational Plasticity. pp. 1-15.
62. He, S., Van Bael, A., Van Houtte, P., Tunckol, Y., Duflou, J., Henrard, C., Bouffioux, C. and Habraken, A.M., 2005. *Effect of FEM choices in the modelling of incremental forming of aluminium sheets*. In: 8th ESAFORM Conference. Cluj-Napoca, Romania. **Vol. II**: pp. 711-714.
63. Bambach, M. and Hirt, G., 2007. *Error analysis in explicit finite element analysis of incremental sheet forming*. In: Numiform '07.
64. Abaqus Inc., 2004. *Abaqus Version 6.5 - Analysis User's Manual*. Abaqus, Inc. Volume IV: Elements.
65. Hirt, G., Junk, S. and Witulsky, N., 2002. *Incremental sheet forming: Quality evaluation and process simulation*. In: Proceedings of the 7th ICTP Conference. Yokohama, Japan. pp. 925-930.
66. Henrard, C., Habraken, A.M., Szekeres, A., Duflou, J.R., He, S., Van Bael, A. and Van Houtte, P., 2005. *Comparison of FEM simulations for the incremental forming process*. In: SheMet '05 International Conference on Sheet Metal. Erlangen, Germany. pp. 533-540.

-
67. Hirt, G., Junk, S., Bambach, M. and Chouvalova, I., 2003. *Process limits and material behaviour in incremental sheet forming with CNC-Tools*. In: THERMEC 2003 International Conference on Processing & Manufacturing of Advanced Materials-Fabrication, Properties, Applications. Madrid, Spain. Institute of Materials Technology/Precision Forming (LWP). pp. 3825-3830.
68. Landert, M., 2006. *Forming behaviour of metal sandwich sheets*. PhD Thesis, Department of Materials Science and Metallurgy, Cambridge University.
69. Franzen, V., Kwiatkowski, L., Martins, P.A.F. and Tekkaya, A.E., 2008. *Single Point Incremental Forming of PVC*. Journal of Materials Processing Technology. Article in Press.
70. Allwood, J.M., King, G.P.F. and Duflou, J., 2005. *A structured search for applications of the incremental sheet forming process by product segmentation*. Proc I Mech E Part B J Eng Manuf. **219(2)**: pp. 239-244.
71. Tanaka, S., Nakamura, T. and Hayakawa, K., 2002. *Minature incremental forming of millimetre-sized thin shell structures*. Advanced Technology of Plasticity (Proceedings of the Seventh ICTP, Yokohama, Japan). pp. 403-408.
72. Jyllilä, M., 2006. Presentation: *'Incremental sheet forming as a part of a sheet metal business'*. In: International Seminar on Novel Sheet Metal Forming Technologies, Jyväskylä, Finland.
73. Jeswiet, J. and Hagan, E., 2003. *Rapid proto-typing with sheet metal. CNC RPIF*. International Journal for Metal Forming Processes. **6(3-4)**: pp. 315-324.
74. Junk, S., Hirt, G. and Chouvalova, I., 2003. *Forming strategies and tools in incremental sheet forming*. In: SheMet '03 International Conference on Sheet Metal. University of Ulster, Ireland. Institute of Materials Technology/Precision Forming (LWP). pp. 57-64.
75. Iseki, H., Kato, K. and Sakamoto, S., 1993. *Forming limit of flexible and incremental sheet metal bulging with a spherical roller*. In: Proceedings of the

- Fourth International Conference on Technology of Plasticity. Advanced Technology of Plasticity. pp. 1635-1904.
76. Park, J.J. and Kim, Y.H., 2003. *Fundamental studies on the incremental sheet metal forming technique*. Journal of Materials Processing Technology. **140**: pp. 447-453.
77. Jeswiet, J. and Young, D., 2005. *Forming limit diagrams for single-point incremental forming of aluminium sheet*. Proc. IMechE: J. Engineering Manufacture Part B. **219**: pp. 1-6.
78. Matsubara, S., 1994. *Incremental backward bulge forming of a sheet metal with a hemispherical head tool - A study of a numerically controlled forming system II*. Journal of the Japanese Society of Technology of Plasticity (Plasticity and Processing). **35 (406)**: pp. 1311-1321.
79. Young, D. and Jeswiet, J., 2004. *Wall thickness variations in single-point incremental forming*. J Engineering Manufacture Part B. **218**: pp. 1453-1459.
80. Sortais, H.C., Kobayashi, S. and Thomsen, E.G., 1963. *Mechanics of conventional spinning*. Journal of Engineering for Industry: Transactions of the ASME Series B. **85**: pp. 346-350.
81. Kalpakcioglu, S., 1961. *On the mechanics of shear spinning*. Transactions of the ASME, Journal of Engineering for Industry. **83**: pp. 125-130.
82. Shankar, R., Jadhav, S., Goebel, R., Homberg, W. and Kleiner, M., 2005. *Incremental sheet metal forming of preformed sheets*. In: 8th ICTP. Verona, Italy.
83. Kim, T.J. and Yang, D.Y., 2000. *Improvement of formability for the incremental sheet metal forming processes*. International Journal of Mechanical Sciences. **42**: pp. 1271-1286.

-
84. Jeswiet, J., Hagan, E. and Szekeres, A., 2002. *Forming parameters for incremental forming of aluminium alloy sheet metal*. *J Engineering Manufacture*. **216**: pp. 1367-1371.
85. Jeswiet, J. and Hagan, E., 2003. *Rapid prototyping non-uniform shapes from sheet metal using CNC single point incremental forming*. *Transaction of the North American Manufacturing Research Institution of SME*. **XXXI**: pp. 65-69.
86. Avitzur, B. and Yang, C.T., 1960. *Analysis of power spinning of cones*. *Trans. ASME, Ser. B, J. Engng for Industry*. **82**: pp. 231-245.
87. Emmens, W.C., 2007. *Strain in shear, and material behaviour in incremental forming*. In: *SheMet '07 International Conference on Sheet Metal*. Palermo, Sicily. pp. 519-526.
88. Allwood, J.M., Shouler, D.R. and Tekkaya, A.E., 2007. *The increased forming limits of incremental sheet forming processes*. In: *SheMet '07 International Conference on Sheet Metal*. Palermo, Italy. pp. 621-628.
89. Sawada, T., Matsubara, S., Sakamoto, M. and Fukuhara, G., 1999. *Deformation analysis for stretch forming of sheet metal with CNC machine tools*. In: *Proceedings of the 6th ICTP. Advanced Technology of Plasticity*. **Vol. II**: pp. 1501-1504.
90. Ambrogio, G., Filice, L., Fratini, L. and Micari, F., 2004. *Process mechanics analysis in single point incremental forming*. In: *NUMIFORM 2004*. Columbus, Ohio.
91. Qin, Q., Masuku, E.S., Bramley, A.N., Mileham, A.R. and Owen, G.W., 2005. *Incremental sheet forming simulation and accuracy*. In: *8th ICTP*. Verona, Italy.
92. He, S., Bael, A.V., Houtte, P.V., Szekeres, A., Duflou, J.R., Henrard, C. and Habraken, A.M., 2005. *Finite element modelling of incremental forming of aluminium sheets*. In: *SheMet '05 International Conference on Sheet Metal*. Erlangen, Germany. pp. 525-532.

-
93. Duflou, J., Tunckol, Y. and Aereens, R., 2007. *Force analysis for single point incremental forming*. In: SheMet '07 International Conference on Sheet Metal. Palermo, Sicily. pp. 543-550.
 94. Micari, F., 2005. *Some remarks on material formability in single point incremental forming of sheet metal*. In: Proc. 8th ICTP. Verona.
 95. Allwood, J.M. and Shouler, D.R., 2007. *Generalised forming limit diagrams showing increased forming limits with non-planar stress states*. International Journal of Plasticity. Under review.
 96. Bambach, M., Todorova, M. and Hirt, G., 2007. *Experimental and numerical analysis of forming limits in CNC incremental sheet forming*. In: SheMet '07 International Conference on Sheet Metal. Palermo, Sicily. pp. 511-518.
 97. Ambrogio, G., Filice, L., Gagliardi, F., Micari, F. and Umbrello, D., 2005. *Application of the neural network technique for reducing springback in incremental forming processes*. In: 8th ESAFORM Conference. Cluj-Napoca, Romania. **Vol. II**: pp. 699-702.
 98. Dai, K., Wang, Z.R. and Fang, Y., 2002. *CNC incremental sheet forming of an axially symmetric specimen and the locus of optimization*. Journal of Materials Processing Technology. **102**: pp. 164-167.
 99. Waller, 1978. *Press tools and press work*.
 100. Ambrogio, G., DiLorenzo, R. and Micari, F., *Analysis of the economical effectiveness of incremental forming: an industrial case study*, in Proc. VI AITeM Conference. 2003.
 101. Micari, F., 2004. *Single point incremental forming: Recent results*. Presentation on CD ROM, given at Seminar on Incremental Sheet Forming, Cambridge University.

102. Hirt, G., Ames, J. and Bambach, M., 2003. *Economical and ecological benefits of CNC incremental sheet forming (ISF)*. In: 9th International Workshop on Ecology and Economy in Manufacturing, ICEM 2003. Miskolc, Hungary. Institute of Materials Science/Precision Forming (LWP).
103. Zenkert, D., 1995. *An introduction to sandwich construction*. Engineering Materials Advisory Services Ltd.: The Chameleon Press Ltd, London, United Kingdom.
104. Karlsson, K.F. and Åström, B.T., 1997. *Manufacturing and applications of structural sandwich components*. Composites Part A. **28A**: pp. 97-111.
105. Miller, W.K., 1981. *Metal-plastic laminates for vehicle weight reduction*. SAE. **800077**: pp. 481-490.
106. DiCello, J.A., 1980. *Steel-polypropylene-steel laminate - A new weight reduction material*. SAE. **800078**: pp. 1-15.
107. McKenna, L.W., Wohl, M.H. and Woodbrey, J.C., 1981. *New light-weight materials for vehicle body panels - Aluminium/nylon laminates*. SAE. **800079**: pp. 506-516.
108. Somoyajulu, T.S.V., 2004. *Vibration and formability characteristics of aluminium-polymer sandwich materials*. PhD Thesis, University of Michigan.
109. Gustafsson, R., 1998. Patent: *Formable sandwich construction material and use of the material as construction material in vehicles, refrigerators, boats etc*. World Intellectual Property Organization. IP number WO 98/01295.
110. Clyne, T.W. and Markaki, A.E., 2001. Patent: *Ultra light stainless steel sheet material*. U.S.P. Office. IP number 6,764,772. App. No. 10/000,117.
111. Markaki, A.E. and Clyne, T.W., 2003. *Mechanics of thin ultra-light stainless steel sandwich sheet material Part I. Stiffness*. Acta Materialia. **51**: pp. 1341-1350.

-
112. Markaki, A.E. and Clyne, T.W., 2003. *Mechanics of thin ultra-light stainless steel sandwich sheet material Part II. Resistance to delamination*. Acta Materialia. **51**: pp. 1351-1357.
 113. Mohr, D., 2005. *On the role of shear strength in sandwich sheet forming*. International Journal of Solids and Structures. **42**: pp. 1491-1512.
 114. Ashby, M.F., Evans, A.G., Fleck, N.A., Gibson, L.J., Hutchinson, J.W. and Wadley, H.N.G., 2000. *Metal foams: A design guide*. Butterworth Heinemann.
 115. Contorno, D., Filice, L., Fratini, L. and Micari, F., 2006. *Forming of aluminium foam sandwich panels: Numerical simulations and experimental tests*. J. Materials Processing Technology. **177(1-3)**: pp. 364-367.
 116. McCormack, T.M., Miller, R., Kesler, O. and Gibson, L.J., 2001. *Failure of sandwich beams with metallic foam cores*. International Journal of Solids and Structures. **38**: pp. 4901-4920.
 117. Bart-Smith, H., 2001. *Measurement and analysis of the structural performance of cellular metal sandwich construction*. International Journal of Mechanical Sciences. **43**: pp. 1945-1963.
 118. Chen, C., Harte, A.-M. and Fleck, N.A., 2001. *The plastic collapse of sandwich beams with a metallic foam core*. International Journal of Mechanical Sciences. **43**: pp. 1483-1506.
 119. Banhart, J., 2001. *Manufacture, characterisation and application of cellular metals and metal foams*. Progress in Materials Science. **46**: pp. 559-632.
 120. Stöbener, K., Baumeister, J., Lehmus, D., Stanzick, H. and Zöllmer, V., 2003. *Composites based on metallic foams: Phenomenology; production; properties and principles*. In: International Conference "Advanced Metallic Materials". Smolenice, Slovakia.

121. Jackson, K.P., 2007. *Incremental sheet forming machine tool path design, machine operation guidelines and tool force system design, Version 1*. University of Cambridge Department of Engineering.
122. Kirkup, L., 1994. *Experimental methods: An introduction to the analysis and presentation of data*. John Wiley & Sons.
123. Hertzberg, R.W., 1996. *Deformation and fracture mechanics of engineering materials*. Fourth.Ed.: John Wiley & Sons, Inc.
124. Anon., 1951. *The welding, brazing and soldering of copper and its alloys*. The Copper Development Association. 47.
125. Roberts, P.M., 1975. *Brazing*. Oxford University Press.
126. Brandes, E.A. and Brook, G.G., 1999. *Smithells Metal Reference Book*. Seventh Edition.Ed.: Butterworth Heinemann.
127. Avitzur, B., 1983. *Handbook of metal-forming processes*. John Wiley and Sons, Inc., Canada.